

# **Evaluation and Retrofitting of Prestressed Concrete Girder Bridge with Excessive Vibration**

Ikram Hasan Efaz

Graduate Research Assistant,

Department of Civil Engineering, University of Texas at Arlington

Presented to the Faculty of the Graduate School of The University of Texas at Arlington in

Partial Fulfillment of the requirements for the Degree of

DOCTOR OF PHILOSOPHY



THE UNIVERSITY OF TEXAS AT ARLINGTON

MAY 2021

Copyright © by Ikram Hasan Efaz 2021

All Rights Reserved



## Acknowledgments

Firstly, I would like to thank The Almighty for giving me opportunities and patience to complete this rigorous but rewarding journey. Then I would like to express my gratitude to my advisor Dr. Nur Yazdani for his continuous support and guidance during my doctoral education. His continuous supports and suggestions with patience and motivation helped me conducting my research and dissertation. I am also grateful to Dr. Raad Azzawi, Dr. Suyun Ham, Dr. Samantha Sabatino and Dr. Kent L Lawrence for serving on my dissertation committee and for their encouragement and support during my study.

I would like to recognize the financial support from the Texas Department of Transportation (TxDOT). I also like to thank Walter Fisher III from TxDOT Dallas District for his valuable advice. I would also like to thank Dr. Ali Abolmaali and every other official from the department of Civil Engineering at UTA for giving me the Graduate Teaching Assistantship several times, for their advice and directions starting from my admission to graduation.

I am thankful to Dr. Eyosias Beneberu for his continuous help and guidance during the research work. Also, I would like to thank Dr. Zaid Momani, Dr. Towfiqul Quadir, Dr. Santosh Timilsina, Mezanur Rahman, Khadiza Binte Jalal, Dr. Yazan Almomani, Dr. Natawut Chaiwino, Dr. Tariq Al Jaafreh, Karzan Habeeb, Sean Natelli, Dr. Adam K Stein and Adam for all the advice and hard work during the experiment. I am deeply grateful to my parents and my wife for their sacrifices and supports without which it would be impossible for me to continue my doctoral journey.

April 26, 2021

## Abstract

### Evaluation and Retrofitting of Prestressed Concrete Girder Bridge with Excessive Vibration

Ikram Hasan Efaz, PhD

The University of Texas at Arlington

Supervising Professor: Dr. Nur Yazdani

Vibration of a highway bridges is a serviceability issue according to American Association of State Highway and Transportation Officials (AASHTO). Though vibration is one of the primary reasons of bridge deck cracking, AASHTO only has a deflection limit to counterpart vibration which is not adequate according to many researchers. For instance, SH-75 SB Bridge over Wilson Creek in McKinney, Texas was observed to have excessive vibration and cracking on the concrete deck. To evaluate the condition of the bridge, Ground Penetrating Radar (GPR) and Impact Echo (IE) were used on the deck as Non-Destructive Evaluation (NDE) methods. A diagnostic load test was also conducted to obtain the load carrying capacity of the deck and the girders. Though GPR showed satisfactory cover, IE showed severe delamination of the top of the deck prevalent on the top of the girder lines. The load test additionally revealed partial-composite action between the girders and the precast panel/cast in place deck system. Moreover, a follow-up load test after a year confirmed the loss of composite action by revealing similar results to the first load test. A combined NDE and load testing method was used to load rate the girders and the deck of the bridge successfully which showed that both deck and girders were able to carry the load. However, propagation of cracks, potholes and severe vibration on deck should be considered as future concerns in terms of serviceability and durability.

Ambient vibration testing was also conducted on the SB bridge and on two other bridges with no vibration issue for comparison. The girders and deck of the SB showed significantly higher lateral and vertical accelerations than the control bridges. On the other hand, the fundamental frequency of the SB bridge was very low compared to the literature. The lower natural frequency can be explained by the reduced stiffness of the girders and the deck-panel system due to the delamination and partial-composite action.

A Finite Element Model (FEM) was prepared in ABAQUS CAE using the geometric and material properties of the SB bridge. The FEM was calibrated based on the load test and vibration test results so that the model could represent the actual condition of the bridge. Several retrofitting and stiffening methods were studied in the model to check the effectivity of the retrofitting methods. Finally, a comparative cost analysis was prepared for these proposed retrofitting methods based on the Average Low Bid Unit Prices from the Texas Department of Transportation (TxDOT) and some general recommendations were made for future research.

## Table of Contents

Chapter 1 .....	19
INTRODUCTION .....	19
1.1 Background .....	19
1.2 Problem Statement .....	22
1.3 Objectives.....	24
1.4 Organization of the Dissertation .....	25
Chapter 2.....	27
LITERATURE REVIEW .....	27
2.1 Bridge Vibration.....	27
2.2 Non-Destructive Evaluation and Diagnostic Load Test of Bridges.....	34
2.3 Finite Element Modeling and Calibration of the Test Bridge.....	43
2.3.1 Concrete Damaged Plasticity Modeling.....	43
2.3.2 Calculating Prestress Loss .....	45
2.3.3 Applying Prestress Using Thermal Loading.....	46
2.3.4 Energy Balance of Finite Element Modeling.....	47
2.3.5 Modeling Partial-Composite Action.....	48
2.4 Retrofitting and Stiffening the Superstructure for Partial-Composite Action.....	50
2.4.1 Welded Headed Studs.....	50
2.4.2 Bolted Shear Connectors .....	51
2.4.3 Coiled Spring Pins:.....	52
2.4.4 Adhesive Anchor .....	53
2.4.5 Stud Welded to a Plate.....	54
2.4.6 Epoxy Plate.....	55
2.4.7 Stiffening Superstructure to Increase Natural Frequency and Reduce Vibration .....	55
Chapter 3.....	57
BRIDGE DESCRIPTION.....	57
3.1 Introduction .....	57
3.2 Material Properties .....	59
3.3 Layout and details .....	60

Chapter 4.....	62
EXPERIMENTAL PROCEDURE.....	62
4.1 Instrumentation for Load Testing.....	62
4.1.1 Phase 1.....	62
4.1.2 Phase 2.....	64
4.2 Load Testing of The Bridge.....	66
4.2.1 Phase 1.....	66
4.2.2 Phase 2.....	69
4.3 Truck Mounted GPR.....	70
4.4 IE Device.....	70
4.5 NDE Procedure.....	72
4.6 Ambient Vibration Test.....	73
4.6.1 SH-75 SB Bridge.....	74
4.6.2 Wilson Creek NB Bridge.....	75
4.6.3 Virginia Parkway NBML Bridge.....	78
4.7 Vibration Test during Static Load Test.....	82
Chapter 5.....	84
FINITE ELEMENT MODELING.....	84
5.1 Initial Model Development.....	84
5.2 Material Properties.....	88
5.2.1 Concrete.....	88
5.2.2 Prestressing Strands.....	91
5.2.3 Mild Reinforcing Steel.....	93
5.3 Loading.....	93
Chapter 6.....	95
RESULTS AND DISCUSSION.....	95
6.1 Load Test.....	95
6.1.1 Phase 1.....	95
6.1.2 Phase 2.....	103
6.2 NDE.....	111
6.2.1 GPR Results.....	111
6.2.2 IE Results.....	112

6.3 Load Rating .....	113
6.3.1 Deck Capacity .....	113
6.3.2 Girder Capacity .....	116
6.4 Dynamic Vibration Test .....	118
6.4.1 Ambient Vibration Test .....	118
6.4.2 Vibration Test During Static Load Test .....	122
6.5 Modeling .....	126
6.5.1 Stability Check .....	126
6.5.2 Static Calibration .....	129
6.5.3 Dynamic Calibration .....	133
Chapter 7 .....	137
<b>BRIDGE REHABILITATION/RETROFITTING .....</b>	<b>137</b>
7.1 Proposed Retrofitting Methods .....	137
7.1.1 Re-casting on the Girder Lines and Shear Pockets on the Panel Lines (High Strength Concrete) .....	137
7.1.2 Re-casting on the Girder Lines and Shear Pockets on the Panel Lines (Regular Strength Concrete) .....	140
7.1.3 Re-casting on the Girder Lines and Panel Lines (High Strength Concrete) .....	141
7.1.4 Re-casting on the Girder Lines and Panel Lines (Regular Strength Concrete) .....	143
7.1.5 Re-casting on the Girder Lines with Additional Shear Connectors .....	144
7.1.6 Undercut Anchors .....	150
7.1.7 Shear Keys .....	159
7.1.8 Dense Concrete Overlay .....	161
7.2 Summary of the Retrofitting Methods .....	163
7.5 Cost Analysis .....	164
7.5.1 Removing 2'' overlay and replacing it with Dense Concrete Overlay .....	164
7.5.2 Constructing Shear Keys at the end of the Girders (Item 420- Class C Concrete Bent, HPC) .....	165
7.5.3 Removing 12'' wide concrete from the girder line/panel line and replacing it with high strength/regular strength concrete .....	165
7.5.4 Removing 12'' wide concrete from the girder line and replacing it with high strength/regular strength concrete (Adding additional shear rebar) .....	166
7.5.5 Removing 24'' wide concrete from the girder line/panel line and replacing it with high strength/regular strength concrete .....	166



7.5.6 Removing 24'' wide concrete from the girder line and replacing it with high strength/regular strength concrete (Adding additional shear rebar) .....	167
7.5.7 Undercut Anchor .....	167
Chapter 8.....	168
CONCLUSION AND RECOMMENDATIONS .....	168
8.1 Summary .....	168
8.1 Findings and Conclusions .....	169
8.1.1 NDE and Load Tests.....	169
8.1.2 Ambient and Dynamic Vibration Tests .....	170
8.1.3 Finite Element Modeling and Retrofitting.....	170
8.2 General Recommendation and Future Research .....	171
Appendix.....	175
Appendix A .....	175
Appendix B .....	177
Appendix C .....	181
Appendix D .....	185
References.....	193

**List of Figures**

Figure 2- 1: Deflection vs span length: (a) Simple spans; and (b) Continuous spans (Barker, 2011) .....	28
Figure 2- 2: First flexural frequency vs static deflection curve (Canadian standards, 1990) .....	29
Figure 2- 3: First flexural frequency vs static deflection curve (Australian codes, 1996).....	30
Figure 2- 4: Maximum vertical accelerations of Bridges for everyday events (curve 1) and storm condition (curve 2) by Irwin (1978).....	30
Figure 2- 5: Fundamental frequency vs maximum span length of bridges (Amman, 1995) .....	32
Figure 2- 6: Ambient window of a signal (Neitzel et al., 2011) .....	33
Figure 2- 7: Averaged frequency spectrum of FFT (Neitzel et al., 2011) .....	34
Figure 2- 8: GPR device: (a) Car-mounted GPR; and (b) 2.16 GHz antenna .....	35
Figure 2- 9: (a) Corroded rebars of post corroded slab; and (b) Concrete slab after accelerated corrosion (right) (Zaki et al., 2018) .....	35

Figure 2- 10: a-scan of the concrete slab: (a) Before; and (b) After accelerated corrosion (Zaki et al., 2018) .....	36
Figure 2- 11: b-scan of the concrete slab: (a) Before; and (b) After accelerated corrosion (Zaki et al., 2018) .....	36
Figure 2- 12: Accelerated corrosion setup (Raju et al., 2018) .....	37
Figure 2- 13: Qualitative relationship between GPR amplitude and rebar mass loss: (a) #4 rebar, 1 in. cover; (b) #4 rebar, 2 in. cover; (c) #7 rebar, 1 in. cover; and (d) #7 rebar, 2 in. cover (Raju et al., 2018) .....	38
Figure 2- 14: Tank for accelerated corrosion (Hasan and Yazdani, 2015) .....	39
Figure 2- 15: Rebars with different degrees of corrosion (Hasan and Yazdani, 2015) .....	39
Figure 2- 16: Maximum amplitude vs rebar area loss: (a) Dielectric constant 2.73; (b) Dielectric constant 5.47; and (c) Dielectric constant 9.3 (Hasan and Yazdani, 2015) .....	40
Figure 2- 17: GPR contour map showing the cover for a new bridge deck (Hasan and Yazdani, 2014) .....	41
Figure 2- 18: Condition assessment maps: (a) Carter Creek Bridge; and (b) Van Buren Bridge (Gucunski et al., 2008) .....	42
Figure 2- 19: Response of concrete to uniaxial loading: (a) Tension; and (b) Compression .....	44
Figure 2- 20: No end slip on full-composite beam with stress-strain distribution (University of Ljubljana, 2016) .....	48
Figure 2- 21: Endsip on partial-composite beam with stress-strain distribution (University of Ljubljana, 2016) .....	49
Figure 2- 22: Welded headed studs mounted onto a girder (Sinoars, 2016) .....	50
Figure 2- 23: Headed studs welded to the steel girder after water blasting (Collin, et al., 2015) .....	51
Figure 2- 24: Various kinds of bolted connectors (Veljkovic, et al., 2013) .....	52
Figure 2- 25: Different bolt connectors used by Known, et. Al. (2009): (a) Double-nut bolt connector; and (b) High-tension friction-grip bolt connector .....	52
Figure 2- 26: Coiled spring pin .....	53
Figure 2- 27: Hydraulic jack used for inserting spiral pins into the bridge (Collin, et al., 2015) .....	53
Figure 2- 28: Adhesive anchor (HASAA) connector (Kwon, et al., 2009) .....	54
Figure 2- 29: Stud welded to a plate .....	54
Figure 2- 30: Epoxy plate .....	55

Figure 2- 31: Widening bent of a pedestrian bridge .....	56
Figure 2- 32: Stiffening bearing pads by installing shear keys: (a) View from the top; and (b) View from the bottom.....	56
Figure 3- 1: Location map of the US 75 over Wilson Creek Bridge .....	57
Figure 3- 2: Wilson Creek Bridge, McKinney.....	58
Figure 3- 3: Visible cracks on the deck .....	58
Figure 3- 4: Repaired pothole on the deck.....	59
Figure 3- 5: Slab plan for span 3.....	60
Figure 3- 6: Typical transverse slab section .....	61
Figure 3- 7: Cross-section of Tx54 prestressed girder.....	61
Figure 4- 1: Instrumentation plan for load testing .....	63
Figure 4- 2: Load testing instrumentation: (a) Rotational tiltmeter; and (b) Attached strain gages .....	64
Figure 4- 3: Instrumentation plan for load test .....	65
Figure 4- 4: Dimension of the test trucks.....	66
Figure 4- 5: Location of trucks during load tests.....	67
Figure 4- 6: Trucks in position for load test .....	68
Figure 4- 7: Trucks in position for the load test.....	69
Figure 4- 8: Truck mounted GPR .....	70
Figure 4- 9: GPR scanning grid .....	70
Figure 4- 10: IE Device.....	71
Figure 4- 11: Working grid for IE scanning .....	72
Figure 4- 12: Segments of Traffic Closure for NDE .....	73
Figure 4- 13: Locations of vibration meter under the deck and the girders for SB Bridge .....	74
Figure 4- 14: Vibration meter under the Wilson Creek SB Bridge: (a) Girder; (b) Deck; (c) Bearing pad; and (d) Bent cap .....	75
Figure 4- 15: Plan view of the NB Bridge .....	76
Figure 4- 16: Typical transverse slab section of the NB Bridge.....	76

Figure 4- 17: Locations of vibration meter under the deck and the girders for SB Bridge .....	77
Figure 4- 18: Google map location of Virginia Parkway bridge .....	78
Figure 4- 19: Accessible space under the Virginia Parkway Bridge .....	78
Figure 4- 20: Plan view of span 1 in Virginia Parkway bridge .....	79
Figure 4- 21: Typical transverse slab section of span 1 in Virginia Parkway Bridge .....	79
Figure 4- 22: Locations of the vibration data logger for the Virginia Parkway Bridge.....	81
Figure 4- 23: Load test paths with the vibration data logger location .....	82
Figure 4- 24: Dump truck for vibration test during static load testing .....	83
Figure 5- 1: Tx54 girder: (a) Mild rebars shown in the girder; and (b) Mild rebars shown separately .....	84
Figure 5- 2: Reinforcements of the girder in ABAQUS (2018) interface .....	85
Figure 5- 3: Typical TxDOT non-skewed panel plan.....	85
Figure 5- 4: Location and placement of typical TxDOT panel for prestressed concrete girders..	86
Figure 5- 5: ABAQUS model: (a) Panels on girders; and (b) Rebar wireframes .....	86
Figure 5- 6: Surfaces for girder to haunch contact: (a) Master surface; and (b) Slave surface ....	87
Figure 5- 7: Contact surfaces between the deck and the panel .....	87
Figure 5- 8: Half-scale bridge model: (a) 5 girders with panels and deck; and (b) 5 in. native mesh .....	88
Figure 5- 9: Concrete strength gain with time .....	89
Figure 5- 10: Concrete modulus of elasticity with time .....	90
Figure 5- 11: Amplitude of the applied prestress in different steps of the model .....	91
Figure 5- 12: Temperature profile of the model during step 1 (0-1 second) .....	92
Figure 5- 13: Applied prestress on the ABAQUS model: (a) Girder strands; and (b) Panel strands .....	92
Figure 5- 14: Live load pattern for designing a highway bridge according to AASHTO (2017). 93	
Figure 5- 15: Amplitudes of the multiple-step loading.....	94
Figure 6- 1: Raw strain data for path P1 run 1.....	95
Figure 6- 2: Strain vs time diagram for Path P1 Run 1.....	96

Figure 6- 3: Strain vs time diagram for Path P1 Run 2.....	96
Figure 6- 4: Strain vs time diagram for Path P2 Run 1.....	97
Figure 6- 5: Strain vs time diagram for Path P2 Run 2.....	97
Figure 6- 6: Strain vs time diagram for Path P3 Run 1.....	98
Figure 6- 7: Strain vs time diagram for Path P3 Run 2.....	98
Figure 6- 8: Strain vs time diagram for the stop location test.....	99
Figure 6- 9: Neutral axis calculation.....	100
Figure 6- 10: Locations of the neutral axis obtained from the load test (Phase 1).....	101
Figure 6- 11: Rotation vs. time for Path P2 Run 1 .....	102
Figure 6- 12: Refined rotation data for Path P2 Run 1 .....	102
Figure 6- 13: Raw strain data for Path P1 Run 1 .....	103
Figure 6- 14: Strain vs time diagram for Path P1 Run 1.....	104
Figure 6- 15: Strain vs time diagram for Path P1 Run 2.....	104
Figure 6- 16: Strain vs time diagram for Path P2 Run 1.....	105
Figure 6- 17: Strain vs time diagram for Path P2 Run 2.....	105
Figure 6- 18: Strain vs time diagram for Path P3 Run 1.....	106
Figure 6- 19: Strain vs time diagram for Path P3 Run 2.....	106
Figure 6- 20: Strain vs time diagram for the stop location test.....	107
Figure 6- 21: Locations of the neutral axis obtained from the load test (Phase 2).....	108
Figure 6- 22: New pothole on the deck of Span 3: (a) View from the top; and (b) View from the side .....	109
Figure 6- 23: Strain response of the deck portions for Path P2 Run 1.....	109
Figure 6- 24: Rotation vs time for Path P1 Run 1 .....	110
Figure 6- 25: Refined rotation data for Path P1 Run 1 .....	111
Figure 6- 26: 2-D contour plots showing rebar covers from GPR data .....	112
Figure 6- 27: Contour plots from IE data showing possible delamination.....	113
Figure 6- 28: Negative moment region (hatched area) and girder center line (black line) on a portion of GPR contour.....	114
Figure 6- 29: Positive moment region (left) and negative moment region (right) from IE data .....	115
Figure 6- 30: Maximum acceleration of the SB Bridge: (a) Transverse acceleration of the girder; and (b) Vertical acceleration of the deck .....	119

Figure 6- 31: Maximum acceleration of the NB Bridge: (a) Transverse acceleration of the girder; and (b) Vertical acceleration of the deck .....	120
Figure 6- 32: Maximum acceleration of the Virginia Parkway Bridge: (a) Transverse acceleration of the girder; and (b) Vertical acceleration of the deck .....	121
Figure 6- 33: Speed vs strain data for path P2 .....	123
Figure 6- 34: Speed vs strain data for path P3 .....	123
Figure 6- 35: Ambient window of the data shown in the box for path P2.....	124
Figure 6- 36: FFT analysis on a 1-second ambient window for path P2 .....	125
Figure 6- 37: History output request showing various components of energies of the model ...	126
Figure 6- 38: Internal energy vs time.....	127
Figure 6- 39: Work done by the externally applied forces ( $E_w$ ) vs time .....	128
Figure 6- 40: Total energy of the model ( $E_{total}$ ) vs time.....	128
Figure 6- 41: Residual energy as a percentage of total energy vs time plot .....	129
Figure 6- 42: Girder/deck and deck/girder surfaces for the cohesive contact interaction .....	130
Figure 6- 43: Panel/deck and deck/panel surfaces for the cohesive contact interaction.....	130
Figure 6- 44: Comparison of the strain data between the experiment and the ABAQUS model	132
Figure 6- 45: Comparison of the rotation data between the experiment and the ABAQUS model .....	132
Figure 6- 46: Cohesive contact between the girder and the deck .....	134
Figure 6- 47: Comparison between the experimental and modal frequencies.....	135
Figure 7- 1: Re-casting with high strength concrete: (a) Girder lines; and (b) Panel lines .....	137
Figure 7- 2: Removed girder lines (left exterior and two interiors).....	138
Figure 7- 3: Full composite tie contacts between the new (re-casted) and the old concrete .....	138
Figure 7- 4: Shear pockets on the girder lines .....	139
Figure 7- 5: Full composite tie contacts between the new (shear pockets) and the old concrete	139
Figure 7- 6: Re-casting with high strength concrete: (a) Girder lines; and (b) Panel lines .....	141
Figure 7- 7: Recasting on the girder lines and the panel lines (high strength concrete).....	142
Figure 7- 8: Re-casting on the girder lines with additional shear connectors.....	144
Figure 7- 9: Typical spacing of shear rebars of TxDOT girders.....	145
Figure 7- 10: Typical spacing of rebars of the calibrated ABAQUS model.....	146

Figure 7- 11: Recasting on the girder lines and the pane line with additional R rebars (R2).....	147
Figure 7- 12: Recasting on the girder lines and the pane line with additional R rebars (R3).....	147
Figure 7- 13: Recasting on the Girder lines and Panel lines.....	149
Figure 7- 14: An undercut anchor embedded inside concrete .....	150
Figure 7- 15: Break-out cone for undercut anchor: (a) Tension; and (b) Shear .....	150
Figure 7- 16: Tension cones of the undercut anchors (red block) .....	151
Figure 7- 17: 80 anchors on each side of the girders .....	152
Figure 7- 18: 60 anchors on each side of the girders .....	153
Figure 7- 19: 40 anchors on each side of the girders .....	153
Figure 7- 20: 20 anchors on each side of the girders .....	154
Figure 7- 21: Tension cones of the undercut anchors (red block) .....	156
Figure 7- 22: 80 anchors on each side of the girders .....	157
Figure 7- 23: 60 anchors on each side of the girders .....	157
Figure 7- 24: 40 anchors on each side of the girders .....	158
Figure 7- 25: 20 anchors on each side of the girders .....	158
Figure 7- 26: Stiffening bearing pads using shear keys: (a) Typical cross-section; and (b) Constructed shear keys .....	159
Figure 7- 27: Shear Keys near the support of a girder .....	160
Figure 7- 28: Dense concrete overlay (2'' on the top) modeled in ABAQUS .....	161
Figure 7- 29: Dense concrete overlay with shear keys (2'' on the top) modeled in ABAQUS..	162

## List of Tables

Table 2- 1: Peak acceleration for human response (Wright and Walker, 1971).....	31
Table 3- 1: Wilson Creek SB Bridge (Span 3) properties .....	59
Table 4- 1: Truck axle weights for load test .....	66
Table 4- 2: Truck speeds and location for Crawl Speed Test .....	68
Table 4- 3: Truck axle weights for load test .....	69
Table 4- 4: Comparison between SB and NB bridges .....	77
Table 4- 5: Comparison between Virginia Parkway Bridge and Wilson Creek SB Bridge .....	80
Table 5- 1: Compressive strength and modulus of elasticity of the elements of the SB bridge ...	90
Table 6- 1: Neutral axes locations .....	108
Table 6- 2: Deck moment capacity .....	115
Table 6- 3: Deck moment rating factor and bridge member rating .....	116
Table 6- 4: Comparison between hand calculation and CSIBridge results .....	117
Table 6- 5: Maximum accelerations for different components of the SB bridge .....	118
Table 6- 6: Maximum accelerations for different components of the NB bridge.....	119
Table 6- 7: Maximum accelerations of different components of Virginia Parkway bridge .....	120
Table 6- 8: Comparison of the maximum accelerations .....	121
Table 6- 9: Modal frequencies of the Wilson Creek SB bridge.....	125
Table 6- 10: Strain values at the bottom of the girder B4B from the experiment and the ABAQUS model .....	131
Table 6- 11: Comparison between the experimental and the modal frequencies .....	135



Table 7- 1: Comparison of the stress, strain and the location of the neutral axis for an interior girder of the calibrated and the retrofitted model .....	140
Table 7- 2: Comparison of the stress, strain and the location of the neutral axis for an interior girder of the calibrated and the retrofitted model .....	141
Table 7- 3: Comparison of the stress, strain and the location of the neutral axis for an interior girder of the calibrated and the retrofitted model .....	143
Table 7- 4: Comparison of the stress, strain and the location of the neutral axis for an interior girder of the calibrated and the retrofitted model .....	144
Table 7- 5: Different spacings of the shear rebars modeled in ABAQUS .....	146
Table 7- 6: Comparison of the stress, strain and the location of the neutral axis for an interior girder of the calibrated and the retrofitted model .....	148
Table 7- 7: Comparison of the natural frequency for an interior girder of the calibrated and the retrofitted model.....	149
Table 7- 8: Different number of anchors per side modeled in ABAQUS .....	152
Table 7- 9: Comparison of the stress, strain and the location of the neutral axis for an interior girder of the calibrated and the retrofitted model .....	154
Table 7- 10: Comparison of the natural frequency for an interior girder of the calibrated and the retrofitted model.....	159
Table 7- 11: Comparison of the natural frequency for an interior girder of the calibrated and the retrofitted model.....	160
Table 7- 12: Comparison of the natural frequency for an interior girder of the calibrated and the retrofitted model.....	162
Table 7- 13: Summary of the proposed retrofitting methods.....	163
Table 7- 14: Cost analysis of removing a 2'' overlay and replacing it with dense concrete overlay .....	164
Table 7- 15: Cost analysis of constructing shear keys at the end of the girders .....	165
Table 7- 16: Cost analysis of removing 12'' wide concrete from the girder/panel line and replacing it with high strength/regular strength concrete .....	165

Table 7- 17: Cost analysis of removing 12’’ wide concrete from the girder line and replacing it with high strength/regular strength concrete (Adding additional shear rebar) .....	166
Table 7- 18: Cost analysis of removing 24’’ wide concrete from the girder line and replace it with high strength/regular strength concrete.....	166
Table 7- 19: Cost analysis of removing 24’’ wide concrete from the girder line and replacing it with high strength/regular strength concrete (Adding additional shear rebar) .....	167
Table 7- 20: Cost analysis of using undercut anchors .....	167
Table 8- 1: General recommendation for the proposed retrofiting .....	172
Table 8- 2: General recommendation for the proposed retrofiting .....	172
Table 8- 3: General recommendation for the proposed retrofiting .....	173
Table 8- 4: General recommendation for the proposed retrofiting .....	173
Table 8- 5: General recommendation for the proposed retrofiting .....	173
Table 8- 6: General recommendation for the proposed retrofiting .....	174

# Chapter 1

## INTRODUCTION

### 1.1 Background

The New York State Department of Transportation correlated bridge deck cracking with vibration by studying 384 bridge spans (Alampalli, 2001). The effect of the parameters such as bridge vibration, span length and traffic volume were examined individually on bridge deck cracking using One-way Analysis of Variance (ANOVA) analyses. The data suggested that the vibration parameter affects deck cracking most severely and longer span length creates a worse situation in terms of cracks and vibration.

The unusual vibration of highway bridges causes human discomfort and long-term durability of the deck/panel system. However, highway bridge vibration has been ignored by codes and researchers as a serviceability issue. For example, the American Association of State Highway Officials (AASHTO, 2017) only enforces a deflection limit which is not sufficient to mitigate vibration (Barker, 2011; Gaunt 1981; Oeheler, 1970; Thunman, 1987). Also, a typical dynamic impact factor (DMF) (Nguyen & Tran 2015; Mohseni et. al. 2018; Malla et. al. 2017) is used to increase the live load without considering the vibration severity. Furthermore, Alampalli (2001) concluded that vibration severity is the most significant parameter affecting deck cracking, especially for long-span bridges. In addition, vibration severity can be accounted for by the peak acceleration of the deck, girder, bearing pad and other components of the highway bridges during the regular flow of traffic.

The majority of the existing research states that humans respond to bridge acceleration rather than other vibration parameters such as deflection. Gaunt and Sutton (1981) stated that humans are more susceptible to the derivatives of displacement (jerk, acceleration, velocity etc.) rather than the displacement itself. Irwin (1978) suggested restrictions for accelerations of bridges for everyday events while Wright and Walker (1971) suggested a peak acceleration limit of 100 in./s<sup>2</sup>. Similar to acceleration, natural frequency is another critical dynamic parameter. The natural frequency depends on the mass, stiffness distribution, boundary condition and continuity condition of bridges (Grimmerlsman, 2006). The mode with the lowest natural frequency is called fundamental frequency (Damodarasamy and Kavitha, 2009) which has a direct relationship with

the stiffness of a structure (Lin and Yang, 2005). Amman (1995) correlated the fundamental frequency with the maximum span length of the highway bridges by analyzing the experimental data of 224 bridges. Likewise, Canadian standards, CSA (1990) determined a relationship between natural frequency and maximum static deflection while Australian codes, Austroads (1996) suggested a similar relationship to mitigate vibration. Additionally, Le and Hwang (2017) recognized that frequency and acceleration-based limits are more rational and efficient than AASHTO (2017) deflection limit.

By obtaining the dynamic properties such as acceleration, natural frequencies and mode shapes, the current condition of highway bridges can be assessed. To obtain the dynamic properties of highway bridges, ambient vibration testing technique is considered as one of the most popular methods since this technique requires less labor, time and cost (Idris et al., 2014). Ambient vibration is the vibration experienced by a structure under its regular operating condition without any traffic closure (Farrar & James, 1997). This testing technique has been used to regulate the dynamic characteristics (acceleration and mode shapes) of different types of bridges such as double-deck bridge (Harik et al., 1997), prestressed concrete box girder bridge (Citak et al., 2012 and Farrar et al., 1984), continuous girder bridge, cable-stayed bridge (Ren et al., 2005) and stone masonry bridge (Krstevska et al., 2008) successfully. Moreover, Idris et al. (2016) designated different modal frequencies and fundamental modes of vibration of a prestressed concrete bridge by conducting ambient vibration.

However, it is not always possible to obtain natural frequency accurately under regular traffic, especially for a very busy bridge. If there is an extreme amount of traffic, it is not realistic to obtain an ambient window to extract the natural frequencies due to extreme noise in the data. To eradicate the excessive noise in the dataset, Siringoringo and Fujino (2012) conducted an analytical and experimental vibration study by using only a model of a two-axle vehicle-bridge system and identified the first natural frequency with acceptable accuracy. Similarly, Nagayama et al. (2015) used two passing vehicles to calculate the natural frequency of a bridge and compared the experimental results with analytical values. It was discovered that under a relatively low driving speed, the analytical and experimental results showed good agreement with the largest discrepancy of 3.2%. Therefore, for the bridges with high-volume traffic on major highways, controlled single or double low-velocity vehicles can be used to obtain exact natural frequency.

After analyzing the dynamic parameters (acceleration and natural frequency), the severity of vibration of a highway bridge can be established and proper mitigations can be generated. To mitigate vibration, the superstructure can be stiffened externally by adding mass with high-level stiffness, comprising bridge members and adding damping to the system (Brown & Kashani, 2017). In addition, Twayana and Mori (2014) concluded that shear keys between the adjacent box-beams followed by transverse post-tensioning improved the fundamental frequency and reduced vibration of a skewed box-beam girder bridge by approximately 10%.

While vibration reduces the deck capacity by introducing cracking, partial-composite action reduces the capacity and the vertical and lateral stiffness of the girders. Cracks and delamination reduce the deck capacity to transfer load effectively to the girders. To evaluate the capacity of highway bridges, a diagnostic load test combined with Non-Destructive Evaluation (NDE) can be used to load rate the bridge girders and deck.

To improve the deck/girder capacity due to cracking or partial composite action, retrofitting methods can be considered without demolishing the bridges. Additionally, past studies showed that steel girder bridges can be retrofitted to increase/introduce composite action between the girder and deck (Olsson, 2017; Collin et al., 2015; Kwon et al., 2009). However, no attempt has been made so far to retrofit prestressed girder bridges to improve the girder-panels/deck composite action.

## 1.2 Problem Statement

Though vibration severity is one of the key parameters contributing to bridge deck cracking, it is often neglected as a serviceability issue. The deflection limit imposed by AASHTO (2017) sometimes yielded misleading results regarding vibration. According to many researchers (Wright & Green, 1964; Wright & Walker, 1971; Le & Hwang, 2017), a better interpretation of vibration is necessary in terms of accelerations and mode shapes.

Several Non-Destructive Evaluation (NDE) techniques are currently used for bridge deck inspection and mapping. For example, Zaki et al. (2018) successfully used Ground Penetrating Radar (GPR) to quantify the presence of rebar corrosion in a concrete slab. Raju et al. (2018) and Hasan and Yazdani (2015) related the rebar corrosion quantity with the maximum reflected wave amplitude from GPR data. Hasan and Yazdani (2014) additionally used GPR to construct a full-scale evaluation of concrete covers in a new bridge deck and determined that a significant portion (48%) of the bridge deck had inadequate cover. Inconsistency of rebar cover depths in a bridge deck might create challenges such as corrosion or reduced moment capacity due to reduced moment arm. Apart from GPR, Impact Echo (IE) can be used to evaluate bridge deck by detecting the possibilities of delamination in concrete successfully. Gucunski et al. (2005) used IE and GPR on asphalt-overlaid bridge decks to estimate concrete deteriorate quantities and possible delamination in the deck. Kee et al. (2012) utilized air-coupled IE and infrared thermography (IR) on a reinforced concrete bridge deck containing simulated delamination and cracking defects and the delamination found from both the NDE methods showed good agreement with most of the actual defects. Gucunski et al. (2008, 2009) proposed a new automated approach based on three-dimensional IE data which effectively enables an impact echo to be used as a bridge deck sonar device.

NDE methods including GPR and IE can help to locate localized cracks and delamination in the superstructure while experimental load testing can accurately determine a bridge's load efficiency and load-carrying capacity (Bujnakova et al., 2018). In general, load testing provides a more comprehensive understanding of the load paths and their distribution through the bridge structure (Lichtenstein, 1995). Additionally, diagnostic load tests are performed to determine bridge characteristics, load response, and distribution or to validate the analytical model (AASHTO,

2017). Several Department of Transportations (DOTs) across the US have been using diagnostic load testing to evaluate condition assessment and load rating of existing bridges effectively (Hag-Elsafi et al, 2006; Lucas et al, 2004; Matta et al, 2005; TxDOT, 2020). However, a combined load test and NDE method has not been used yet to examine a prestressed concrete girder bridge with vibration issue.

While vibration reduces the serviceability of the deck, partial-composite action reduces the load-carrying capacity and stiffness of the system by inducing slip between composite surfaces. Deck capacity is also altered by longitudinal and transverse cracking due to unusual vibration. To resolve unusual vibration and deck crackings, retrofitting can be a viable solution to improve composite action for steel girder bridges. Nevertheless, there is no traditional method to retrofit a prestressed concrete girder bridge. Most likely, the cohesion and friction between contact surfaces and dowel action from the shear rebars will provide 100% composite action to the girders-deck and deck-panels surfaces. However, slip can take place between surfaces due to inefficient shear rebars, construction errors, surface corrosion, or poor material quality. Overall, partial-composite action affects the overall performance of the bridge by causing strength and serviceability issues.

### 1.3 Objectives

The current study involved instrumentation, load testing (Phase 1 and Phase 2), ambient vibration testing, dynamic load testing, dynamic vibration testing, modeling, model calibration and evaluating effective retrofitting methods for the SH-75 SB Bridge over Wilson Creek. The objectives of this research are as follows:

1. Investigate the overall performance of a highly vibrating highway bridge through instrumentation and static load testing.
2. Compare the performance after one year to evaluate the rate of deterioration through a follow up static load testing.
3. Utilize Non-Destructive Evaluation (NDE): Ground Penetrating Radar (GPR) and Impact Echo (IE) on the deck to assess the condition of the deck for surface wearing, cracks and delamination.
4. Propose a novel technique to rate the girder and deck of the bridge by combined load testing and NDE method.
5. Conduct ambient vibration testing under regular traffic for the SB Bridge and compare the results with other control bridges that do not have significant vibration problem.
6. Conduct dynamic vibration testing under controlled traffic to find the natural frequency and mode shapes of the bridge.
7. Prepare a realistic 3D finite element model of the bridge to simulate geometrical and material properties as well as boundary conditions to understand the overall behavior of the bridge.
8. Calibrate the 3D FEM model based on the experimental load testing and dynamic vibration testing result, hence capturing the behavior of the in-site bridge.
9. Study several retrofitting methods to increase the composite action and lateral stiffness of the girders and panels/deck and evaluate their effectiveness.



## 1.4 Organization of the Dissertation

The dissertation is organized in eight different chapters. The content of the chapters is described below:

### *Chapter 1: Introduction*

This chapter provides a brief introduction of the background and motivation of the research, problem statement and objective.

### *Chapter 2: Literature Review*

This chapter presents a history of bridge vibration, previously conducted research regarding vibration, vibration related codes and specifications, NDE and load test evaluation, FEM modeling and model calibration. This chapter also highlights the history of bridge retrofitting and stiffening.

### *Chapter 3: Bridge Description*

This chapter presents the background, material properties and detailing of the SH-75 SB bridge.

### *Chapter 4: Experimental Procedure*

The instrumentation of the load tests, NDE (GPR and IE) tests, Ambient Vibration Test and Vibration test during static load test are provided in detail in this chapter.

### *Chapter 5: Finite Element Modeling*

This chapter details the step-by-step model development including the material properties and loading condition and steps.

### *Chapter 6: Results and Discussion*

The results obtained the NDE, load tests and vibration tests are presented in this chapter. Also, the model stability and calibration are discussed in this chapter.

### *Chapter 7: Bridge Rehabilitation/Retrofitting*

This chapter presents the proposed retrofitting methods, their modeling results and a comparative cost analysis of each methods.

## *Chapter 8: Conclusion and Recommendation*

This chapter concludes with a summary and findings of the NDE and load tests, vibration tests and FEM modeling of the retrofitting methods. Some general recommendations are also provided for future research in this specific area.

## Chapter 2

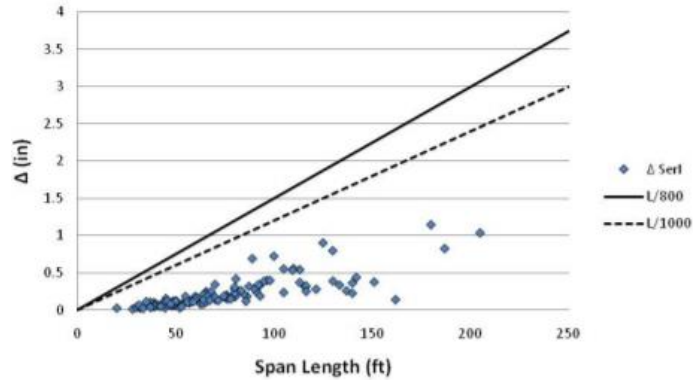
### LITERATURE REVIEW

#### 2.1 Bridge Vibration

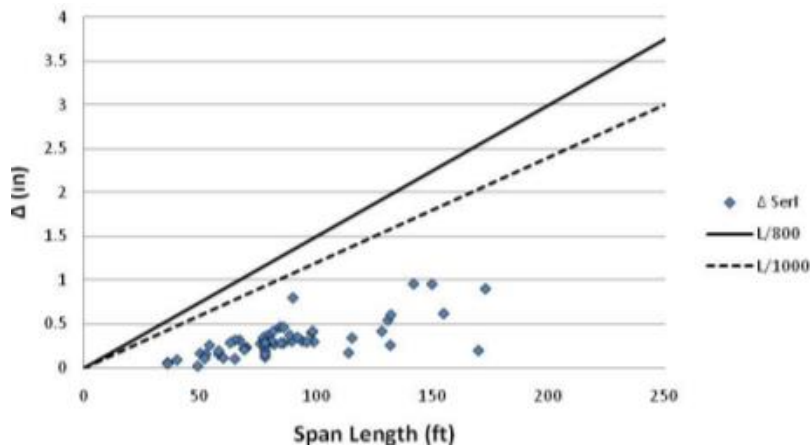
Serviceability is one of the most important concerns during bridge design, construction, and evaluation. By studying various vibration parameters such as deflection, acceleration, velocity, and frequency, researchers concluded that the deflection limit is the most commonly used parameter since it can be easily calculated theoretically and experimentally. AASHTO LRFD specification (2017) imposed deflection limit of  $L/800$  ( $L$ = span length) for regular highway bridges and  $L/1000$  for the pedestrian bridge which was also adopted by the Korean code (MLTM, 2010). After a comprehensive study on live load deflection, Roeder et al. (2002) concluded that AASHTO (2017) deflection limits are not sufficient to control the bridge vibration after conducting extensive research on live load deflection. Though the AASHTO (2017) deflection limit was initially introduced to control bridge vibration, more effective alternative methods have been developed. However, there is wide variability in the alternative methods due to variability in load magnitude, load pattern, load factors and lane load distribution factors. Moreover, a few limitations also decrease the efficiency of the alternative methods.

The difference between the live load deflection limits in different states may go beyond 1,000% due to various load patterns and magnitude used by various states. While some states use truck as the load, other states use lane loads and some use a combination of the two. Maximum deflection is recorded for truckloads and lanes loads for short span and long span bridges, respectively. Therefore, the AASHTO (2017) live-load deflection regulates the design of bridges for large  $L/D$  ( $L$ =span length,  $D$ =depth) ratios and vice versa.

Some of the bridges which satisfied the AASHTO (2017) deflection limits showed poor vibration performance. After studying 195 steel girder bridges, Barker (2011) posited that current AASHTO (2017) criteria may be inadequate to counter bridge vibration. The deflections vs the span length plots for simple and continuous spans are provided in Figures 2-1 (a) and 2-1 (b), respectively to clarify the behavior of the bridges. The figures also compare the results with the current AASHTO (2017) criteria.



(a)



(b)

Figure 2- 1: Deflection vs span length: (a) Simple spans; and (b) Continuous spans (Barker, 2011)

It can be concluded from the figures that all the bridges meet with the current AASHTO (2017) service I criteria. Therefore, these bridges should be vibration resistant: should not cause human discomfort or vibration induced deterioration problem if the AASHTO (2017) criteria controls. In contrast, several bridges showed significant vibration induced human discomfort and deterioration. Additionally, most of the pedestrian bridges also meet the service I criteria. However, several pedestrian bridges are affected with vibration even though they comply with the code. This is another indication that the current AASHTO (2017) Service I criteria is insufficient to control bridge vibration.

While AASHTO (2017) criteria only focuses on deflection, researchers have been studying other vibration criteria such as acceleration and frequency and their effects on human susceptibility. In fact, acceleration parameter can capture human susceptibility more accurately than the displacement parameter for vibration (Gaunt, 1981). Oehler (1970) concluded that the deflection limit cannot mitigate vibration consistently. Fountain and Thunman (1987) had a similar conclusion stating that the deflection limit does not prevent human reactions inducing vibration and acceleration. Canadian standards, CSA (1990) provided a relationship between natural frequency and maximum static deflection of the superstructure of pedestrian bridges. Wright and Green (1964) also proposed a relationship after extensive analytical and field study. Figure 2-2 shows a plot of first flexural frequency vs static deflection based on Canadian standards. Australian codes, Austroads (1996) proposed a similar relationship such as the Canadian standards which is shown in Figure 2-3.

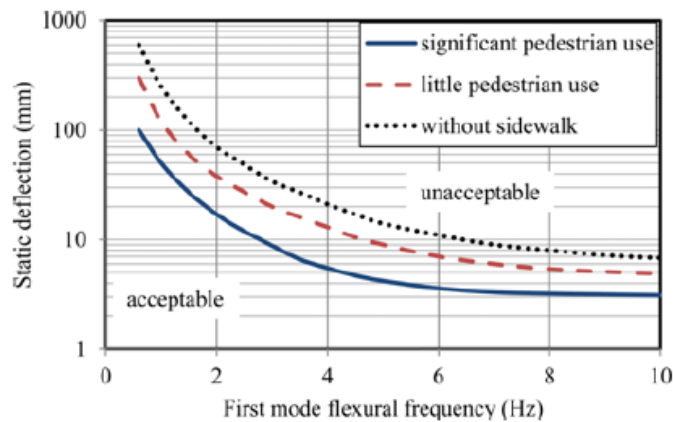


Figure 2- 2: First flexural frequency vs static deflection curve (Canadian standards, 1990)

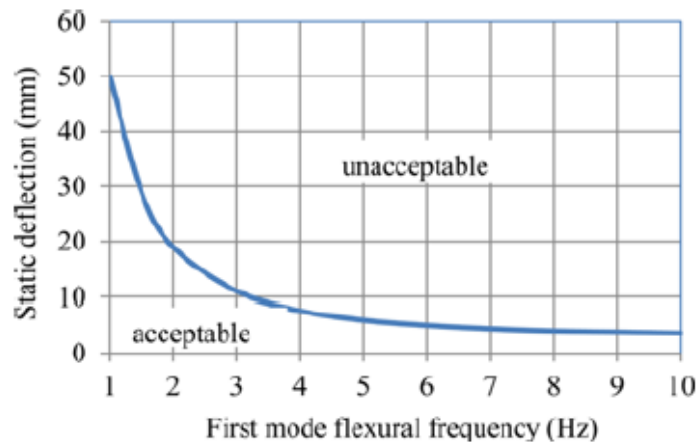


Figure 2- 3: First flexural frequency vs static deflection curve (Australian codes, 1996)

Irwin (1978) suggested limits for root-mean-square accelerations for everyday usage and storm conditions which are shown in Figure 2-4.

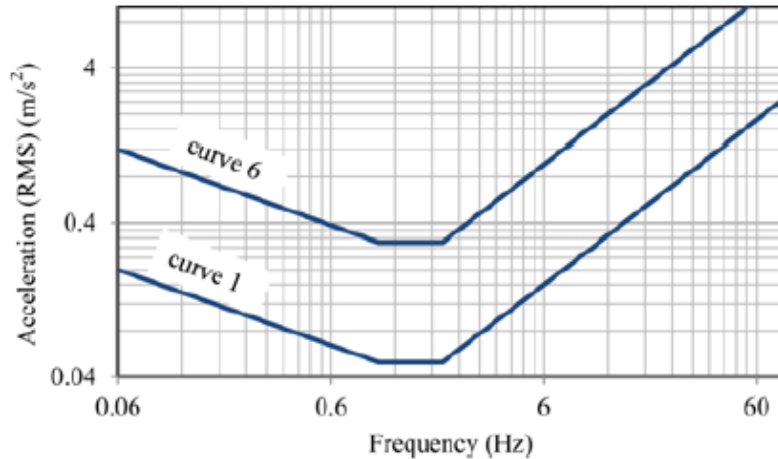


Figure 2- 4: Maximum vertical accelerations of Bridges for everyday events (curve 1) and storm condition (curve 2) by Irwin (1978)

Mallock (1902) concluded that acceleration is the primary reason for human discomfort caused by passing vehicles. Goldman (1948) produced a curve where the minimum acceleration for human discomfort and the perceptible values were set to 0.046 g and 0.025 g respectively (g = acceleration due to gravity). The acceleration response between 0.015 g- 0.025 g was established for slightly perceptible, 0.052 g for distinctly perceptible and 0.076 g for strongly perceptible (Billing & Green, 1984). Similarly, International Organization for Standards (ISO 2631-1) (1997) distinguished six levels of reactions in public transport from not uncomfortable (0.315 m/s<sup>2</sup>) to extremely uncomfortable (2 m/s<sup>2</sup>). Wright and Walker (1971) recommended the peak acceleration to prevent bridge vibration which is provided in Table 2-1.

Table 2- 1: Peak acceleration for human response (Wright and Walker, 1971)

<b>Human response</b>	<b>Peak acceleration (in./s<sup>2</sup>)</b>	
	<b>Transient</b>	<b>Sustained</b>
Imperceptible	5	0.5
Perceptible to some	10	1
Perceptible to most	20	2
Perceptible	50	5
Unpleasant to few	100	10
Unpleasant to some	200	20
Unpleasant to most	500	50
Intolerable to some	1000	100
Intolerable to most	2000	200

After conducting an extensive literature review and experimental study on different codes, Le and Hwang (2017) concluded that AASHTO (2017) deflection limits are very conservative while frequency-based limits are more effective and practical. It was also stated that Wright and Walker criteria and Canadian standards are the most appropriate for human sensitivity.

By obtaining the dynamic properties such as acceleration, natural frequencies and mode shapes, the current condition of highway bridges can be assessed. One of the assessment tools is ambient vibration which is the vibration experienced by a structure under its regular operating condition (Farrar & James, 1997). Again, ambient vibration testing technique is one of the most popular methods to acquire the dynamic properties of bridges since this technique requires less labor, time and cost (Idris et al., 2014). Since no traffic control is required to test a bridge under regular traffic, many researchers have used this technique. To regulate the dynamic characteristics of bridges,

researchers applied ambient vibration technique on different types of bridges such as a double-deck bridge (Harik et al., 1997), prestressed concrete box girder bridge (Citak et al., 2012, Farrar et al., 1984), continuous girder bridge, cable-stayed bridge (Ren et al., 2005) and stone masonry bridge (Krstevska et al., 2008). Furthermore, Idris et al. (2016) conducted an ambient vibration test on a prestressed concrete bridge and identified the different modal frequencies of the bridge and the fundamental mode of vibration. Fundamental mode is the mode with the lowest natural frequency (Damodarasamy & Kavitha, 2009). Due to its direct relationship with stiffness, the natural frequency of the bridge is a very important parameter (Lin & Yang, 2005). The natural frequency of a bridge is a function of its mass and stiffness distribution, boundary condition, and continuity conditions between various components of the structure (Grimmerlsman, 2006). Amman's (1995) study indicated that there is a correlation between fundamental frequency and maximum span length of the bridge from the experimental data analysis of 224 bridges (Figure 2-5).

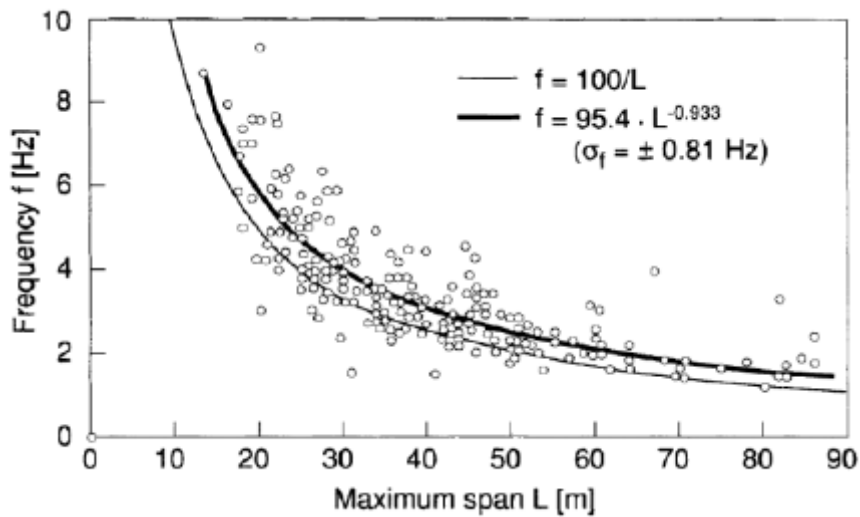


Figure 2- 5: Fundamental frequency vs maximum span length of bridges (Amman, 1995)

Furthermore, Zenunovic et al. (2015) conducted a case study and concluded that the natural frequencies and mode shapes obtained from ambient vibration tests and finite element software showed good agreement in results. The mathematical response of the new bridge was quite close to the experimental result while some deviations were observed for the older ones.



It is not always possible to obtain exact natural frequencies of bridges under regular traffic, especially for a very busy bridge. If there is an excessive amount of traffic, it is not practical to obtain an ambient window from the data to extract the natural frequencies due to extreme noise in the data. Therefore, some researchers such as Siringoringo and Fujino (2012) and Nagayama et al. (2015) used controlled traffic (one or two passing vehicles of known speed) to accurately obtain natural frequency. In addition, Siringoringo and Fujino (2012) conducted an analytical and experimental vibration study by using a model of a two-axle vehicle-bridge system and concluded that the first natural frequency can be detected with maximum error of 11.4% under 30 Km/h driving velocity. Moreover, Nagayama et al. (2015) used two passing vehicles to compute the natural frequency of a bridge and compared the results with analytical values. It was revealed that under a relatively low driving speed, the analytical and experimental results showed fair agreement with the largest discrepancy of 3.2%.

To calculate the fundamental frequency from ambient vibration data, Fast Fourier Transform (FFT) or Power Spectral Density (PSD) analyses are used on vibration signals to extract the frequencies and modes. An ambient window was found just after excitation and analyzed using FFT or PSD. Figure 2-6 shows a typical ambient window of a signal while Figure 2-7 shows FFT analyzed data.

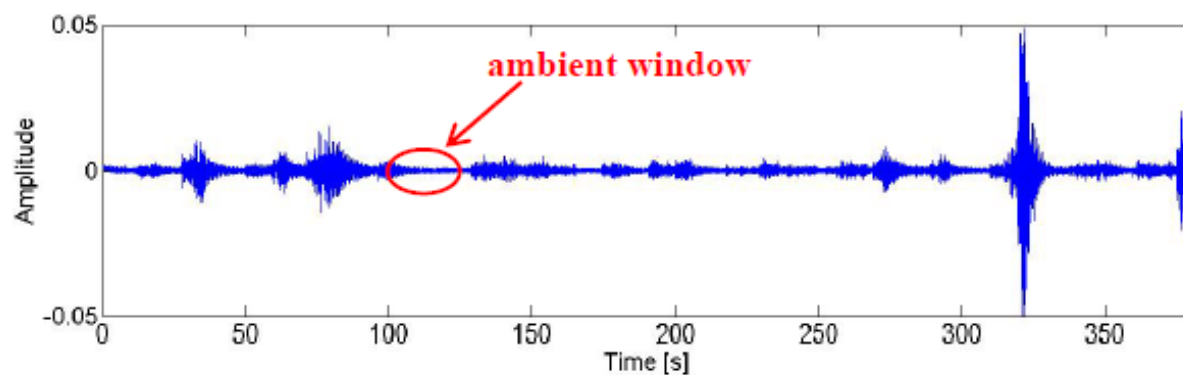


Figure 2- 6: Ambient window of a signal (Neitzel et al., 2011)

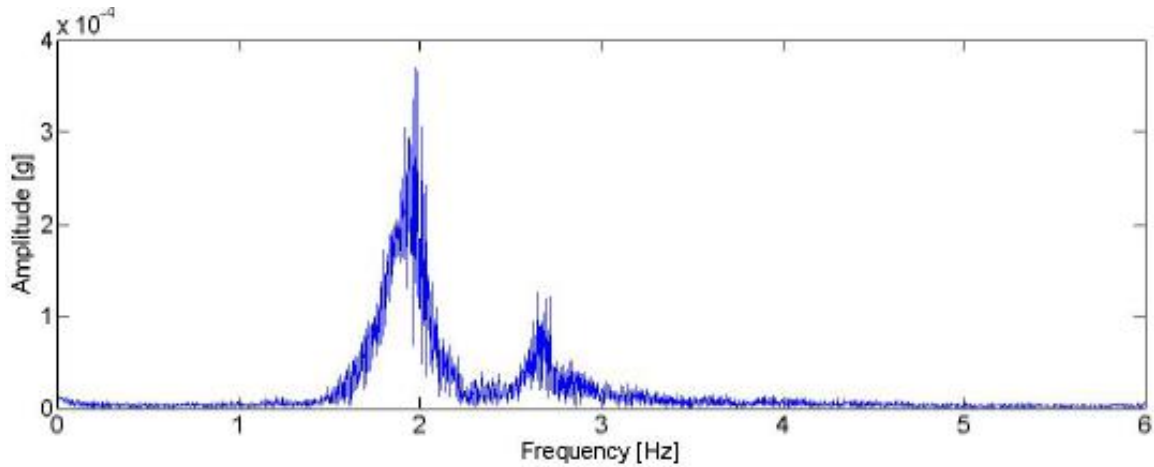


Figure 2- 7: Averaged frequency spectrum of FFT (Neitzel et al., 2011)

## 2.2 Non-Destructive Evaluation and Diagnostic Load Test of Bridges

Several Non-Destructive Evaluation (NDE) methods are used for bridge deck inspection and mapping nowadays. For example, Ground Penetrating Radar (GPR) is a cutting-edge geophysical instrument which uses radar pulses to scan the deck surface. In a bridge evaluation project, GPR is used to identify rebars, concrete cover, changes in material properties, voids, and cracks in the deck. Antennae with higher frequency (e.g., 2.6 GHz) is used for low depth analysis (0-12 inch), while lower frequency (e.g., 270 MHz) is used for higher depth evaluation (0-18 ft). Figures 2-8 (a) and (b) show a cart mounted GPR and 2.6 GHz antenna with a hand scanner, respectively.



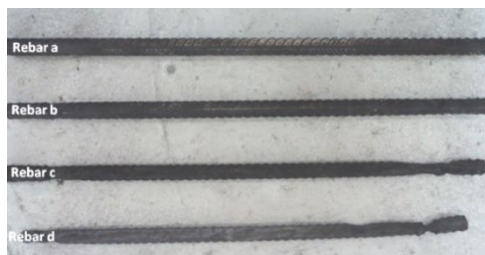
(a)



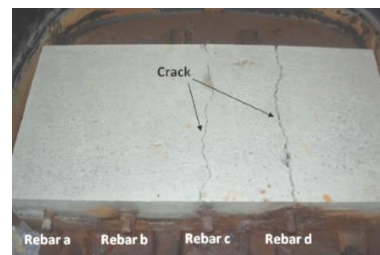
(b)

Figure 2- 8: GPR device: (a) Car-mounted GPR; and (b) 2.16 GHz antenna

Zaki et al. (2018) used GPR to scan a concrete slab and successfully detected rebar corrosion in the sample. The process involved casting the concrete slab and then scanning the slab using GPR with a 2 GHz antenna. After the scanning, imposed current technique was used to collect data from the GPR. Four different levels of corroded rebars were used to embed inside the slab (Figure 2-9) to identify and compare the corrosion.



(a)

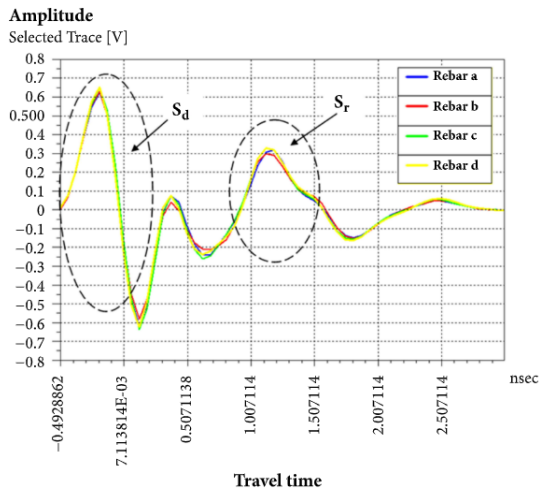


(b)

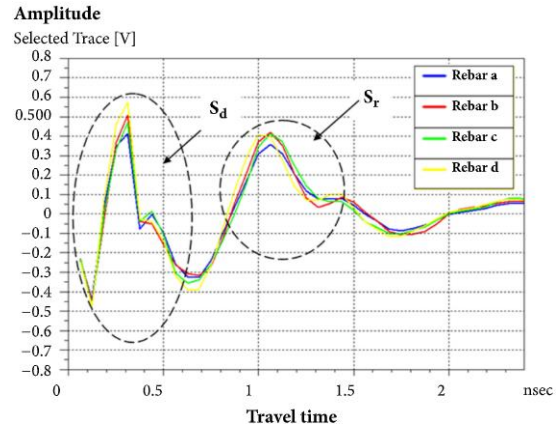
Figure 2- 9: (a) Corroded rebars of post corroded slab; and (b) Concrete slab after accelerated corrosion (right) (Zaki et al., 2018)

The a-scan and b-scan results of GPR were analyzed to identify the rebar corrosion in the concrete slab. The corrosion of the rebar can be detected successfully using the scans at an early age even before any visual corrosion damage. A-scan results showed lower amplitude and larger wave travel

times which can be explained by the corrosion products and chloride contents presented in the corroded rebars (Figure 2-10). The b-scan image was blurred and distorted indicating rebar corrosion due to the presence of chloride and other corrosive contents. Figure 2-11 shows the distorted threshold level of the image for the GPR b-scan. To sum up, the scans obtained from the GPR can successfully detect localized damage of the rebars of the concrete slab due to corrosion.

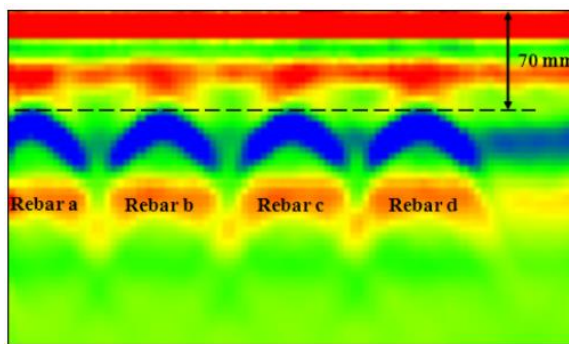


(a)

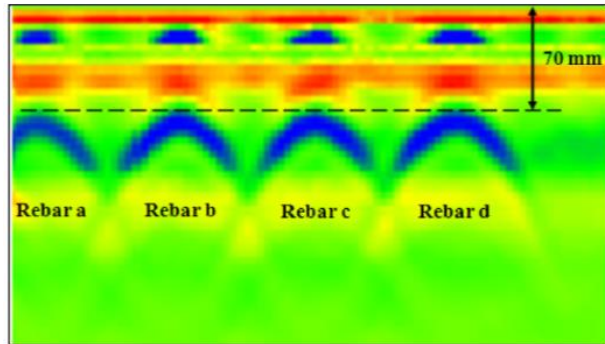


(b)

Figure 2- 10: a-scan of the concrete slab: (a) Before; and (b) After accelerated corrosion (Zaki et al., 2018)



(a)



(b)

Figure 2- 11: b-scan of the concrete slab: (a) Before; and (b) After accelerated corrosion (Zaki et al., 2018)

Raju et al. (2018) related the rebar corrosion quantity with the maximum reflected waveform amplitude from GPR scanning. Accelerated corrosion was used to induce rebar corrosion (Figure

2-12), and GPR scanning monitored corrosion at three stages: before and after submersion into the salt-water solution and at the end of a pre-set corrosion period. As expected, the rebar corrosion mass loss was greater for longer duration corrosion periods, larger rebar sizes, and lower cover. The data analysis showed that the GPR amplitude increased with increased corrosion activity. Again, a polynomial curve with high reliability, normalized for rebar size and cover, was proposed for rebar corrosion loss for a given concrete dielectric constant (Figure 2-13). Correspondingly, the model was calibrated with the GPR scan data from a portion of a demolished old concrete bridge deck.



Figure 2- 12: Accelerated corrosion setup (Raju et al., 2018)

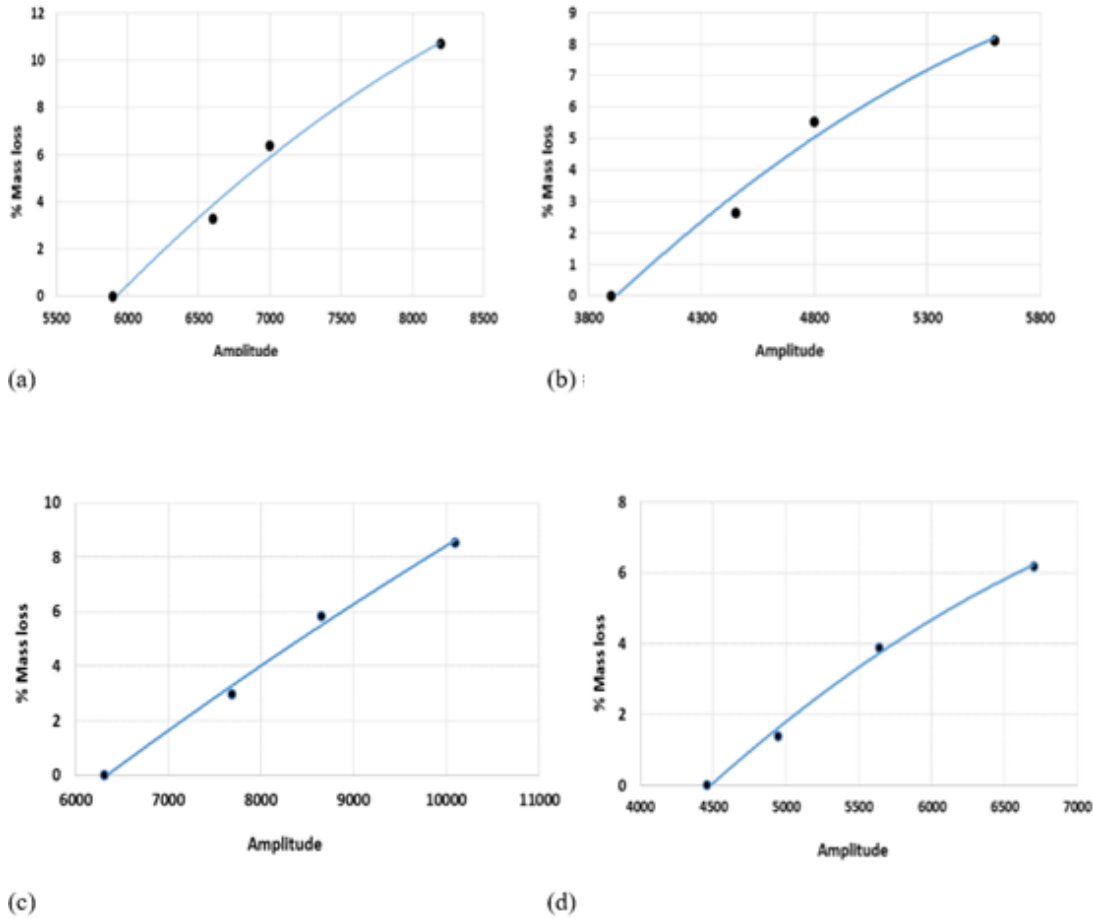


Figure 2- 13: Qualitative relationship between GPR amplitude and rebar mass loss: (a) #4 rebar, 1 in. cover; (b) #4 rebar, 2 in. cover; (c) #7 rebar, 1 in. cover; and (d) #7 rebar, 2 in. cover (Raju et al., 2018)

Hasan and Yazdani (2015) correlated the maximum positive amplitude of GPR with the reinforced concrete corrosion quantity. At first, steel rebars were immersed in a 5% brine solution and then direct current was applied to the rebar ends simulating an accelerated corrosion situation (Figure 2-14). Different levels of corrosion (0% to 45%) were simulated and the extent of corrosion was altered from 0% to 45% (Figure 2-15). Then the rebars were put inside three oil emulsion tanks with various dielectric constants similar to concrete and the maximum amplitudes from GPR were documented for the corroded bars. The maximum positive amplitude of GPR and the area loss due to corrosion of rebars demonstrated a linear relationship (Figure 2-16). It was concluded that the linear relationship between the GPR maximum amplitude and the rebar corrosion can be used as a quantitative NDE technique to assess corrosion.



Figure 2- 14: Tank for accelerated corrosion (Hasan & Yazdani, 2015)



Figure 2- 15: Rebars with different degrees of corrosion (Hasan & Yazdani, 2015)

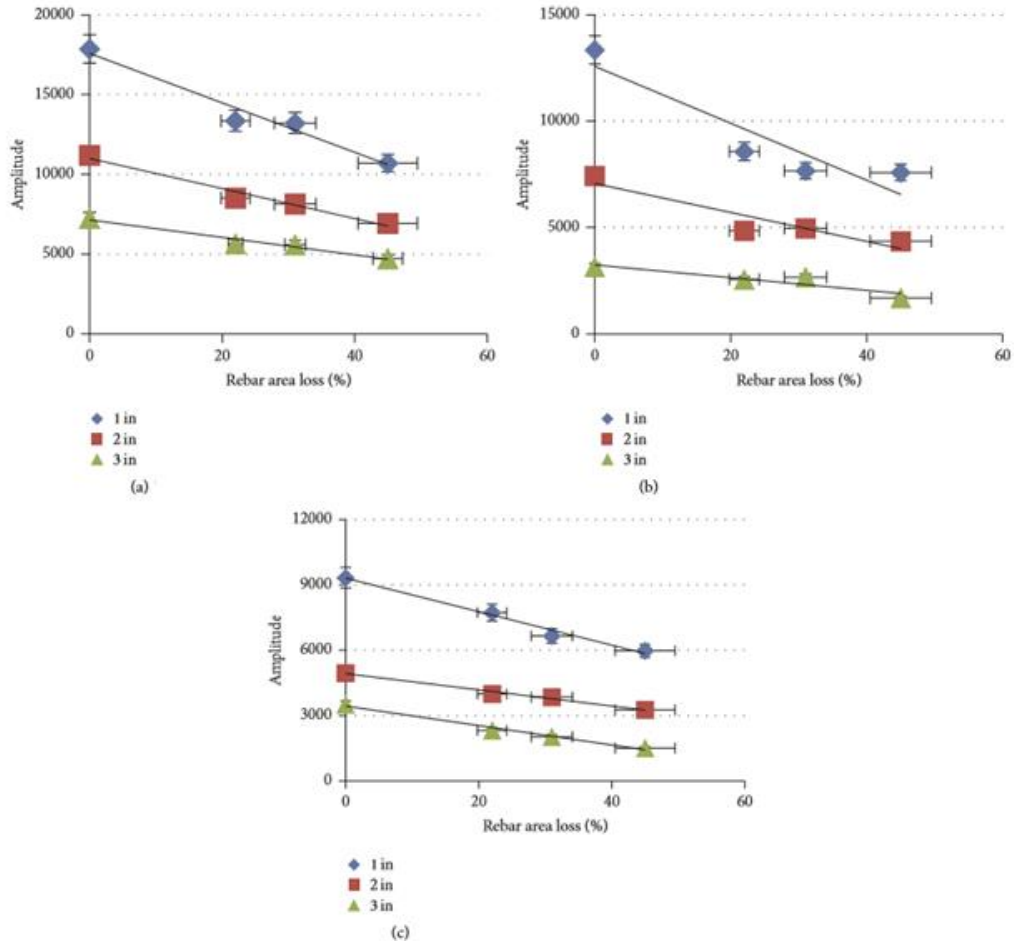


Figure 2- 16: Maximum amplitude vs rebar area loss: (a) Dielectric constant 2.73; (b) Dielectric constant 5.47; and (c) Dielectric constant 9.3 (Hasan & Yazdani, 2015)

Hasan and Yazdani (2014) used GPR contour map to construct a full-scale evaluation of concrete covers in a new bridge deck (Figure 2-17) and concluded that a significant portion (48%) of the bridge deck had inadequate cover. Inconsistency of rebar cover depths in a bridge deck might create challenges such as corrosion or reduced moment capacity due to reduced moment arm.



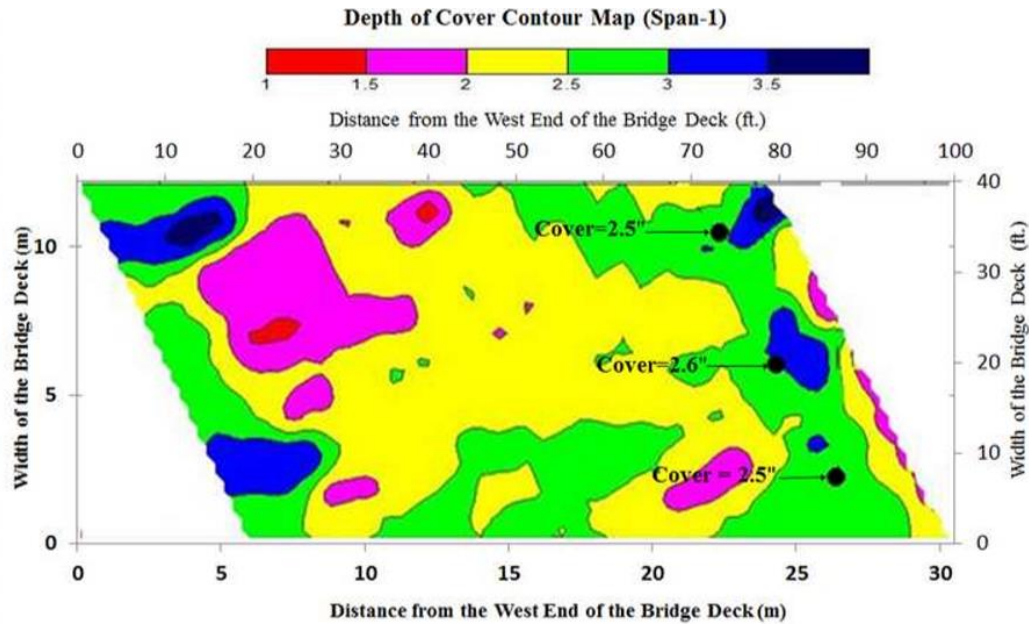
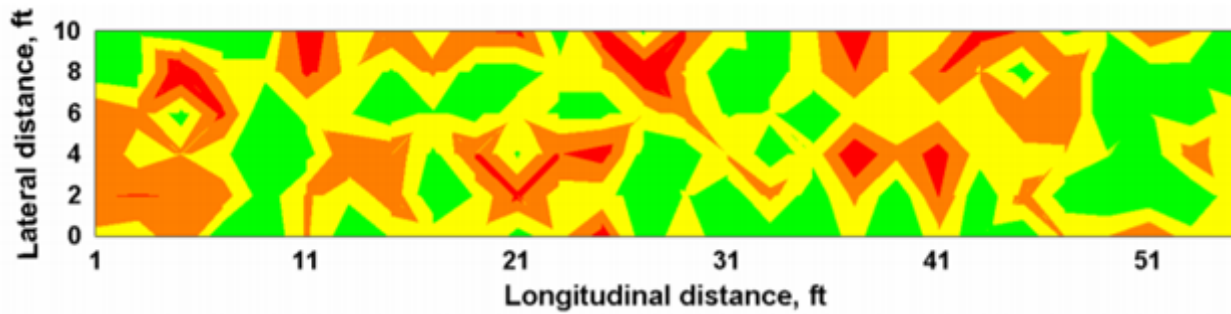


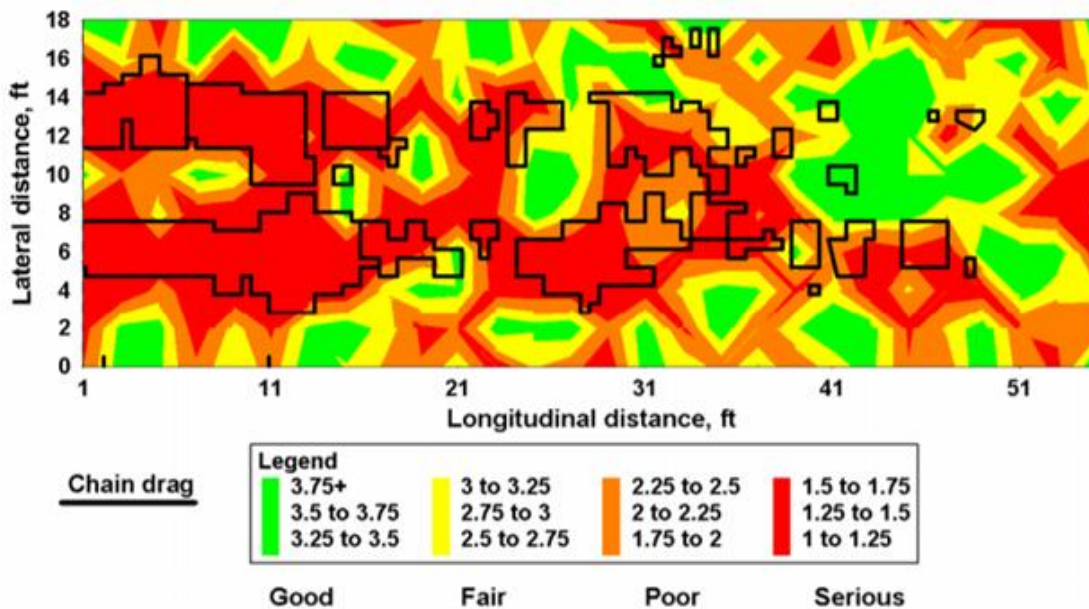
Figure 2- 17: GPR contour map showing the cover for a new bridge deck (Hasan & Yazdani, 2014)

Apart from GPR, Impact Echo (IE) can be used to evaluate bridge deck by detecting the possibilities of delamination in concrete successfully. Gucunski et al. (2005) used IE and GPR on asphalt-overlaid bridge decks to estimate concrete deteriorate quantities and possible delamination in the deck. Similarly, Kee et al. (2012) simulated delamination and cracks on a concrete bridge deck, assessed the defects with air-coupled IE and infrared thermography (IR) and the results from both the NDE methods showed good agreement with most of the actual defects. Furthermore, Gucunski et al. (2008, 2009) combined IE with other ultrasonic seismic devices to create an improved system of a bridge deck sonar device. For example, Phase Array Ultrasonic Testing (PSPA) device can be used to evaluate the surface of the pavement layers of bridge decks. Figure 2-18 (a) shows the upper condition assessment plot of the Carter Creek Bridge and the deck appeared to be in good condition with few initial and propagated delamination with a minor zone of serious delamination. On the contrary, Figure 2-18 (b) shows the bottom condition assessment plot of Van Buren bridge deck which showed significant deck deterioration and delamination. The deck was tested for delamination with chain drag and the results obtained from the drags were compared with the PSPA results. Both the chain drags and PSPA indicated seriously propagated delamination. However, chain drag is a very basic method which can only detect serious delamination with frequencies in the audible range. Therefore, the initial mild delamination

detected by the PSPA could not be identified by the chain drags. The advanced mechanism of PSPA enables the device to detect initial delamination which allows more accurate assessment of the delamination boundary and precise prediction of future propagation. Also, a better rehabilitation measure can be taken initially when minor delamination is detected before the member is too deteriorated to be recovered.



(a)



(b)

Figure 2- 18: Condition assessment maps: (a) Carter Creek Bridge; and (b) Van Buren Bridge (Gucunski et al., 2008)

NDE methods including GPR and IE can help to locate localized cracks and delamination in the superstructure while experimental load testing can accurately determine a bridge’s load efficiency

and load-carrying capacity (Schulz, 1993; El Shahawy & Garcia, 1989; Fu et al., 1992; Bakht & Jaeger 1990; Markey 1991; Moses et al., 1994, Bujnakova et al.,2018). Additionally, load testing provides a better understanding of the load paths and their distribution through the bridge structure (Lichtenstein, 1995). Diagnostic load tests are performed to determine bridge characteristics, load response, and distribution or to validate the analytical model (AASHTO, 2017). Not to mention, several DOT's have been using diagnostic load testing to evaluate condition assessment and load rating of existing bridges effectively (Lucas et al, 2004; Hag-Elsafi et al, 2006; Matta et al, 2005; TxDOT, 2020).

## **2.3 Finite Element Modeling and Calibration of the Test Bridge**

Finite Element (FE) modeling has been used extensively by researchers for load rating and evaluation purposes (Barr et al., 2006, Mabsout et al. 1997). Chung and Sotelino (2006) compared the deflection, strain, and distribution of a bridge superstructure using four different modeling techniques, and their FE model was in good agreement compared to the experimental results. Yost et al. (2005) concluded that a calibrated FE model shows a higher load rating value than a traditional FE model by conducting load rating on 200 highway bridges. Their results were used to remove the load posting of numerous bridges.

### **2.3.1 Concrete Damaged Plasticity Modeling**

Modeling material properties accurately plays a significantly important role in FE. While there are different constitutive models available to model the behavior of concrete, the smeared crack model and the plastic damage model are the two most commonly used methods. For example, concrete compressive and tensile properties are often modeled as concrete damaged plasticity in ABAQUS (2018). Because concrete damaged plasticity has a higher probability of convergence than the smeared crack model. The nonlinear behavior of concrete is related to the process of damage and plasticity which can be attributed to microcracking, strain softening, and volumetric expansion. The damaged plasticity leads to loss of strength and stiffness of concrete (Cicekli et al. 2007; Grassl & Jirásek 2006; Lubliner et al. 1989). ABAQUS (2018) uses the plasticity model proposed by Lubliner et al. (1989). The compressive and tensile behavior of concrete is as shown in Figure 2-19.

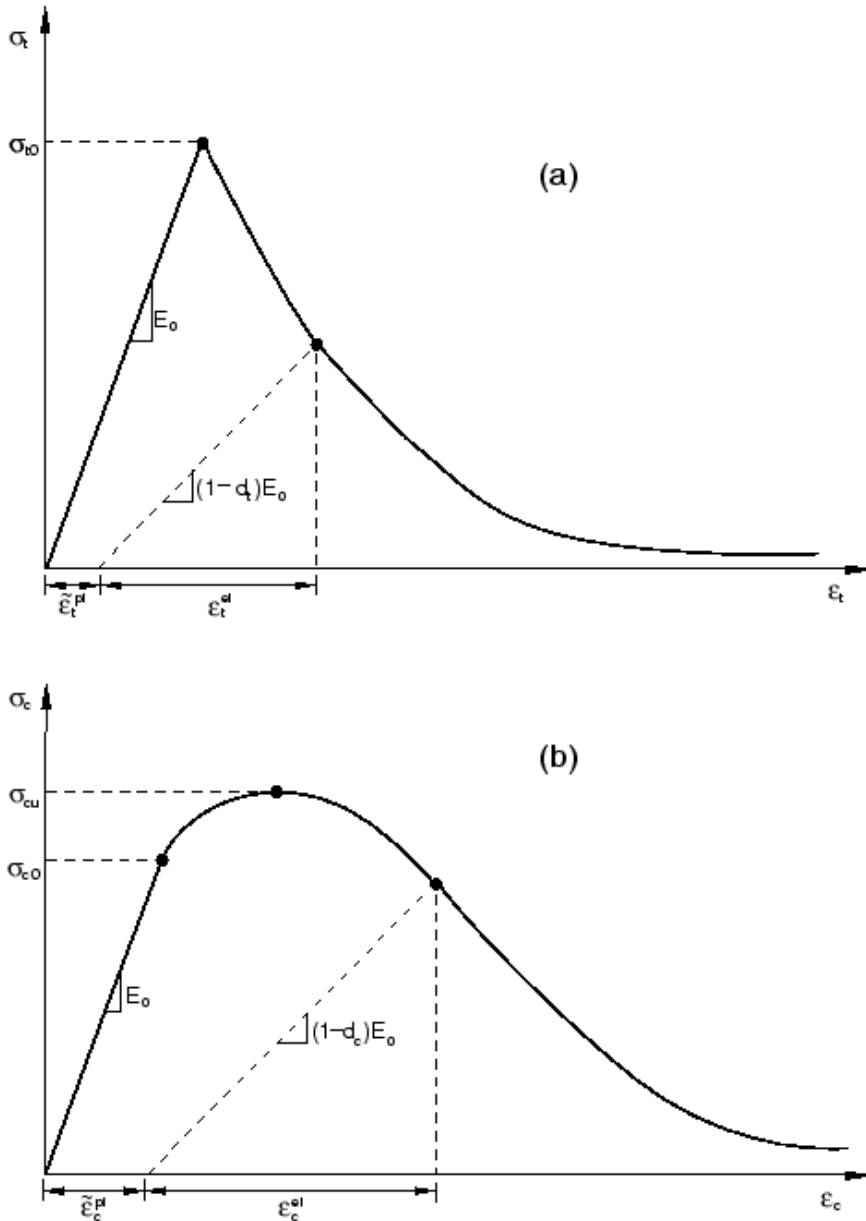


Figure 2- 19: Response of concrete to uniaxial loading: (a) Tension; and (b) Compression

Under uniaxial tension, the stress-strain response follows a linear elastic relationship until the value of the failure stress,  $\sigma_{to}$ , is reached. The failure stress corresponds to the onset of microcracking in the concrete material. Beyond the failure stress, the formation of micro-cracks is represented macroscopically with a softening stress-strain response, which induces strain localization in the concrete structure. Under uniaxial compression, the response is linear until the value of initial yield,  $\sigma_{co}$ . In the plastic regime, the response is typically characterized by stress hardening followed by strain-softening beyond the ultimate stress,  $\sigma_{cu}$  (ABAQUS, 2018). The stiffness degradation of concrete after the onset of microcracking is defined by a damage factor,  $d$

which has a value of zero for the undamaged section and one for the damaged section. Lubliner et al. (1989) proposed a simple damage model where plastic degradation occurs only in the softening range and is proportional to the compressive strength of the concrete. The damage factor,  $d$  is defined by the equation 2-1 where  $f$  is either the compressive strength or the tensile strength of concrete.

$$d = 1 - \sigma/f \quad (2-1)$$

### 2.3.2 Calculating Prestress Loss

Prestress forces are calculated according to AASHTO (2017) LRFD Bridge Design Specification by applying short-term and long-term losses for the girders' and the panels' low-relaxation strands as a part of model calibration with the experimental results. The calculated forces are applied to the model to simulate the actual prestress in the strands.

Prestress loss for the strands of the girders and the deck is calculated based on equation 2-2,

$$f_{PT} = f_{PES} + f_{PLT} \quad (2-2)$$

Where:

$f_{PT}$  = Total Prestress loss

$f_{PES}$  = Prestress loss due to elastic shortening

$f_{PLT}$  = Prestress loss due to long-term effects

Prestress loss due to elastic shortening is calculated based on equation 2-3,

$$f_{PES} = \frac{A_{ps} f_{pi} (I_g + e_m^2 A_g) - e_m M_g A_g}{A_{ps} (I_g + e_m^2 A_g) + \frac{A_g I_g E_{ci}}{E_{ps}}} \quad (2-3)$$

Where:

$A_{ps}$  = Area of prestressing strands

$f_{pi}$  = Initial prestress,  $(0.75 f_{pu})$

$f_{pu}$ = Ultimate strength of prestressing strands

$I_g$ = Moment of inertia of girder/panel

$e_m$ = Eccentricity

$A_g$ = Area of girder/deck

$M_g$ = Moment due to self-weight

$E_{ci}$ = Modulus of elasticity of concrete during the release

$E_{ps}$ = Modulus of elasticity of steel

Long term prestress loss is calculated based on equation 2-4,

$$f_{PLT} = 10 \frac{f_{pi} A_{ps}}{A_g} Y_H \cdot Y_{ST} \quad (2-4)$$

Where:

$Y_H = 1.7 - 0.01H$ ,  $H$ = Humidity in percentage

$Y_{ST} = \frac{5}{1 + f_{ci}}$ ,  $f_{ci}$ = Concrete strength during the release

### 2.3.3 Applying Prestress Using Thermal Loading

The prestressing effect can be modeled in ABAQUS (2018) using either initial strain or initial temperature (thermal load). The thermal load is used in the critical cases since it can be controlled during loading steps by varying the strand temperature. The applied temperature,  $C$  ( $^{\circ}C$ ) for the required prestress can be obtained from equation 2-5 (Ren et al., 2015).

$$C = - \frac{P}{c.E.A} \quad (2-5)$$

Where:

$P$  = Prestressing force considering all losses

$c$  = Coefficient of linear expansion ( $1 \times 10^{-5}$ )

$E$  = Modulus of elasticity of tendons

$A$  = Cross-sectional area of the tendons

### 2.3.4 Energy Balance of Finite Element Modeling

Energy balance is an important part of the linear and non-linear Finite Element Analysis (FEA). For both static and transient dynamic analyses, the total energy should remain constant throughout the solution duration. Energies are often overlooked in FEA, leading to inappropriate responses in the structure. However, comparisons between various energy components should be used to evaluate whether an analysis provides an appropriate response or not. This is required in problems involving significant instabilities which can either be global or local. The global instabilities can arise due to the release of accumulated strain energy as a result of buckling or snap, while the latter can be a result of localized buckling, localized material softening or contact separation (Optimec Consultants, 2020).

The most general means of evaluating the accuracy of response in FEA involves studying various model energies. The energy balance equation in ABAQUS (2018) is shown in equation 2-6.

$$E_I + E_V + E_{FD} + E_{KE} + E_{IHE} - E_W - E_{PW} - E_{CW} - E_{MW} - E_{HF} = E_{total} = \text{constant} \quad (2-6)$$

Where:

$E_I$  = Internal energy

$E_V$  = Viscous energy dissipated

$E_{FD}$  = Frictional energy dissipated

$E_{KE}$  = Kinetic energy

$E_{IHE}$  = Internal heat energy

$E_W$  = Work done by the externally applied force

$E_{PW}$ = Work done by contact penalties

$E_{CW}$ = Work done by constraint penalties

$E_{MW}$ = Work done by propelling added mass

$E_{HF}$ = External heat energy through external fluxes

$E_{total}$ = Total energy

In the numerical model, the total energy is only approximately constant, generally with an error of less than 1%.

### 2.3.5 Modeling Partial-Composite Action

During designing a composite beam of a bridge, an assumption is made that full interaction or full composite action is achieved. However, even under the smallest loads, a slip will emerge in the structure and change the behavior of the bridge by developing partial-composite action characteristics. Normally full composite action develops when a total interaction between the elements is achieved as a result of the shear connectors preventing slip to arise in the interface between the elements. This allows the two elements to act together with a common neutral axis and a linear strain distribution that is illustrated in Figure 2-20. Full composite action requires that the mechanical shear connectors are strong enough to withstand any type of failure or slip of the dowel i.e. the steel girders or concrete goes to failure first.

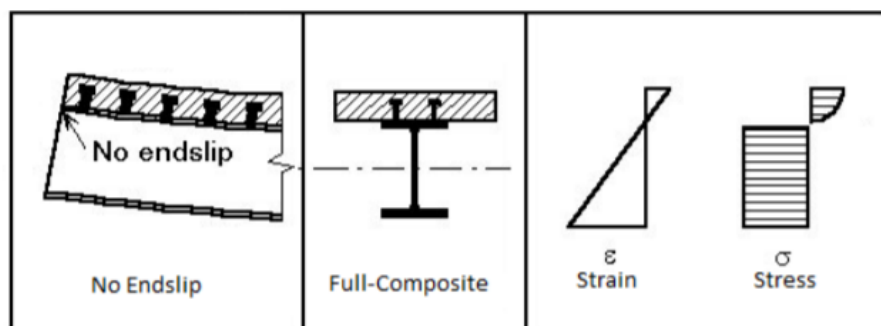


Figure 2- 20: No end slip on full-composite beam with stress-strain distribution (University of Ljubljana, 2016)



Partial-composite action on a girder is when the flexural strength will be decided by the mechanical shear connector's strength instead of the concrete plastic limit state which is the deciding factor on full composite action (Kwon, et al., 2007). The neutral axis location for a partial-composite beam will be somewhere between the neutral axis for a fully-composite and non-composite beam. Nevertheless, knowing the exact location of the neutral axis depends on several parameters for the beam including the percentage of shear connector ratio chosen. A simplified view of the stresses on a partial-composite beam can be seen in Figure 2-21.

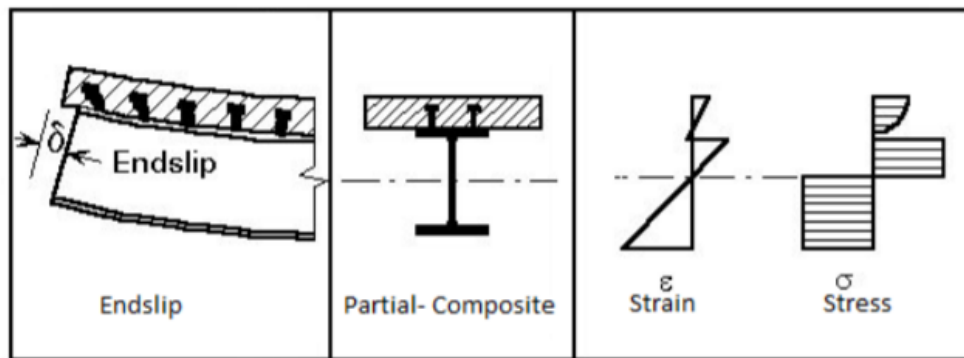


Figure 2- 21: Endslip on partial-composite beam with stress-strain distribution (University of Ljubljana, 2016)

Currently, no design codes exist in Eurocode or AASHTO (2017) for using partial-composite action in bridges so a bridge using shear connectors must either be designed as non-composite or fully composite.

To model the partially-composite action in FEA, the contact properties of the elements have to be varied. In this case, cohesive contact behavior can be used which is primarily intended for situations in which the interface thickness is negligibly small. This specific contact is defined as a surface interaction property which can be used to model the delamination at interfaces indirectly in terms of traction versus separation. To emphasize, cohesive contact assumes that the failure of the cohesive bond is characterized by progressive degradation of the cohesive stiffness (Benzeggagh et al., 1996).

The cohesive contact behavior requires three parameters to be defined:  $K_{nn}$ ,  $K_{ss}$ , and  $K_{tt}$ . The first parameter is the normal stiffness coefficient while the other two refer to shear stiffness. Albraheemi (2018) set the first parameter to a large number (109 lb./in<sup>2</sup>) during modeling partially

composite girder-deck system of a steel-girder bridge since this parameter is related to surface separation. He assumed the other two parameters (shear stiffness coefficients in the plane of the cohesive element) as equal.

## **2.4 Retrofitting and Stiffening the Superstructure for Partial-Composite Action**

No retrofitting methods have been applied on the prestressed concrete girder bridges yet to increase composite action between the girders and the deck/panel system. During design and construction, shear rebars are provided which are embedded inside the girders and the cast in place deck. Regardless, there are several methods for post-installing shear connectors onto existing steel bridges. Four different methods were examined by Olsson (2017) which are presented here:

### **2.4.1 Welded Headed Studs**

Welded headed studs can withstand horizontal and vertical tensile forces from all directions due to their cylindrical head. Figure 2-22 shows the simple method of installing these studs. However, post installing these connectors during retrofitting an existing bridge is difficult and time-consuming since the girders and the concrete deck must be exposed.



Figure 2- 22: Welded headed studs mounted onto a girder (Sinoars, 2016)

In Norway, water blasting was used to uncover the steel girder without damaging the reinforcement which is shown in Figure 2-23 (Collin, et al., 2015).



Figure 2- 23: Headed studs welded to the steel girder after water blasting (Collin, et al., 2015)

In order to expose the rebars and post installing shear connectors, traffic has to be closed which is costly and time-consuming. Traffic disturbance can be reduced by installing connectors on one girder at a time. First, the pavement and the waterproofing membrane need to be removed, the concrete can be removed by using water blasting to expose the steel girders later. Next, the studs need to be welded on the steel girder and concrete can be poured to fill the gaps. Finally, waterproofing and pavement should be installed to complete the retrofitting.

### 2.4.2 Bolted Shear Connectors

Bolted connectors use friction to transfer the stresses into the steel girders. Similar to the welded connectors, pavement and waterproofing must be removed before installing the connectors. However, access from both top and bottom is required during tightening the connectors. Various types of bolted connectors are shown in Figure 2-24 and their installation procedures are quite similar.

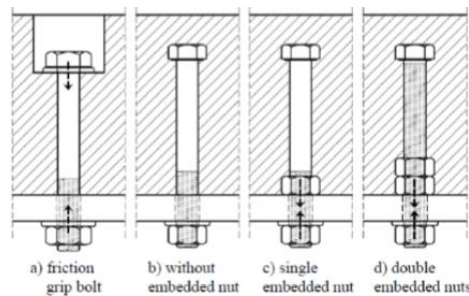


Figure 2- 24: Various kinds of bolted connectors (Veljkovic, et al., 2013)

Kwon, et al. (2009) used different types of bolted connectors successfully during retrofitting a three-span steel girder bridge in Hondo, Texas which is shown in Figure 2-25.

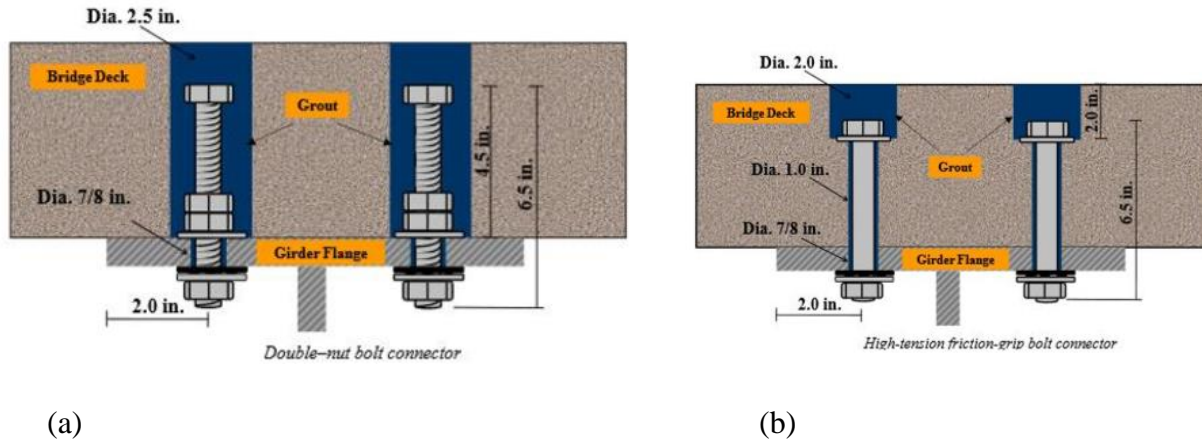


Figure 2- 25: Different bolt connectors used by Kwon, et. al. (2009): (a) Double-nut bolt connector; and (b) High-tension friction-grip bolt connector

The procedure of installing bolted shear connectors involves removing pavement and waterproofing membrane, drilling concrete from the top side of the slab (the hole needs a sufficient diameter to fit the head of the bolt), drilling a second smaller hole through the steel top flange from the top side of the slab using the same hole as in the previous step and putting the bolt, nut, and washer into place as well as tightening the anchors with a torque wrench and pouring grout to fill the gap of the concrete slab.

### 2.4.3 Coiled Spring Pins:

Coiled spring pins are cylindrical with no specific shapes and are force-fit during installation. These can be installed from the bottom of the steel girders without any adhesive or grouts with no traffic interruptions. (Craig, et al., 2001). Figure 2-26 shows a sample of the coiled spring pin.



Figure 2- 26: Coiled spring pin

Coiled spring pins have also been successfully used in creating composite action on a non-composite bridge (Pitsund Bridge). The installation involves drilling through the steel flange and into the concrete deck from underneath, applying lubricant and corrosion protection into the hole and pressing the spring pins into place by using a hydraulic jack. Figure 2-27 shows the installation of a spiral pin into a bridge.



Figure 2- 27: Hydraulic jack used for inserting spiral pins into the bridge (Collin, et al., 2015)

#### **2.4.4 Adhesive Anchor**

The adhesive anchor consists of a threaded rod, nut, and an adhesive compound which relies on adhesive forces to create the connection with concrete. The method of installing the anchors is very similar to coiled spring pins. The anchors have lower fatigue strength compared to the welded and bolted connectors thus more anchors need to be installed (Kwon, et al., 2009). Figure 2-28 shows adhesive anchor used by Kwon, et. al (2009) on a bridge near Hondo, Texas.

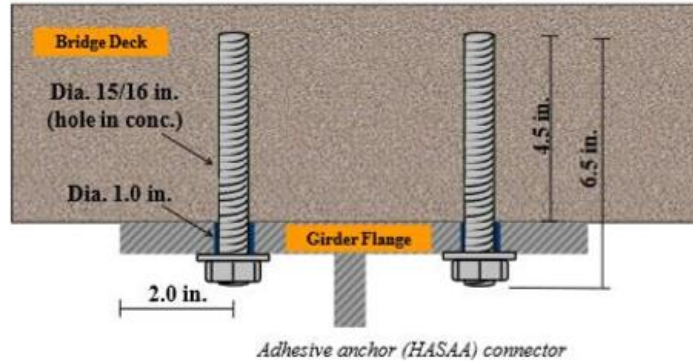


Figure 2- 28: Adhesive anchor (HASAA) connector (Kwon, et al., 2009)

Installation of the adhesive anchor consists of the following steps: Drilling through the steel top flange and partly into the concrete deck from underneath, injecting adhesive into the hole, inserting the threaded rod in a twisting motion and installing the nut and washer with a torque wrench after the curing of the adhesive.

Kwon, et al. (2007) offered two other methods to introduce composite action between non-composite steel girders and concrete deck which are: stud welded to a plate; and epoxy plate.

#### 2.4.5 Stud Welded to a Plate

The stud is welded to a separate plate that is then fillet welded onto the side of the girder (Figure 2-29)

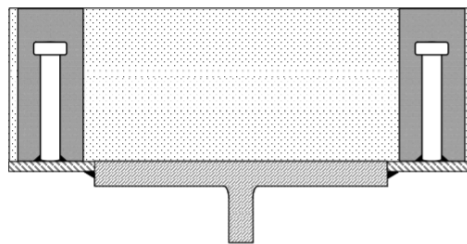


Figure 2- 29: Stud welded to a plate

## 2.4.6 Epoxy Plate

The epoxy plate uses adhesion to transfer shear between the girder and the deck. Next, a steel plate is welded to the edge of the top girder flange. Epoxy is then injected to fill the gap between the slab and plate until epoxy ejects through the holes (Figure 2-30).

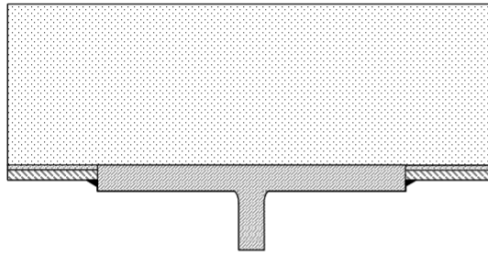


Figure 2- 30: Epoxy plate

## 2.4.7 Stiffening Superstructure to Increase Natural Frequency and Reduce Vibration

Besides providing shear connectors to develop composite action, increasing stiffness of the system can be another way of increasing the natural frequency hence reducing the vibration of highway bridges. TxDOT-Bridge Division (2009) provided some ideas and implemented them on a pedestrian bridge in Oklahoma state. These methods are as follows:

### 2.4.7.1 Continuous Deck Slab

This method stiffens the superstructure by eliminating hinges at bents. The idea is to remove the last few feet of the slab ends and re-cast them without an expansion joint. One disadvantage of this method is that it disrupts traffic, which could be mitigated by staged construction.

### 2.4.7.2 Widening Bent

This involves stiffening the bent through additional columns and frame action. Figure 2-31 shows a typical bent widening by adding additional columns to a pedestrian bridge. This method is very expensive but requires no traffic interruption.



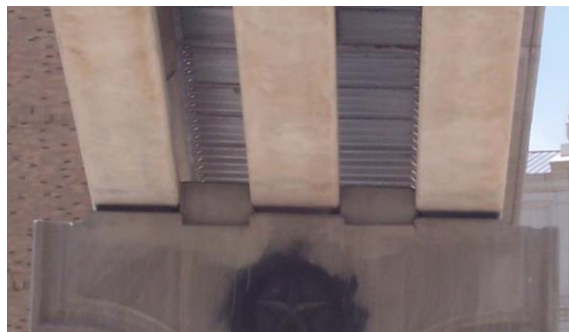
Figure 2- 31: Widening bent of a pedestrian bridge

#### 2.4.7.3 Stiffening Bearing Pad

Shear keys keep the bearing pads from translating laterally. This is the least expensive method that requires no disruptive installation. Figure 2-32 shows the shear keys installed between the bearing pads of a pedestrian bridge.



(a)



(b)

Figure 2- 32: Stiffening bearing pads by installing shear keys: (a) View from the top; and (b) View from the bottom



# Chapter 3

## BRIDGE DESCRIPTION

### 3.1 Introduction

The Sh-75 SB Bridge over Wilson Creek is located in McKinney, TX (Figure 3-1). The bridge consists of prestressed concrete girders with four spans in the SB direction (Figure 3-2). The total length of all spans is 440 feet. The deck thickness is 8.5 in., consisting of cast-in-place (CIP) deck on precast prestressed concrete deck panels. Span 3 was chosen for evaluation to optimize the work.

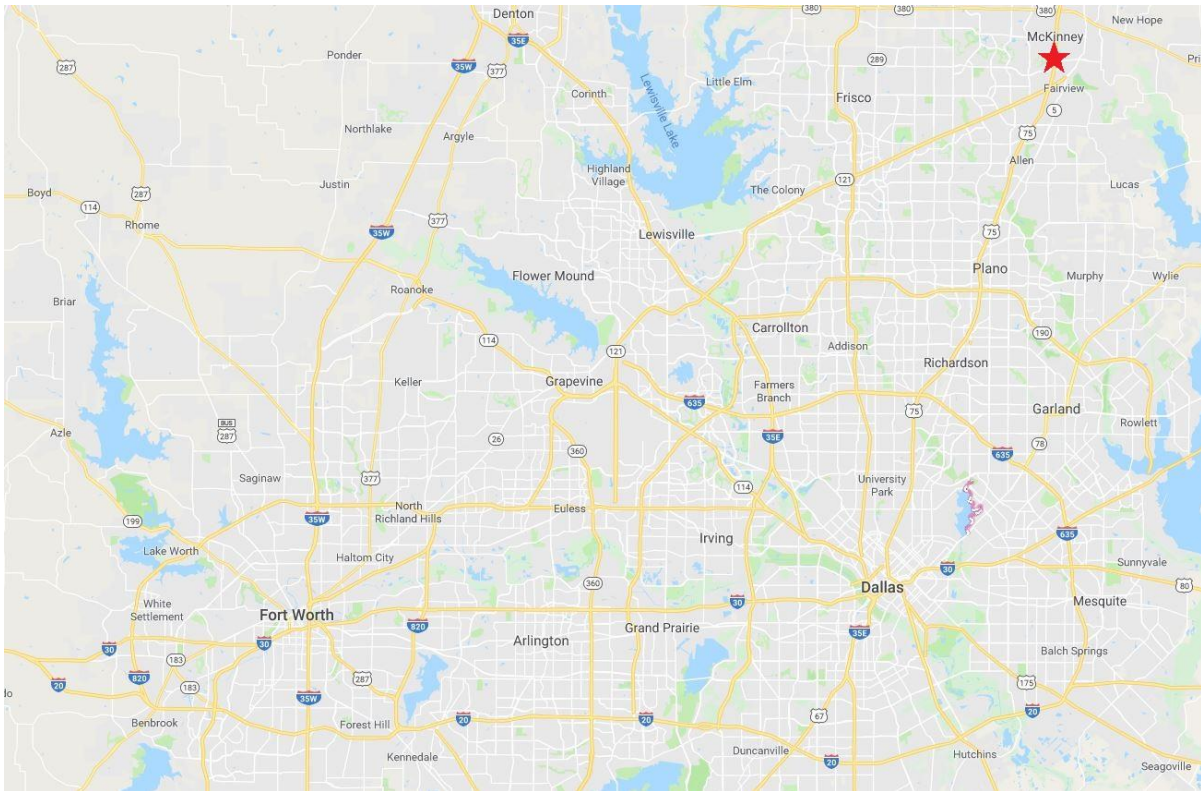


Figure 3- 1: Location map of the US 75 over Wilson Creek Bridge



Figure 3- 2: Wilson Creek Bridge, McKinney

The Bridge was observed to have excessive vibration, cracking, and potholes on the concrete deck. The University of Texas at Arlington (UTA) team was, therefore, requested by the Dallas District Bridge Section to evaluate the subject bridge. The bridge is fairly new and was constructed in 2011. Therefore, it is unusual for it to experience excessive vibration, cracking, and potholes. The UTA team initially visited the bridge site on January 29, 2018, with personnel from the Bridge Section and Area Office. Extensive transverse and longitudinal cracks, marked by the red lines in Figure 3- 3, were observed on top of the deck surface. TxDOT officials informed the team that a pothole appeared on top of the deck and was subsequently repaired (Figure 3-4). Unusually high vibration was also felt on the deck as heavy traffic flowed over the bridge.

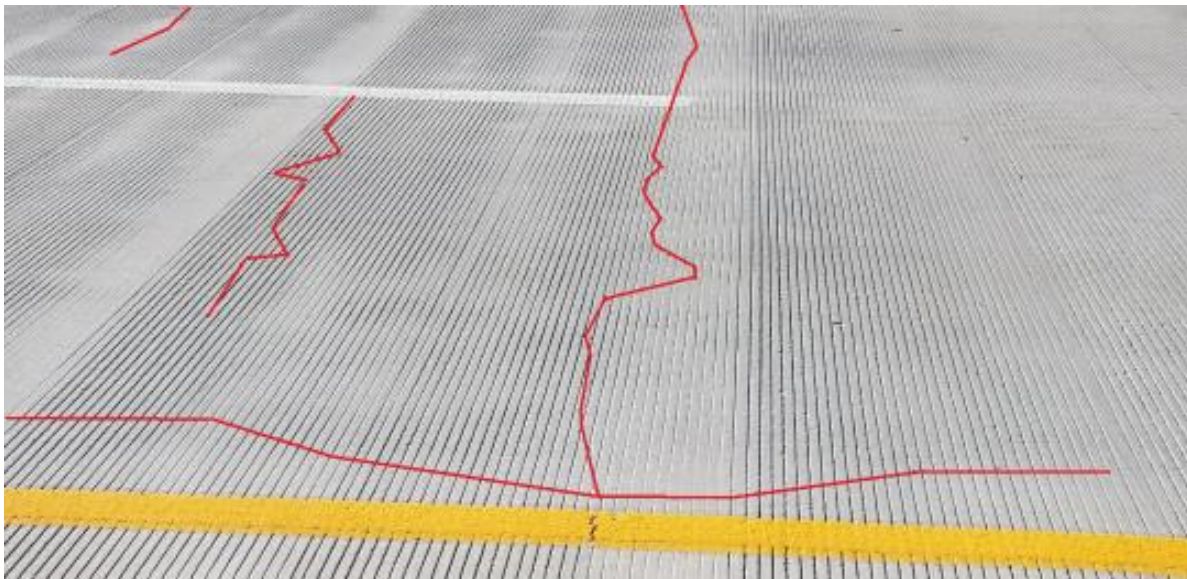


Figure 3- 3: Visible cracks on the deck



Figure 3- 4: Repaired pothole on the deck.

### 3.2 Material Properties

Relevant material properties of span 3 are shown in Table 3-1.

Table 3- 1: Wilson Creek SB Bridge (Span 3) properties

<b>Properties</b>	<b>Value</b>
Concrete compressive strength (deck) ( $f'c_{deck}$ )	4 ksi
Concrete compressive strength (girder) ( $f'c_{girder}$ )	6.2 ksi
Number of prestressing strands in each Tx54 girder	50
Strand size	0.5 in.
Strand ultimate strength	270 ksi

### 3.3 Layout and details

The slab plan and transverse typical sections of span 3 are shown in Figures 3-5 and 3-6, respectively. Tx54 prestressed girders were used, and the typical section is shown in Figure 3-7.

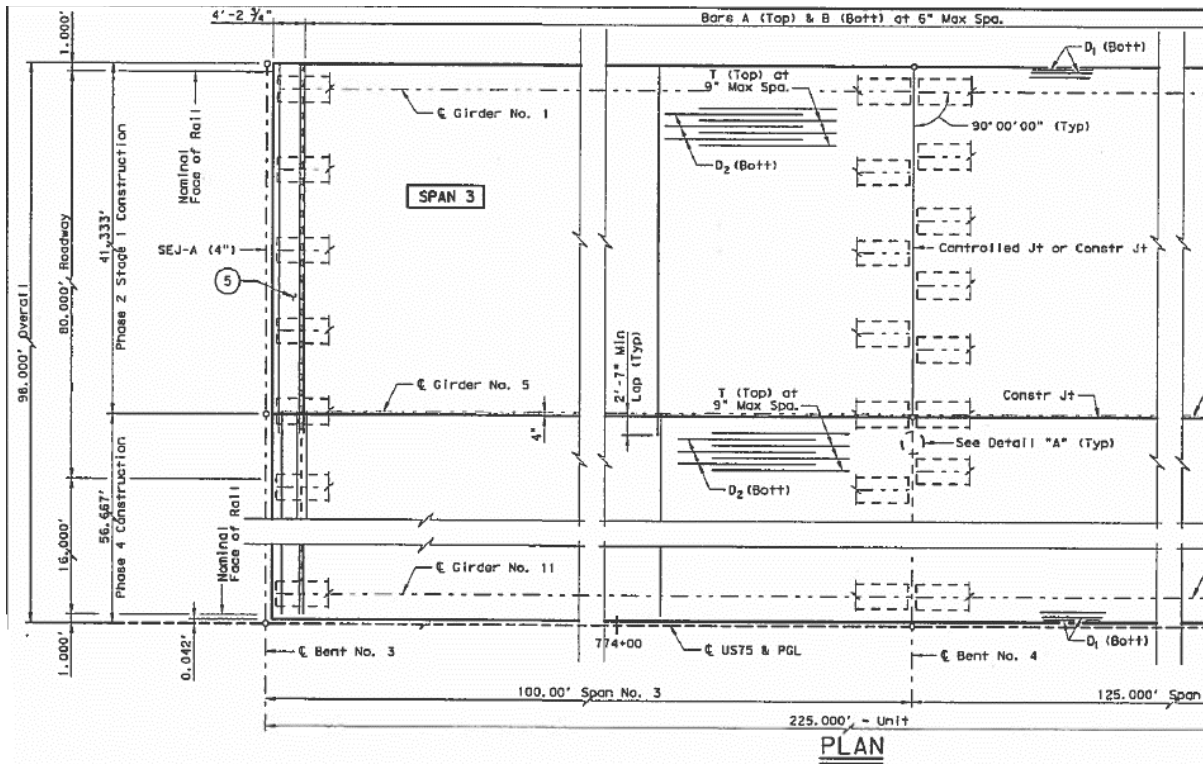


Figure 3- 5: Slab plan for span 3

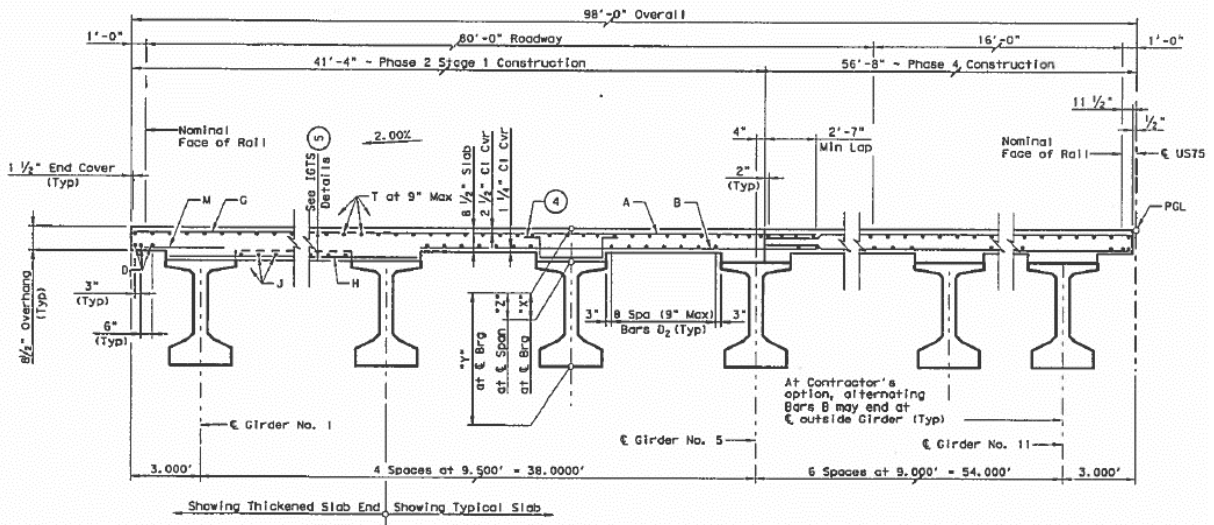


Figure 3- 6: Typical transverse slab section

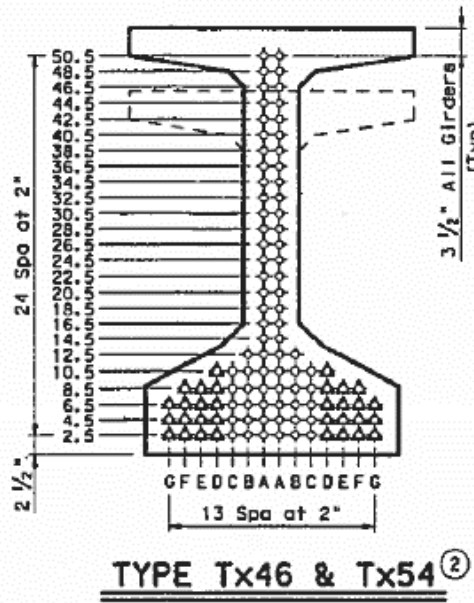


Figure 3- 7: Cross-section of Tx54 prestressed girder

## **Chapter 4**

### **EXPERIMENTAL PROCEDURE**

#### **4.1 Instrumentation for Load Testing**

A detailed plan was prepared for the instrumentation and static load testing. Only the superstructure behavior was investigated herein. Span 3 of the SB Bridge was selected for both phase 1 and 2 load tests to optimize strain gages and rotational tiltmeters instrumentation. Additionally, traffic closure was not required for the instrumentation since there were vacant spaces under the bridge for boom-lift operation. The instrumentation was conducted in three different sections along the length of the girders. The data acquisition system was placed in the middle of the bridge under Bent 4. All strain gauge wires were run along the length of the girders to the middle of Bent 4 where these were connected to the data acquisition box. The wireless data acquisition system for the rotational tiltmeters were kept on the top of Bent 4. DS-50A and STS4 DAQ boxes were used to collect the data from the instrumentation at a rate of 10 data per second. The instrumentation procedure is provided in the following sub-sections.

##### **4.1.1 Phase 1**

A total of 26 strain gauges and 12 rotational tiltmeters were installed on the concrete surface. The strain gauge and tiltmeters locations are shown in Figure 4-1.

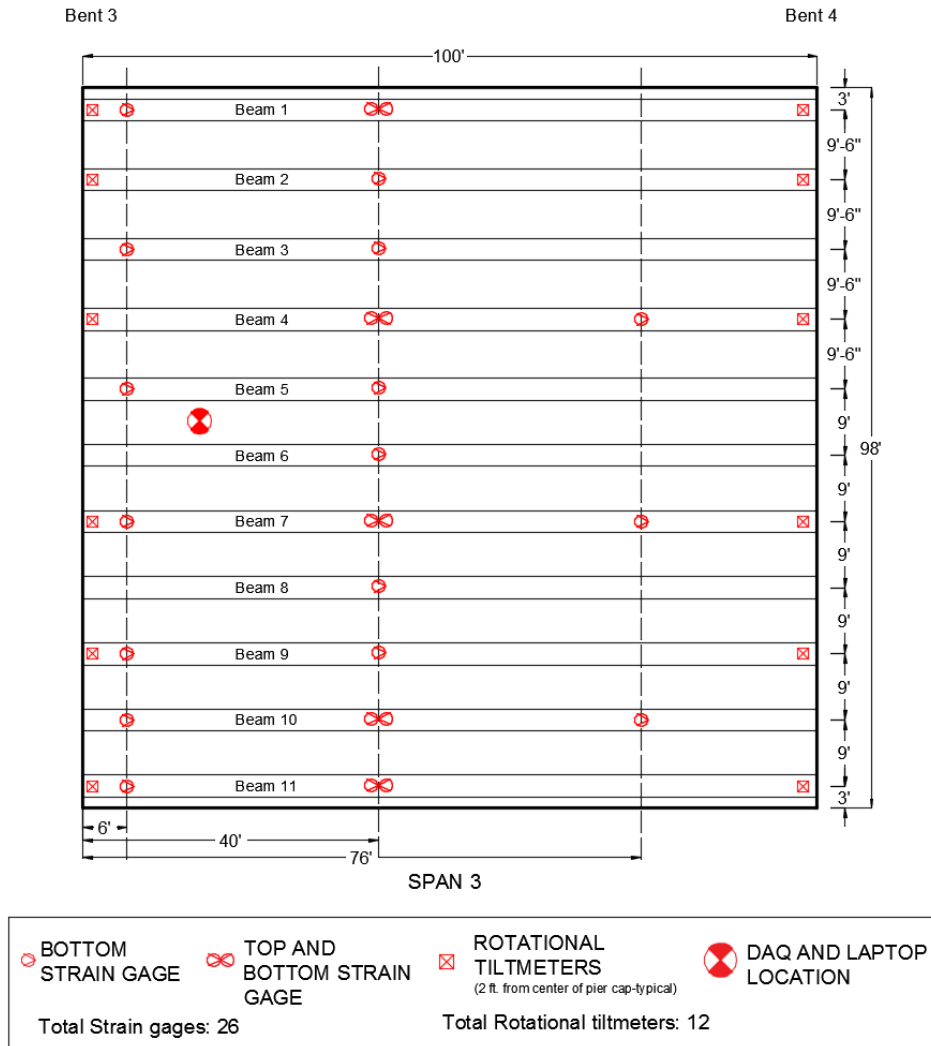


Figure 4- 1: Instrumentation plan for load testing

Some girders were equipped with both top and bottom strain gages to find the location of the neutral axis.

The installation process of strain gauges on the concrete surface was as follows:

- The locations for the strain gages were marked on the concrete surface.
- The concrete surface was made smooth by sanding or grinding.
- The area was cleaned by acetone to remove dirt, dust, and other particles. Water was used to clean off the acetone.

- A fast-setting epoxy was used to fill the voids in the concrete and provide a smooth surface for strain gages.
- Gauges were attached to the concrete with CN-E adhesive.
- The wires were run along the length of the girders and collected at the top of the bent cap.

Rotational tiltmeters were installed at a distance of 2 ft. from the center of bents. A strong setting epoxy was used to attach the tiltmeters to the bottom center of the girders. The strain gauge and rotational tiltmeter installation was performed with a man lift. Figure 4-2 (a) and (b) show an attached rotational tiltmeter and the attached bottom strain gages under the girders, respectively.



(a)



(b)

Figure 4- 2: Load testing instrumentation: (a) Rotational tiltmeter; and (b) Attached strain gages

#### 4.1.2 Phase 2

Ten strain gages from the first test were left in place to be used for the proposed follow-up test. Moreover, 16 new strain gages were installed at the top and bottom flanges of the girders, as shown in Figure 4-3. As per the request from the Dallas District Bridge Division, six strain gages (shown by green circles in Figure 4-3) were placed at the bottom of the deck. The rotations of the girders were monitored by 12 rotational tiltmeters installed on six selected girders.



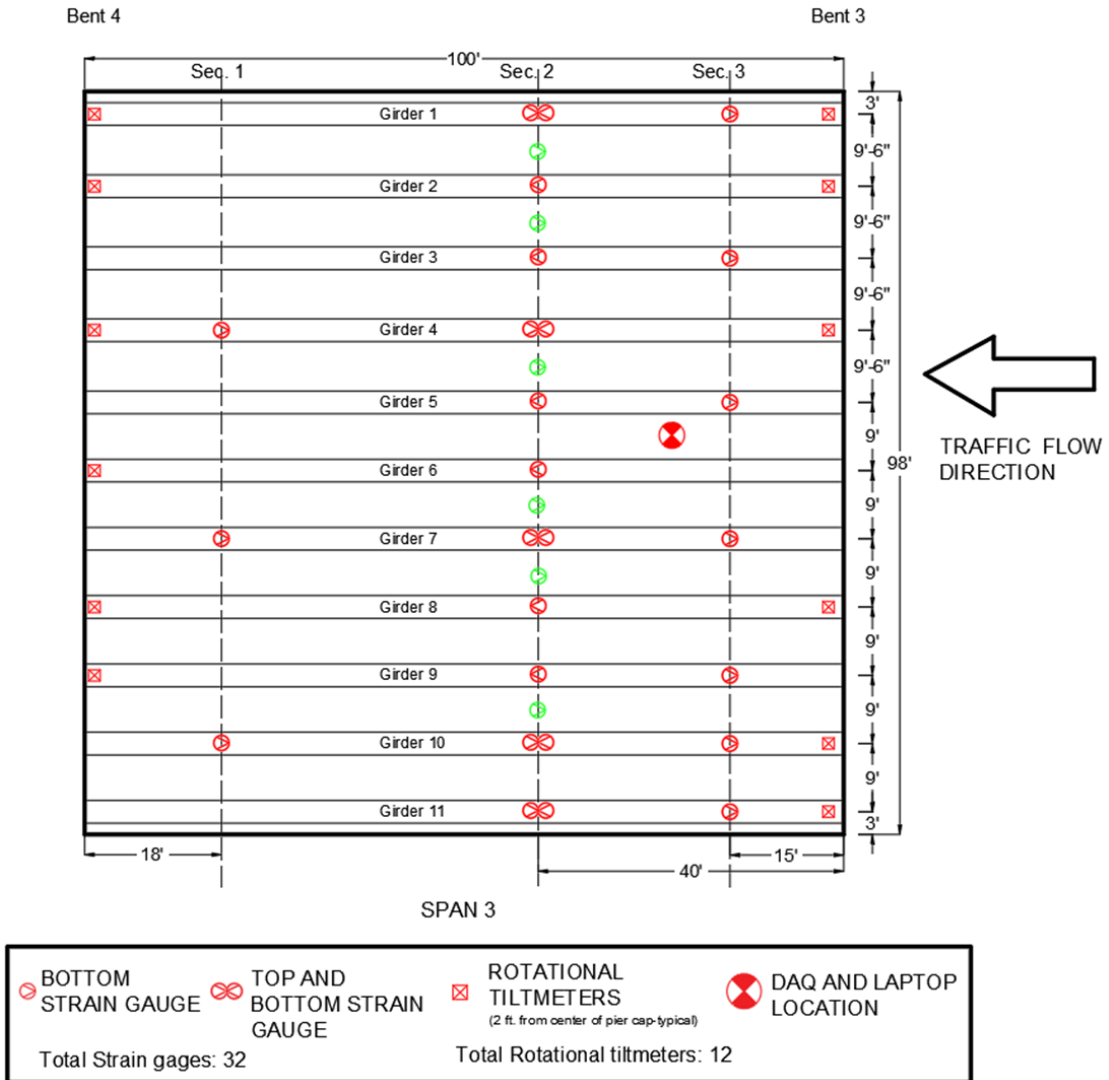


Figure 4- 3: Instrumentation plan for load test

The installation process of strain gauges and rotational tiltmeters on the concrete surface was similar to the previous instrumentation method.

## 4.2 Load Testing of The Bridge

### 4.2.1 Phase 1

A static load test was conducted on Span 3 (between Bents 3 and 4) of the Wilson Creek Bridge. Three trucks were used for this purpose. The distance between the front wheel axle and the first back wheel axle was 13.5 ft. while the distance between the two back wheel axles was 4.5 ft. The dimension of the test trucks is shown in Figure 4-4 and the weights of each axle are shown in Table 4-1.

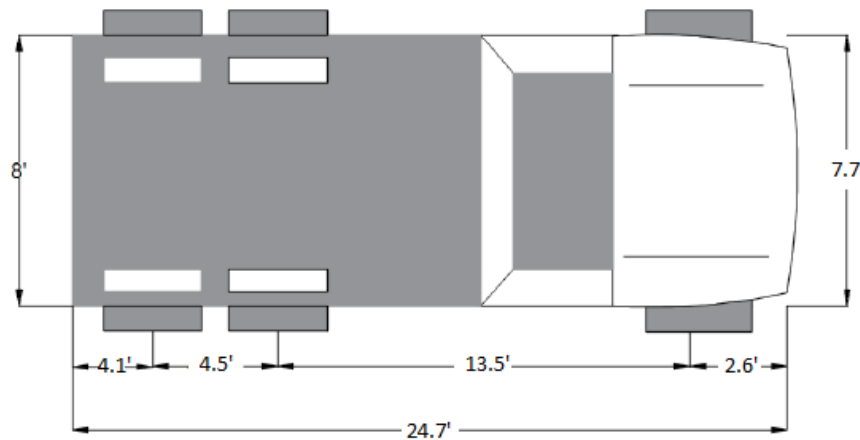


Figure 4- 4: Dimension of the test trucks

Table 4- 1: Truck axle weights for load test

Weights	Truck A (kip)	Truck B (kip)	Truck C (kip)
Gross vehicle weight (GVW)	42.98	44.38	46.92
Axle 1 weight	9.5	9.76	10.58
Axle 2 weight	16.74	17.31	18.17
Axle 3 weight	16.74	17.31	18.17

The following procedure was followed for the static load testing:

- Marking on top of the bridge was made on the day of the load testing. The start of the bridge, the end of the bridge, and intermediate span locations were marked.

- Spray paint was used to mark the paths so that it would be visible to the truck during the test. Stop locations were also marked on the paths for trucks to stop at certain locations.
- The crawl speed test was carried out according to the AASHTO Manual for Bridge Evaluation (2018). The truck started from the beginning of Bent 4 and stopped at the end of Bent 3. Only truck C was used for the crawl speed test.
- In the stop location test based on the AASHTO Manual for Bridge Evaluation (2018), three trucks were used simultaneously. The trucks were moved to a predetermined stop location on Span 3 of the bridge (mid-span) so that the effect on the bridge could be recorded.
- The deflection and strain readings from the crawl speed test and stop location test were collected through a data acquisition system.

Figure 4-5 shows the location of the trucks during the crawl speed test and stop location test. The details of the path location, speed, and truck wheel location for each test are shown in Table 4-2.

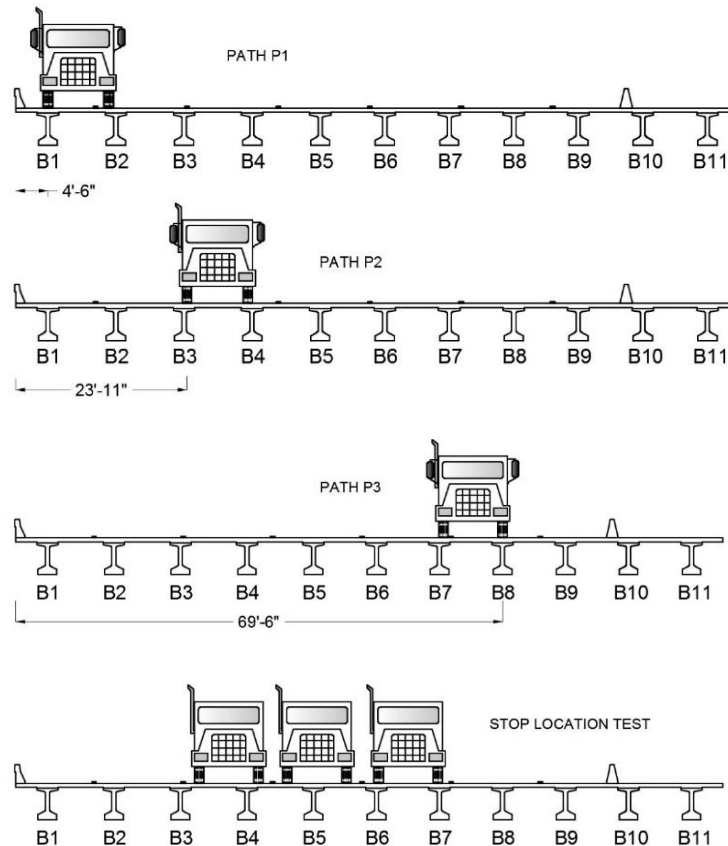


Figure 4- 5: Location of trucks during load tests

Table 4- 2: Truck speeds and location for Crawl Speed Test

Path	Run	Speed (ft./s)	Location of the right wheel from the west edge of the deck (ft.)
P1	1	7.33	4.5
	2		
P2	1	7.33	23.9
	2		
P3	1	7.33	69.5
	2		

Two runs with different speeds were conducted for Paths P1, P2, and P3 for a better understanding of the behavior of the bridge. From Figure 4-5, Path P1 was selected to produce maximum effect on the exterior girder B1, as the right wheel was located on the top of girder B1. Paths P2 and P3 were selected to investigate the effects on the interior girders (B2 - B10). The Paths for stop location test were selected to produce maximum effects on girders B3-B7. Figure 4-6 shows the trucks in position for the load test.



Figure 4- 6: Trucks in position for load test

### 4.2.2 Phase 2

The area office was requested to provide three dump trucks with axle weights similar to the first load test for the follow-up test. The dimension of the trucks was similar to the previous ones. The weight of each axle is shown in Table 4-3.

Table 4- 3: Truck axle weights for load test

<b>Weights</b>	<b>Truck A (kip)</b>	<b>Truck B (kip)</b>	<b>Truck C (kip)</b>
Gross vehicle weight (GVW)	42.46	44.28	44.84
Axle 1 weight	9.74	11.20	10.88
Axle 2 weight	16.36	16.54	16.98
Axle 3 weight	16.36	16.54	16.98

A similar procedure, load paths, and vehicle speeds were maintained for the Phase 2 load test to achieve comparable results. Two runs for each Path, P1, P2, and P3 were again conducted to verify the repeatability of results. Figure 4-7 shows the trucks in position for the stop location test.



Figure 4- 7: Trucks in position for the load test

### 4.3 Truck Mounted GPR

A GSSI SIR-30 brand GPR was utilized herein. Multiple antennae with truck mount were used (Figure 4-8) at a speed of about 5 mph which is a very efficient and time-saving method for bridge deck scanning compared to the usual method of GPR scanning with a tri-wheel pushcart using a single antenna.



Figure 4- 8: Truck mounted GPR

GPR scanning was performed in parallel lines every 2.5 ft. apart towards the direction of traffic. Figure 4-9 shows the GPR scanning grid.

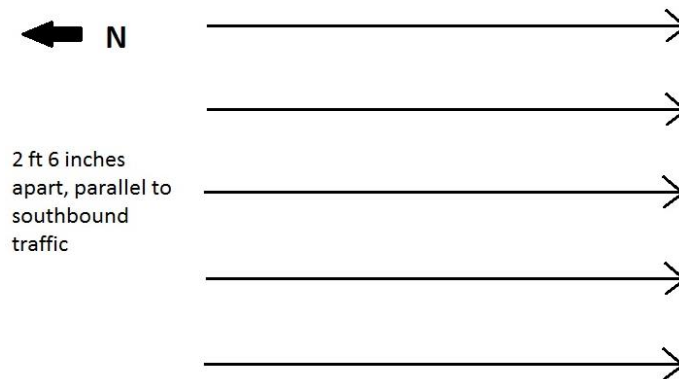


Figure 4- 9: GPR scanning grid

### 4.4 IE Device

The IE system is used to determine the delamination condition and thickness of concrete structural members when voids, honeycombs, and/or cracks are suspected. The device creates an impact at

a spot on the surface and then records and analyzes the echo. Unlike the GPR, the IE system is a spot scanning device, which is used to scan discrete data points in a pre-determined grid on the concrete deck surface. Figure 4-10 shows the IE device that was used herein.



Figure 4- 10: IE Device

The IE data were gathered at discrete points with variable spacings (2.5 ft. to 5 ft. spacing) on a pre-selected grid pattern, post-processed and then analyzed. Results of IE data analysis at each point provided the state of any delamination at that point. The IE scanning grid showing the data points is shown in Figure 4-11.

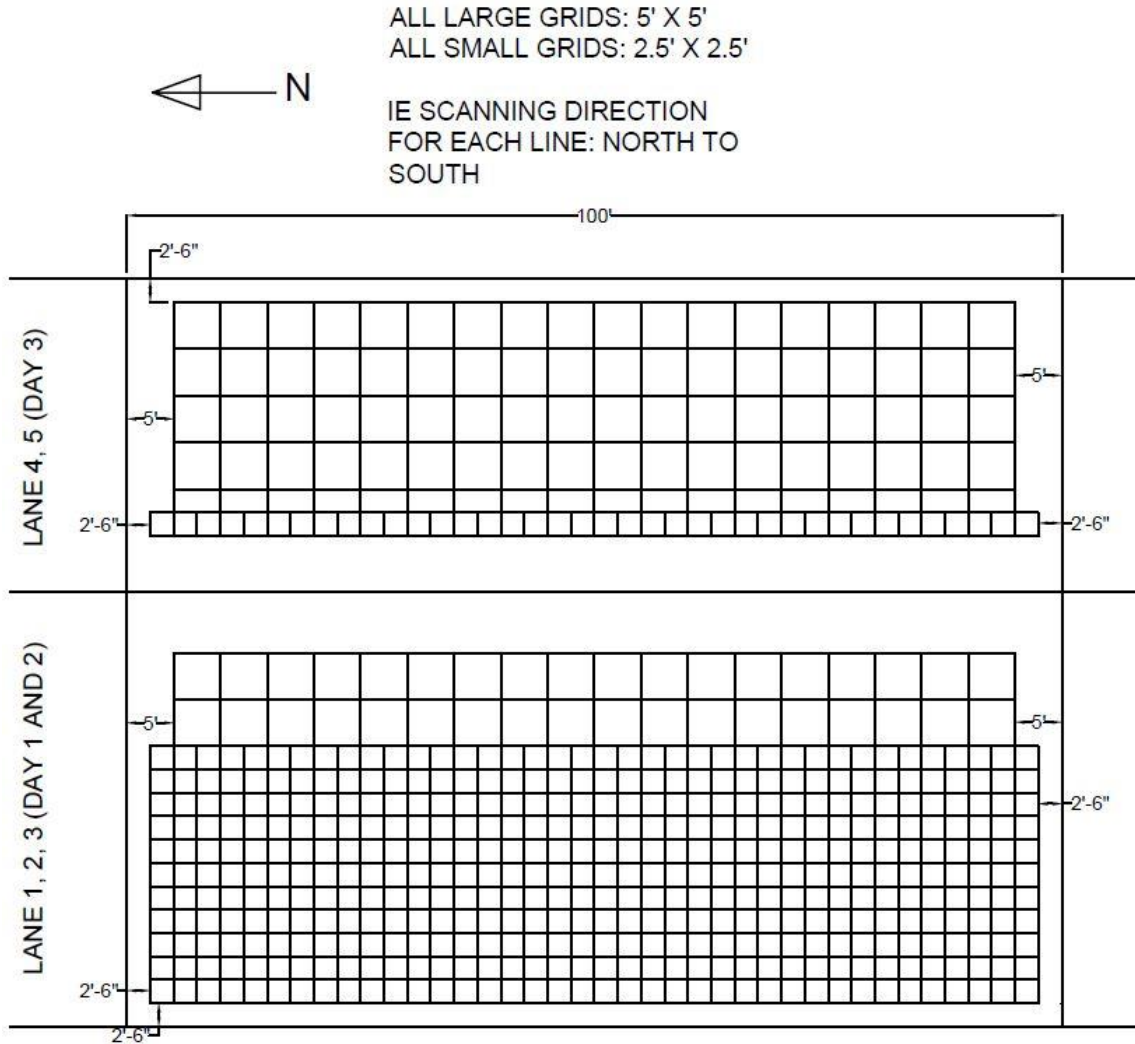


Figure 4- 11: Working grid for IE scanning

## 4.5 NDE Procedure

- Firstly, the traffic on top of the bridge was controlled to facilitate the NDE work on Span 3 of the SB bridge.
- Square grids with 2 feet 6 inches spacing were marked on the deck surface.
- IE and GPR were used to scan the top of the bridge deck along the grid lines.
- IE scan was done one spot at a time and the GPR scan was performed by line scanning using the truck mount (two 2.6 GHz and one 400 MHz antennae covering multiple depths).



- Scanning was performed over three days. Lanes 1, 2, and 3 and west side shoulder were scanned on the first two days and the remaining two lanes (Lanes 4, 5, and east side shoulder) were scanned on the third day. Lane closure segments are shown in Figure 4-12.
- The data were analyzed according to the grid to find out any possible delamination or debonding.

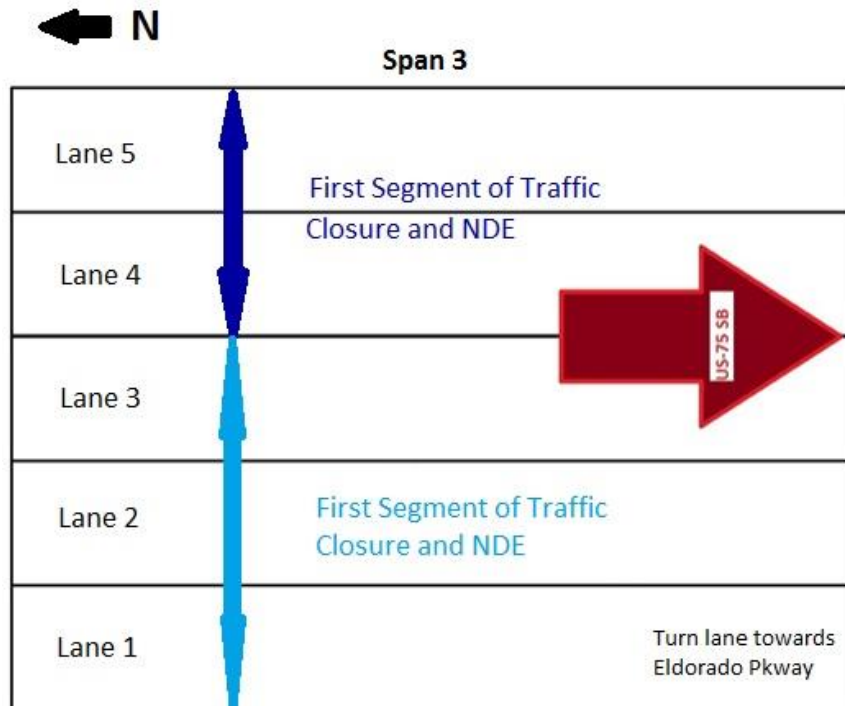


Figure 4- 12: Segments of Traffic Closure for NDE

#### 4.6 Ambient Vibration Test

Ambient vibration test under regular traffic was conducted for the SH-75 SB Bridge to obtain the accelerations of the girders and the deck in different directions. Two other control bridges with no significant vibration issue (Wilson Creek NB Bridge and Virginia Parkway NBML Bridge) were also tested to compare the accelerations with the SB Bridge. The data collection at each location involved taking readings for 15 minutes at a rate of 100 data/sec using a slamstick vibration meter. The vibration testing procedures for the three test bridges are described here in this section.

### 4.6.1 SH-75 SB Bridge

Ambient vibration test was conducted on span 3 of the SB Wilson Creek Bridge and data was collected from six girders, five locations on the deck, two bearing pads, and three locations on the bent caps. Figure 4-13 shows the locations of the vibration meter under the deck and the girders.

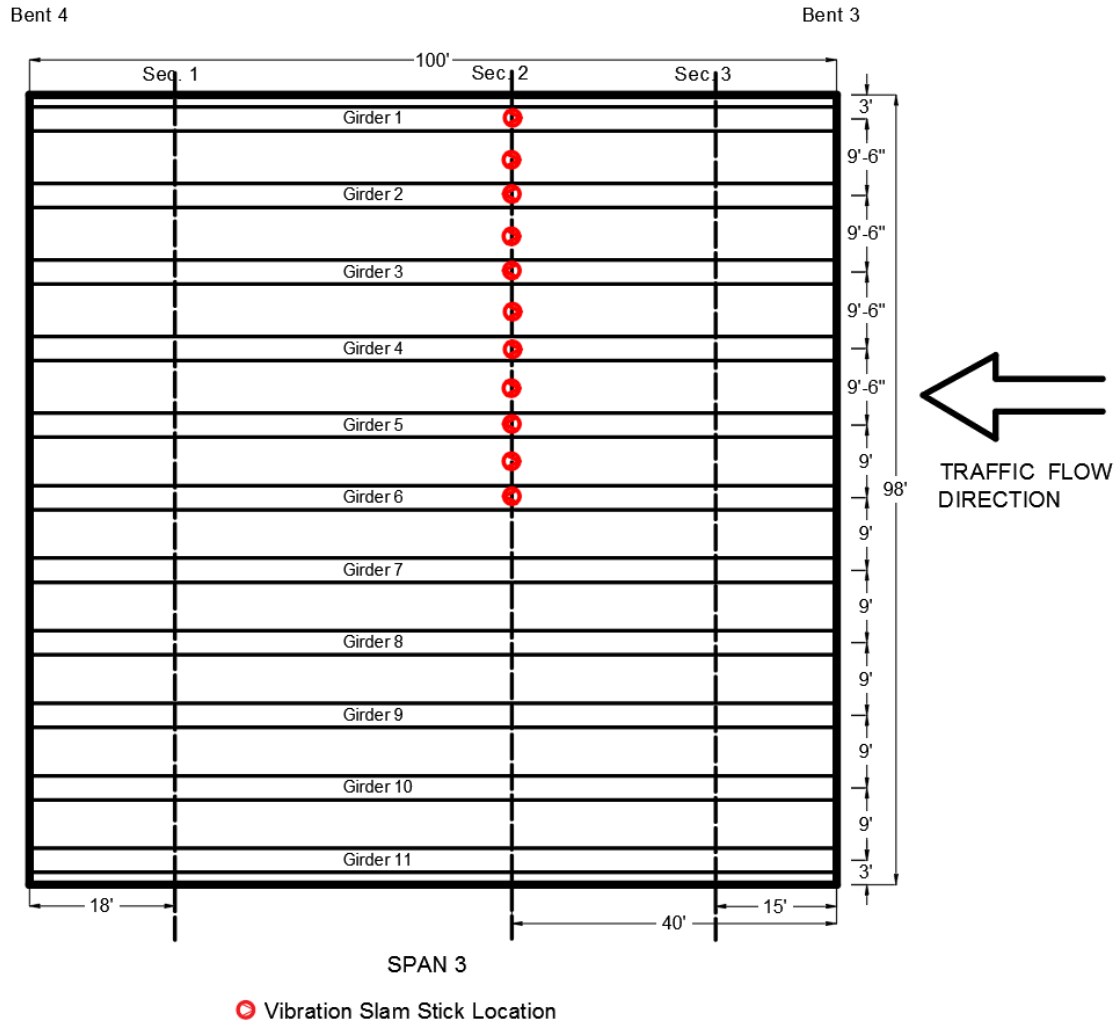


Figure 4- 13: Locations of vibration meter under the deck and the girders for SB Bridge

Figure 4-14 shows the vibration meter under a girder, under a portion of the deck, on a bearing pad, and in the middle of the bent cap of the bridge.



(a)



(b)



(c)



(d)

Figure 4- 14: Vibration meter under the Wilson Creek SB Bridge: (a) Girder; (b) Deck; (c) Bearing pad; and (d) Bent cap

#### 4.6.2 Wilson Creek NB Bridge

The Wilson Creek NB Bridge was tested for ambient vibration to compare with the SB Bridge. Span 3 was selected for the ambient vibration to avoid traffic closure. Figures 4-15 and 4-16 show the plan and typical transverse section of span 3 of the bridge, respectively while Table 4-4 shows a comparison between the SB and NB bridge data.

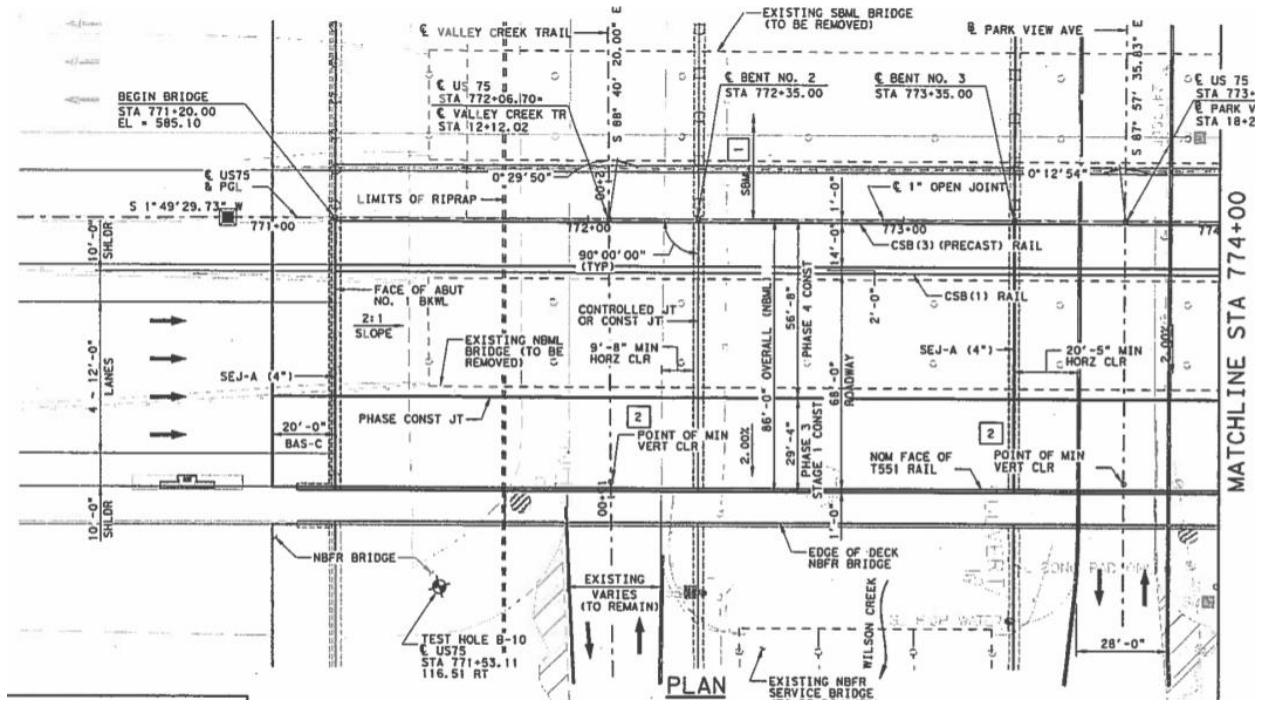


Figure 4- 15: Plan view of the NB Bridge

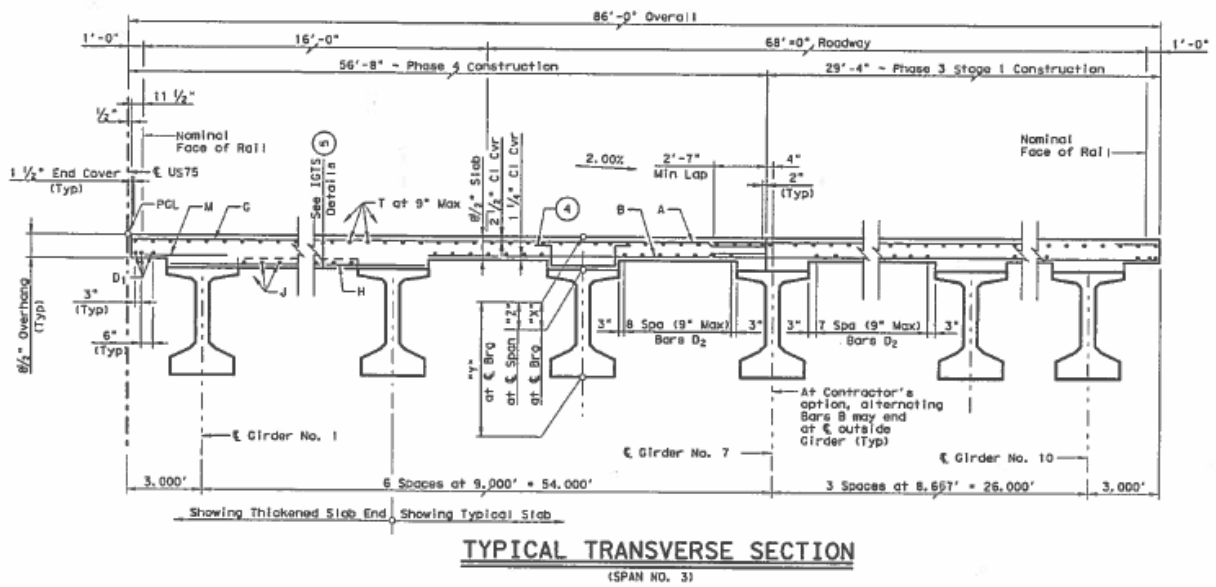


Figure 4- 16: Typical transverse slab section of the NB Bridge

Table 4- 4: Comparison between SB and NB bridges

Properties	SB Bridge	NB Bridge
Span length	100 ft.	100 ft.
Width	98 ft.	86 ft.
Girder type	Tx54	Tx54
The spacing of the girders	9-9.5 ft.	8.67-9 ft.
Number of girders	11	10

Vibration data were collected from five girders and some portions of the deck. The ambient vibration testing plan of the NB Wilson Creek Bridge is shown in Figure 4-17.

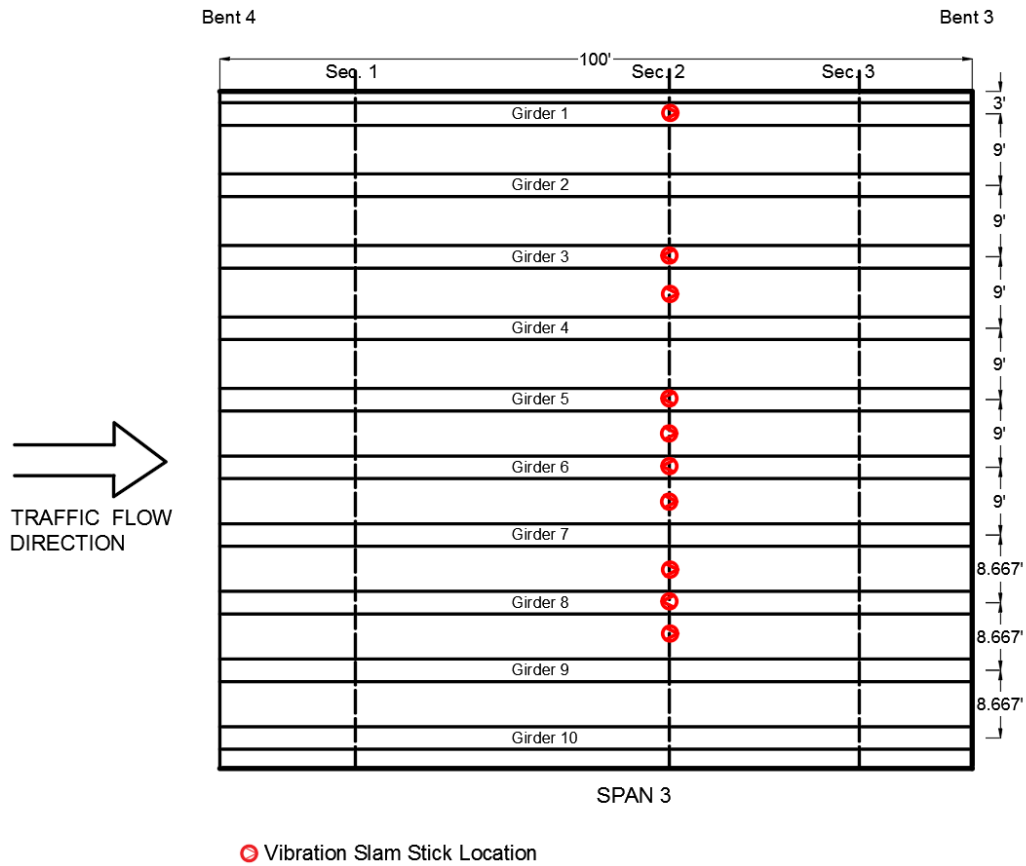


Figure 4- 17: Locations of vibration meter under the deck and the girders for SB Bridge

### 4.6.3 Virginia Parkway NBML Bridge

To obtain a comprehensive reference data set for comparison with the SB Wilson Creek Bridge, the Dallas District Bridge Division suggested the UTA team to identify a nearby similar bridge with no unusual vibration issues. Thus, Virginia Parkway NBML Bridge on US 75 in McKinney, TX was identified for ambient vibration testing (Figure 4-18). The bridge was selected since it has open space under the first span, making it readily accessible for instrumentation without requiring traffic lane closure (Figure 4-19).



Figure 4- 18: Google map location of Virginia Parkway bridge



Figure 4- 19: Accessible space under the Virginia Parkway Bridge

Span 1 was selected for the ambient vibration test to avoid traffic closure under the bridge. Figures 4-20 and 4-21 show the plan and typical transverse section of span 1 of the bridge, respectively. Table 4-5 shows a comparison between the Virginia Parkway Bridge and Wilson Creek SB Bridge since their vibration data were compared.

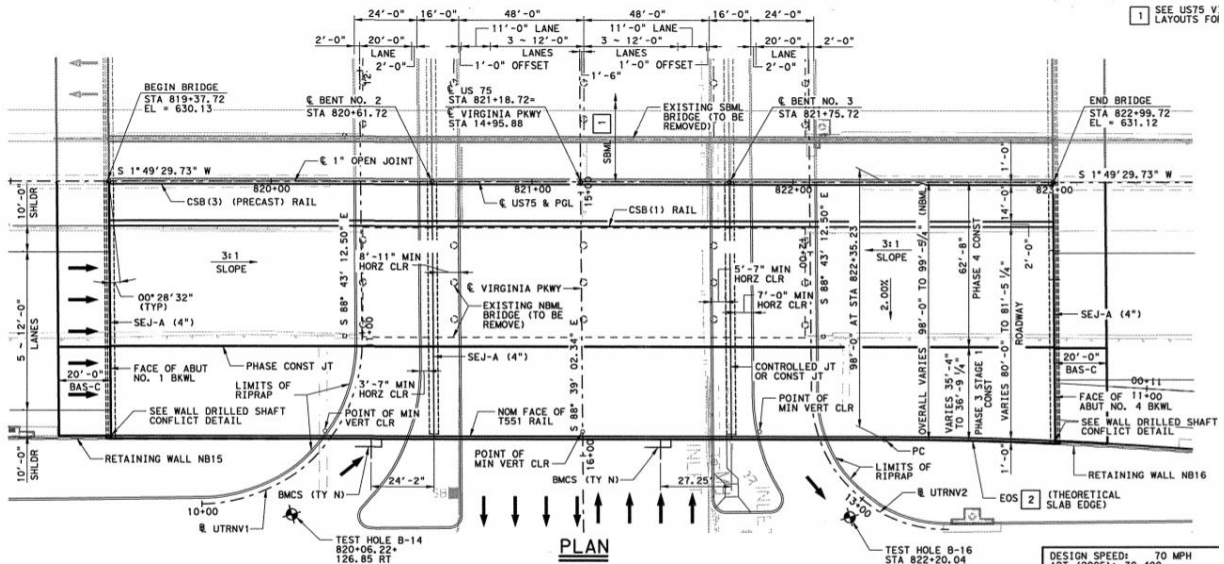


Figure 4- 20: Plan view of span 1 in Virginia Parkway bridge

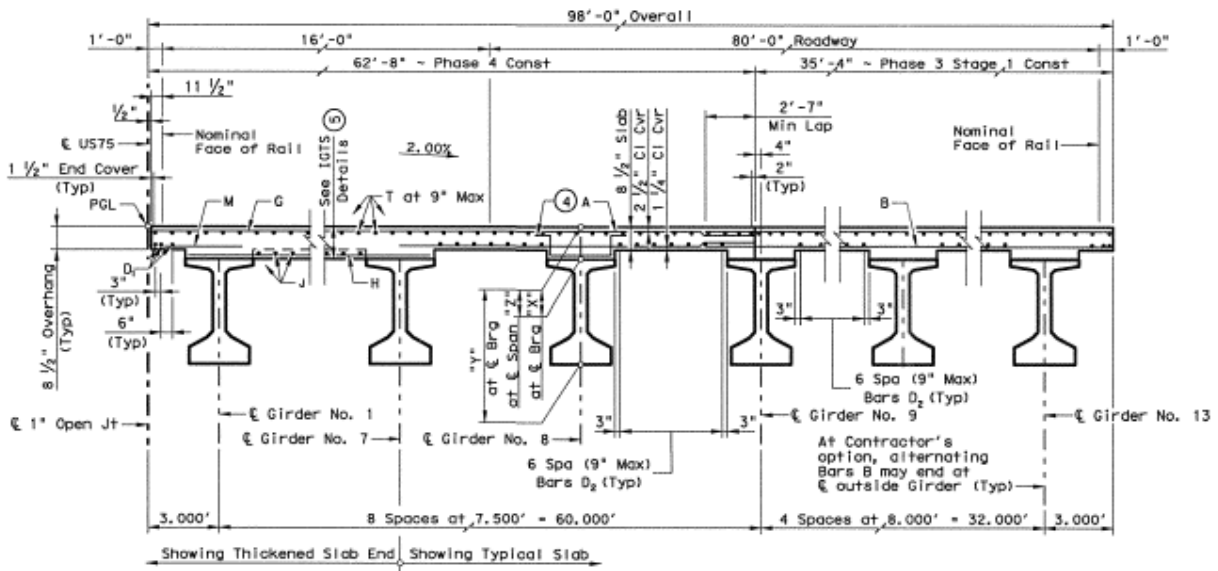


Figure 4- 21: Typical transverse slab section of span 1 in Virginia Parkway Bridge

Table 4- 5: Comparison between Virginia Parkway Bridge and Wilson Creek SB Bridge

<b>Properties</b>	<b>Wilson Creek SB Bridge</b>	<b>Virginia Parkway Bridge</b>
Span length	100 ft.	125 ft.
Width	98 ft.	98 ft.
Girder type	Tx54	Tx54
The spacing of the girders	9-9.5 ft.	7.5-8 ft.
Number of girders	11	13

Vibration data was collected under nine girders and six segments of the deck. Some of the bearing pads and some locations of the bent cap were also instrumented. Each data set was collected for 15 minutes for optimization purposes.

Figure 4-22 shows the locations of the vibration slam stick under the girders and deck during the vibration testing.



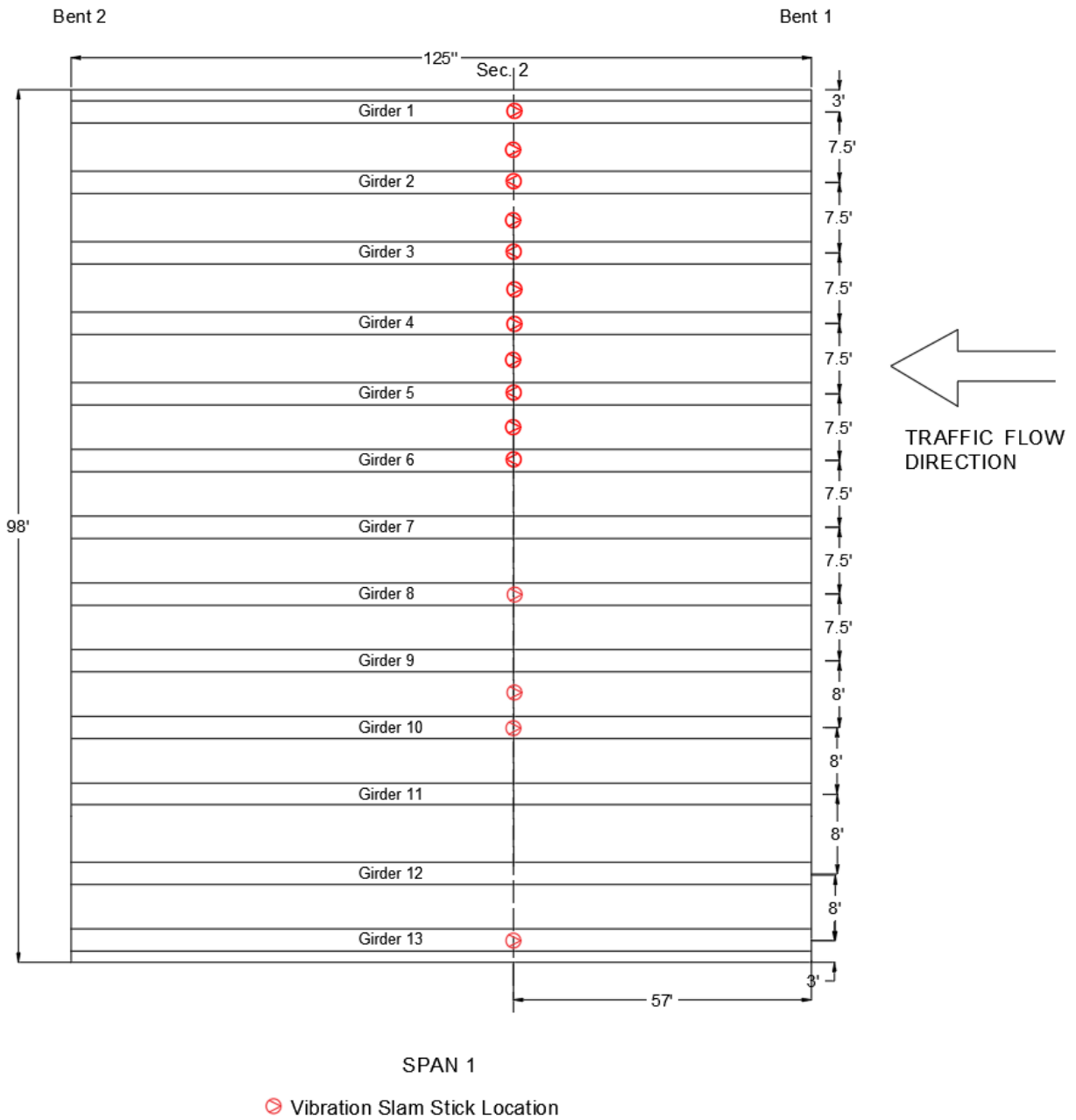


Figure 4- 22: Locations of the vibration data logger for the Virginia Parkway Bridge

## 4.7 Vibration Test during Static Load Test

During a static load test, some of the girders (Girder 1 during Path P1, girder 4 during Path P2 and girder 8 during Path P3) and a portion of the deck (between girders 3 and 4 during Path P2) were instrumented with the vibration data logger. Then, the load test was repeated at velocities of 10, 20, 25, 30, 50, and 60 mph along paths P1, P2, and P3. The instrumentation plan for the vibration data logger is shown in Figure 4-23. Figure 4-24 shows a dump truck on the span for the load test while the vibration meter was placed under a girder.

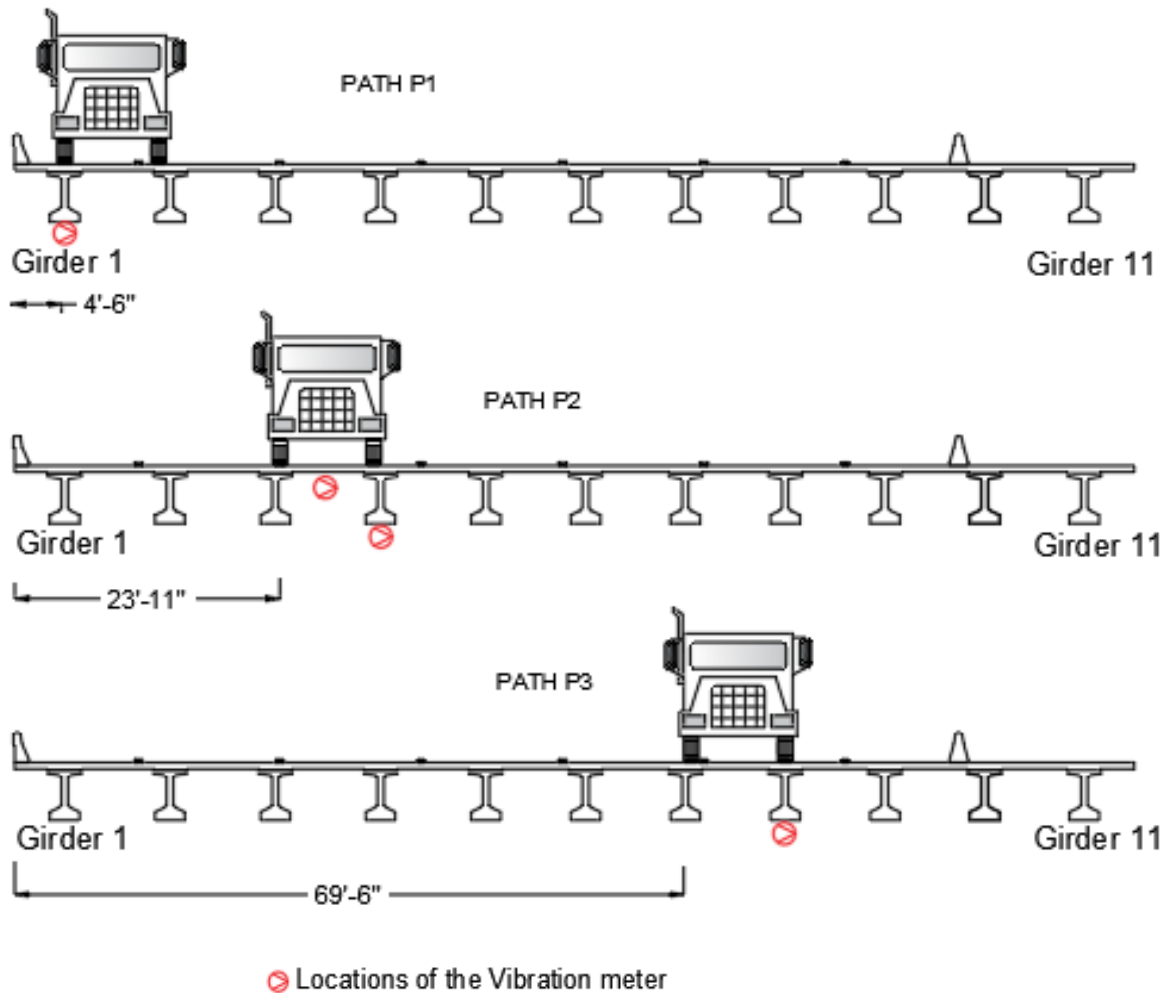


Figure 4- 23: Load test paths with the vibration data logger location



Figure 4- 24: Dump truck for vibration test during static load testing

# Chapter 5

## FINITE ELEMENT MODELING

### 5.1 Initial Model Development

Modeling of a girder of span 3 of SH-75 SB bridge was done using ABAQUS CAE (2018). To optimize the modeling work, five girders with the precast panel and composite deck were modeled in ABAQUS (2018). The justification for modeling five girders can be provided by this fact that a single dump truck only has major effects on nearby three to four girders during a load test. Tx54 girders were used for this bridge with 50 prestressing strands each having 0.5 in. diameter. The girders consist of seven types of mild steel including the shear reinforcement. Figure 5-1 (a) shows the Tx54 girders with mild rebars while Figure 5-1 (b) shows the mild steels of the girders separately.

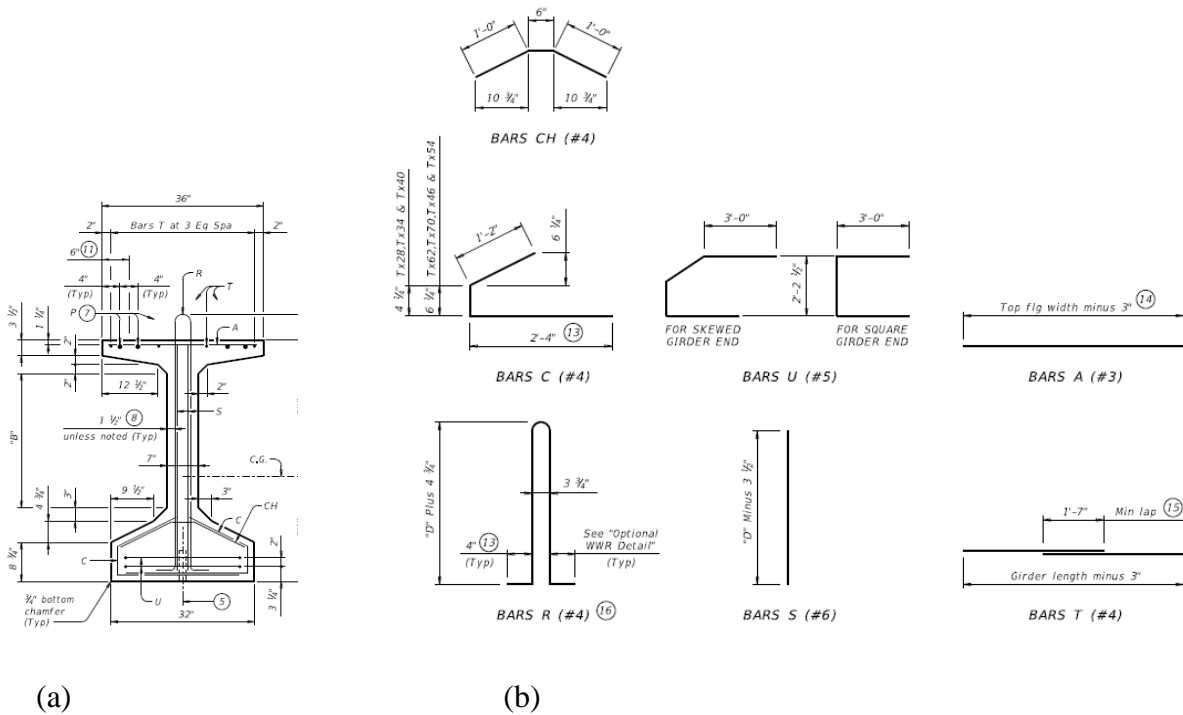


Figure 5- 1: Tx54 girder: (a) Mild rebars shown in the girder; and (b) Mild rebars shown separately

All the prestressing steels and the mild steels were modeled and assembled inside the girder. Figure 5-2 shows the reinforcements of the girder in the ABAQUS (2018) interface.

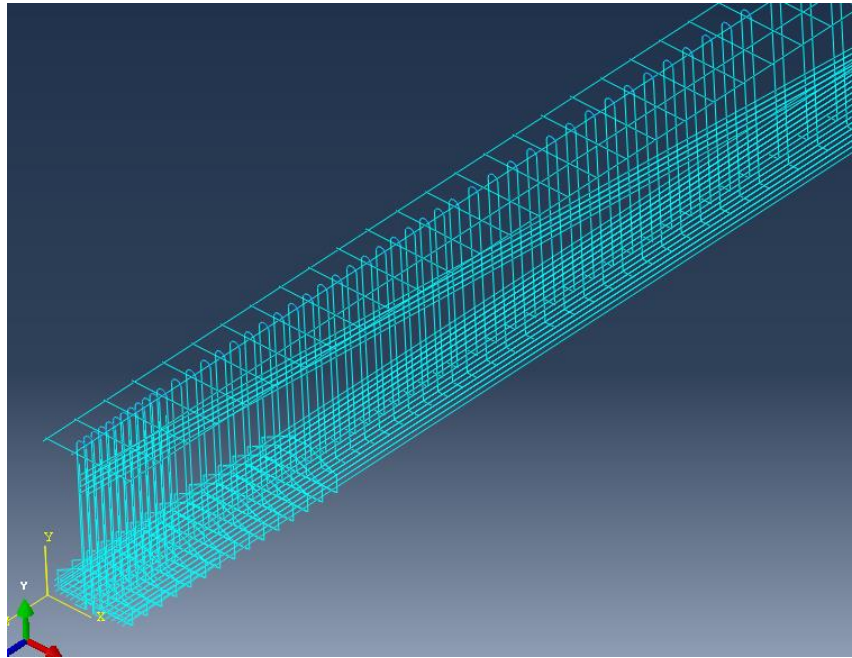


Figure 5- 2: Reinforcements of the girder in ABAQUS (2018) interface

The materials, sections, and prestressing strands properties were defined following the as-built drawing. The panels were modeled according to the typical TxDOT non-skewed panel plan which is shown in Figure 5-3.

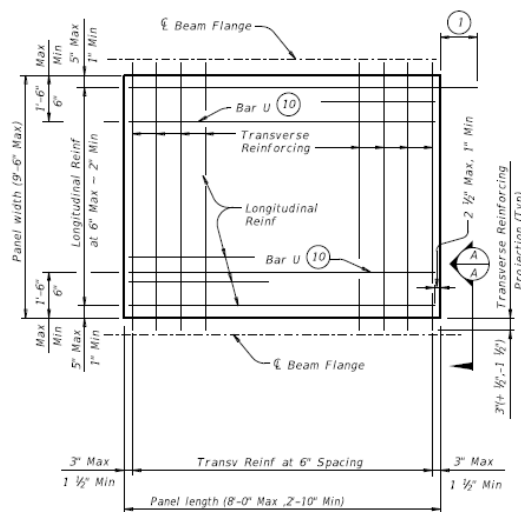


Figure 5- 3: Typical TxDOT non-skewed panel plan

0.5 in. diameter 270 ksi prestressing steels with a spacing of 6 in. were used as transverse reinforcement while #3 mild steels with 6 in. spacing were used for the longitudinal reinforcement for the panel. The thickness of the panels was 4 in. with concrete compressive strength of 5 ksi. The location and placement of the panels are shown in Figure 5-4 according to standard TxDOT panel drawings.

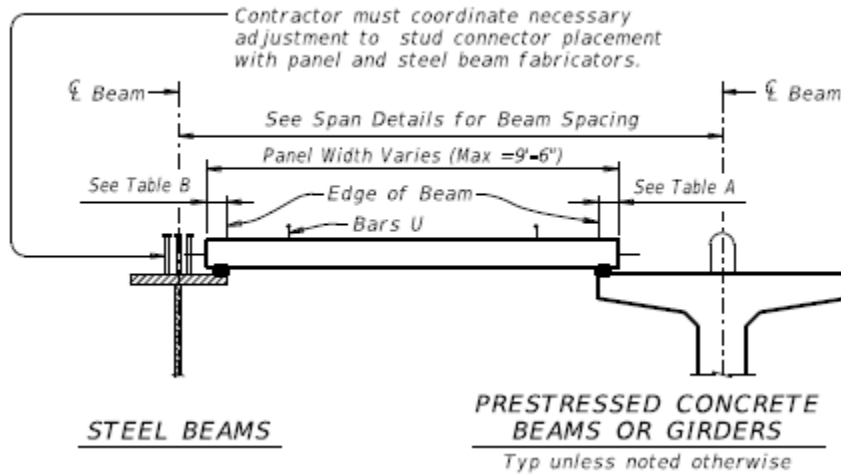
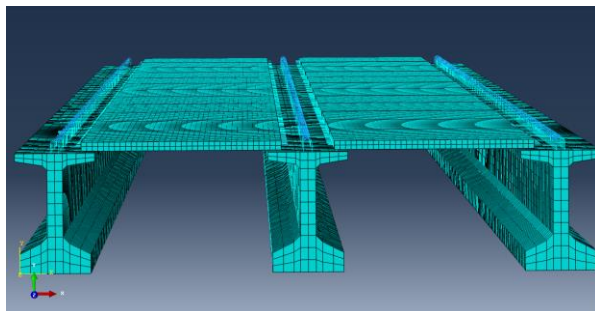
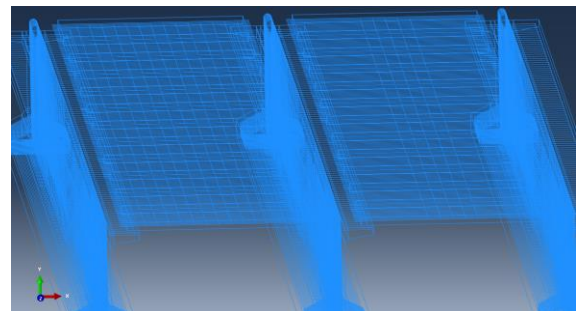


Figure 5- 4: Location and placement of typical TxDOT panel for prestressed concrete girders

The panels were meshed accordingly and translated on the top of the girders according to the standard TxDOT panel plan. Figure 5-5 (a) shows the panels translated on the duplicated girders in ABAQUS (2018) interface while Figure 5-5 (b) shows the rebar wireframes of the panels and the girders.



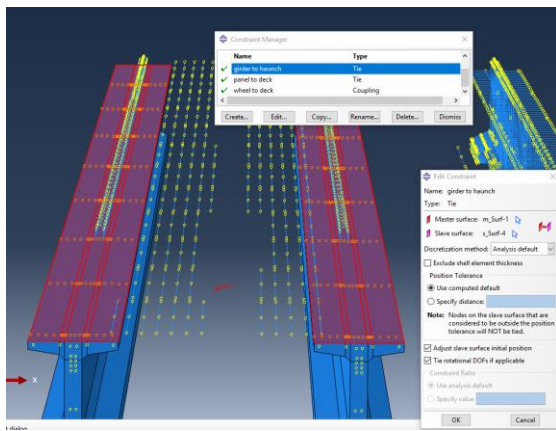
(a)



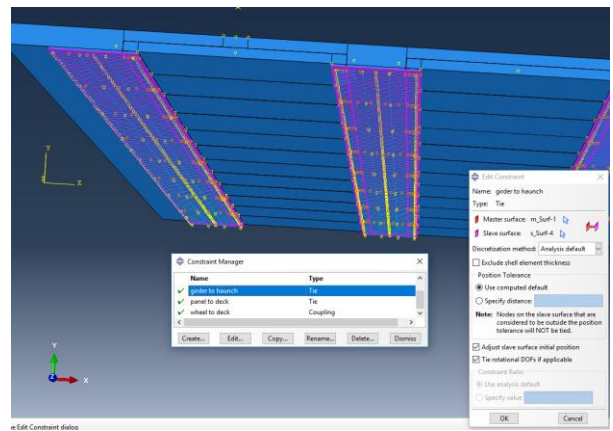
(b)

Figure 5- 5: ABAQUS model: (a) Panels on girders; and (b) Rebar wireframes

The contact properties between the top flange of the girders and the haunch were assigned as tie constraints to simulate full composite behavior between these elements. The girder surface was selected as a master surface since it had more stiffness while the haunch was a slave. Figures 5-6 (a) and (b) show the master and slave haunch surface for girder to haunch contact of the tie constraint respectively.



(a)



(b)

Figure 5- 6: Surfaces for girder to haunch contact: (a) Master surface; and (b) Slave surface

Similarly, tie constraint was assigned between the deck and the panel and the panel surface was selected as the master surface for its higher stiffness value than the deck. Figure 5-7 shows the contact between the deck and panel surfaces.

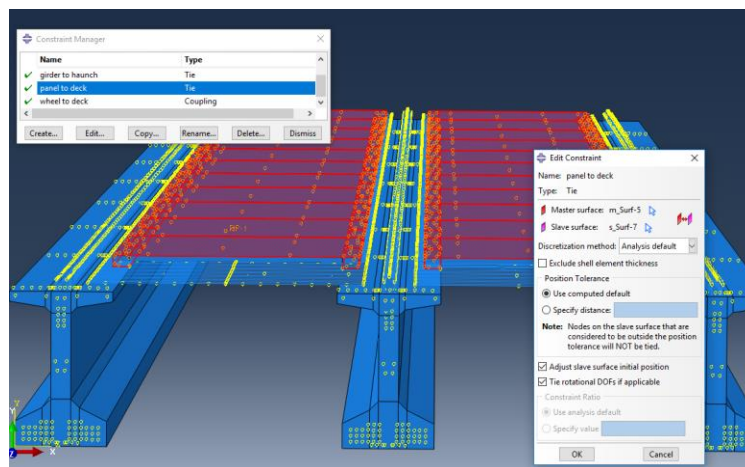


Figure 5- 7: Contact surfaces between the deck and the panel

Figures 5-8 (a) and (b) show a completed half-scale bridge with 5 girders and 5 in. native mesh of the model respectively.

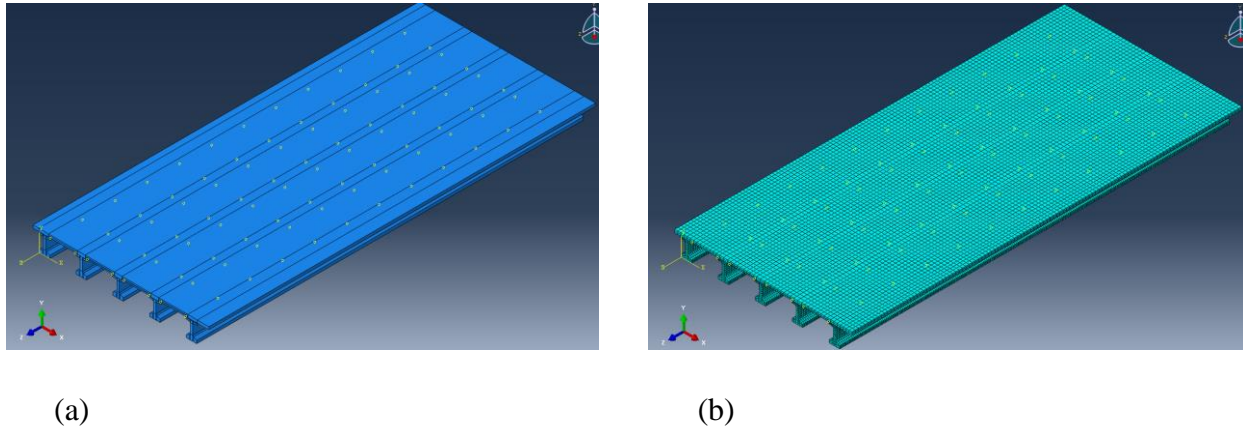


Figure 5- 8: Half-scale bridge model: (a) 5 girders with panels and deck; and (b) 5 in. native mesh

## 5.2 Material Properties

### 5.2.1 Concrete

Concrete damaged plasticity model was used according to section 2.3.1 to model the concrete of the girders, deck, and panels. Standardized testing classifies strength at an age of 28 days. However, concrete continues to increase in strength over time. The increase in concrete compressive strength acts to increase other material characteristics that are related to strength (tensile strength, modulus of elasticity, time-dependent effects, etc.). As a result, it is important to be able to consider the change in concrete strength with time. The AASHTO LRFD (2017) specifications do not specifically address this feature of concrete. The CEB-FIP model code (1990) provides the relationship for the change in concrete compressive strength over time which is shown in equation 5-1.

$$f_{cm}(t) = \beta_{cc}(t)f_{cm} \quad (5 - 1)$$

Where:

$f_{cm}$  = 28-day concrete compressive strength



$f_{cm}(t)$  = concrete compressive strength at time  $t$

$$\beta_{cc}(t) = \exp \left\{ s \left[ 1 - \left( \frac{28}{t} \right)^{\frac{1}{2}} \right] \right\} = \text{time-dependent coefficient dependent on the age of concrete}$$

$t$  = age of concrete at which  $f_{cm}(t)$  is computed (days)

$t_1 = 1$  day

$s$  = cement rate of hardening coefficient

$s$  is 0.20 for rapid hardening high strength concretes, 0.25 for normal and rapid hardening cements and 0.38 for slow hardening cements.

Figure 5-9 shows a plot of the ratio of concrete compressive strength to 28-day compressive strength ( $\beta_{cc}$ ) for normal hardening cement.

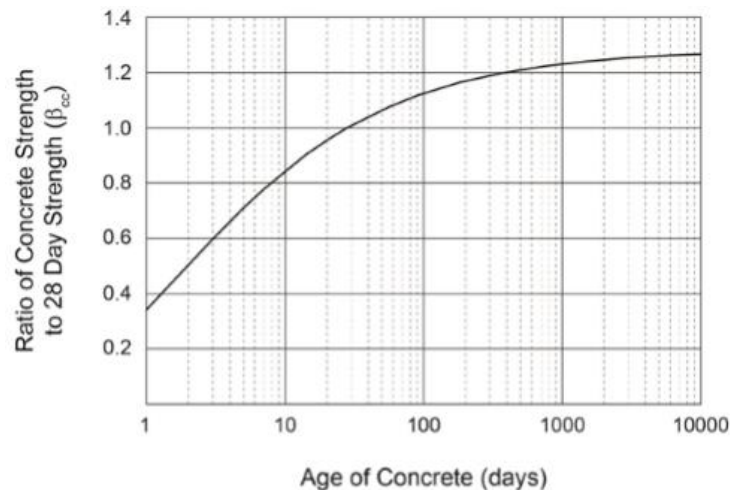


Figure 5- 9: Concrete strength gain with time

The variation in modulus of elasticity with time is predicted by CEB-FIP and is shown in equation 5-2.

$$E_{ci}(t) = \beta_E(t)E_{ci} \quad (5 - 2)$$

Where,

$E_{ci}$  = the modulus of elasticity of concrete at an age of 28 days

$E_{ci}(t)$  = the modulus of elasticity at time  $t$

$$\beta_E(t) = (\beta_{cc}(t))^{\frac{1}{2}} = \text{coefficient depending on the age of concrete at } t \text{ (days)}$$

$\beta_{cc}$  = coefficient defined by equation 5-1

Figure 5-10 shows a plot of the ratio of concrete modulus of elasticity to 28-day compressive strength ( $\beta_E$ ) for normal hardening cement.

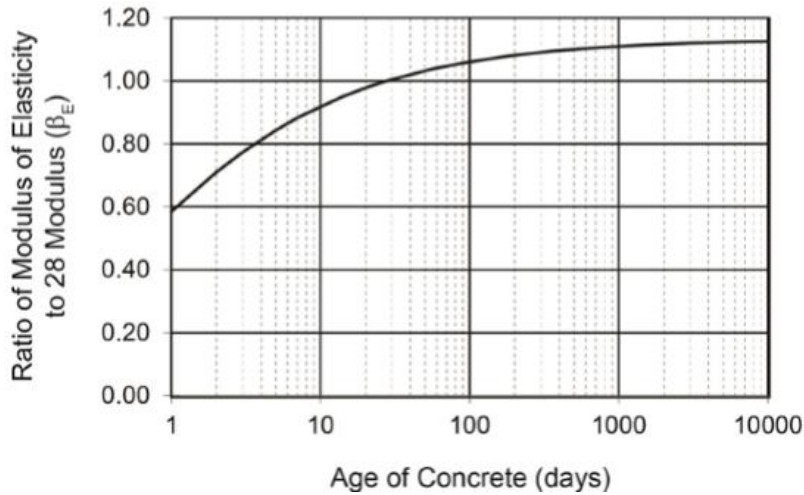


Figure 5- 10: Concrete modulus of elasticity with time

The increased compressive strength and modulus of elasticity of the girders, panels and deck of the SB bridge were calculated and are shown in Table 5-1.

Table 5- 1: Compressive strength and modulus of elasticity of the elements of the SB bridge

<b>Superstructure elements</b>	<b>Concrete compressive strength from the as-built drawing (ksi)</b>	<b>Concrete compressive strength from CEB-FIP (ksi)</b>	<b>Modulus of elasticity from the as-built drawing (ksi)</b>	<b>Modulus of elasticity from CEB-FIP (ksi)</b>
Girder	6.2	7.78	4774	5346
Panel	5	6.28	4287	4801
Deck	4	5	3834	4294

### 5.2.2 Prestressing Strands

Thermal loading was used according to section 2.3.3 to apply prestress on the prestressing strands of the girders and the deck. Initially, the temperature of the tendons of the girders was set as 0 °C. During step 1 (0-1 second), the temperature was set as -520 °C to achieve the required prestress. During step 2 (1-2 seconds), the temperature was kept constant at -520 °C to sustain the prestress obtained from step 1. Figure 5-11 shows the amplitude of the applied prestress due to thermal shrinkage in different steps of the model while Figure 5-12 shows the temperature profile of the model in step 1.

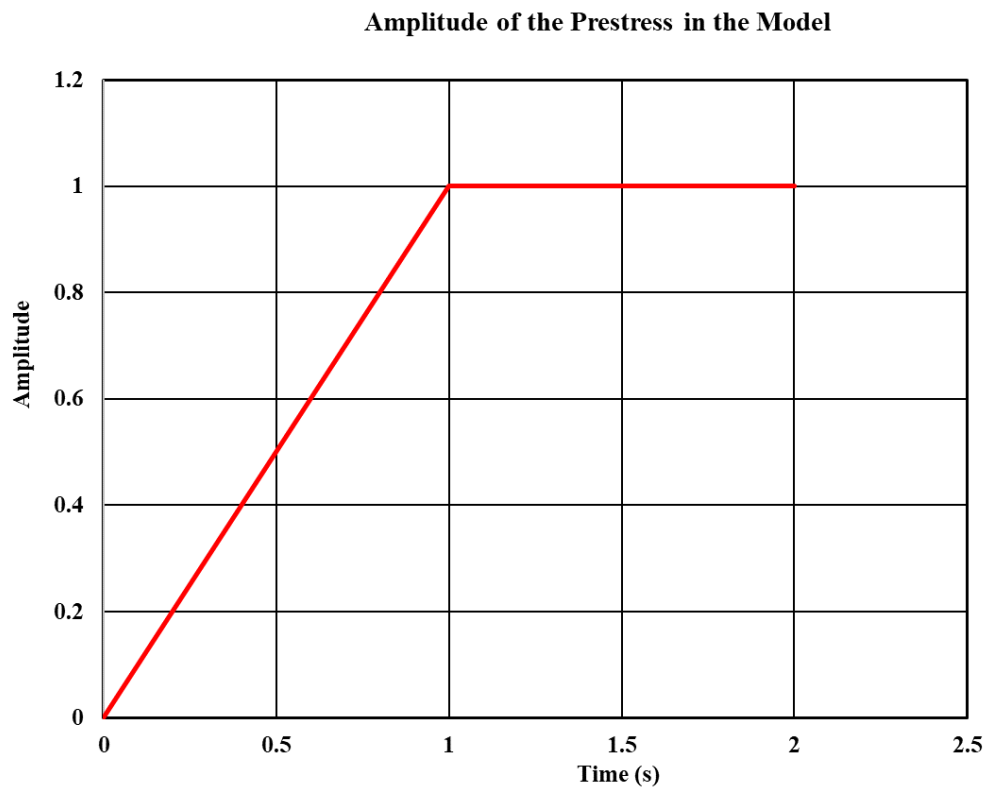


Figure 5- 11: Amplitude of the applied prestress in different steps of the model

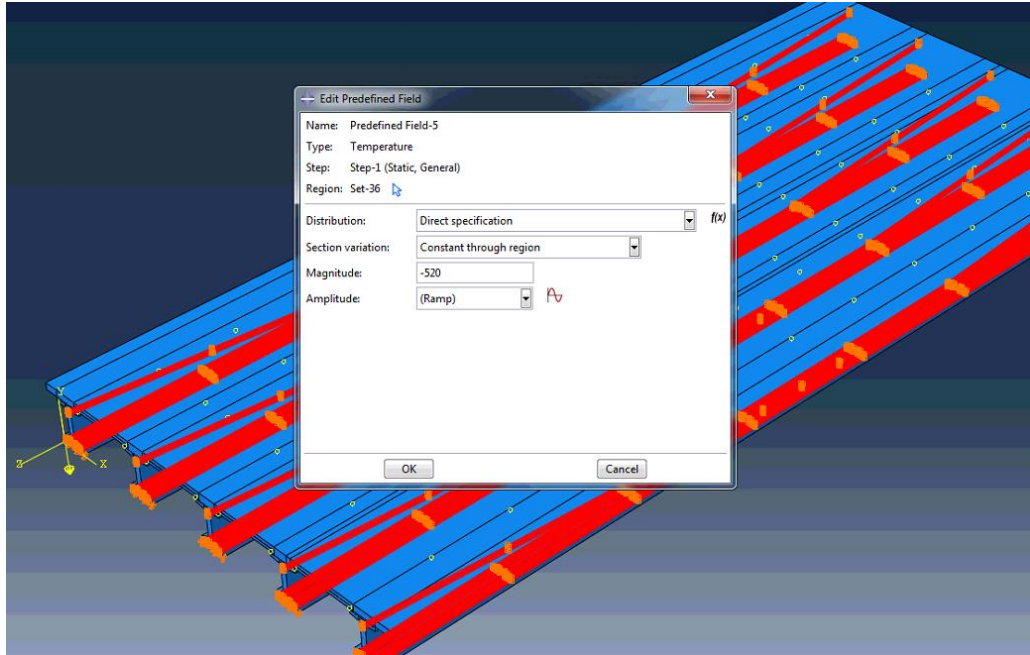
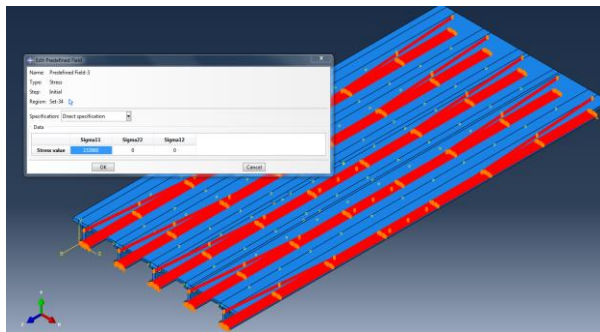
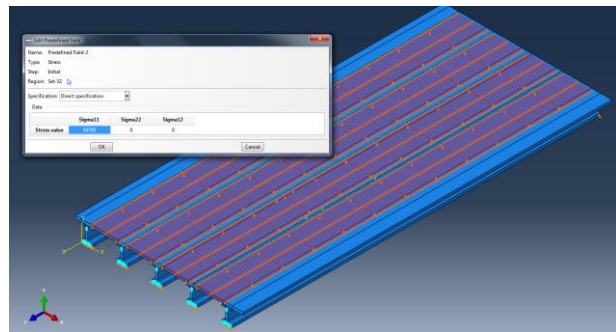


Figure 5- 12: Temperature profile of the model during step 1 (0-1 second)

The prestressing stress in the strands of the panels was also applied following this procedure. The total prestress loss of the girder and panel strands were calculated as 48.61 ksi and 26.82 ksi respectively. The effective prestress was calculated as 153.9 ksi and 64.7 ksi and applied on the girder and panel strands respectively in the ABAQUS (2018) model (Figure 5-13).



(a)



(b)

Figure 5- 13: Applied prestress on the ABAQUS model: (a) Girder strands; and (b) Panel strands

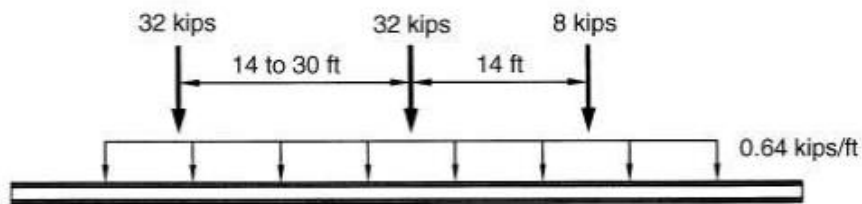
### 5.2.3 Mild Reinforcing Steel

Steel reinforcement which corresponds to the ASTM A306-49 was used in the bridge. The minimum yield strength of the reinforcement was 60,000 psi. The nonlinear stress-strain relationship of steel was approximated as a bilinear strain hardening model having different slopes. The ultimate stress of the steel was taken as 72,000 psi based on the ultimate strain of 0.021 calculated according to Eurocode 1993-1-1:2005 (CEN 2005). The ultimate strain in steel was defined as 15 times the yield strain.

### 5.3 Loading

For the model calibration purpose, the heaviest load test truck from the Phase 2 load test (section 4.2.2, Table 4-3) was used at the midspan of the bridge as a live load. For the retrofitting purpose, standard HL-93 loading was used on the calibrated model. HL-93 is a type of theoretical vehicular loading proposed by AASHTO (2017) in 1993. It is a combination of three different loads: design truck, design tandem, and design lane load. Figure 5-14 shows the live load pattern for designing a highway bridge according to AASHTO (2017).

#### Load pattern 1: Design lane + Design Truck



#### Load pattern 2: Design lane + Design Tandem

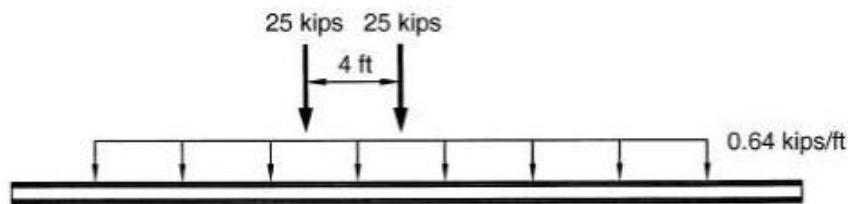


Figure 5- 14: Live load pattern for designing a highway bridge according to AASHTO (2017)

On the calibrated model, the design truckload was applied alongside with a lane load similar to the AASHTO (2017) proposed one to achieve sufficient live load response from the girders.

Since the model is required to be calibrated based on the live load effect only, it was necessary to distinguish the effect of the live load from the prestress and the dead load. Therefore, a multiple-step loading was used which has the potential to solve such problems. Prestress was applied at 0 second which reached its maximum at 1 second. The dead load was applied at 1 second which reached its peak during 1.5 seconds. The live load was applied at 1.5 seconds which reached its peak at 2 seconds. After reaching their peaks, all the loads were kept constant for the rest of the time of the job. Figure 5-15 shows the amplitudes of the loads during different stages of the model.

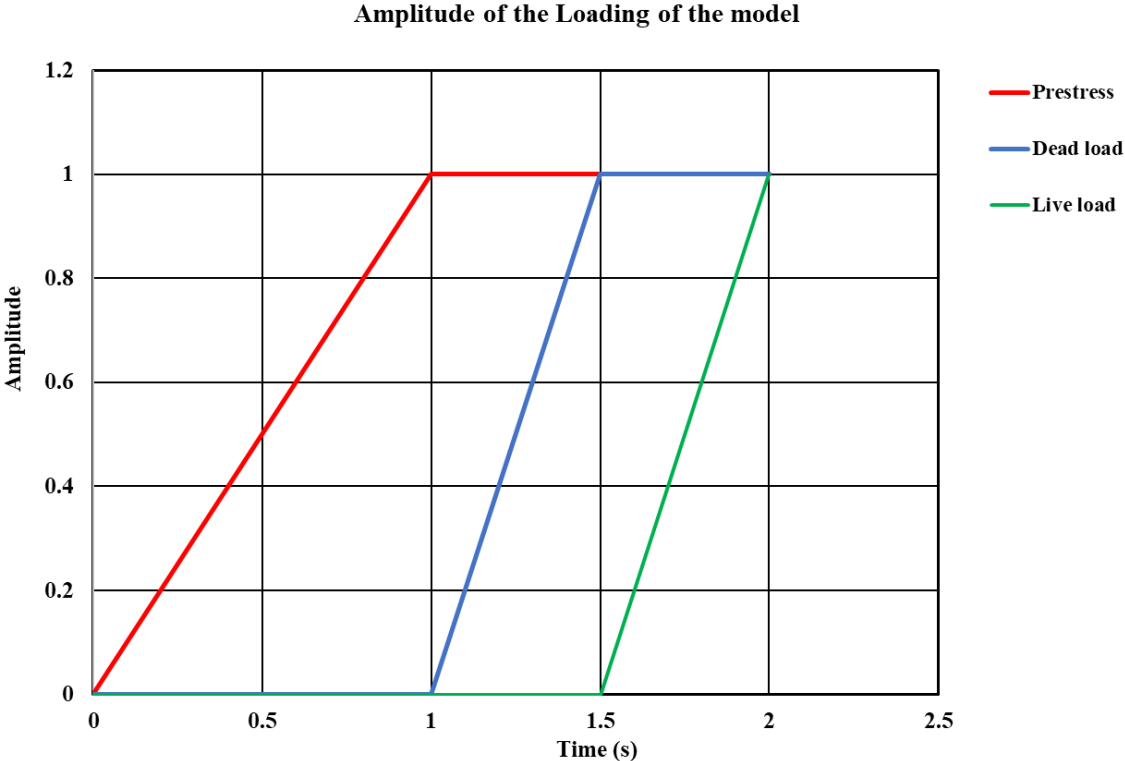


Figure 5- 15: Amplitudes of the multiple-step loading

According to Figure 5-15, to obtain the effect of only the live load, the effect of 1.5 seconds has to be subtracted from that of 2 seconds.

## Chapter 6

### RESULTS AND DISCUSSION

#### 6.1 Load Test

##### 6.1.1 Phase 1

The strain gage and the rotational tiltmeter data were analyzed to evaluate the load response of the bridge. Figure 6-1 shows a typical strain response of a strain gauge at mid-span of the girder. The strain response exhibited excessive noise and vibration as a result of the vibration observed in the bridge when the truck passed across the bridge. The strain values were refined to better evaluate the bridge behavior.

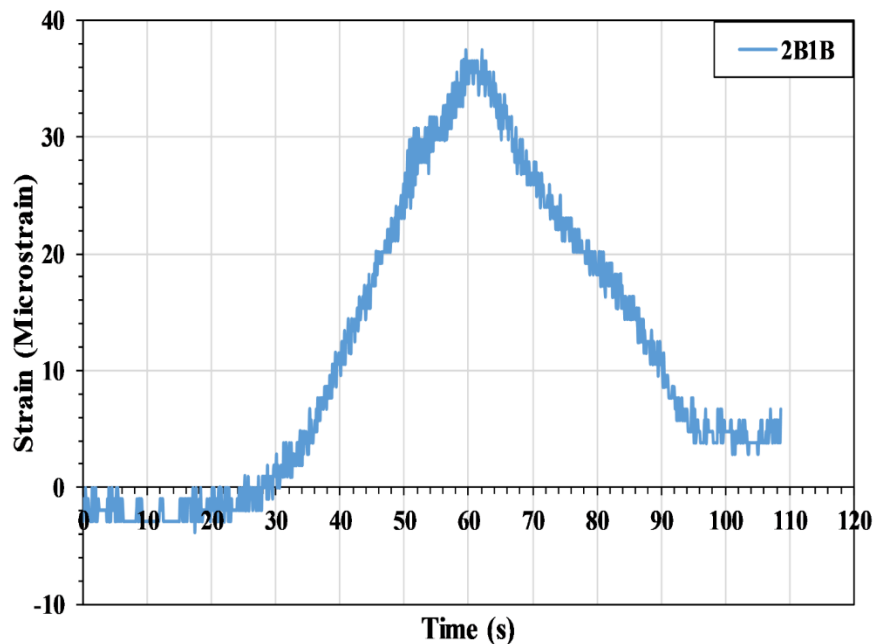


Figure 6- 1: Raw strain data for path P1 run 1

Figures 6-2 and 6-3 show the strain time history of Runs 1 and 2 for Path P1 for the bottom strain gages near the mid-span. The trucks were moved across Span 3 at a uniform speed. The strain responses at girders B1 and B2 were maximum as expected when the truck was on Path P1. Strain gages were designated as follows: 1st number denotes the section (2, 3), 2nd letter and 3<sup>rd</sup> number

show the girder no (B1, B2..., B9) and the last letter shows the location (T-top, B-bottom). The strain across other girders gradually decreased with distance from the truck tires.

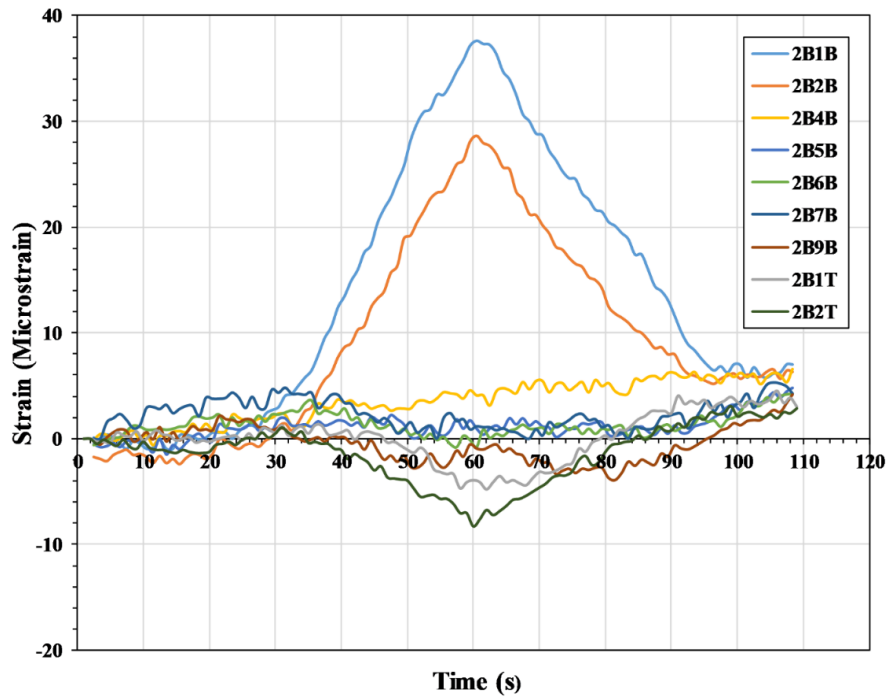


Figure 6- 2: Strain vs time diagram for Path P1 Run 1

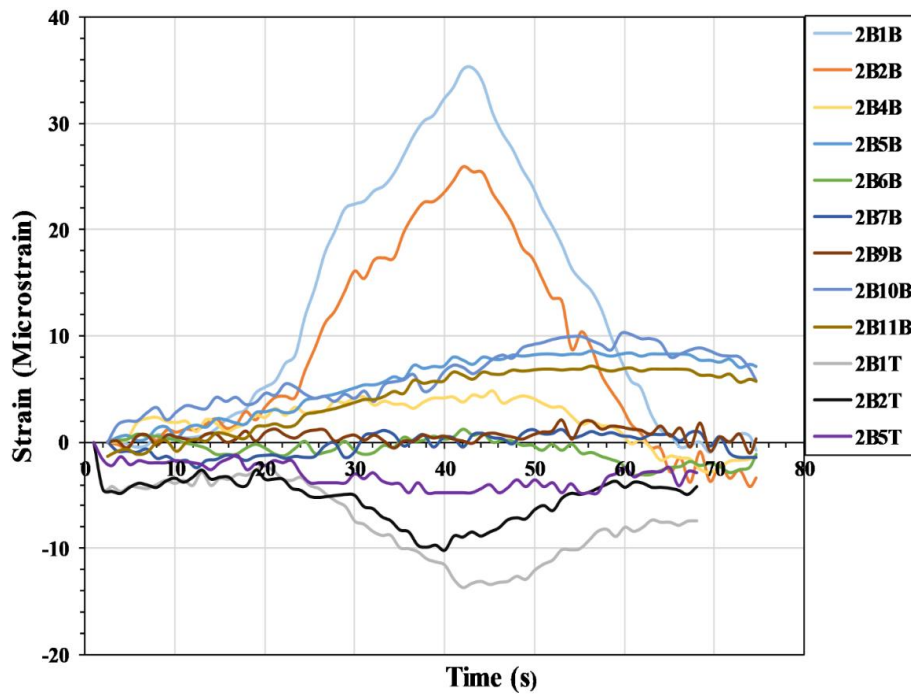


Figure 6- 3: Strain vs time diagram for Path P1 Run 2



Figures 6-4 and 6-5 demonstrate the strain vs time diagrams for Path P2 Run 1 and Run 2 for the bottom strain gages near the mid-span. The data were similar to Path P1. Girder B4 showed the maximum response as the wheel was located directly over the girder.

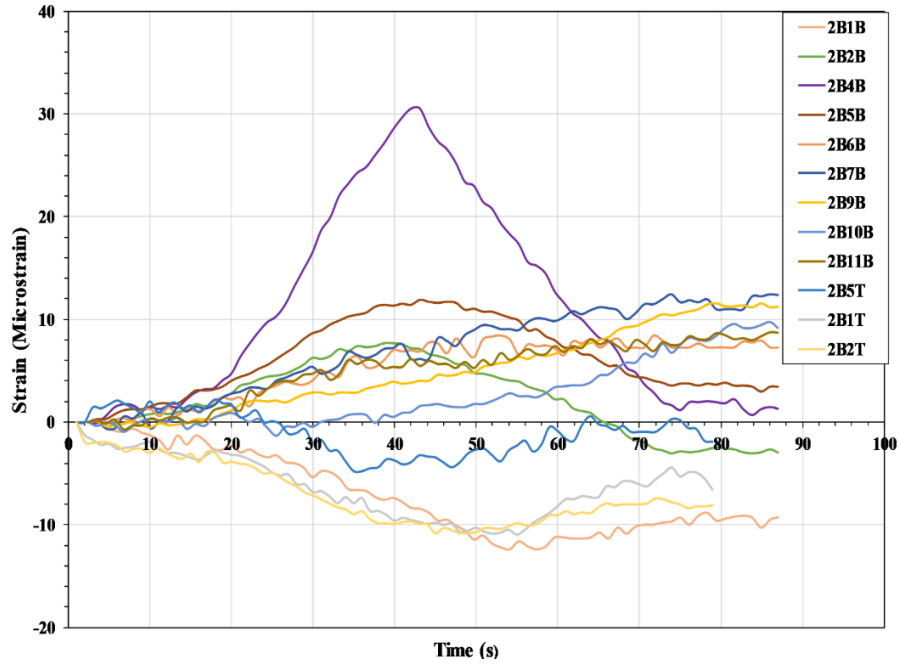


Figure 6- 4: Strain vs time diagram for Path P2 Run 1

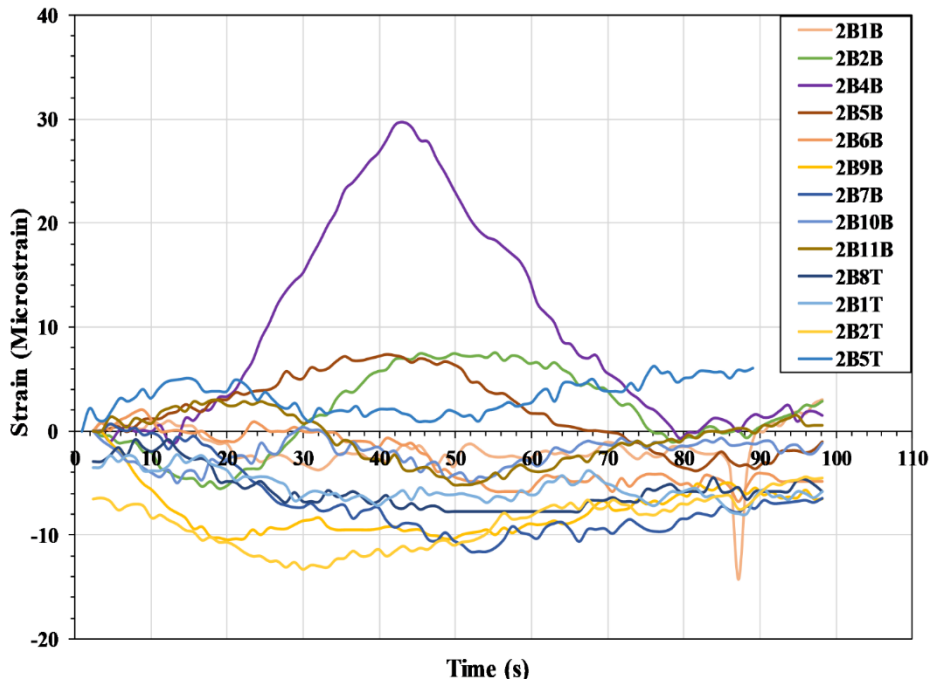


Figure 6- 5: Strain vs time diagram for Path P2 Run 2

Figures 6-6 and 6-7 show the strain data of Path P3 Run 1 and Run 2 for the bottom strain gauges near the mid-span where the girder B7 showed the maximum response.

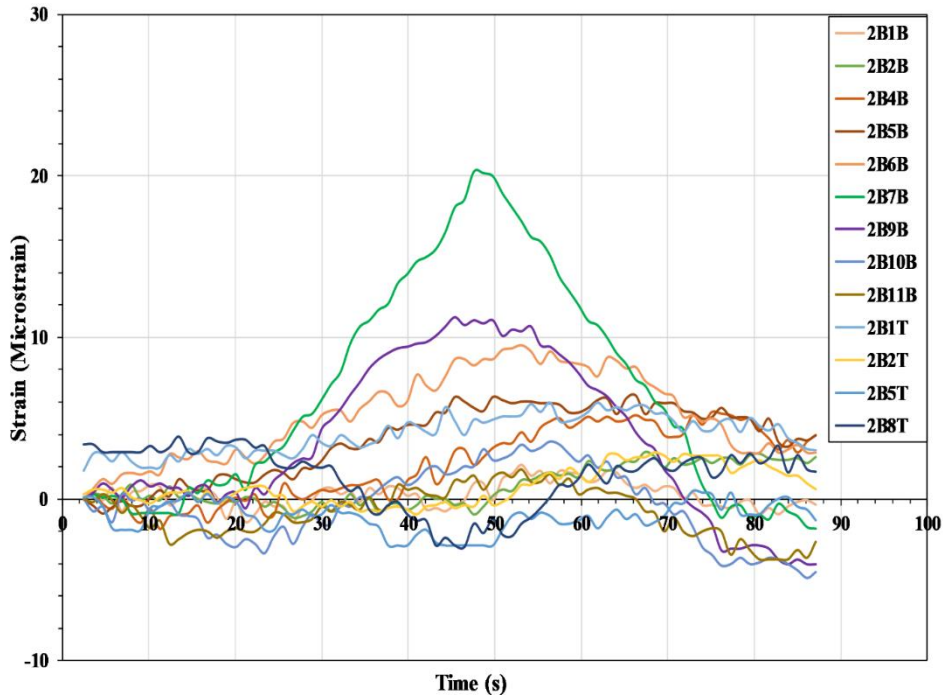


Figure 6- 6: Strain vs time diagram for Path P3 Run 1

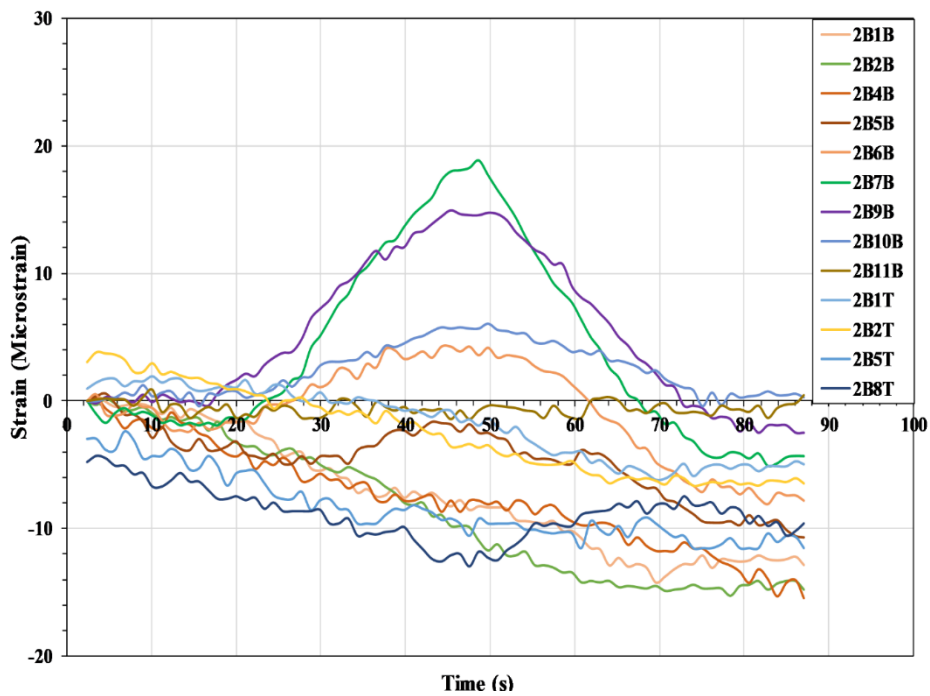


Figure 6- 7: Strain vs time diagram for Path P3 Run 2

Figure 6-8 shows the strain vs. time diagram for the bottom strain gages of the girders near mid-span for the stop location test. Girders B4, B5, and B6 showed the maximum response since the girders were located near the position of the three trucks.

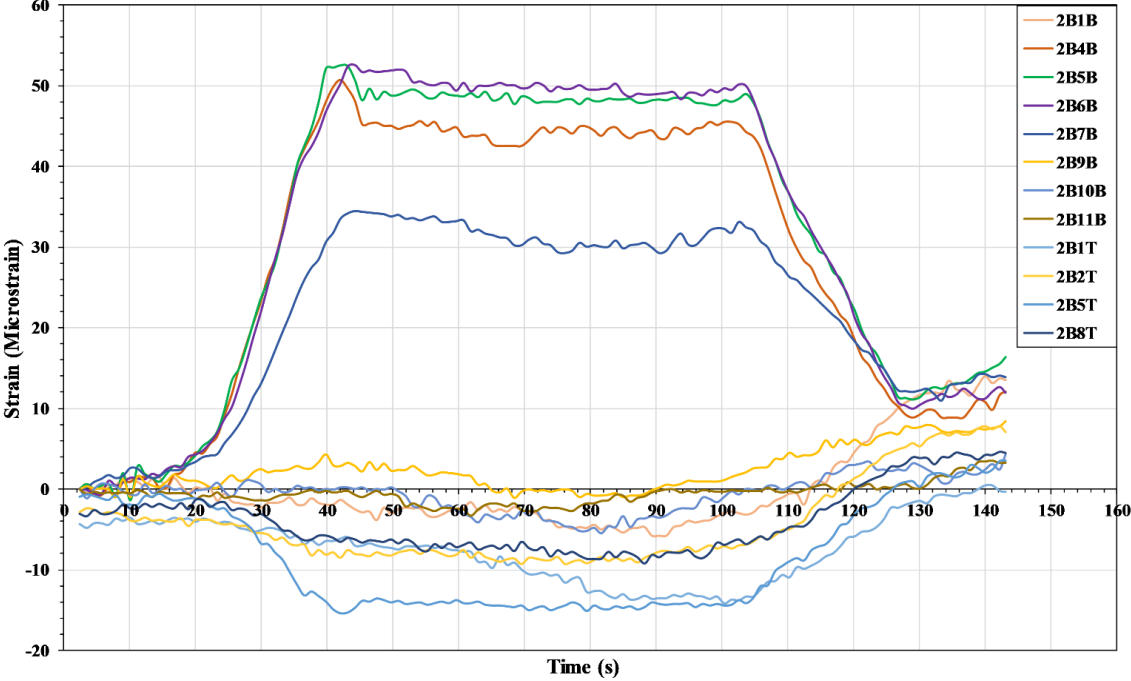


Figure 6- 8: Strain vs time diagram for the stop location test

Analysis of data from Figures 6-2 to 6-8 shows that the strain values at the mid-span showed some residual strains even after the trucks left the span. The strain values started from zero and increased to the maximum values when the trucks were on midspan, but the strain values did not return to zero after the trucks left the span. This behavior was observed for almost all the girders for all the paths. These remaining residual strains indicate nonlinear behavior, which may be caused by the loss of composite action or delamination between the deck and the girder, or within the composite deck.

To check whether the composite action is compromised, the neutral axis of the composite girder section was calculated from the collected top and bottom strain data from the girders. The theoretical neutral axis for full composite action was also calculated according to AASHTO LRFD Bridge Design Specifications (2017). The average location of the neutral axis from the load test (Phase 1) was around 41 in. from the bottom of the girder (on the web). However, the theoretical neutral axis from AASHTO (2017) was calculated as 57 in. from the bottom of the girder for the

composite section (in the deck) while it was calculated as 40 in. from the bottom for a non-composite girder (App. A). This change in the position of the neutral axis indicates a loss of composite action between the girder-deck and deck-panel system. The calculations for the experimental neutral axis were performed using equation 6-1 as shown by the process in Figure 6-9. Figure 6-10 shows the locations of the neutral axis for the load test (Phase 1).

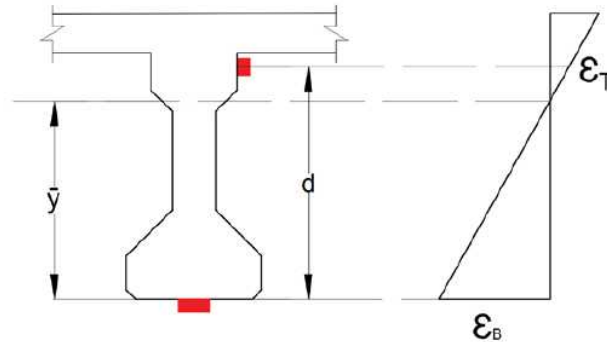


Figure 6- 9: Neutral axis calculation

$$\bar{y} = \frac{\epsilon_B d}{\epsilon_B + \epsilon_T} \quad (6-1)$$

Where:

$\bar{y}$  = Neutral axis location from the bottom (in.)

$d$  = distance between the top and bottom gauges (in.)

$\epsilon_B$  = Strain in bottom gauge ( $\mu\epsilon$ ) (Absolute value)

$\epsilon_T$  = Strain in top gauge ( $\mu\epsilon$ ) (Absolute value)

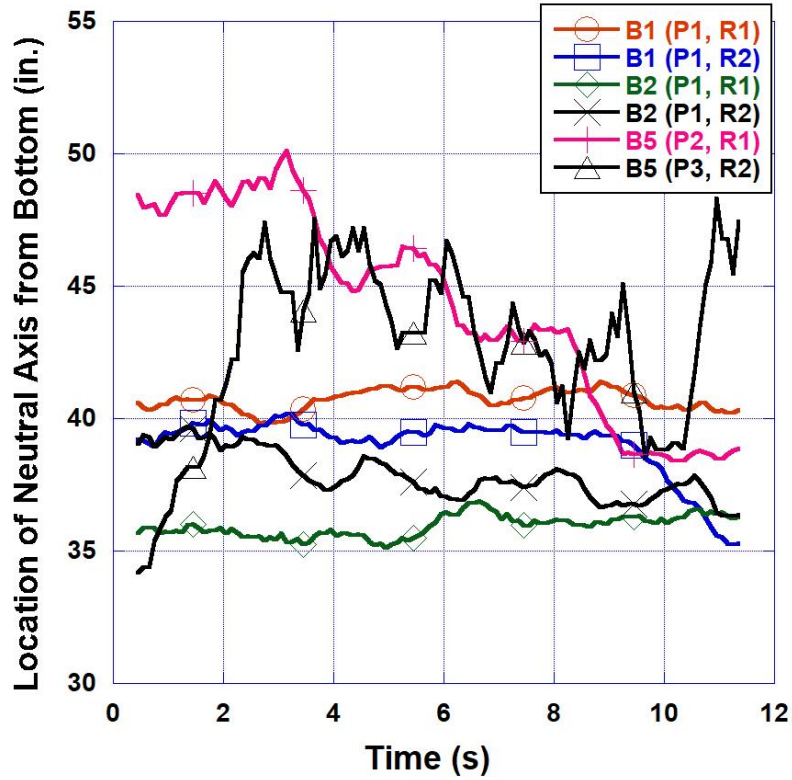


Figure 6- 10: Locations of the neutral axis obtained from the load test (Phase 1)

The rotational tiltmeters provided the end rotations of the girders. Figure 6-11 shows the rotation vs time diagram for girder B4 of Path P2 Run 1. It can be seen from the figure that the data has a excessive amount of noise and vibration. This is also the case for the rotation of all the other load tests for this bridge. This noise might be caused due to the vibration of the bridge. The rotation data were then refined as previously and were used to calibrate the Finite Element Model. Figure 6-12 shows the refined rotation data for girder B4 of Path P2 Run 1.

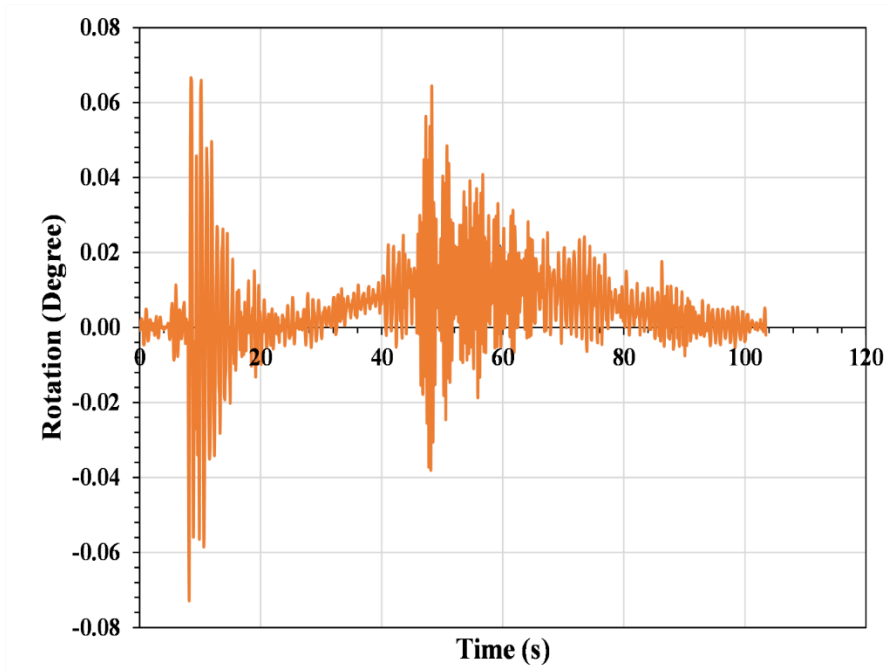


Figure 6- 11: Rotation vs. time for Path P2 Run 1

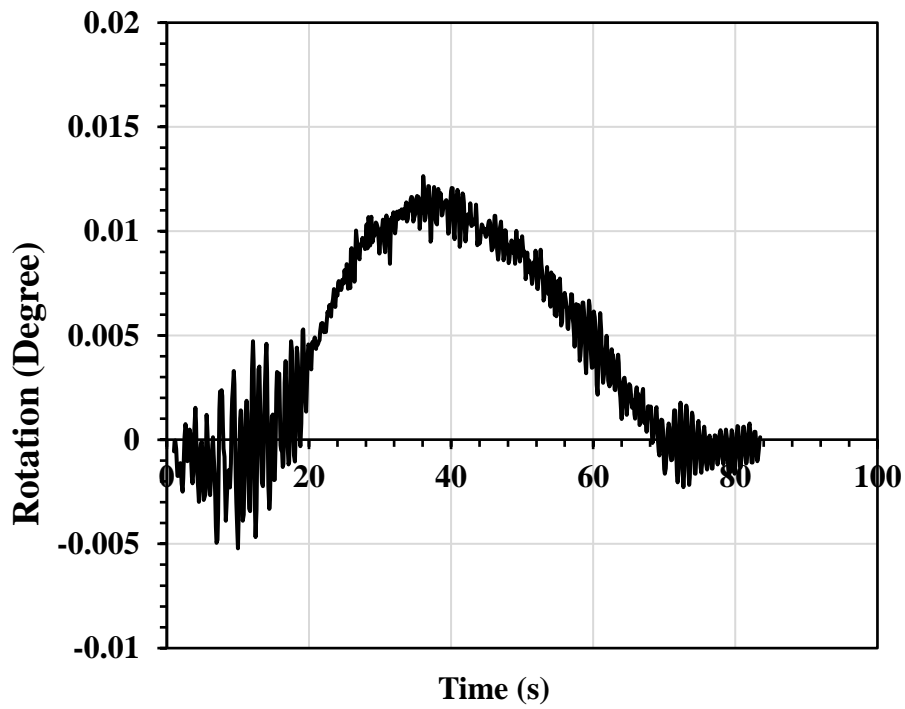


Figure 6- 12: Refined rotation data for Path P2 Run 1

### 6.1.2 Phase 2

The strain gage and the rotational tiltmeter data were analyzed to evaluate the load response of the bridge. Figure 6-13 shows a typical strain response from a strain gage at mid-span of the girder. Additionally, the strain response exhibited ample noise and vibration as a result of the vibration when the truck passed across the bridge. The strain values were refined by calculating the moving average between 10 data points to remove the noise and vibration in the measured data. This refinement provided one data point for every second which was accurate enough for all evaluation purposes. Only the refined results are presented further in the report.

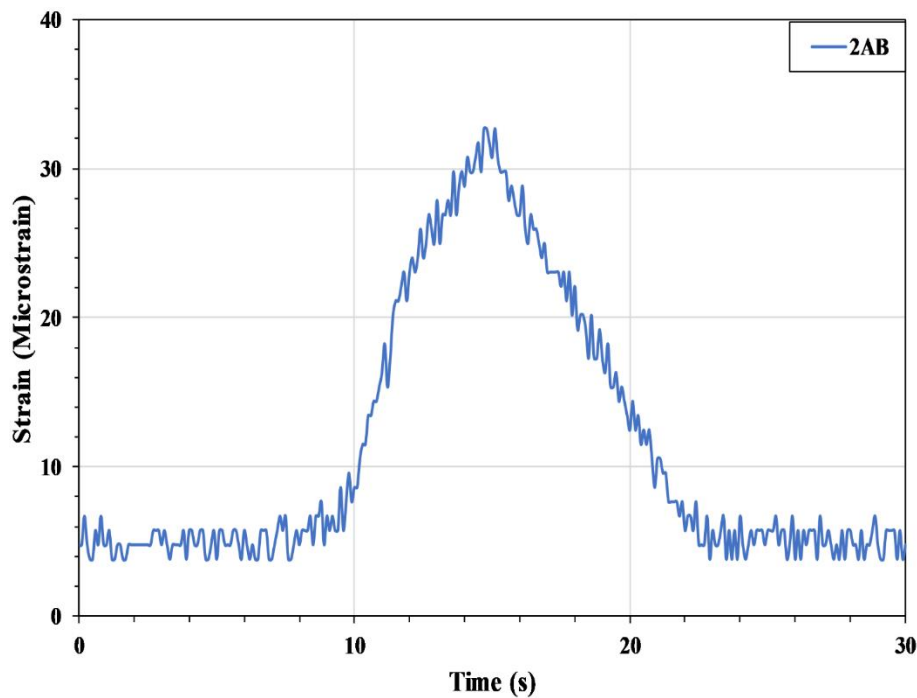


Figure 6- 13: Raw strain data for Path P1 Run 1

Figures 6-14 and 6-15 show the strain vs. time diagram for Run 1 and Run 2 of Path P1 for the bottom strain gages near the mid-span. The data from the girders B1, B2, and B3 are shown here since their responses were significant for this path. The response of other girders gradually decreased with distance from the truck wheel.

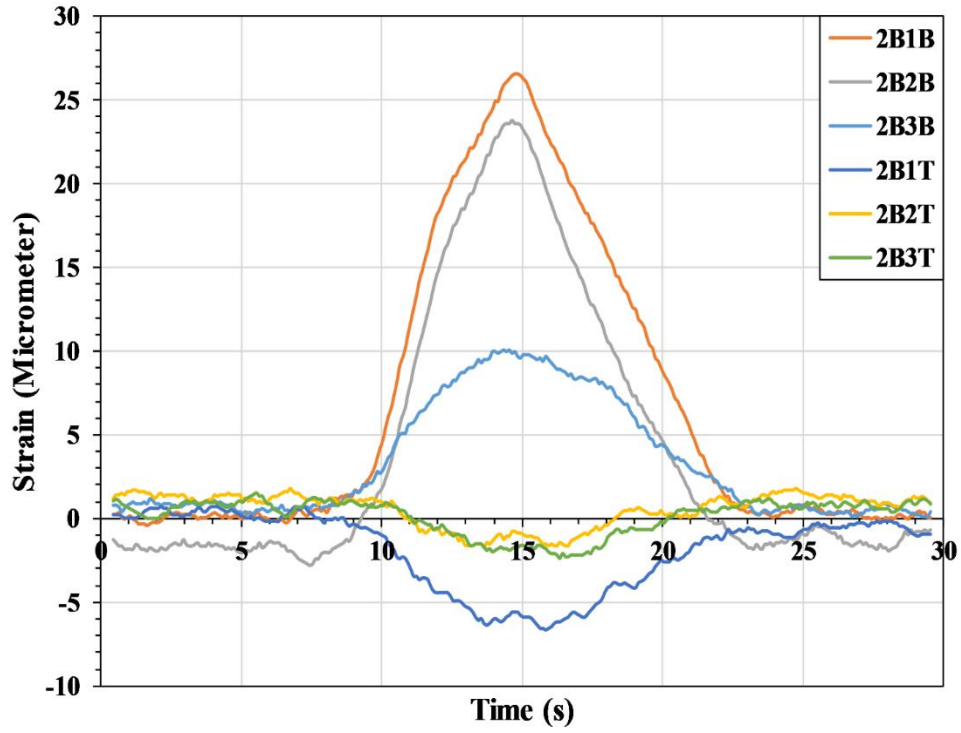


Figure 6- 14: Strain vs time diagram for Path P1 Run 1

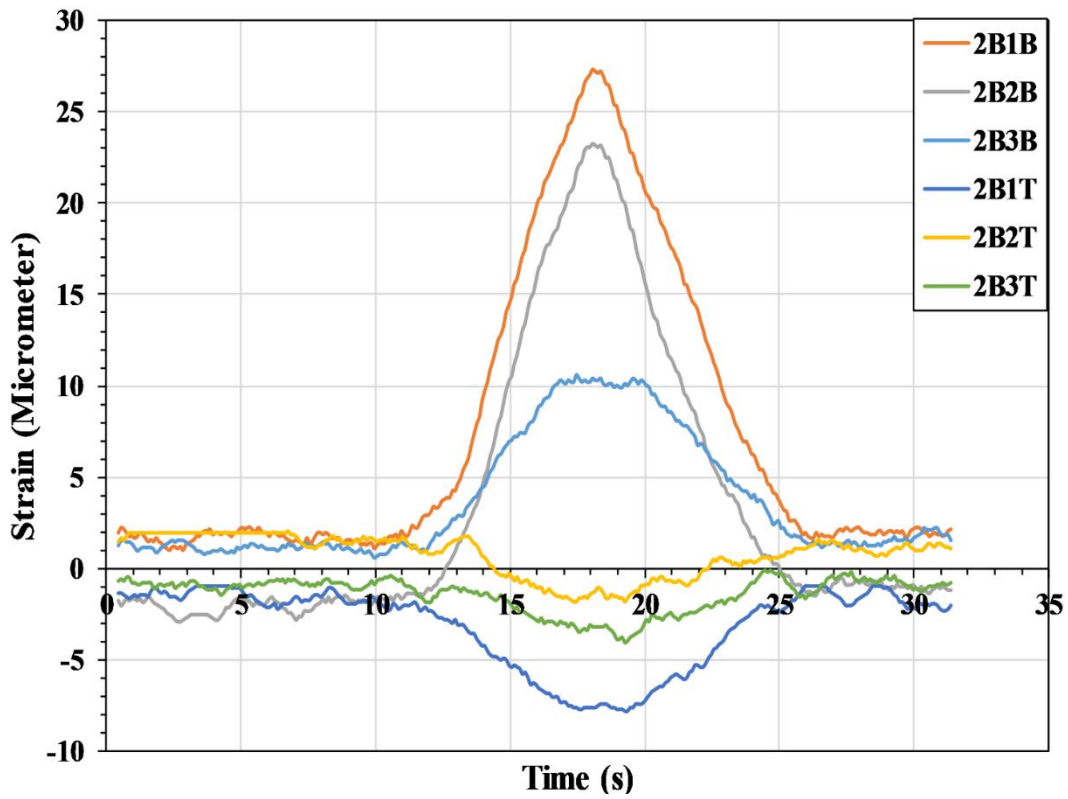


Figure 6- 15: Strain vs time diagram for Path P1 Run 2



The responses were similar for Path P2 and P3. Figures 6-16 to 6-20 show the responses for Path P2 (Run 1 and 2), Path P3 (Run 1 and 2), and stop location test respectively.

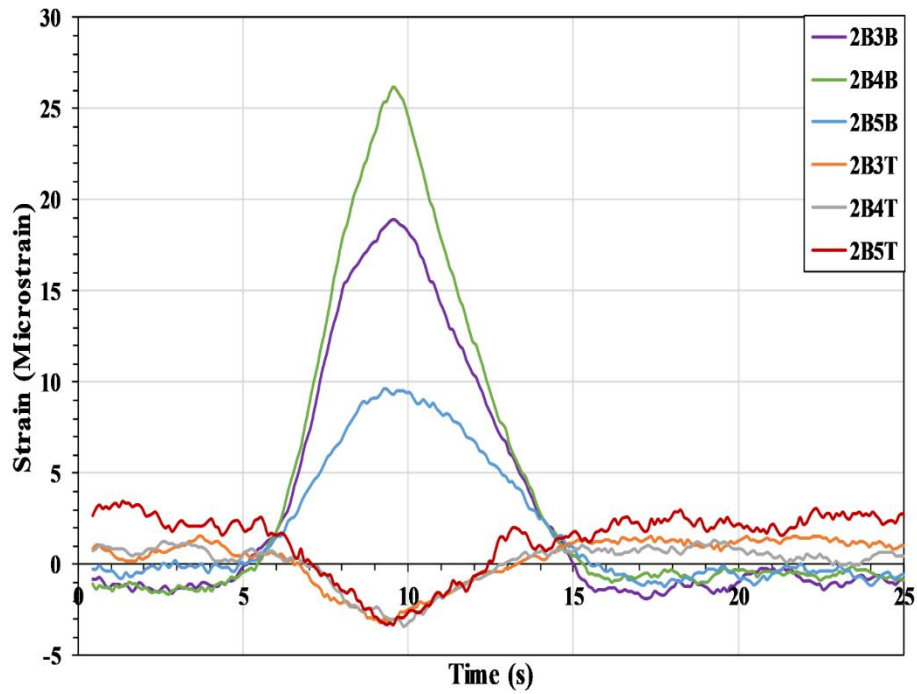


Figure 6- 16: Strain vs time diagram for Path P2 Run 1

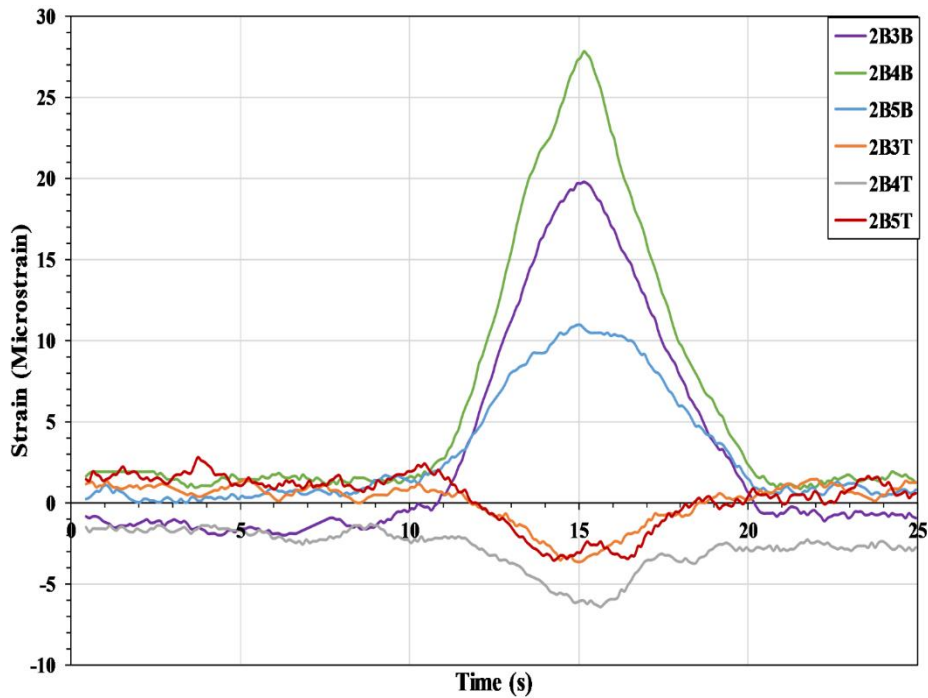


Figure 6- 17: Strain vs time diagram for Path P2 Run 2

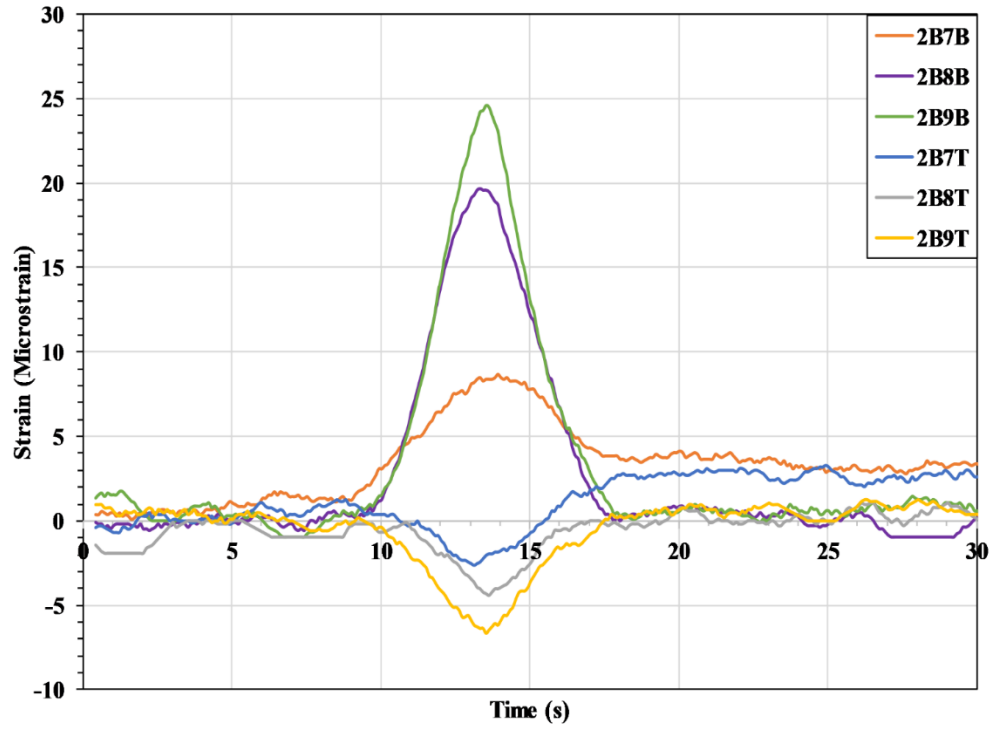


Figure 6- 18: Strain vs time diagram for Path P3 Run 1

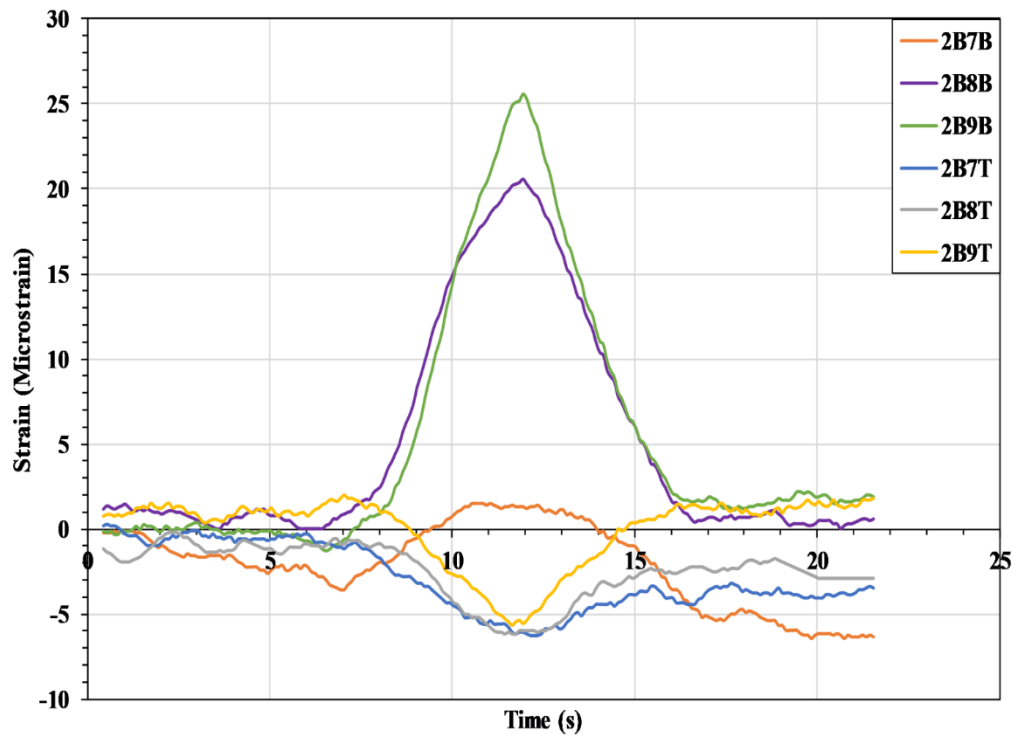


Figure 6- 19: Strain vs time diagram for Path P3 Run 2

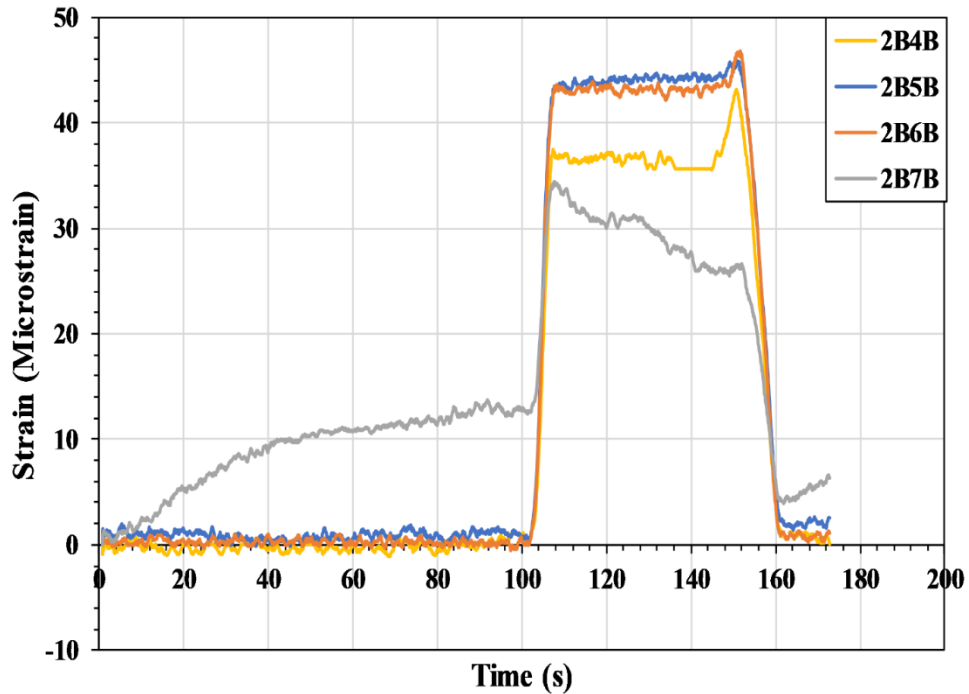


Figure 6- 20: Strain vs time diagram for the stop location test

Analysis of data showed that the strain values at the mid-span showed some residual strains even after the truck left the span like the previous load test. The presence of residual strain and inconsistent results between two different runs indicated that the load distribution characteristics are compromised, and the bridge is exhibiting unusual behavior.

The location of the neutral axis for the load test (phase 2) was calculated from equation 6-1. A comparison of the locations of the neutral axes between Phase 1 and Phase 2 load tests and their theoretical values are provided in Table 6-1. The neutral axis location for a single girder was found from averaging the locations from all load test paths, except those where the trucks were too far from the girder to make a significant response. Figure 6-21 shows the locations of the neutral axis for the load test (Phase 2).

Table 6- 1: Neutral axes locations

	Load test (Phase 1)	Load test (Phase 2)
Theoretical NA from the bottom (composite), in.	57	
Theoretical NA from the bottom (non- composite), in.	40	
Experimental NA from the bottom (in.)	41	42

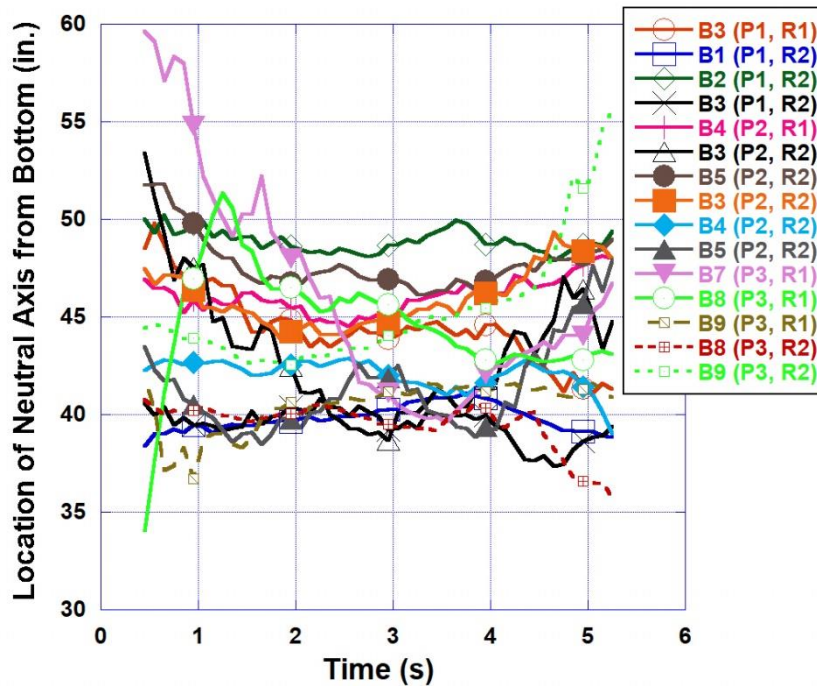
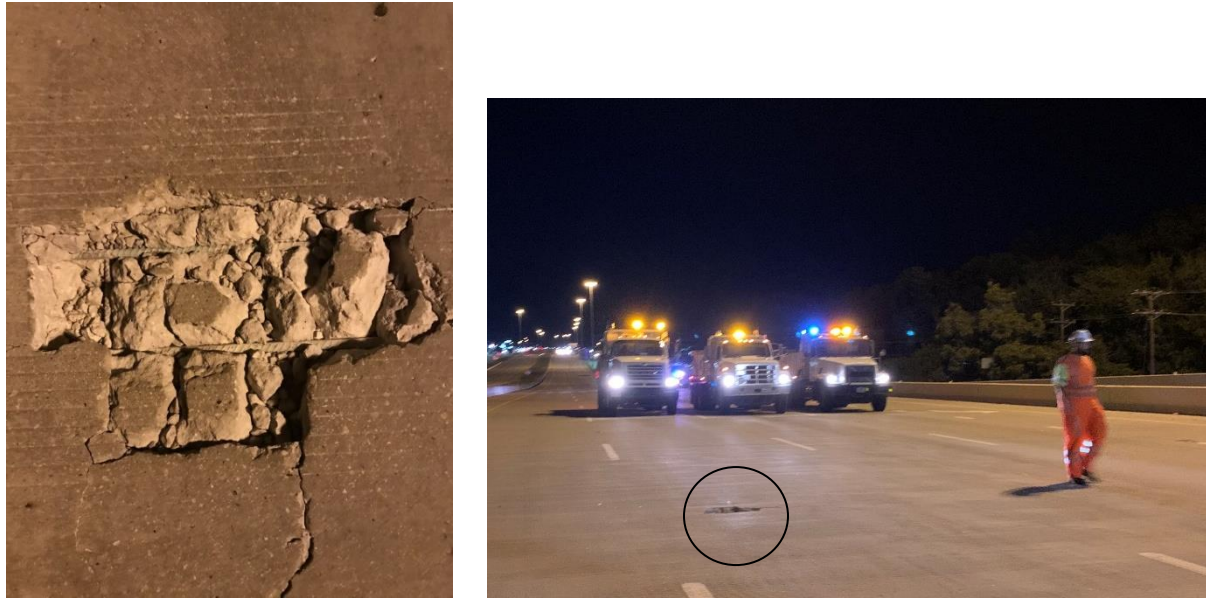


Figure 6- 21: Locations of the neutral axis obtained from the load test (Phase 2)

From Table 6-1, it is evident that there is a small discrepancy (1 in.) between the neutral axis locations from the two load tests. The possible reason behind this is the temperature and/or the humidity difference during the two load tests. Also, during Phase 2, additional girders were instrumented to locate the neutral axes which yielded more precise results. The new potholes and cracks on the deck (Figure 6-22) may be due to this almost non-composite behavior of the bridge.



(a)

(b)

Figure 6- 22: New pothole on the deck of Span 3: (a) View from the top; and (b) View from the side

The noise to response ratio was very high for the deck. Since the strain data showed very little response for all the paths, the noise and the response were almost inseparable for the deck. Figure 6-23 shows the response of different portions of the deck due to Path P2 Run 1 with extreme noise and vibration.

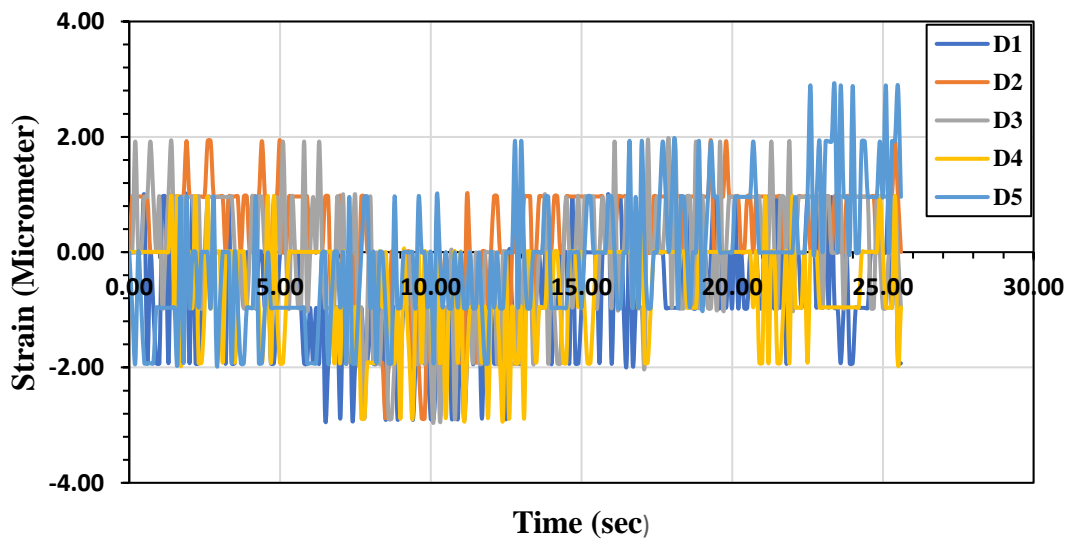


Figure 6- 23: Strain response of the deck portions for Path P2 Run 1

Figure 6-24 shows the rotation vs. time diagram for the girders from Path P1 Run 1. The signal to noise ratio for the rotation results was very low as seen by the fluctuations in the measured response when the truck entered the bridge. This was also the case for the rotation of all the other load paths for this bridge similar to the Phase 1 tests. Figure 6-25 shows the refined rotation data for the girders from Path P1 Run 1.

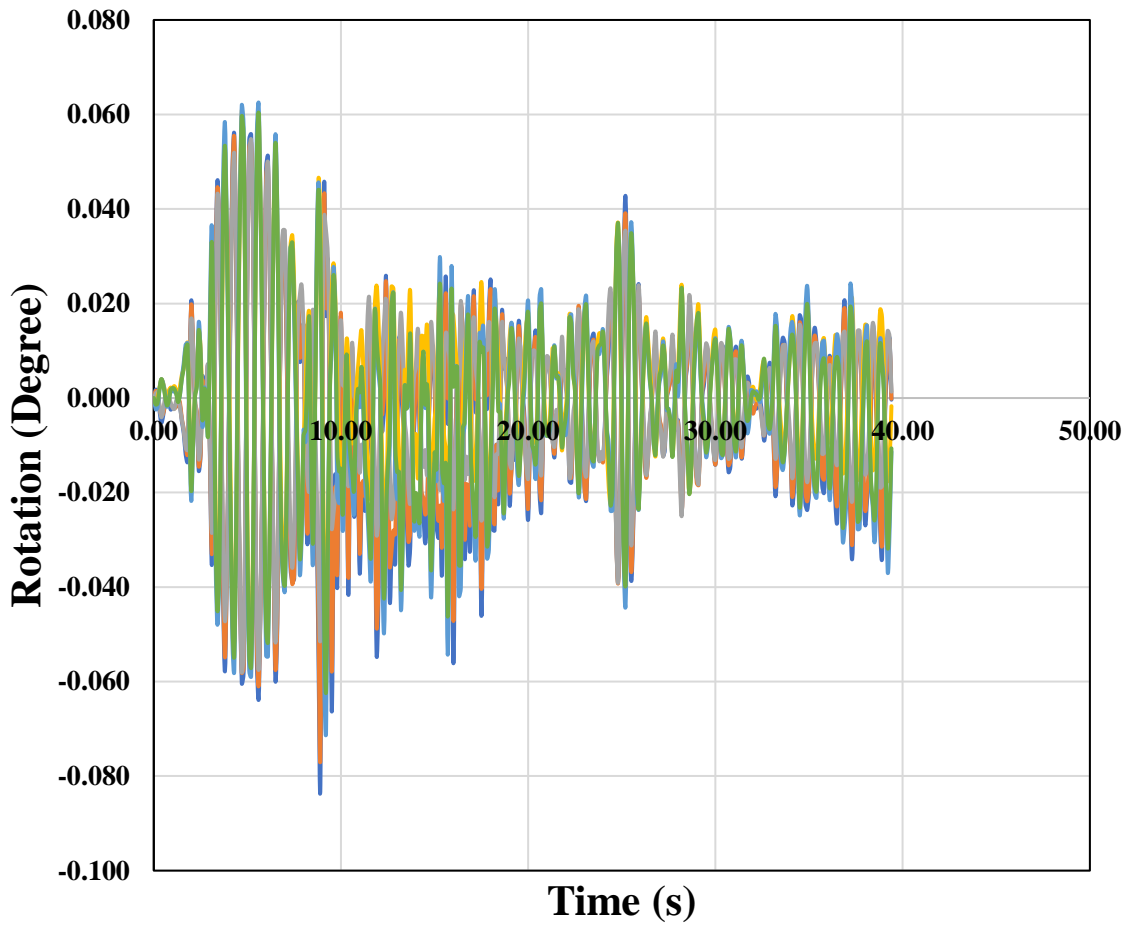


Figure 6- 24: Rotation vs time for Path P1 Run 1

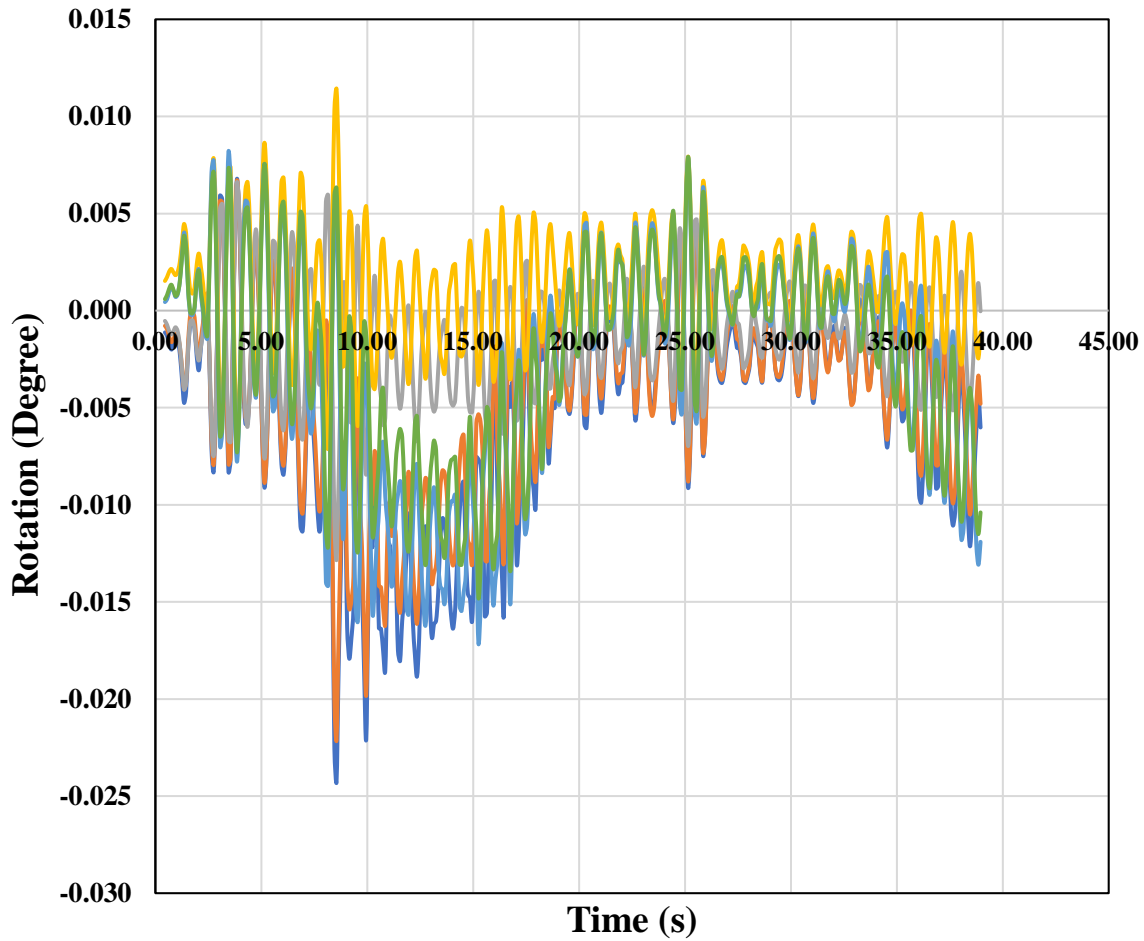


Figure 6- 25: Refined rotation data for Path P1 Run 1

## 6.2 NDE

### 6.2.1 GPR Results

The GPR scans were post-processed and analyzed with the RADAN (2017) software. No delamination could be observed from the GPR scans. One possible reason is that the cracks, voids or delamination should be of at least 0.25 in. wide to be visible in the B-scans achieved from GPR. The reinforcement profile was visible. A 2-D contour plan prepared from the top reinforcement cover depths found through the 2.6 GHz antenna of the GPR is presented in Figure 6-26.

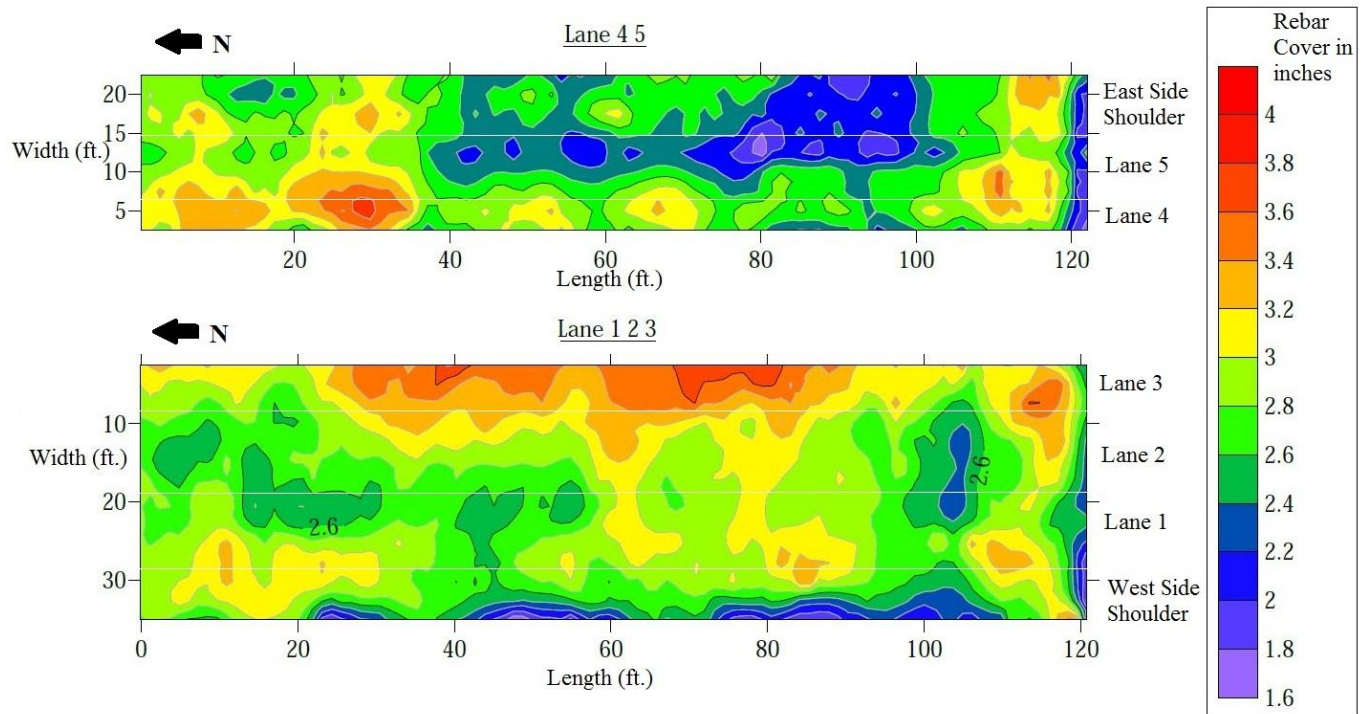


Figure 6- 26: 2-D contour plots showing rebar covers from GPR data

The covers seem to be satisfactory throughout the layout as expected for a new bridge. This indicates less or very little surface corrosion.

### 6.2.2 IE Results

The IE results on discrete data grids were then plotted in 2-D contour maps, as shown in Figure 6-27. In the contour maps, the color red indicates a very high possibility of the presence of delamination. The blue areas indicate sound concrete without any debonding or delamination.

Contours from both segments showed strong signs of delamination in the red areas. The delamination depths are expected to be at or near the rebar level within 4 in. from the top surface. The delamination seemed to be more prevalent in the areas on top of the girders as compared to the areas between the girders.

While the state of the delamination was assessed in discrete discontinuous grid points on the bridge deck, the results presented above are in the form of continuous contour maps, where linear interpolation was used between the data points.



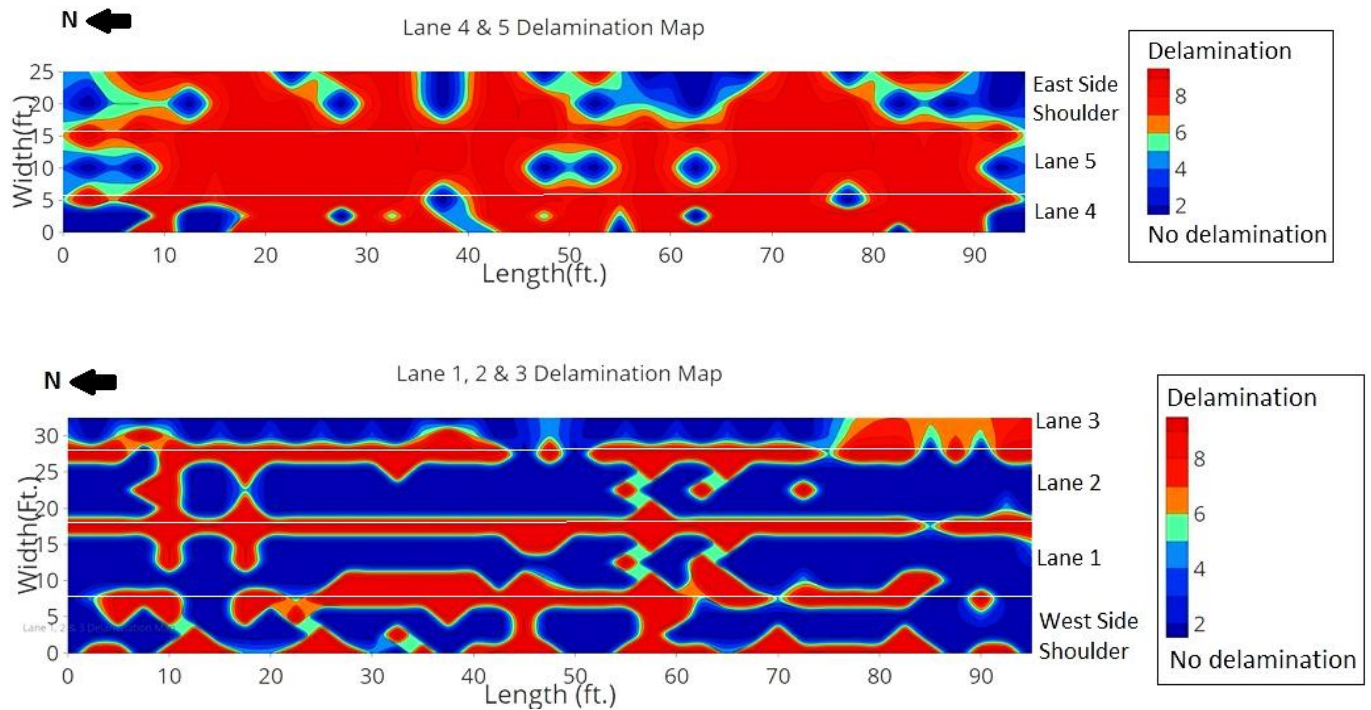


Figure 6- 27: Contour plots from IE data showing possible delamination

## 6.3 Load Rating

Two cases were considered herein for the load rating of the Wilson Creek SB Bridge:

1. Deck capacity alone in the transverse bridge direction.
2. Girder capacity.

### 6.3.1 Deck Capacity

The deck capacity of the bridge was calculated using the previous NDE data (GPR and IE) following the procedure outlined below:

- The material properties used for calculating deck capacity was mentioned in the material properties section of the report. The mild steel rebar size and spacing of the top mat were found as #5@6'' o.c. from standard TxDOT drawing. The panel dimensions were taken as 8.33 ft. x 7.5 ft. x 4in. using the TxDOT standard panel drawing. A total of 17 prestressing steel strands were used assuming 6 in. spacing (maximum spacing specified by TxDOT). Half inch diameter

270 ksi low relaxation steel strands were used in the calculation as this is the most popular size used by TxDOT.

- The moment capacity of the deck was calculated for a 12 in. wide strip along the length of the girder. The length of the strip was measured as 9 ft. which is the spacing of the girders.
- GPR data was used to find the concrete cover for the negative mild steel near the girder lines. The negative region was found to be 2.49 ft. from both sides of the centerline of the girder. This length was found from calculating the point of contra-flexure in a continuous deck. The detailed calculation was also verified using SAP2000 (2016). For more than 90% of the negative moment region, the top cover was found to be around 2.4 - 3.0 in. from the GPR data analysis. So, 2.5 in. cover was used in the negative moment calculations. Figure 6-28 shows the girder center line (black line) and the analyzed negative moment region (hatched area) on a portion of GPR data from where the average top cover of 2.5 in. was found.

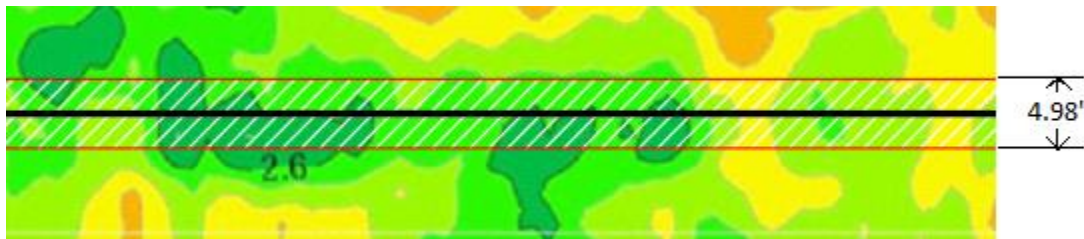


Figure 6- 28: Negative moment region (hatched area) and girder center line (black line) on a portion of GPR contour

- Positive moment capacity was not affected by the GPR data, because GPR detected only the top deck rebars which contribute to the negative moment capacity only. The precast panels mainly contribute to the positive moment capacity.
- From the IE data, the percentage of delamination for both the negative and positive moment regions were calculated. The former was taken as 2.49 ft. from both sides of the centerline of the girder, while the latter was taken as 4.02 ft., using a similar procedure as above. Figure 6-29 shows the positive and negative moment regions (hatched area) and the girder center lines (black lines) from where the percentage delamination was extracted.

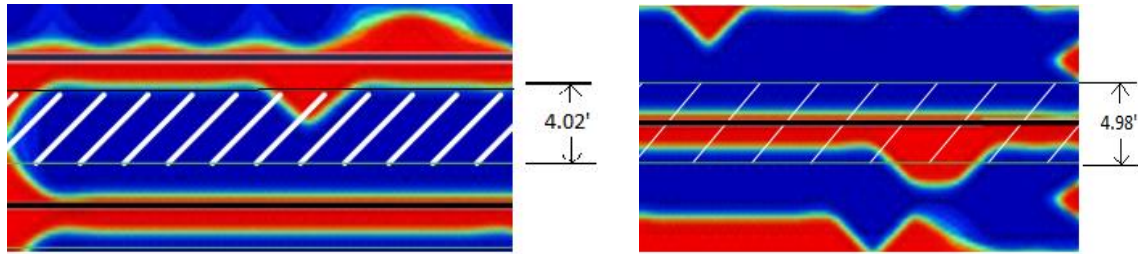


Figure 6- 29: Positive moment region (left) and negative moment region (right) from IE data

- The percentage of delamination for the positive region and negative regions was found to be 11% and 49%, respectively. It should be noted that the 2-D IE contour cannot verify the depth of delamination. To be conservative, an average between the delamination of both regions (30%) was applied to reduce both the positive and negative moment capacity. Table 8-2 shows the moment capacities of the deck calculated from GPR and IE data.

Table 6- 2: Deck moment capacity

<b>Moment Type</b>	<b>Moment Capacity (k- ft./ft.) (From GPR data) <math>M_n = A_s f_y (d - \frac{a}{2})</math></b>	<b>Average Percentage delamination for positive/negative region</b>	<b>Modified Design Moment Capacity (k-ft./ft.) (From IE)</b>
<b>Positive</b>	35	30%	25
<b>Negative</b>	19.48	30%	13.64

According to the Load Factor Method (LF) obtained from the AASHTO Manual for Bridge Evaluation (2018), the moment rating factor of concrete components can be calculated using equation 6-2:

$$\text{Moment Rating Factor, RF} = \frac{\text{Moment Capacity} - A_1 X \text{ Dead load Moment}}{A_2 X (\text{Live load Moment} + \text{Impact})} \quad (6 - 2)$$

The moment capacities used in moment rating were obtained from Table 6-2 (modified design moment capacity) and the negative moment governed the rating. A1 and A2 are AASHTO (2018) rating factors, with A1=1.3 and A2 varying depending on the rating level desired (A2 = 2.17 for

inventory level and 1.3 for operating level). The live load moment was determined using HS-20 loading including an impact factor of 1.3. Bridge member ratings were determined by equation 6-3 where the rating factors were multiplied by the weight of the rating vehicle (HS-20 for this case) to find the allowable safe live load (inventory level) and the maximum permissible live load (operating level). The detailed hand calculations are provided in the App. B. Table 8-3 shows a summary of the Load Factor Rating Method.

$$\text{Member rating} = WXR F \quad (6 - 3)$$

Where: W= Weight of rating vehicle.

RF= Rating factor.

Table 6- 3: Deck moment rating factor and bridge member rating

<b>Rating Level</b>	<b>Rating Factor (RF)</b>	<b>Bridge Member Rating (lb.)</b>
Inventory level	1.00	72,000
Operating level	1.60	114,770

### 6.3.2 Girder Capacity

Girder rating was conducted using CSIBridge (2015) assuming composite girder and deck. Load rating was also done using hand calculations by the Load Factor Method (AASHTO Manual for Bridge Evaluation, 2018) to verify the results. Appendix C shows a sample calculation for load rating. Comparison of hand calculations and CSI bridge load rating are shown in Table 6-4.

Table 6- 4: Comparison between hand calculation and CSIBridge results

<b>Rating Level</b>	<b>Rating Factor (RF) assuming full-composite action, from hand calculations</b>	<b>Bridge Member Rating (lb.) assuming full composite action</b>	<b>Rating Factor (RF) assuming partial-composite action, from hand calculations</b>	<b>Bridge Member Rating (lb.) assuming partial-composite action</b>	<b>Rating Factor (RF) from CSI Bridge</b>
Inventory level	1.74	125,280	1.51	108,955	1.59
Operating level	2.91	209,520	2.53	181,870	

Upon reviewing the data, it is reasonable to conclude that when partial-composite action was applied (using the average neutral axis location from the load test), the girders were still safe for HS-20 standard vehicle for both inventory and operating levels. Since CSIBridge (2015) assumed full composite action, the load rating value from CSIBridge (2015) was similar to the hand calculated load rating value, that assumes full composite action between the girder and the panels/deck for inventory level. The model rating factor was slightly different because CSIBridge (2015) follows the current LF method in the analysis.

Using the rating factor assuming partial-composite action is more practical in this case because the load test confirmed partial-composite action and a reduced girder capacity. Based on the rating, both the deck and girders were capable of carrying the HS-20 load. However, since the components are not acting monolithically, the serviceability and the durability of the deck are a matter of concern for the bridge.

## 6.4 Dynamic Vibration Test

### 6.4.1 Ambient Vibration Test

While investigating unpleasant vibration caused by passing traffic, Mallock (1902) concluded that acceleration is the primary reason for discomfort. Wright and Walker (1971) declared a peak acceleration of more than 16.67 ft./s<sup>2</sup> as ‘unpleasant to some’ while their limit of perceptible acceleration was less than 4.17 ft./s<sup>2</sup>. According to the International Organization for Standards (ISO 2631-1) (1997), acceleration of more than 6.5 ft./s<sup>2</sup> is extremely uncomfortable.

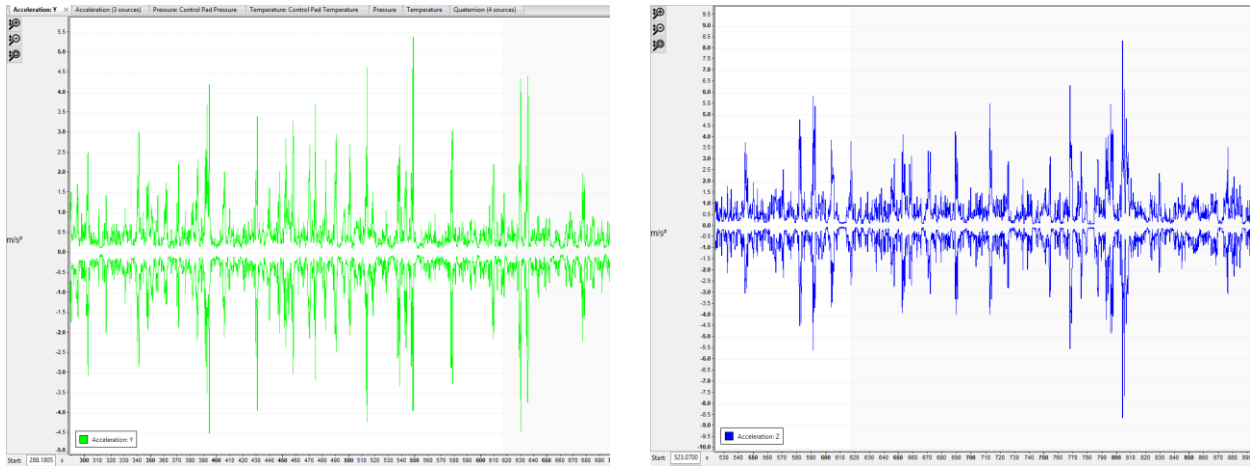
Table 6-5 shows the maximum accelerations in three directions (along the traffic, transverse to the traffic and vertical) for different components of Wilson Creek SB bridge under regular traffic during rush hours. Deck 1-2 denotes the portion of the deck between girders 1 and 2.

Table 6- 5: Maximum accelerations for different components of the SB bridge

Designation	Maximum acceleration (ft./s <sup>2</sup> )		
	Along with traffic	Transverse to traffic	Vertical
Girder 1	3.61	15.75	7.22
Girder 2	4.59	17.72	6.73
Girder 3	3.61	14.76	8.20
Girder 4	3.94	13.78	5.91
Girder 5	3.28	17.72	6.89
Girder 6	8.20	14.76	9.19
Deck 1-2	1.51	1.31	4.53
Deck 2-3	3.94	1.51	11.81
Deck 3-4	8.53	4.27	27.56
Deck 4-5	2.9	1.6	7.4
Deck 5-6	8.53	8.53	21.65
Deck 6-7	9.2	8.6	25.1
Bearing pad (Girder 4)	18.04	8.20	24.61
Bearing pad (Girder 1)	13.45	4.60	10.66

The data in Table 6-5 indicates that the accelerations were significantly higher in the transverse direction than the vertical ones for the girders. This phenomenon was reversed for the deck. The bearing pads showed maximum accelerations in the vertical directions. Figures 6-30 (a) and (b)

show the maximum transverse and vertical accelerations for girder 5 and deck 3-4 of the SB bridge respectively.



(a)

(b)

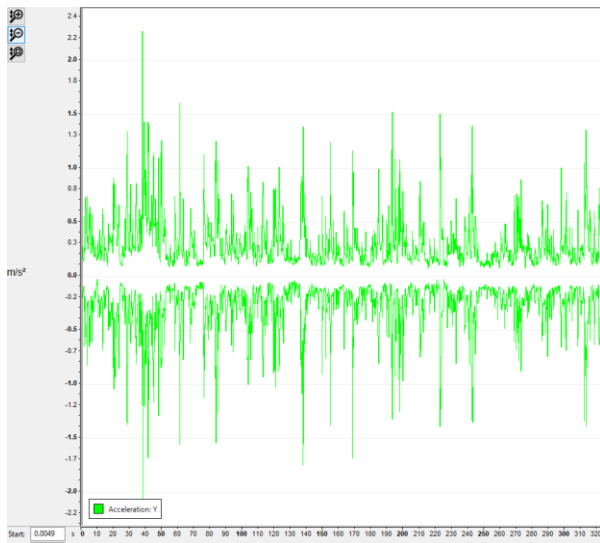
Figure 6- 30: Maximum acceleration of the SB Bridge: (a) Transverse acceleration of the girder; and (b) Vertical acceleration of the deck

Table 6-6 shows the maximum accelerations for some of the girders and an interior portion of the deck for the NB bridge.

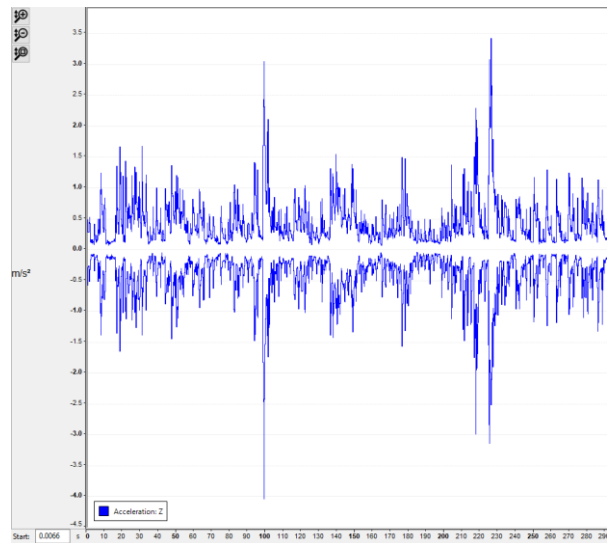
Table 6- 6: Maximum accelerations for different components of the NB bridge

Designation	Maximum acceleration (ft./s <sup>2</sup> )		
	Along with traffic	Transverse to traffic	Vertical
Girder 1	2.30	4.43	2.13
Girder 3	2.62	7.22	2.62
Girder 4	2.5	5.5	2.22
Girder 5	2.55	6.17	2.3
Deck 3-4	3.28	3.28	11.48
Deck 2-3	3.1	3.3	12
Deck 4-5	3.4	2.9	9.52

Figures 6-31 (a) and (b) show the maximum transverse (girder 3) and vertical (deck 3-4) accelerations of the NB bridge respectively.



(a)



(b)

Figure 6- 31: Maximum acceleration of the NB Bridge: (a) Transverse acceleration of the girder; and (b) Vertical acceleration of the deck

Table 6-7 shows the maximum acceleration values for different components of the Virginia Parkway NBML bridge under regular rush hour traffic.

Table 6- 7: Maximum accelerations of different components of Virginia Parkway bridge

Designation	Maximum acceleration (ft./s <sup>2</sup> )		
	Along with traffic	Transverse to traffic	Vertical
Girder 5	1.97	8.53	5.25
Girder 6	3.28	6.89	6.23
Girder 8	3.61	9.51	6.89
Girder 10	2.30	8.20	5.58
Girder 11	1.51	3.28	2.62
Girder 13	1.80	3.61	6.23
Deck 6-7	4.92	5.25	14.44



Deck 7-8	8.2	6.89	19.69
Deck 8-9	3.2	4.1	13.87
Bearing pad (Girder 8)	16.73	12.14	5.25

Figures 6-32 (a) and (b) show the maximum accelerations in the transverse (girder 8) and vertical (deck 7-8) directions for Virginia Parkway bridge respectively.

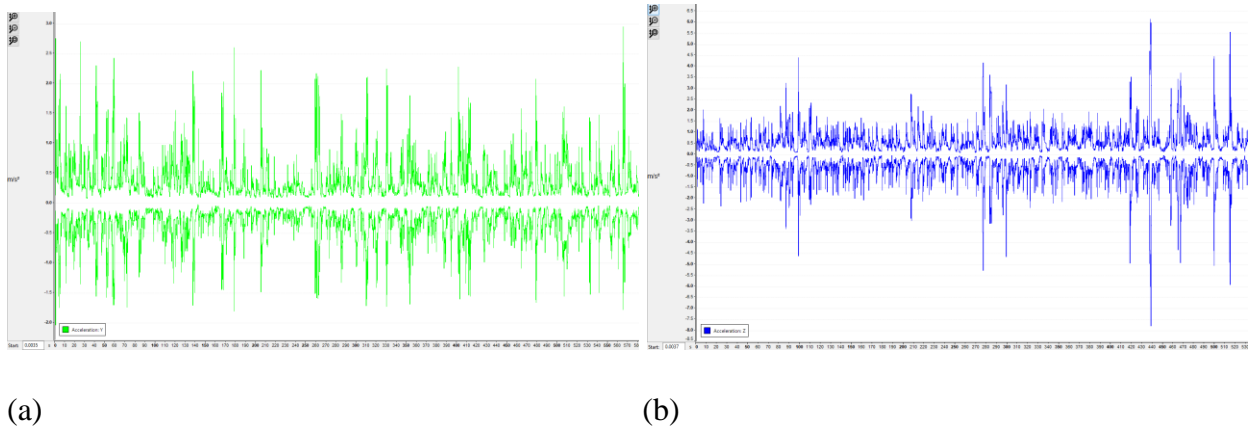


Figure 6- 32: Maximum acceleration of the Virginia Parkway Bridge: (a) Transverse acceleration of the girder; and (b) Vertical acceleration of the deck

Table 6-8 shows a comparison of the maximum accelerations of different components of the three bridges.

Table 6- 8: Comparison of the maximum accelerations

Maximum/average accelerations	Wilson Creek SB (ft./s <sup>2</sup> )	Wilson Creek NB (ft./s <sup>2</sup> )	Virginia Parkway (ft./s <sup>2</sup> )
Maximum transverse acceleration of the girders	17.72	7.22	9.51
Maximum vertical acceleration of deck	27.56	11.48	19.69

The data in Table 6-8 suggests that the maximum transverse acceleration of the girders for the Wilson Creek SB bridge was 145% and 86% higher than the NB and the Virginia Parkway bridges

respectively. The average transverse acceleration also yielded significantly higher value for the SB bridge compared to the NB and the Virginia Parkway bridges (170% and 136% respectively). The higher values of transverse accelerations of the girders of the SB bridge indicate a significant loss of composite action between the girders and the deck/panel system in the transverse direction which also explains the progressive transverse cracks and potholes on the SB bridge deck. The maximum vertical acceleration values of the decks were also significantly higher for the SB bridge than the other two bridges due to the partial-composite action.

#### 6.4.2 Vibration Test During Static Load Test

The dynamic magnification factor (DMF) of a bridge can be defined by equation 8-4 (Nguyen & Tran 2015; Mohseni et. al. 2018; Malla et. al. 2017). The responses could be displacement, stress, or strain.

$$DMF = \frac{\text{Dynamic response}}{\text{Static response}} \quad (6-4)$$

Szerszen et. al. (2019) conducted a case study on different composite and non-composite bridges by conducting static and dynamic load tests. From their load test results, the researchers concluded that for the non-composite bridges, the static strains yielded higher values than the dynamic strains and vice versa. This phenomenon took place due to the complex, non-linear load path of the non-composite system.

Both the static and dynamic strain data were analyzed for paths P2 and P3 with different speeds of the dump truck to find the dynamic impact factor. The data were smoothed by applying a ten-point moving average on each data set. Figure 6-33 shows the strain response of the girders C, D, and E for different speeds on path P2.

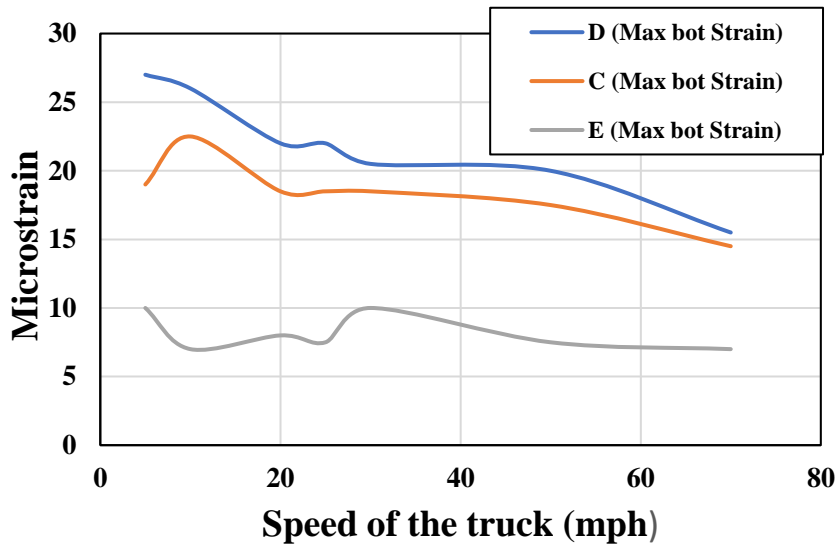


Figure 6- 33: Speed vs strain data for path P2

Girders C, D, and E showed maximum responses for path P2 because the truck was placed near to these girders during these runs on this path. Additionally, the dynamic strains reduced with the increasing speeds for the girders and yielded zero values for the DMF in equation 8-4. This phenomenon further suggests a partially composite action between the girders and the deck/panels. Due to partially composite action, the load path becomes more complex for the girders, deck, and panels. Figure 6-34 shows the speed vs strain data of the girders G, H, and I for path P3.

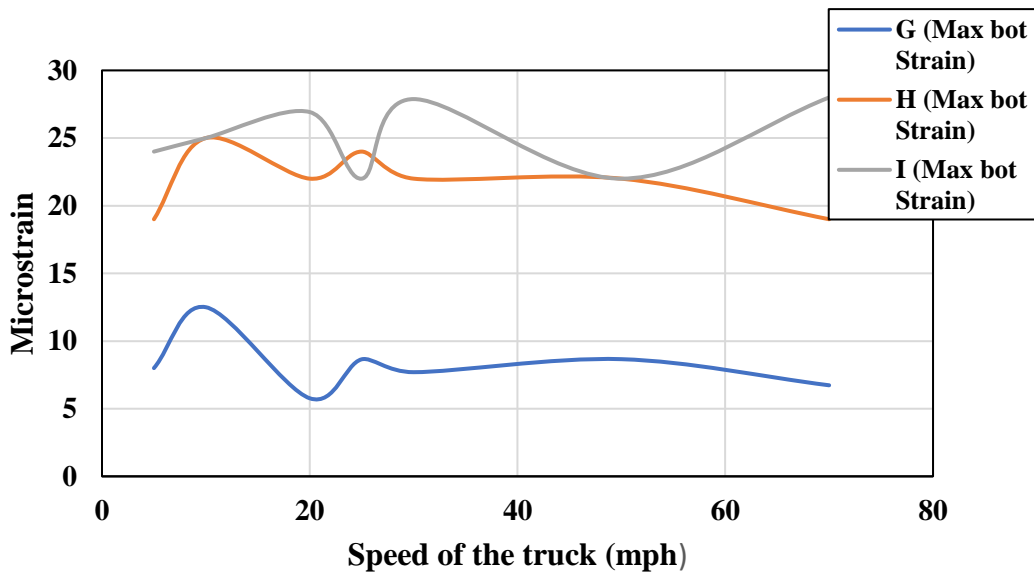


Figure 6- 34: Speed vs strain data for path P3

Girders G, H, and I showed maximum responses for path P3 because the truck was placed near to these girders during these runs on this path. Furthermore, the data were erratic for this case and no unique pattern could be found from the data set. Due to the increase of truck speeds, the strain data did not increase linearly which indicates complex load paths of the partial-composite girders and deck/panel system.

The natural frequency of the bridge was extracted from the dynamic vibration data by applying FFT on the ambient window of a data set. An ambient window is the portion of the data where the truck passes the deck and the bridge vibrates on its free vibration modes. Figure 6-35 shows an ambient window of the vibration data for path P2 while the vibration meter was placed under girder 4. Figure 6-36 shows the FFT analysis on an ambient window of 1 second for path P2.

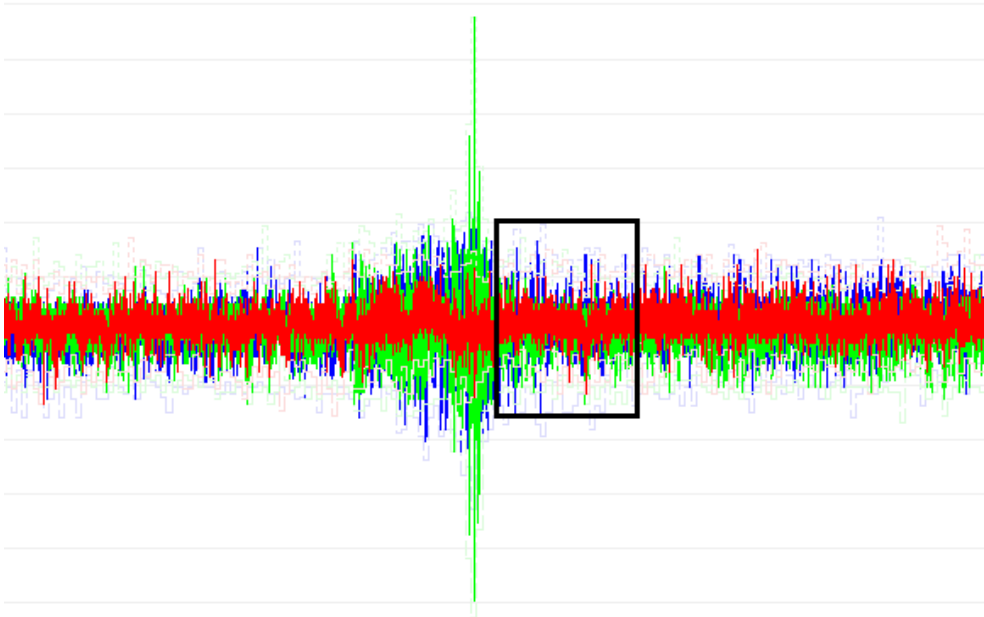


Figure 6- 35: Ambient window of the data shown in the box for path P2

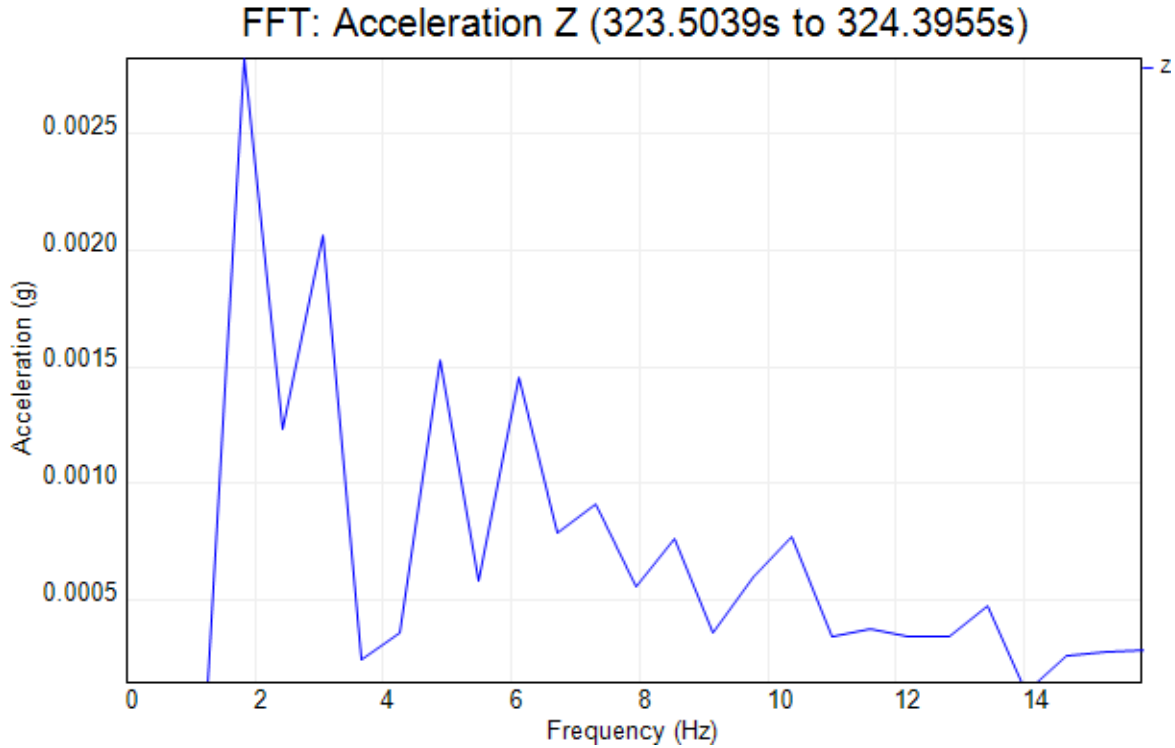


Figure 6- 36: FFT analysis on a 1-second ambient window for path P2

From FFT analysis of the data, the frequencies of various modes were found for the Wilson Creek SB bridge. Table 6-9 shows the frequencies of different modes of vibration found from FFT analysis of the vibration data.

Table 6- 9: Modal frequencies of the Wilson Creek SB bridge

<b>Modes of Vibration</b>	<b>Frequencies (Hz)</b>
1 <sup>st</sup> mode	2.03
2 <sup>nd</sup> mode	4.35
3 <sup>rd</sup> mode	6.275
4 <sup>th</sup> mode	8.9
5 <sup>th</sup> mode	11
6 <sup>th</sup> mode	12.25

From Table 6-9, it can be observed that the natural frequency of the bridge was 2.03 Hz. Amman (1995) proposed an empirical relation between fundamental natural frequency and maximum span length of highway bridges which suggests that the fundamental natural frequency of the SB bridge should be in a range between 3.28 Hz- to 3.96 Hz. Nevertheless, the fundamental frequency was relatively lower compared to the frequency mentioned in literature because of the stiffness reduction due to partial-composite action between the girders and the deck/panel. A reduced stiffness resulted in lower fundamental frequency and higher vibration.

## 6.5 Modeling

### 6.5.1 Stability Check

To obtain various energy components of the ABAQUS model, a history output request was created in the whole model domain in every one-second frequency increment. The energy was selected as the only output variable to save time and occupied physical memory during the analysis. Figure 6-37 shows the history output request window of the model.

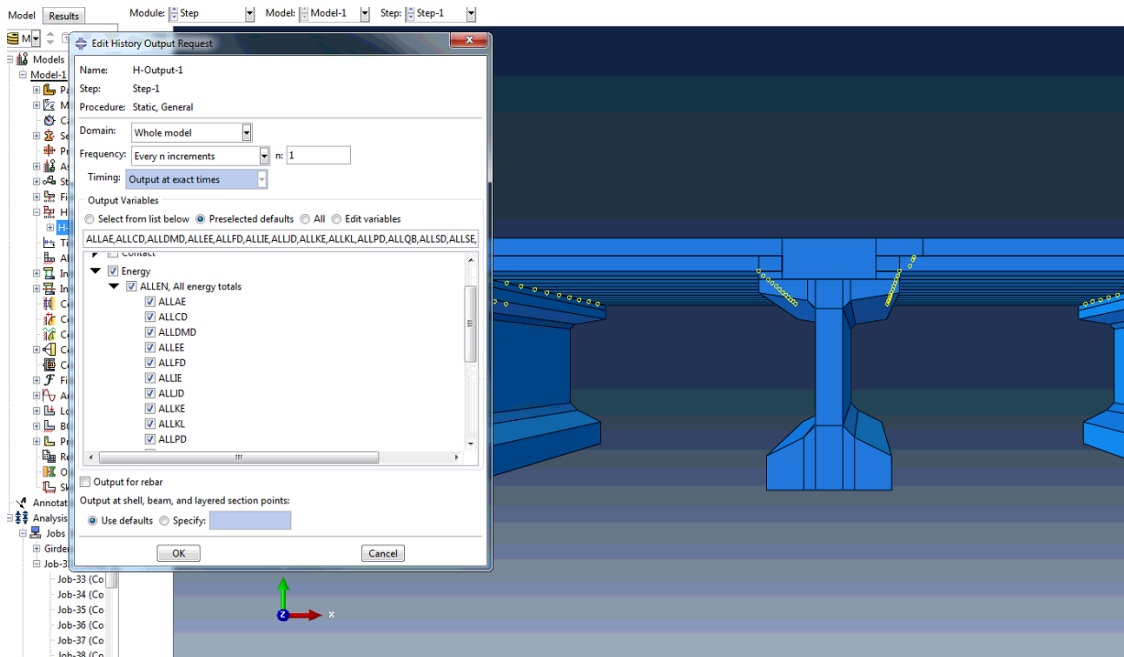


Figure 6- 37: History output request showing various components of energies of the model

After the successful execution of the history output command, various components of the energies were plotted against the time from the ABAQUS (2018) output. Figure 6-38 shows the internal energy ( $E_i$ ) vs time plot.

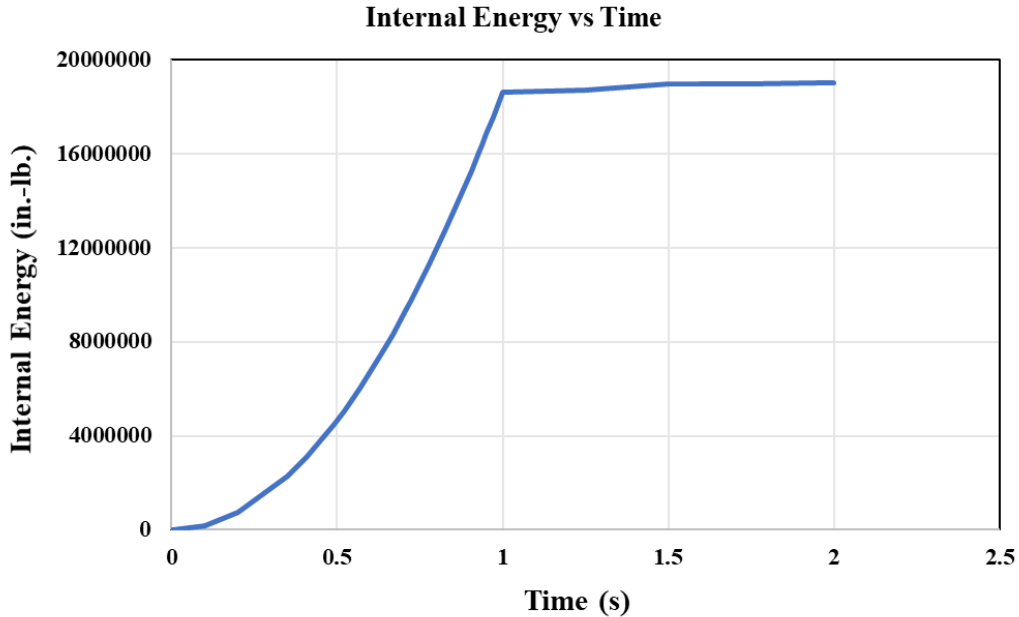


Figure 6- 38: Internal energy vs time

According to the data presented in Figure 6-38, it is clear that the internal energy of the model was very high. The internal energy value started from zero initially and reached its maximum ( $1.9 \times 10^7$  in.-lb.) at one second. After one second, the internal energy became almost constant for the rest of the simulation time. This phenomenon took place due to the high prestress in the strands of the girders and the panels. Prestress forces in the strands induced high internal energy into the model which reached its maximum at one second.  $E_V$ ,  $E_{FD}$ ,  $E_{KE}$ , and  $(E_{IHE} - E_{HF})$  were zero since the model did not have any viscous fluid, frictional co-efficient, dynamic property, or heat-transfer property. Figure 6-39 shows the work done by the externally applied forces ( $E_W$ ) vs time plot.

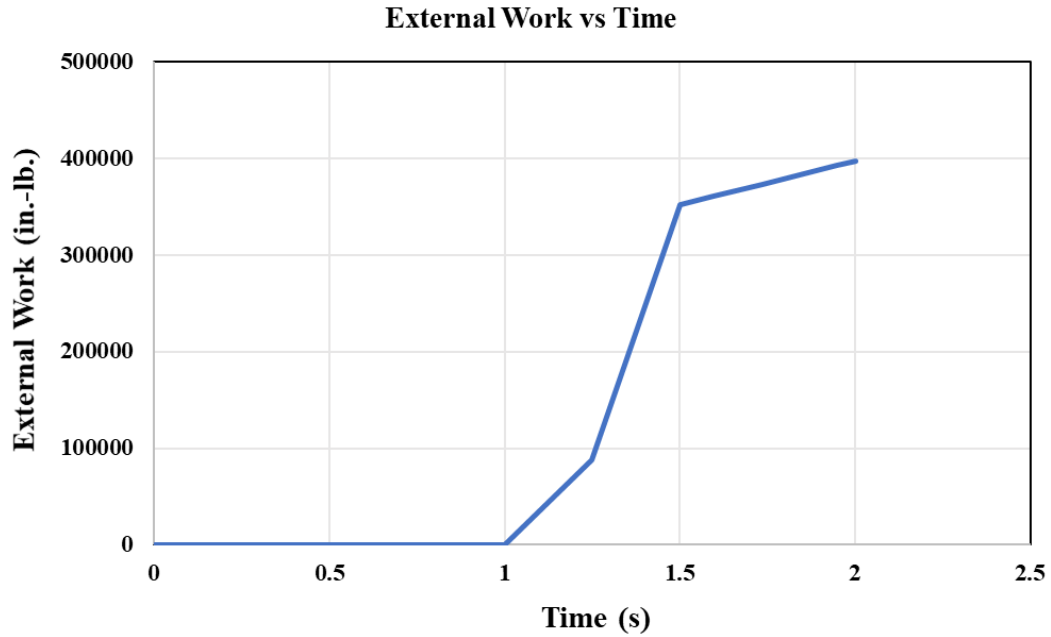


Figure 6- 39: Work done by the externally applied forces ( $E_w$ ) vs time

$E_{PW}$ ,  $E_{CW}$ , and  $E_{MW}$  were also zero since the model was not involved with any contact/constraint penalty or propelling added mass. Figures 6-40 shows the total energy of the whole model ( $E_{total}$ ) vs time plot.

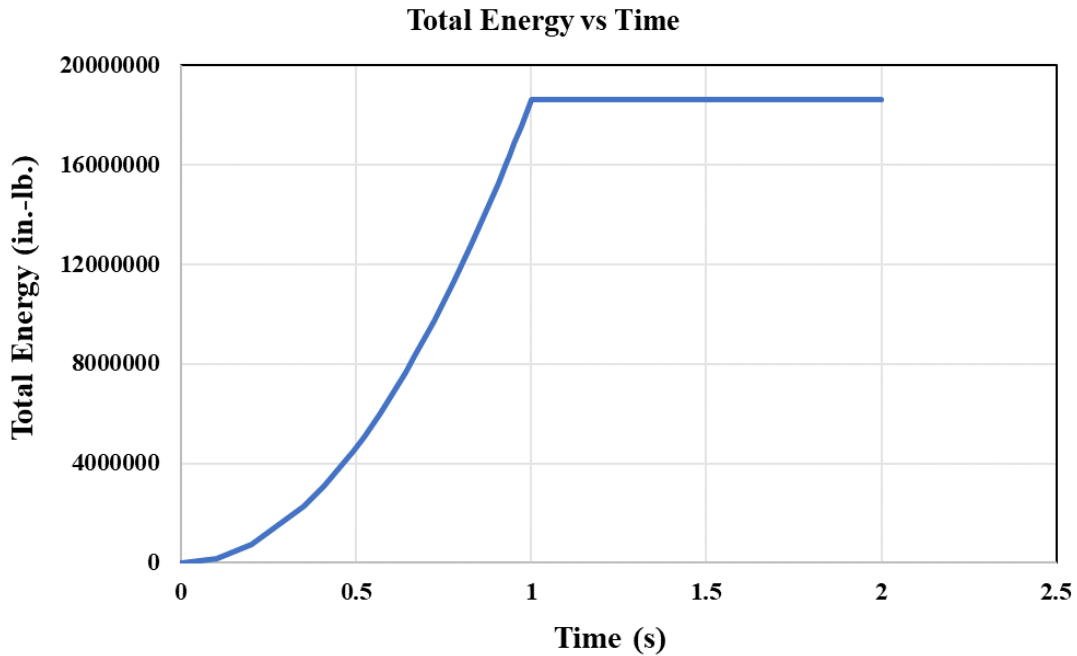


Figure 6- 40: Total energy of the model ( $E_{total}$ ) vs time



According to the energy balance theory, the residual energy ( $E_r - E_w - E_{total}$ ) should be zero or approximately close to zero. Figure 6-41 shows the residual energy plotted as a percentage of total energy vs time.

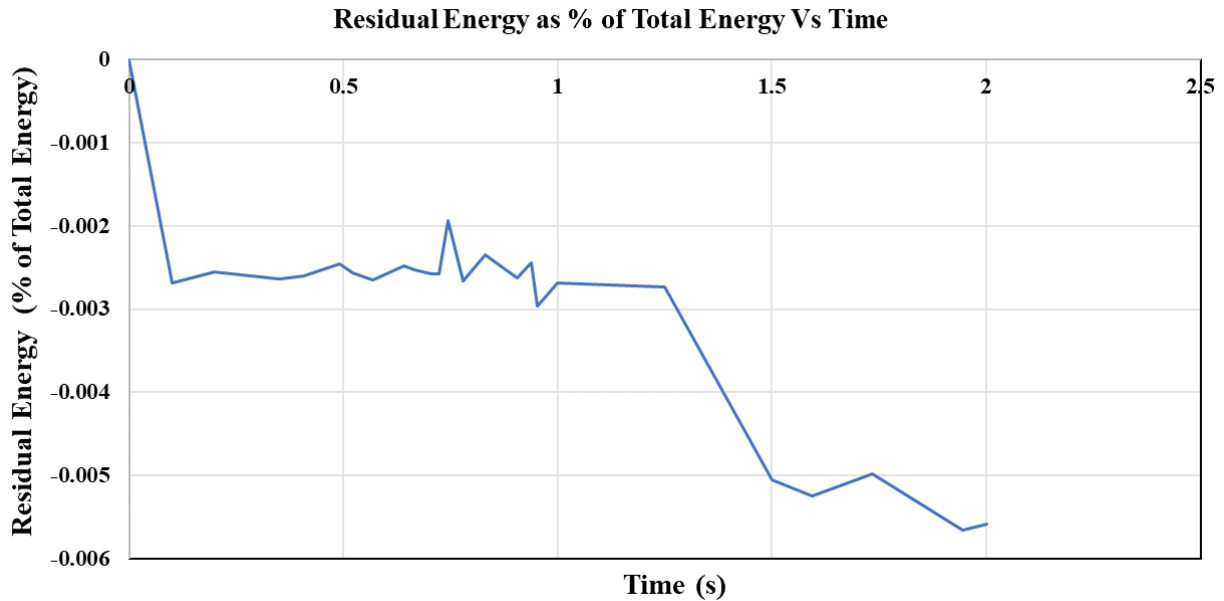


Figure 6- 41: Residual energy as a percentage of total energy vs time plot

The data presented in Figure 6-41 suggest that the residual energy was very low compared to the total energy ( $\ll 1\%$ ) which indicates an accurate Finite Element simulation with no local or global instabilities.

The rationale of this research was to figure out the total residual energy which is an indicator of the accuracy of the output of a Finite Element simulation. If the residual energy is low ( $<1\%$ ), the model does not have any local or global instabilities and vice versa.

### 6.5.2 Static Calibration

From the previous load test and NDE data, it is apparent that severe delamination was present in between the girder/deck and the panel/deck system of the SH-75 SB bridge. Partial-composite action between the prestressed girders and the deck was also detected. Hence, cohesive contact behavior was applied on both the girder/deck and deck/panel surfaces of the ABAQUS (2018)

model to simulate the surface delamination and partial-composite action between the elements. The shear stiffness parameters ( $K_{ss}$  and  $K_{tt}$ ) were varied between these surfaces while keeping the normal stiffness coefficient as a constant large number ( $10^9$  lb./in<sup>2</sup>).

At first, the girder/deck and the deck/girder surfaces were created in ABAQUS (2018) as master and slave, respectively. Figure 6-42 shows the girder/deck and the deck/girder surfaces with cohesive contact properties.

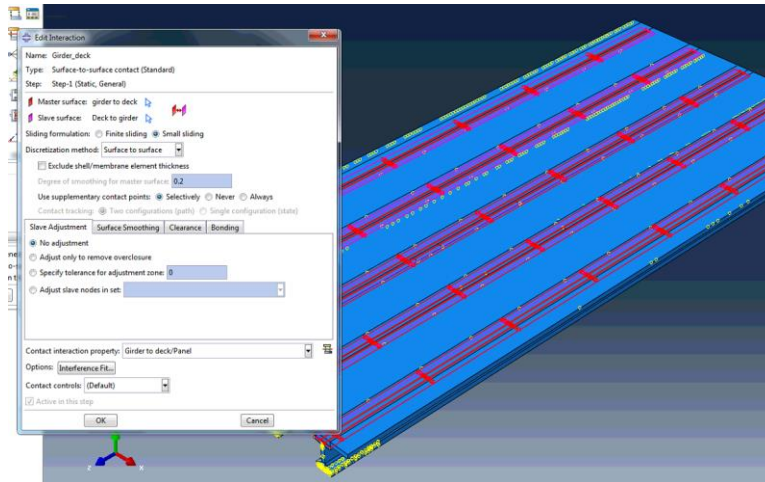


Figure 6- 42: Girder/deck and deck/girder surfaces for the cohesive contact interaction

Similarly, the panel/deck and the deck/panel surfaces were created as master and slave, respectively and the stiffness coefficients were assigned. Figure 6-43 shows the panel/deck and the deck/panel surfaces with cohesive contact properties.

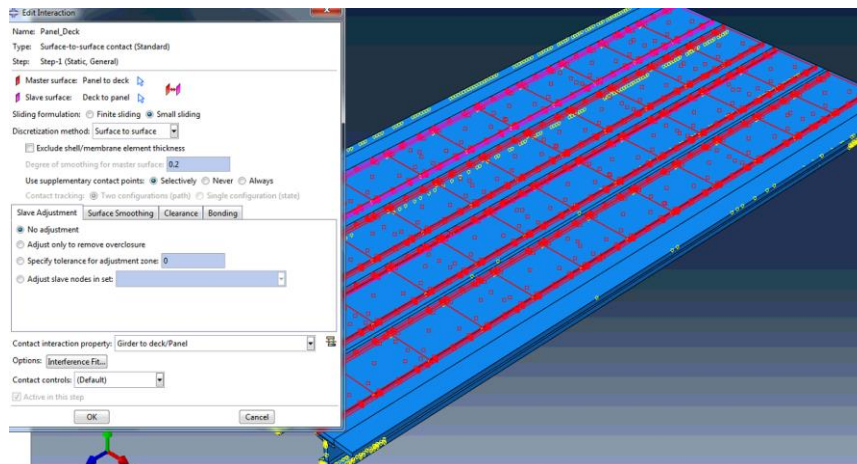


Figure 6- 43: Panel/deck and deck/panel surfaces for the cohesive contact interaction

To calibrate the model, the values of  $K_{ss}$  and  $K_{tt}$  were varied from  $10^8$  lb./in<sup>2</sup> to 1000 lb./in<sup>2</sup>. The values of the strain from the bottom of the girder B4B (B4 denotes the girder number while the last B denotes bottom strain) were extracted from the model and then compared with the experimental data since this girder had the maximum responses for the modeled path. Table 6-10 shows the  $K_{ss}$  and  $K_{tt}$  values and the corresponding strains from the model and the experiment.

Table 6- 10: Strain values at the bottom of the girder B4B from the experiment and the ABAQUS model

$K_{nn}$ (lb./in <sup>2</sup> )	$K_{ss}$ (lb./in <sup>2</sup> )	$K_{tt}$ (lb./in <sup>2</sup> )	Bottom Strain from Model (Micro strain)	Bottom Strain from Experiment (Micro strain)
1000000000	100000000	100000000	25.55	27
1000000000	1000000	1000000	25.6	
1000000000	15000	15000	26.9	
1000000000	5000	5000	30	
1000000000	1000	1000	49.6	

The data suggest that for  $K_{ss}=K_{tt}= 15000$  lb./in<sup>2</sup>, the strain values from the experiment and the model were very close. The strain and rotation data from other girders were also compared to verify the calibration. Figure 6-44 shows the comparison of the strain data between the experiment and the ABAQUS model while Figure 6-45 shows the comparison of the rotation values.



Figure 6- 44: Comparison of the strain data between the experiment and the ABAQUS model

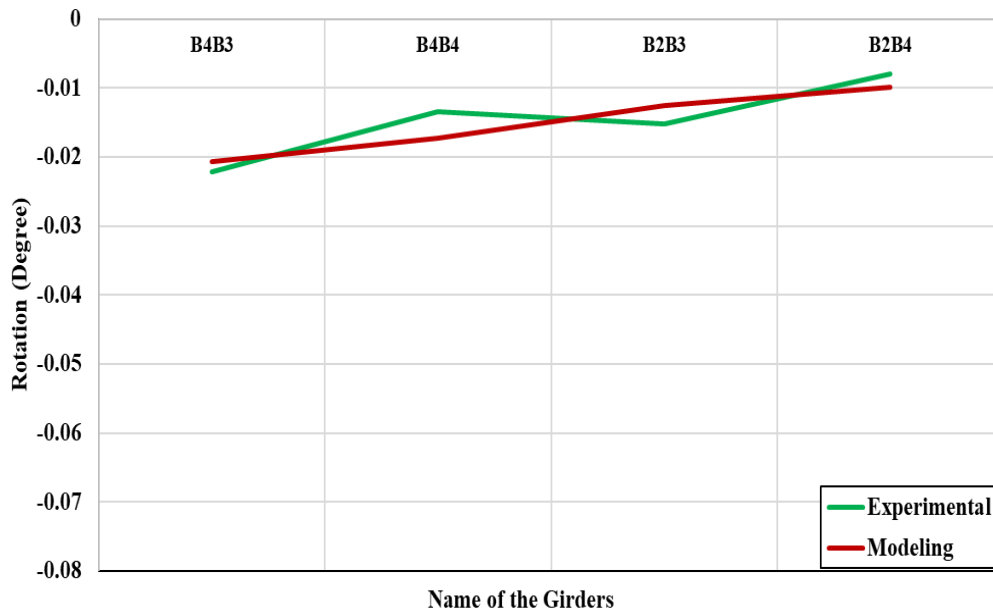


Figure 6- 45: Comparison of the rotation data between the experiment and the ABAQUS model

After comparing the strain and rotation data of the model with the experiment, it can be concluded that the data from the model fit quite well with the experiment with very little deviation. This slight deviation might take place due to the uncertainty in the material uniformity, non-uniform delamination, approximation in prestress loss, creep and relaxation, redundancy, or support fixity.

Since the model represented the experimental bridge with minimum deviation, it was used as a calibrated model for future retrofiting purposes.

### **6.5.3 Dynamic Calibration**

Throughout the dynamic vibration test of the Wilson Creek SB Bridge, the vibration meter was installed under a few girders during the load test runs. Since partial-composite action between the girders and the deck/panel system was confirmed based on the load test results, the modal analysis of a single girder with the partial-composite deck is more appropriate than that of the entire system when compared to the experimental dynamic frequencies. ABAQUS CAE (2018) estimates the frequency of the entire system while the experimental dynamic data were collected from a single girder with partial-composite action.

A single girder was modeled following the as-built drawing for the material and the geometric properties. All of the prestressing steels and the mild steels were modeled and assembled inside the girder. The material properties and section properties were defined accordingly and the girder and reinforcements were meshed. The prestressing force in the steel was defined considering the long term and short term loss using AASHTO LRFD Bridge Design Specification (2017).

To introduce partial-composite action between the girder and the deck, cohesive contact properties were assigned between the surfaces of the girder and the deck. The shear stiffness parameters ( $K_{ss}$  and  $K_{tt}$ ) were assigned as 15000 lb./in<sup>2</sup> between these surfaces while keeping the normal stiffness coefficient as a constant large number (10<sup>9</sup> lb./in<sup>2</sup>) based on the static calibration of the bridge. Figure 6-46 shows the cohesive contact between the girder and the deck surfaces system.

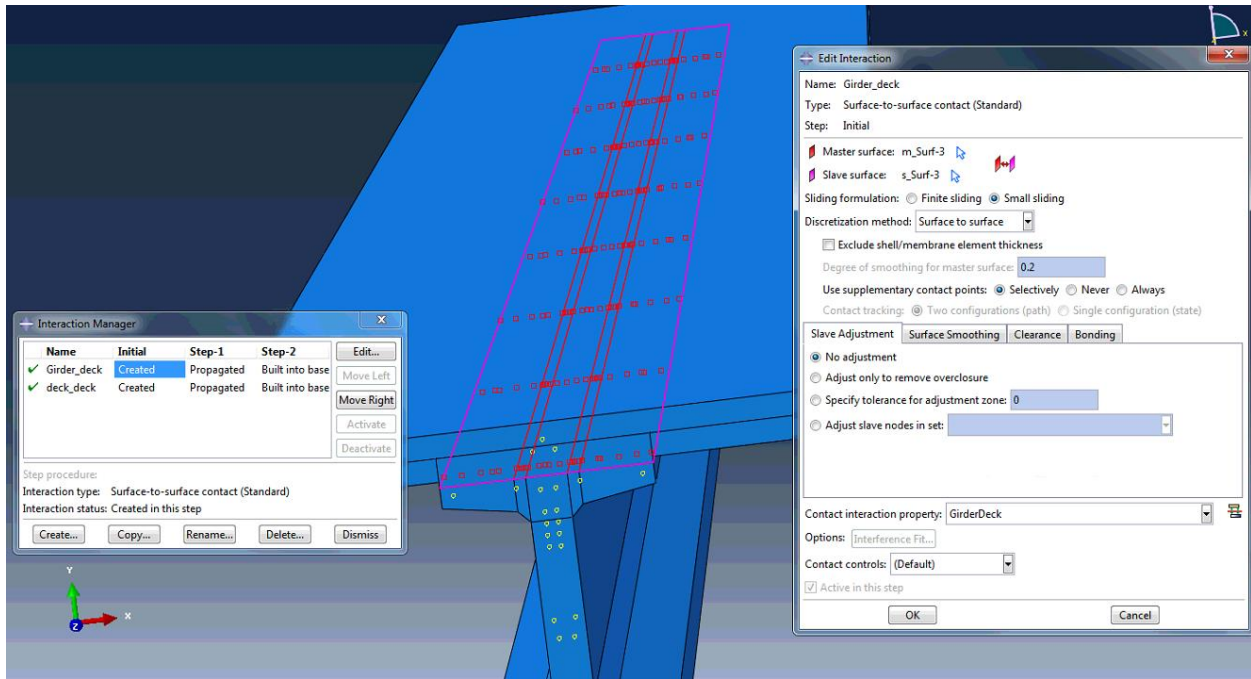


Figure 6- 46: Cohesive contact between the girder and the deck

A dynamic frequency step was created in the model with the first ten eigenvalues after the general static step. To calibrate the dynamic model, the stiffness of the deck was varied from 100% to 60% of its initial value since IE results previously confirmed severe delamination and reduction of stiffness of the deck/panel system. With 60% remaining stiffness of the deck, the modal frequencies yielded similar results to the experiments with little deviation. Table 6-11 shows the comparison between the experimental and modal frequencies of the different modes of vibration.

Table 6- 11: Comparison between the experimental and the modal frequencies

Modes of vibration	Experimental frequencies	Modal frequencies	Remarks
1	2.03	2.41	1st lateral bending
2	Not found	2.98	1st vertical bending
3	4.35	4.65	2nd lateral bending
4	6.275	7.17	1st torsion
5	8.9	9.27	2nd torsion
6	11	10.65	2nd vertical bending
7	12.25	11.72	3rd torsion
8	14	15.14	4th torsion
9	15.8	17.706	3rd vertical bending

Figure 6-47 shows the comparison between the experimental and modal frequencies as a graphical representation.

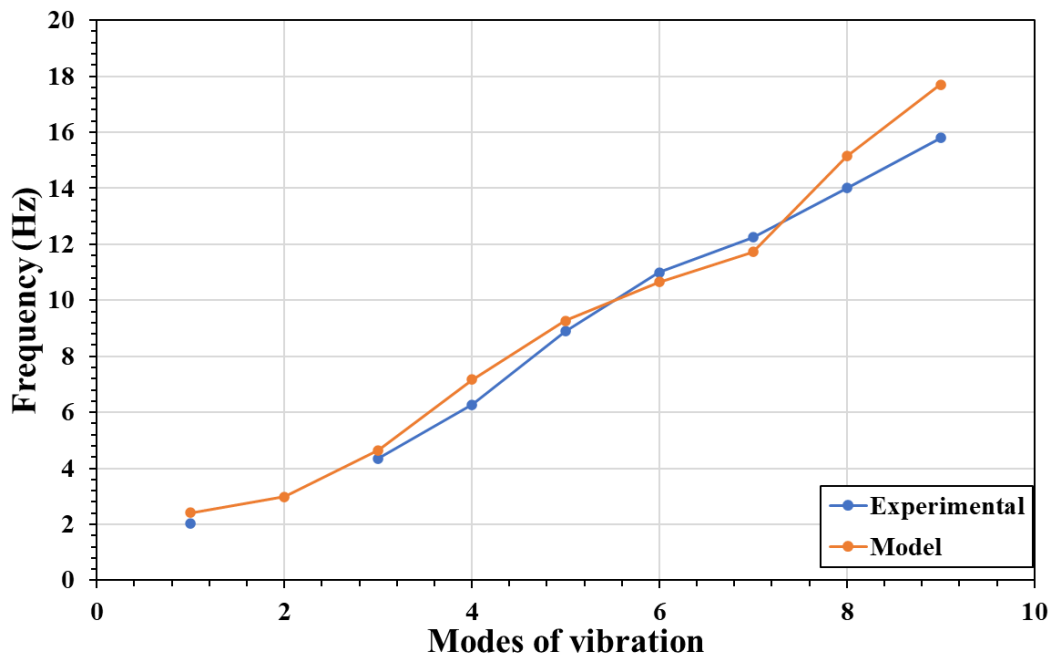


Figure 6- 47: Comparison between the experimental and modal frequencies

The second mode of vibration from the modal analysis (1st vertical bending) did not appear in the experimental data. Since the 1st and 2nd modes were very close, there is a possibility of superimposition between these two in the experimental data which explains the disappearance of the 2nd mode. Other than this phenomenon, the experimental and modal frequencies matched well with very little deviation.



## Chapter 7

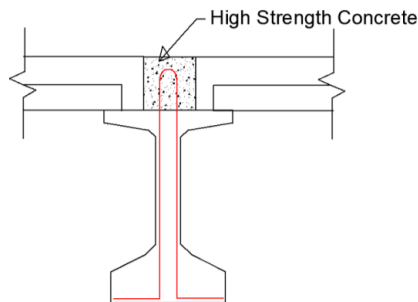
# BRIDGE REHABILITATION/RETROFITTING

### 7.1 Proposed Retrofitting Methods

The objectives of the retrofitting methods are to improve the composite action and stiffen the superstructure system. Some of the proposed methods are similar to the methods proposed or applied by previous researchers (provided in section 2.4 of this report) to improve/introduce composite action in steel girder bridges while the others are unique. Some of the methods have already been applied to the calibrated FE model while others are still in progress.

#### 7.1.1 Re-casting on the Girder Lines and Shear Pockets on the Panel Lines (High Strength Concrete)

1 ft. or 2 ft. strips are proposed to be removed from the top of the girder lines and re-casted with high strength (6 ksi) concrete. The modification should counteract the severe delamination on top of the girder lines confirmed by IE earlier. At the same time, shear pockets are proposed to be created on the top of the girder lines and re-casted with high strength (6 ksi) concrete. Previously, shear pockets were created on the top of the girder lines during the construction of full-depth precast deck panels according to the Prestressed Concrete Institute (PCI) by several DOTs during the construction phase. The spacings of the pockets were specified as 2 ft. and 4 ft. respectively by AASHTO (2017) and Wis. DOT. These measures will reduce the delamination between the interfaces of the deck and the panel. Figure 7-1 shows the proposed retrofitting option.



(a)



(b)

Figure 7- 1: Re-casting with high strength concrete: (a) Girder lines; and (b) Panel lines

Traffic closure will be required on top of the bridge for this retrofitting method. To reduce traffic disturbance, one girder and one panel line can be re-casted at once. However, this method is expensive and time-consuming.

To improve the composite action between the girders and the deck, 2 feet strips were removed from one exterior and two interior girder lines and re-casted with high strength (6 ksi) concrete. It was assumed that the re-casted concrete strips would create perfect bonds with the deck and the girders, thus tie contacts were created between the deck-girders surfaces. Figure 7-2 shows the removed girder lines while Figure 7-3 shows the contacts between the new concrete and the deck-girder interfaces.

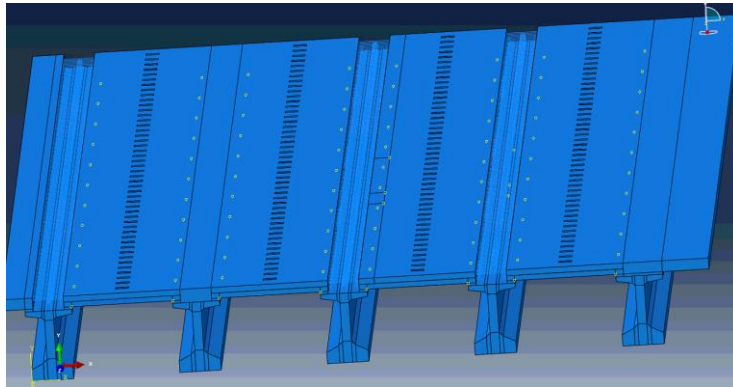


Figure 7- 2: Removed girder lines (left exterior and two interiors)

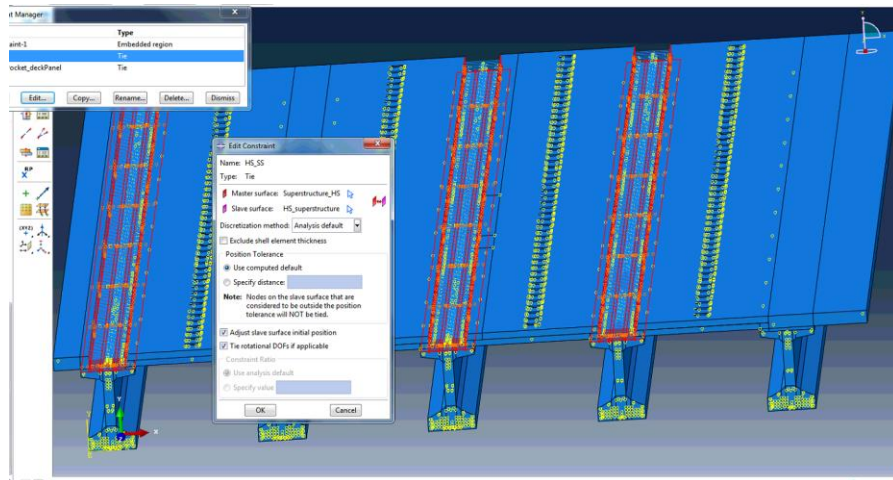


Figure 7- 3: Full composite tie contacts between the new (re-casted) and the old concrete

10''X6'' shear pockets were created alongside the panel lines and re-casted with high strength concrete (6 ksi) at equal spacings of 2 feet according to PCI (2011) guidelines. Tie contacts were used between the new concrete and the pockets-panel interfaces to create full bonding. Figure 7-4 shows the shear pockets on the girder lines while Figure 7-5 shows the contact between the new concrete and the pocket-panel interfaces.

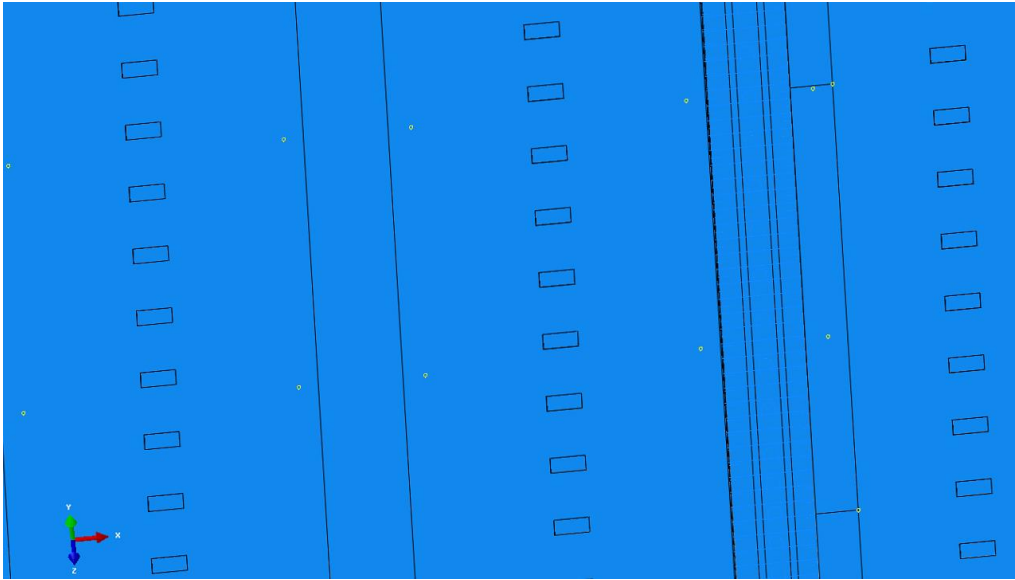


Figure 7- 4: Shear pockets on the girder lines

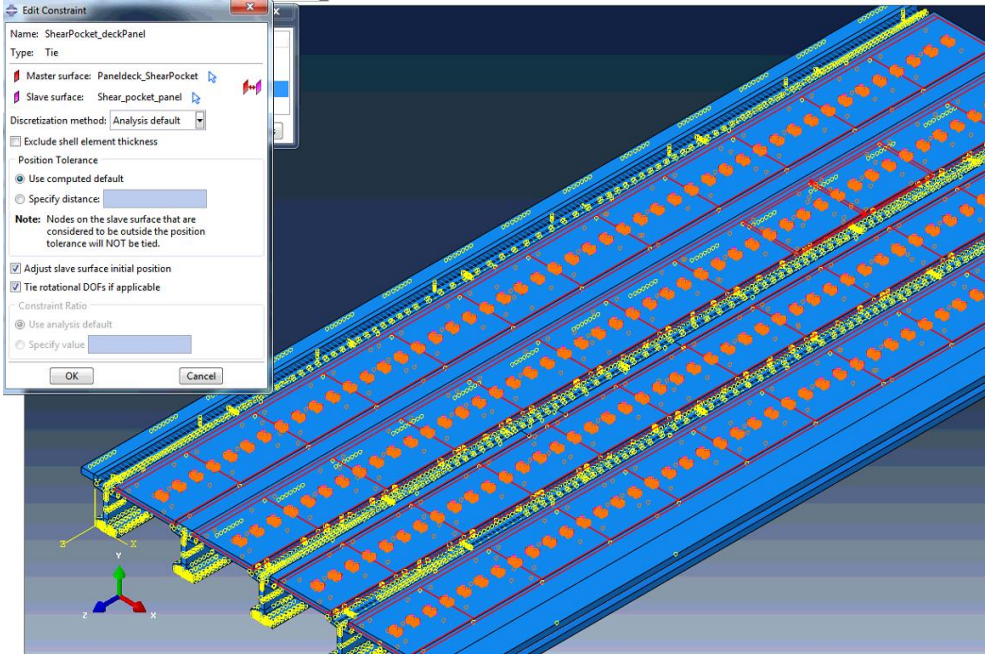


Figure 7- 5: Full composite tie contacts between the new (shear pockets) and the old concrete

The retrofitted model was run successfully in ABAQUS and the results were compared with the calibrated bridge model. Table 7-1 shows a comparison of the stress, strain, and the location of the neutral axis from the bottom for the third interior girder of the calibrated and the retrofitted model.

Table 7- 1: Comparison of the stress, strain and the location of the neutral axis for an interior girder of the calibrated and the retrofitted model

	<b>Stress (psi)</b>	<b>Remark</b>	<b>Strain</b>	<b>Remark</b>	<b>Deflection (in.)</b>	<b>Remark</b>	<b>Composite Action</b>
Calibrated Model	1804	11% decrease in stress for the retrofitted model.	0.000337	11% decrease in strain for the retrofitted model.	-1.63	18% decrease in deflection for the retrofitted model.	Composite action was increased from 32% to 83% for the retrofitted model
Retrofitted Model	1616		0.00030		-1.34		

### 7.1.2 Re-casting on the Girder Lines and Shear Pockets on the Panel Lines (Regular Strength Concrete)

This proposed method is similar to the previous one except for regular strength (4 ksi) concrete will be used instead of high strength concrete for re-casting. Since the cast-in-place deck is 4 ksi in strength, the regular strength re-casting concrete is supposed to make a better bond with the deck compared to the high strength concrete.

A similar procedure to the previous retrofitting method was followed for the retrofitting except using normal strength concrete (4 ksi) instead of the high strength concrete. The retrofitted model was run successfully in ABAQUS and the results were compared with the calibrated bridge model. Table 7-2 shows a comparison of the stress, strain, and the location of the neutral axis from the bottom for the third interior girder of the calibrated and the retrofitted models.

Table 7- 2: Comparison of the stress, strain and the location of the neutral axis for an interior girder of the calibrated and the retrofitted model

	Stress (psi)	Remark	Strain	Remark	Deflection (in.)	Remark	Composite Action
Calibrated Model	1804	9% decrease in stress for the retrofitted model.	0.000337	11% decrease in strain for the retrofitted model.	-1.63	10% decrease in deflection for the retrofitted model.	Composite action was increased from 32% to 70% for the retrofitted model
Retrofitted Model	1648		0.00030		-1.47		

### 7.1.3 Re-casting on the Girder Lines and Panel Lines (High Strength Concrete)

1 ft. or 2 ft. strips are proposed to be removed from the top of the girder lines and re-casted with high strength (6 ksi) concrete. This should offset the severe delamination on top of the girder lines. At the same time, 1 ft. or 2 ft. strips are proposed to be removed on the top of the girder lines and re-casted with high strength (6 ksi) concrete. This measure will reduce the delamination between the deck and the panel. Figure 7-6 shows the proposed retrofitting option.

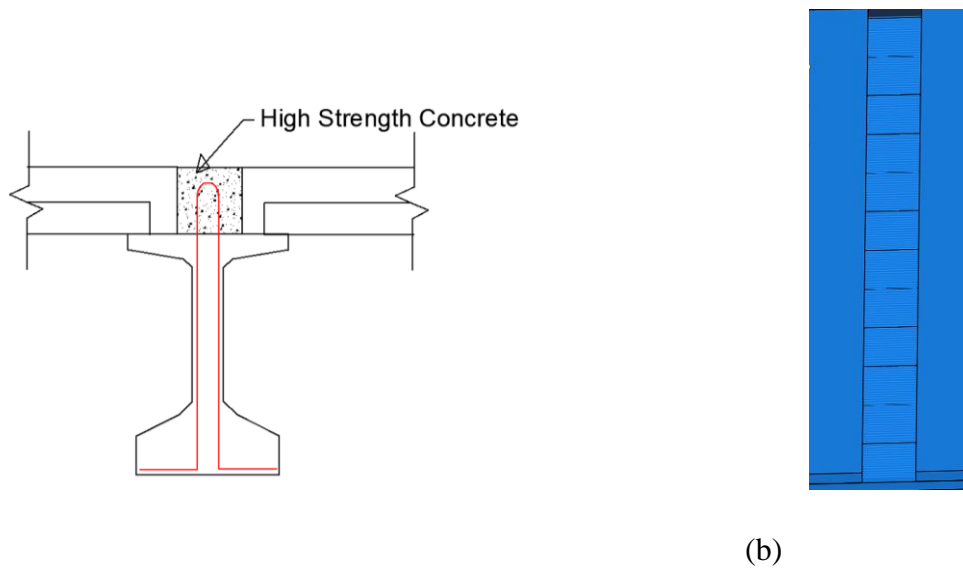


Figure 7- 6: Re-casting with high strength concrete: (a) Girder lines; and (b) Panel lines

Traffic closure will be required on top of the bridge for this retrofitting method. To reduce traffic disturbance, one girder and one panel line can be re-casted at once. This method is expensive and time-consuming.

To improve the composite action between the girders and the deck, 2 feet strips were removed from one exterior and two interior girder lines and re-casted with high strength (6 ksi) concrete. It was assumed that the re-casted concrete strips would create perfect bonds with the deck and the girders, thus tie contacts were created between their surfaces.

Next, 12” strips were created alongside the panel lines and re-casted with high strength concrete (6 ksi). Tie contacts were used then between the new concrete and the pockets-panel interfaces to create full bonding. Figure 7-7 shows the retrofitting method while Table 7-3 provides a comparison of the stress, strain, and the location of the neutral axis from the bottom for the third interior girder of the calibrated and the retrofitted model.

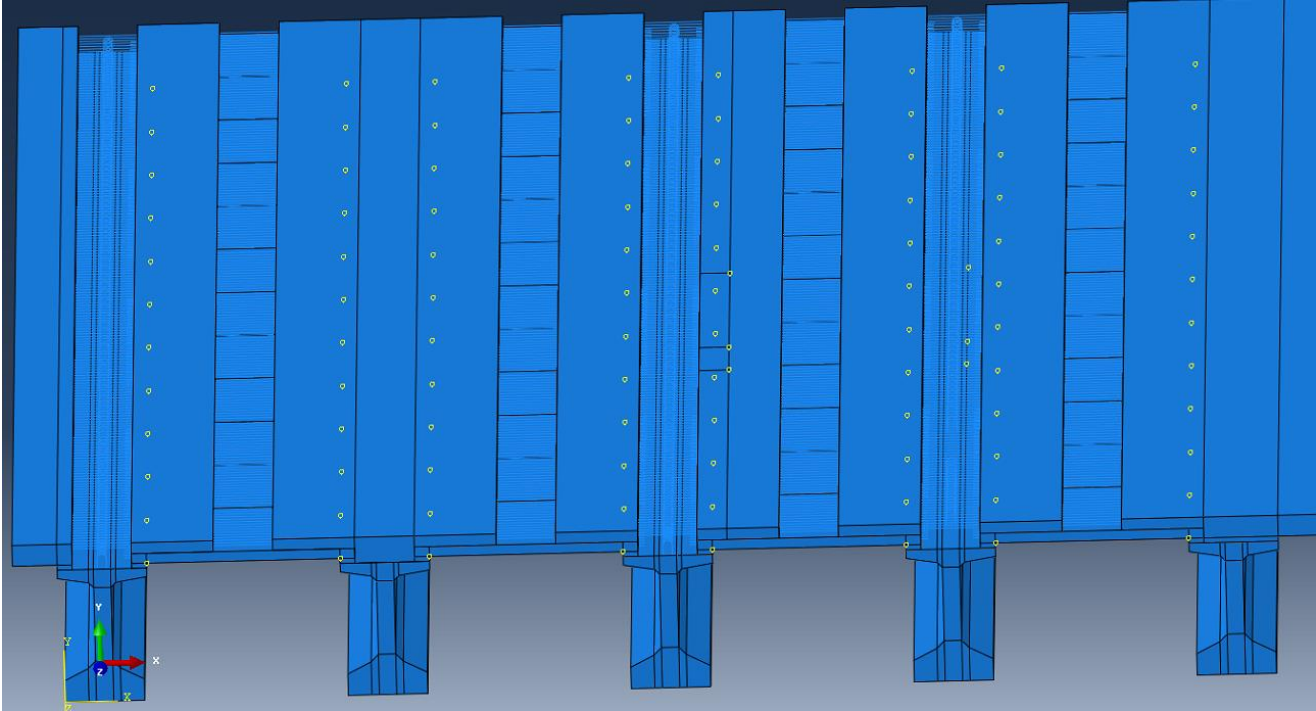


Figure 7- 7: Recasting on the girder lines and the panel lines (high strength concrete)

Table 7- 3: Comparison of the stress, strain and the location of the neutral axis for an interior girder of the calibrated and the retrofitted model

	<b>Stress (psi)</b>	<b>Remark</b>	<b>Strain</b>	<b>Remark</b>	<b>Deflection (in.)</b>	<b>Remark</b>	<b>Composite Action</b>
Calibrated Model	1804	5.32% decrease in stress for the retrofitted model.	0.000337	5% decrease in strain for the retrofitted model.	-1.63	18% decrease in deflection for the retrofitted model.	Composite action was increased from 32% to 91% for the retrofitted model
Retrofitted Model	1708		0.00032		-1.34		

#### 7.1.4 Re-casting on the Girder Lines and Panel Lines (Regular Strength Concrete)

This proposed method is similar to the previous one except for regular strength (4 ksi) concrete will be used instead of high strength concrete for re-casting. Since the cast-in-place deck is 4 ksi in strength, the regular strength re-casting concrete is supposed to make a better bond with the deck compared to the high strength concrete.

A similar procedure to the previous retrofitting method was followed for the retrofitting although using regular strength concrete (4 ksi) instead of the high strength concrete. The retrofitted model was run successfully in ABAQUS and the results were compared with the calibrated bridge model. Table 7-4 shows a comparison of the stress, strain, and the location of the neutral axis from the bottom for the third interior girder of the calibrated and the retrofitted models.

Table 7- 4: Comparison of the stress, strain and the location of the neutral axis for an interior girder of the calibrated and the retrofitted model

	<b>Stress (psi)</b>	<b>Remark</b>	<b>Strain</b>	<b>Remark</b>	<b>Deflection (in.)</b>	<b>Remark</b>	<b>Composite Action</b>
Calibrated Model	1804	4.6% decrease in stress for the retrofitted model.	0.000337	5% decrease in strain for the retrofitted model.	-1.63	10.5% decrease in deflection for the retrofitted model.	Composite action was increased from 32% to 79% for the retrofitted model
Retrofitted Model	1721		0.00032		-1.46		

### 7.1.5 Re-casting on the Girder Lines with Additional Shear Connectors

1 ft. or 2 ft. strips are proposed to be removed from the top of the girder lines and re-casted with high strength/regular strength concrete. While doing so, some additional shear connectors will be inserted inside the girder to ensure a full bond between the surfaces. At the same time, 1 ft. or 2 ft. strips are proposed to be removed on the top of the girder lines and re-casted with high strength/regular strength concrete. Figure 7-8 shows the proposed retrofitting method.

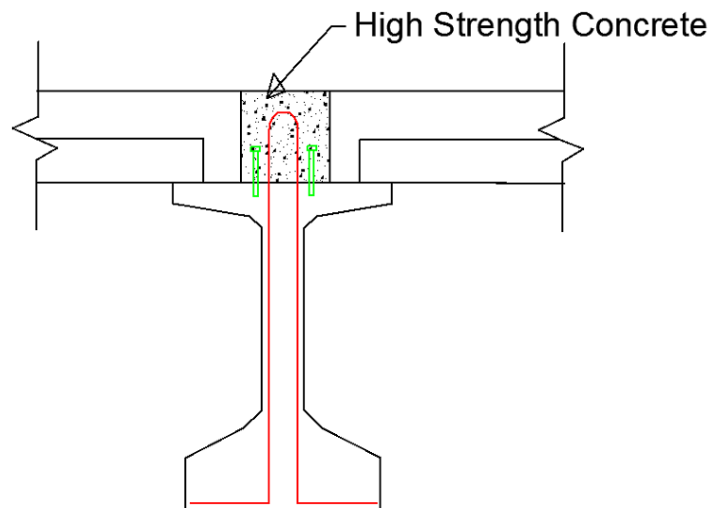


Figure 7- 8: Re-casting on the girder lines with additional shear connectors



Traffic closure will be required on top of the bridge for this retrofitting method. This is expensive and time-consuming.

Shear rebars were placed on the top of the precast prestressed girders to provide composite action between the girders and the cast in place deck. TxDOT has specific provisions for shear connectors of Tx girders for prestressed I girder bridges. Figure 7-9 shows the typical spacings of the shear rebars of Tx girders suggested by TxDOT. The shear rebars are designated as R rebars in the figure.

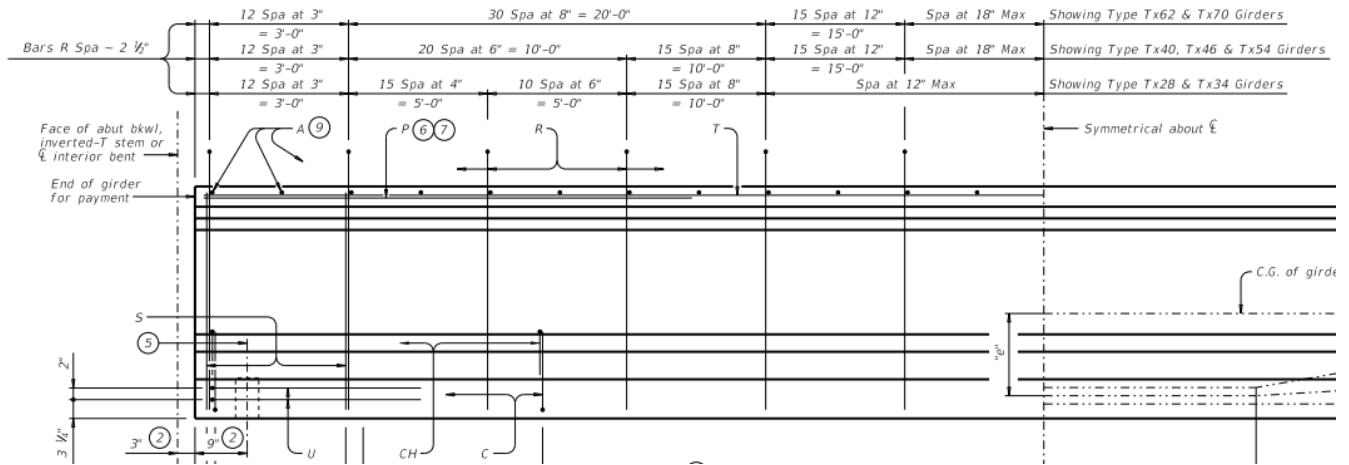


Figure 7- 9: Typical spacing of shear rebars of TxDOT girders

All the proposed retrofitting methods with the exception of the current one were conducted in accordance with the spacing requirement of the R rebars. For the Tx54 girder, the spacings of the R rebars for a half scale girder are as follows: 3'' for the first 3 feet, 6'' for the next 10 feet, 8'' for the next 10 feet, 12'' for the next 15 feet with a maximum of 18'' spacing for the rest half of the girder. Figure 7-10 shows the typical spacings of the R rebars in the calibrated ABAQUS model of the SB bridge.

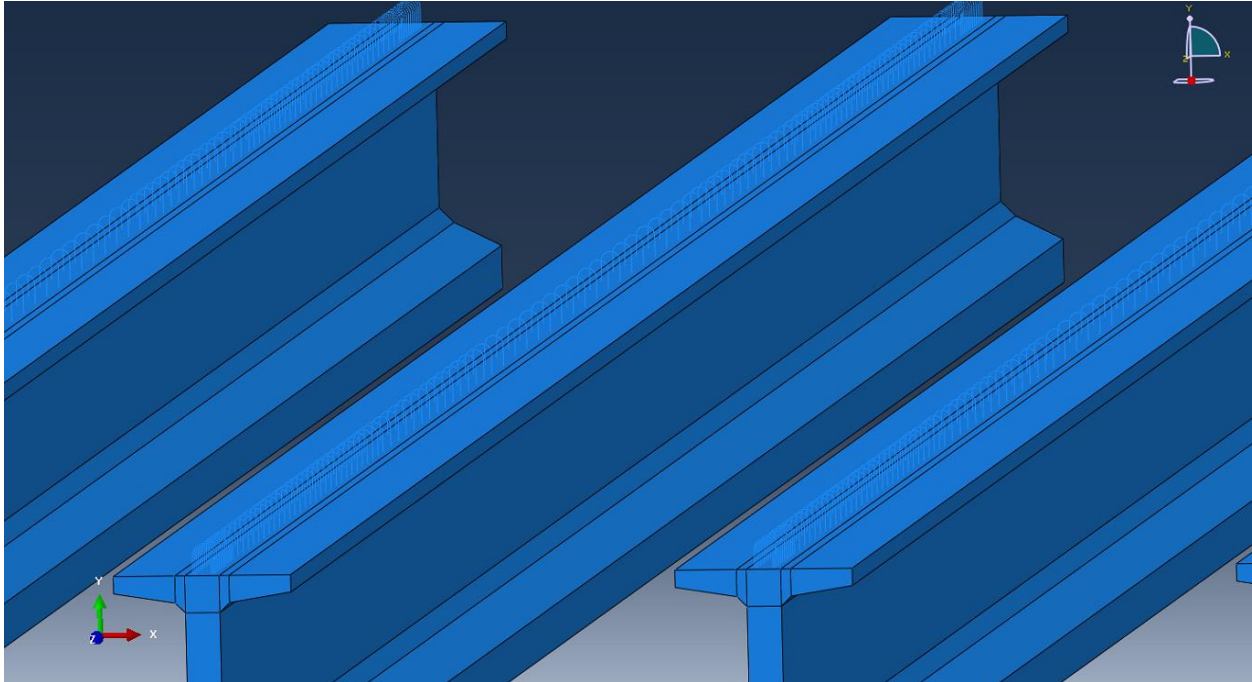


Figure 7- 10: Typical spacing of rebars of the calibrated ABAQUS model

To improve the composite action between the girders and the deck, 2 feet strips were removed from one exterior and two interior girder lines and re-casted with regular strength (4 ksi) concrete. It was assumed that the re-casted concrete strips would create perfect bonds with the deck and the girders, thus tie contacts were created between strip-girder surfaces similar to the previous retrofitting procedure. Furthermore, additional shear rebars (R rebars) were inserted inside the girders before recasting to improve the composite action between the girders and the deck. Table 7-5 shows the spacings of the shear rebars which were modeled in ABAQUS.

Table 7- 5: Different spacings of the shear rebars modeled in ABAQUS

<b>Designation</b>	<b>Spacings</b>
R1 (Control)	3'' for the first 3 feet, 6'' for the next 10 feet, 8'' for the next 10 feet, 12'' for the next 15 feet, 18'' for the rest half
R2	3'' for the first 3 feet, 6'' for the next 20 feet, 12'' for the next 15 feet, 18'' for the rest half
R3	3'' for the first 3 feet, 6'' for the next 35 feet, 12'' for the for the rest half

12” strips were created alongside the panel lines and re-casted with regular strength concrete (4 ksi). Tie contacts were additionally used between the new concrete and the pockets-panel interfaces to create full bonding. Figures 7-11 and 7-12 show the retrofitting methods R2 and R3 respectively while Table 7-6 provides a comparison of the stress, strain, and the location of the neutral axis from the bottom for the third interior girder of the calibrated and the retrofitted models.

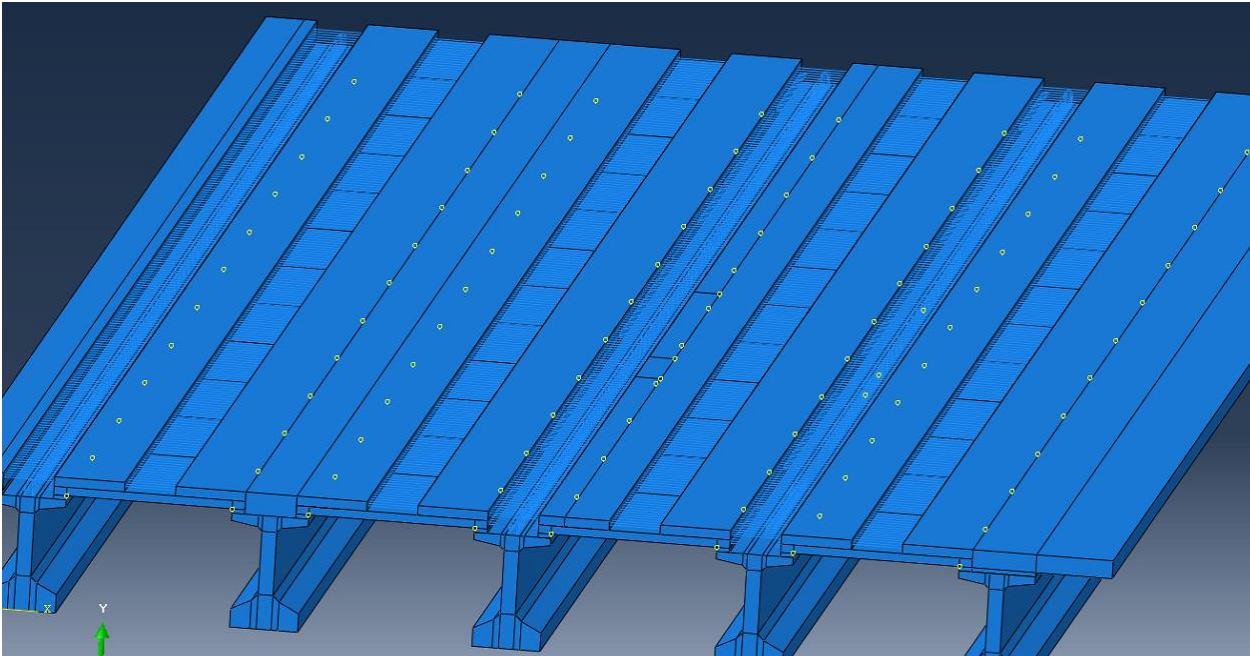


Figure 7- 11: Recasting on the girder lines and the pane line with additional R rebars (R2)

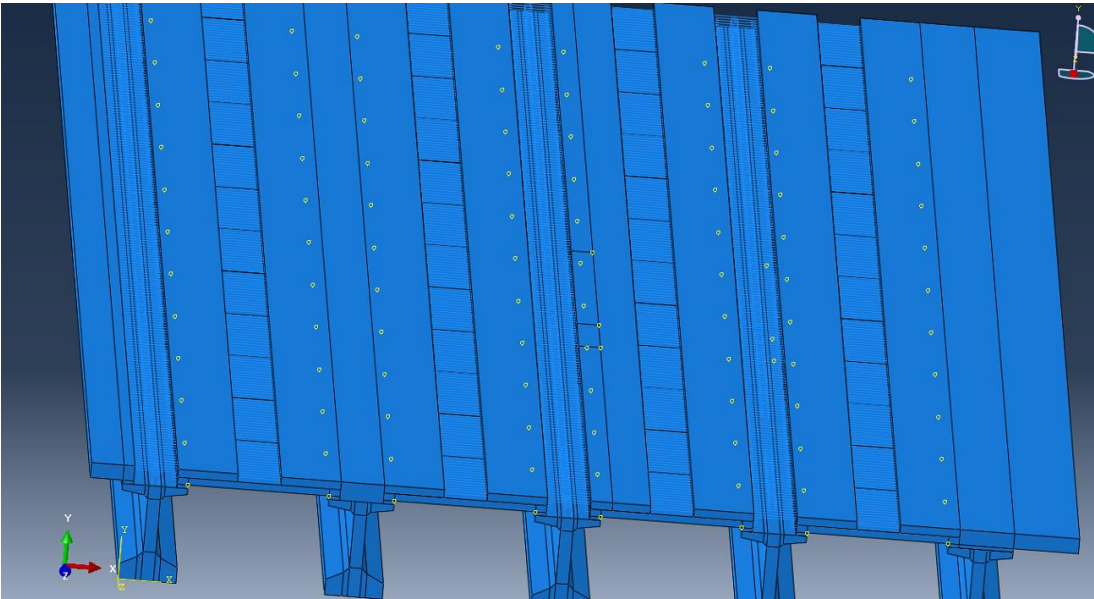


Figure 7- 12: Recasting on the girder lines and the pane line with additional R rebars (R3)

Table 7- 6: Comparison of the stress, strain and the location of the neutral axis for an interior girder of the calibrated and the retrofitted model

	<b>Stress (psi)</b>	<b>Remark</b>	<b>Strain</b>	<b>Remark</b>	<b>Deflection (in.)</b>	<b>Remark</b>	<b>Composite Action</b>
Calibrated Model	1804	4.93% decrease in stress for the retrofitted model.	0.000337	5% decrease in strain for the retrofitted model.	-1.63	15% decrease in deflection for the retrofitted model.	Composite action was increased from 32% to 83% for the retrofitted model
Retrofitted Model (R2)	1715		0.00032		-1.39		
Retrofitted Model (R3)	1711	5.15% decrease in stress for the retrofitted model.	0.00032	5% decrease in strain for the retrofitted model.	-1.36	16% decrease in deflection for the retrofitted model.	Composite action was increased from 32% to 86% for the retrofitted model

Figure 7-13 shows the dynamic retrofitting model while Table 7-7 provides a comparison of the natural frequency for an interior girder of the calibrated and the retrofitted models.

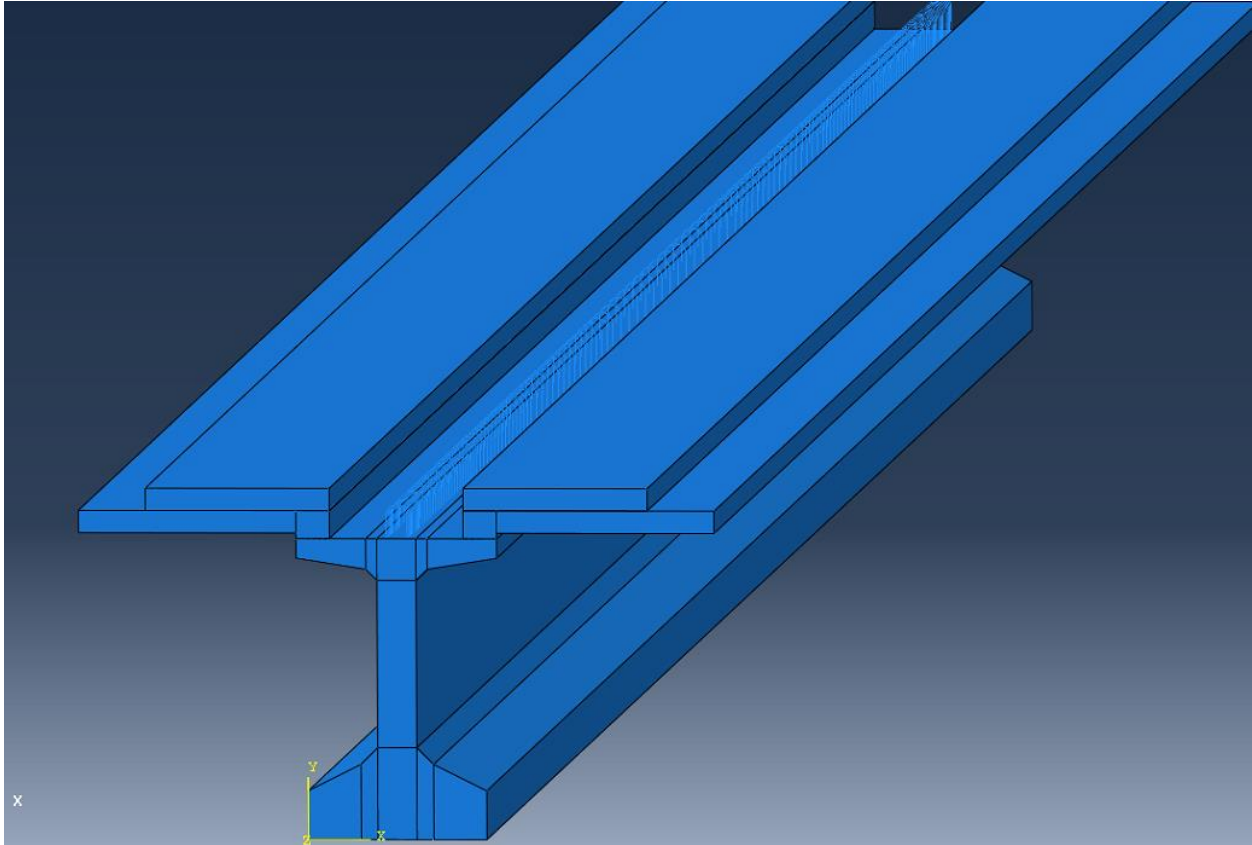


Figure 7- 13: Recasting on the Girder lines and Panel lines

Table 7- 7: Comparison of the natural frequency for an interior girder of the calibrated and the retrofitted model

Model	Natural Frequency (Hz.)	Remark
Calibrated Model	2.41	Natural Frequency increased by 20%
Recasting with Regular Concrete	2.89	
Recasting with High Strength Concrete	3.0	Natural Frequency increased by 24.5%
Recasting with Regular Concrete+ Shear Keys	3.4	Natural Frequency increased by 41%
Recasting with High Strength Concrete+ Shear Keys	3.5	Natural Frequency increased by 45%
Recasting with Regular Concrete+ R2	3.05	Natural Frequency increased by 26.5%
Recasting with Regular Concrete+ R3	3.11	Natural Frequency increased by 29%

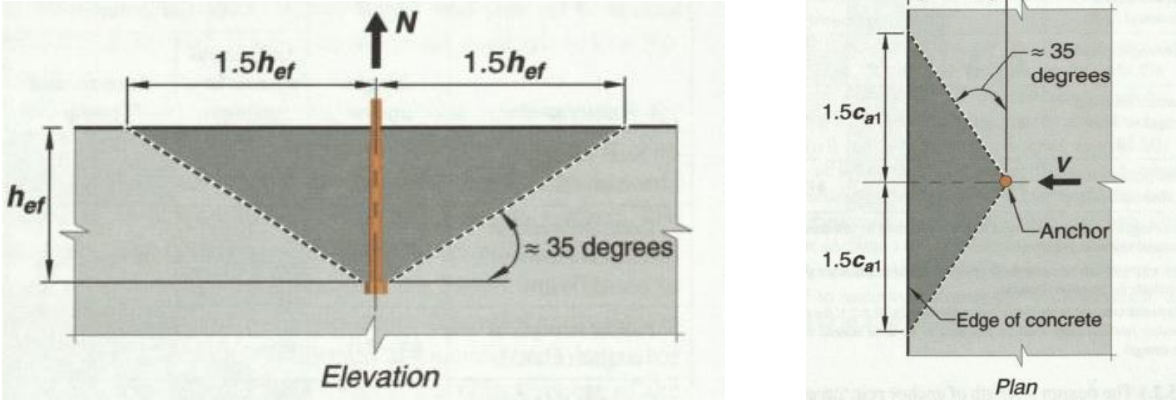
**7.1.6 Undercut Anchors**

The provisions of undercut anchors are provided in ACI 318-19, chapter 17. The undercut of the anchors ensures safe mechanical interlock with concrete (Figure 7-14).



Figure 7- 14: An undercut anchor embedded inside concrete

The break-out cone for tension and shear of the undercut anchors are shown below in Figure 7-15 based on ACI-318-19.



(a)

(b)

Figure 7- 15: Break-out cone for undercut anchor: (a) Tension; and (b) Shear

Undercut anchors were modeled using this break out cone assuming the perfect bond in the critical areas. The embedment of the anchor in the girder would be approximately 5", which makes a

critical length of 7.5". So, each anchor was assumed to create a perfect bond to a critical area of 15"X 15" on the girder-deck interfaces.

Undercut anchors were modeled according to the tension cone showed in ACI-318. The embedment of the anchors to the girders was assumed as 5.5 in. while the embedment of the deck was 5 in. Therefore, the total length of the modeled anchors was around 10 in. Due to the 5 in. embedment inside the deck, a 15''X15'' rectangular area was assigned as tie contact on the deck-girder interface to ensure perfect bond between the tension cone area, while the rest of the contact between the girder and deck was assigned as cohesive. Figure 7-16 shows the tie areas (red blocks) between the deck-girder interfaces indicating the tension cones of the undercut anchors.

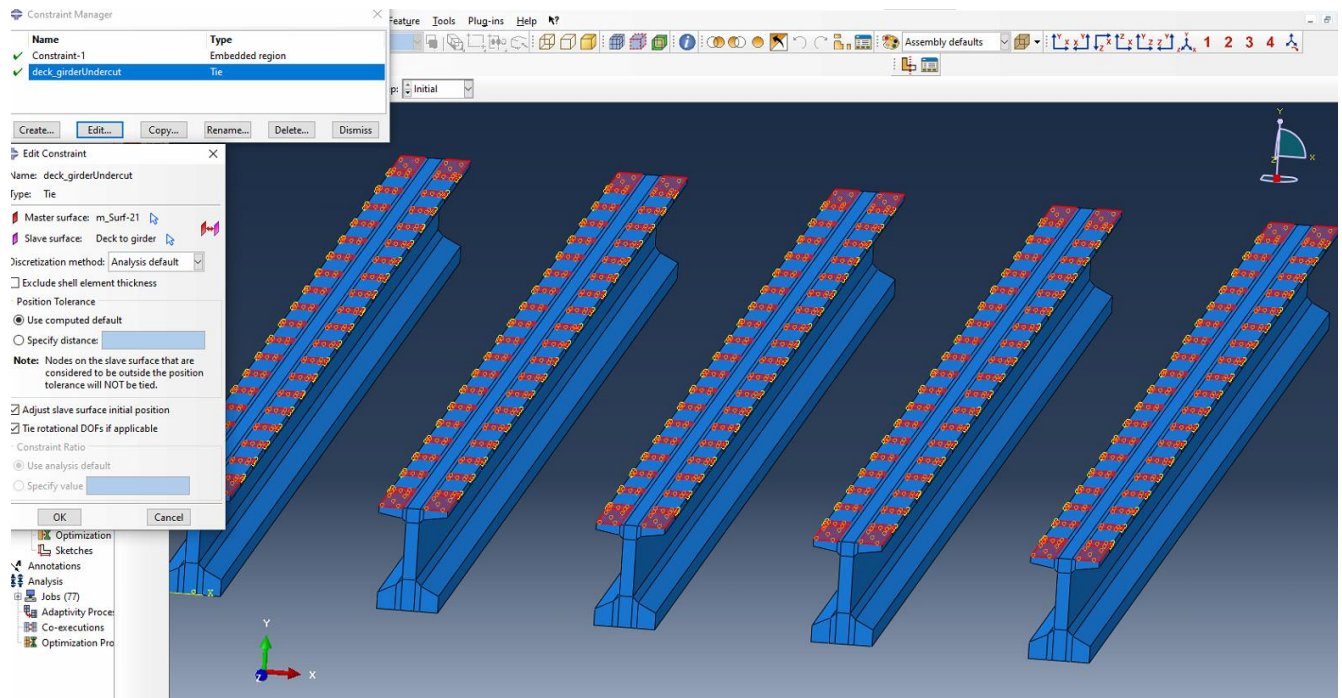


Figure 7- 16: Tension cones of the undercut anchors (red block)

Since each anchor creates a perfectly bonded rectangular area of 15''X15'' on the deck-girder interfaces, the maximum spacing of the anchors in this case can be 15''. Therefore, for a 100 feet girder, the maximum number of anchors per side should be 80 which creates fully perfect bond between the girder-deck interface. Table 7-8 shows the number of anchors per side of the girders that were modeled in ABAQUS.

Table 7- 8: Different number of anchors per side modeled in ABAQUS

Number of Undercut Anchors per side per girder	Anchors needed/Anchors Provided
80	100%
60	75%
40	50%
20	25%

Figures 7-17, 7-18, 7-19 and 7-20 show the modeled undercut anchors (80, 60, 40 and 20 respectively) in ABAQUS. Table 7-9 provides a comparison of the stress, strain, and the location of the neutral axis from the bottom for the third interior girder of the calibrated and the retrofitted models.

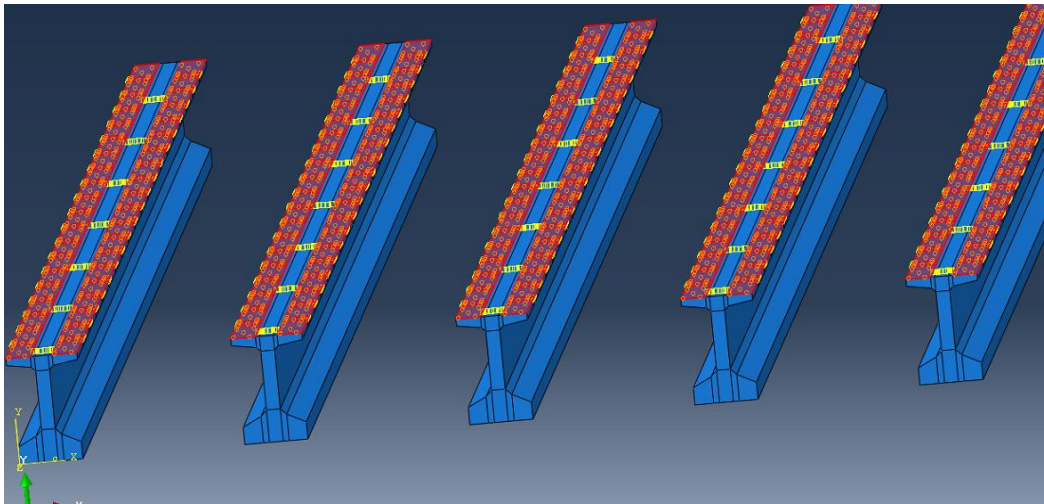


Figure 7- 17: 80 anchors on each side of the girders



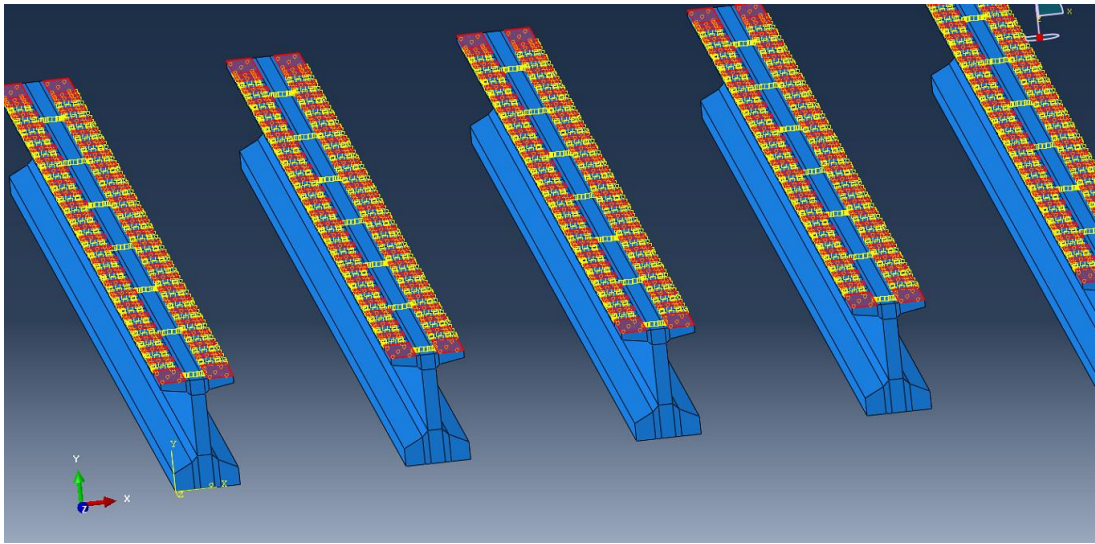


Figure 7- 18: 60 anchors on each side of the girders

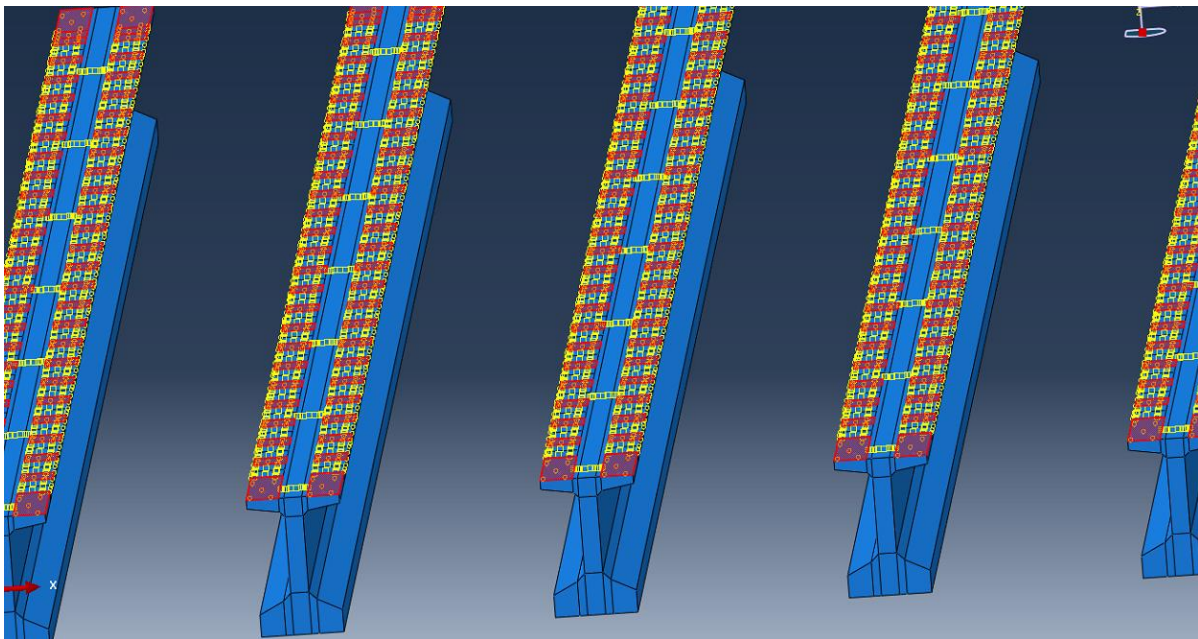


Figure 7- 19: 40 anchors on each side of the girders

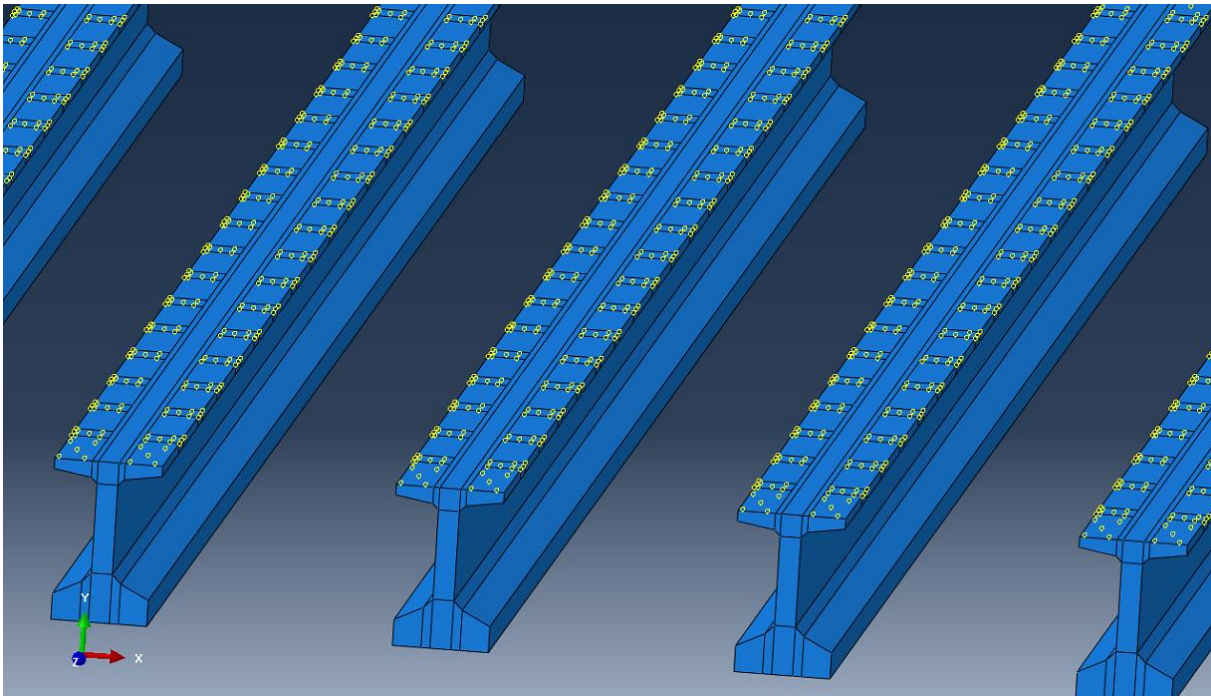


Figure 7- 20: 20 anchors on each side of the girders

Table 7- 9: Comparison of the stress, strain and the location of the neutral axis for an interior girder of the calibrated and the retrofitted model

	<b>Stress (psi)</b>	<b>Remark</b>	<b>Strain</b>	<b>Remark</b>	<b>Deflection (in.)</b>	<b>Remark</b>	<b>Composite Action</b>
Calibrated Model	1804	4.87% decrease in stress for the retrofitted model.	0.000337	8% decrease in strain for the retrofitted model.	-1.63	16% decrease in deflection for the retrofitted model.	Composite action was increased from 32% to 82% for the retrofitted model
80 Anchors/side	1716		0.00031		-1.37		
60 Anchors/side	1721	4.6% decrease in stress for the	0.00031	8% decrease in strain for the	-1.38	15% decrease in deflection for the	Composite action was increased from 32% to 78% for

		retrofitted model.		retrofitted model.		retrofitted model.	the retrofitted model
40 Anchors/side	1724	4.43% decrease in stress for the retrofitted model.	0.00032	5% decrease in strain for the retrofitted model.	-1.41	13.5% decrease in deflection for the retrofitted model.	Composite action was increased from 32% to 74.5% for the retrofitted model
20 Anchors/side	1728	4.21% decrease in stress for the retrofitted model.	0.00032	5% decrease in strain for the retrofitted model.	-1.44	12% decrease in deflection for the retrofitted model.	Composite action was increased from 32% to 69% for the retrofitted model

For the dynamic model, undercut anchors were modeled similarly according to the tension cone showed in ACI-318. Figure 7-21 shows the tie areas (red blocks) between the deck-girder interfaces indicating the tension cones of the undercut anchors.

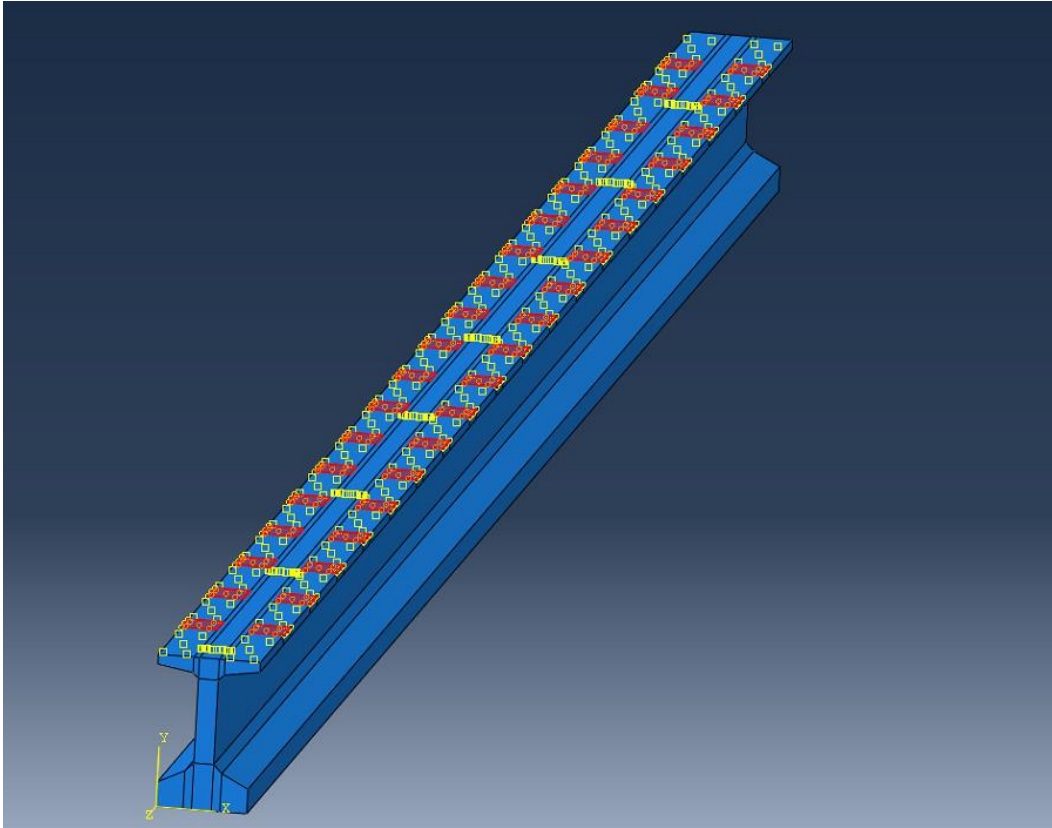


Figure 7- 21: Tension cones of the undercut anchors (red block)

Figures 7-22, 7-23, 7-24 and 7-25 show the modeled undercut anchors (80, 60, 40 and 20 respectively) in ABAQUS. Table 7-10 provides a comparison of the natural frequency for an interior girder of the calibrated and the retrofitted models.

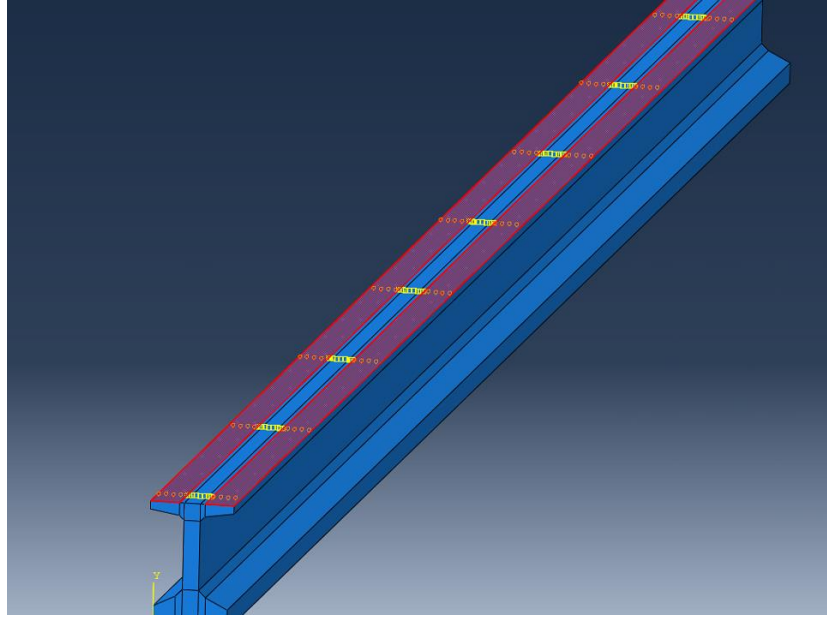


Figure 7- 22: 80 anchors on each side of the girders

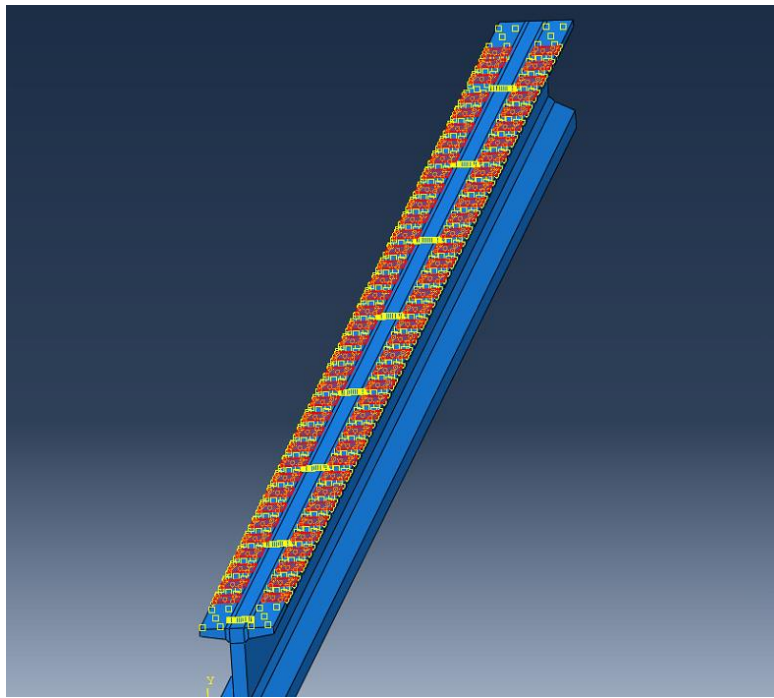


Figure 7- 23: 60 anchors on each side of the girders

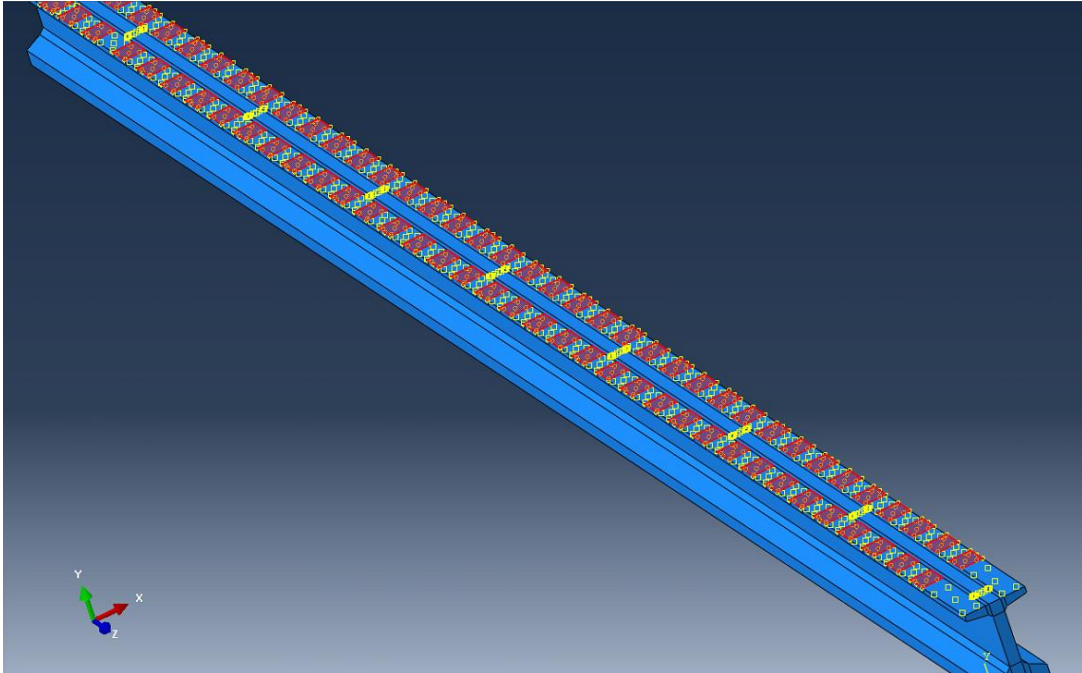


Figure 7- 24: 40 anchors on each side of the girders

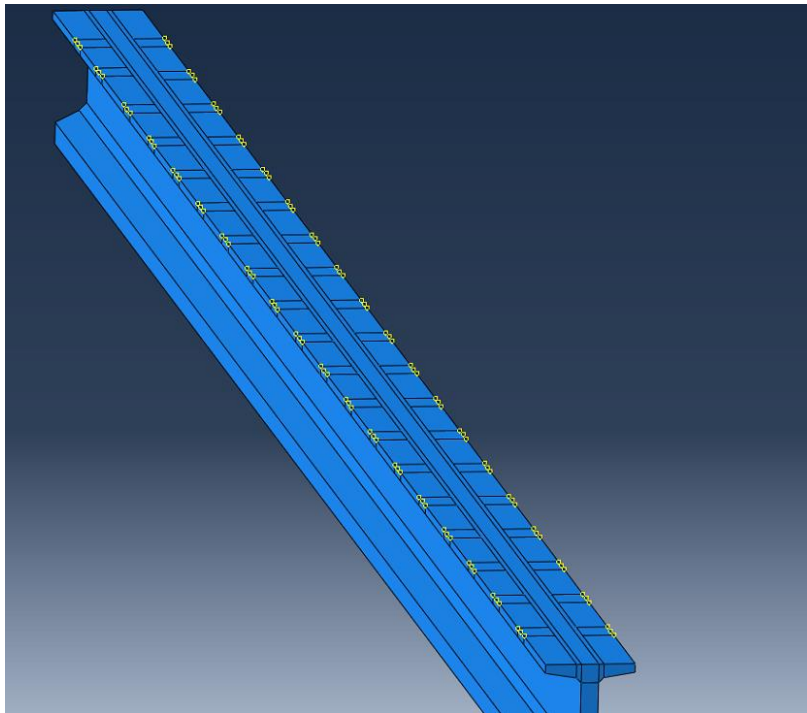


Figure 7- 25: 20 anchors on each side of the girders

Table 7- 10: Comparison of the natural frequency for an interior girder of the calibrated and the retrofitted model

Model	Natural Frequency (Hz.)	Remark
Calibrated Model	2.41	Natural Frequency increased by 5%
20 Anchors each side	2.53	
40 Anchors each side	2.70	Natural Frequency increased by 12%
60 Anchors each side	2.85	Natural Frequency increased by 18.25%
80 Anchors each side	3.13	Natural Frequency increased by 30%
20 Anchors+ Shear Keys	3.19	Natural Frequency increased by 32.5%
40 Anchors+ Shear Keys	3.40	Natural Frequency increased by 41%
60 Anchors+ Shear Keys	3.61	Natural Frequency increased by 50%
80 Anchors+ Shear Keys	3.85	Natural Frequency increased by 60%

### 7.1.7 Shear Keys

Concrete shear keys are proposed to be constructed between the bearing pads to reduce the lateral movement of the superstructure (Figure 7-26). This method is a stiffening method that will have a major impact on the dynamic properties of the bridge. This is very cheap and can be used alongside other retrofitting methods without any traffic interference.

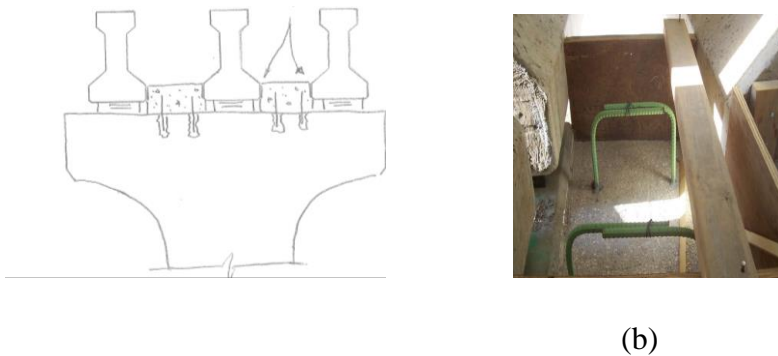


Figure 7- 26: Stiffening bearing pads using shear keys: (a) Typical cross-section; and (b) Constructed shear keys

Shear keys were modeled to provide lateral fixity to the girders and hence to the entire system. The length of the keys was assumed as 15 in. along the girder based on the TxDOT standard bent cap drawing. In the model, a 15 in. lateral fixity was modeled in each corner sides of the girder to simulate the shear keys. Figure 7-27 shows the lateral fixities of the girders which represent the lateral shear keys.

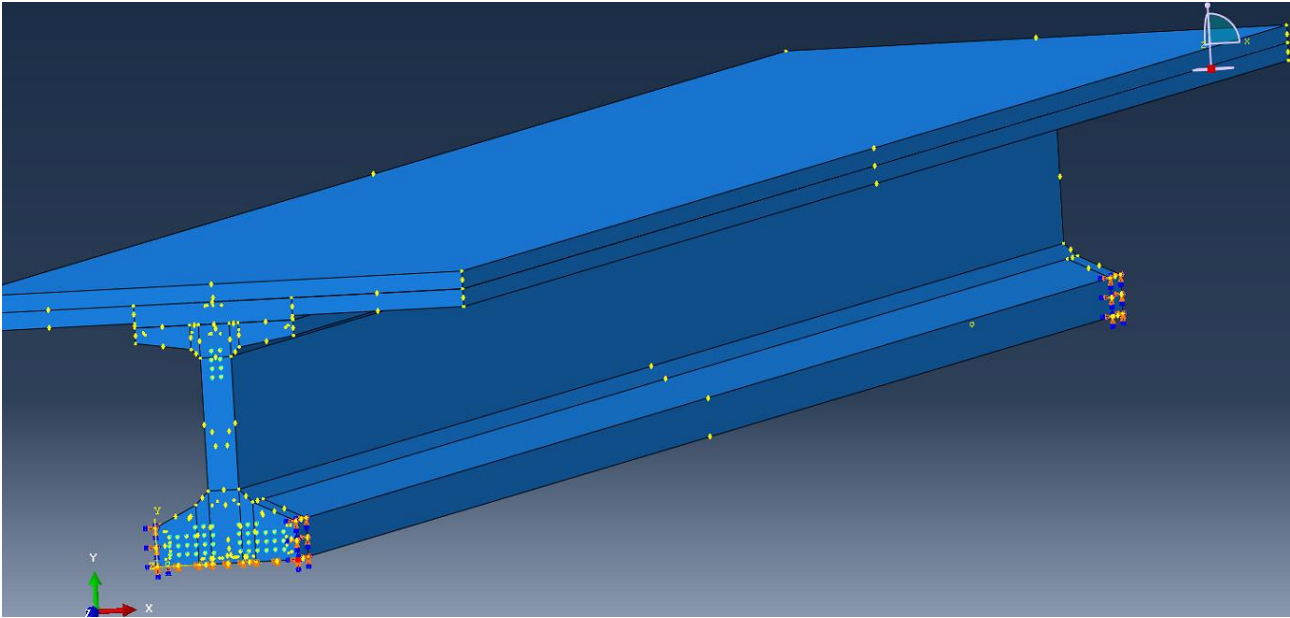


Figure 7- 27: Shear Keys near the support of a girder

To prevent lateral vibration, shear keys can be used as low cost and high-performance lateral resisting system which requires no traffic interruption. Table 7-11 provides a comparison of the natural frequency for an interior girder of the calibrated and the retrofitted models.

Table 7- 11: Comparison of the natural frequency for an interior girder of the calibrated and the retrofitted model

Model	Natural Frequency (Hz.)	Remark
Calibrated Model	2.41	Natural Frequency increased by 29%
Retrofitted Model with Shear Keys	3.11	



### 7.1.8 Dense Concrete Overlay

Bridge Deck concrete overlay or dense concrete overlay has high stiffness due to its increased compressive strength of 4600 psi. Since the concrete of the deck is delaminated, 2''/4'' delaminated concrete from the top of the deck is proposed to be removed and then re-casted using hydraulic cement concrete. This method is supposed to diminish delamination to some extent and increase the natural frequency of the system by providing additional stiffness. The vibration of the bridge is supposed to be reduced due to higher stiffness and reduced delamination of the dense concrete overlay.

As a part of the process, 2''/4'' deck concrete was removed and re-casted with high strength hydraulic cement concrete overlay. This retrofitting method increased the natural frequency of the deck by improving the stiffness and removing deck-delamination on the top layer. Figure 7-28 shows the 2'' dense concrete overlay modeled in ABAQUS.

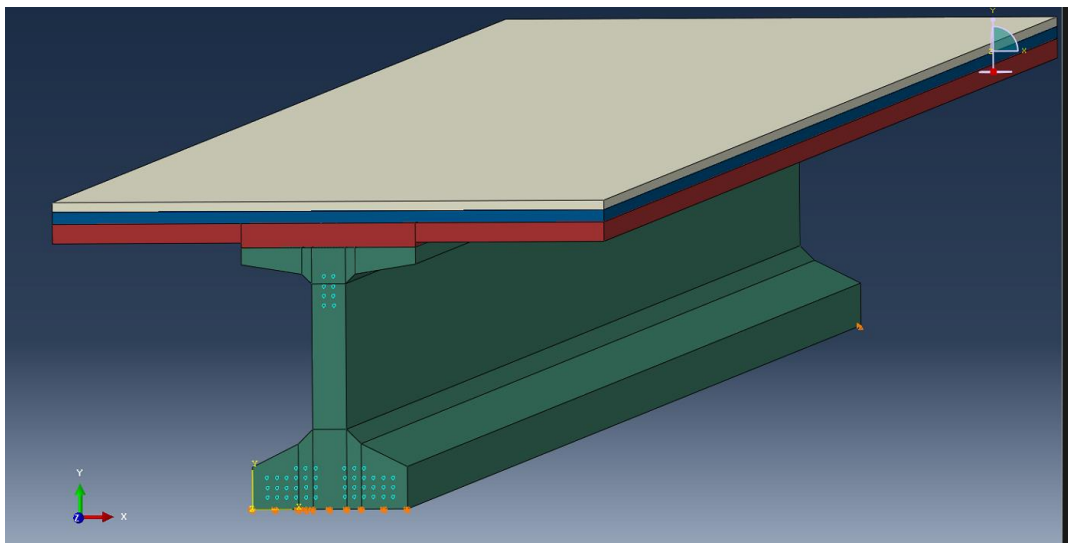


Figure 7- 28: Dense concrete overlay (2'' on the top) modeled in ABAQUS

Shear keys were also modeled with dense concrete overlay to observe the combined effect. Figure 7-29 shows dense concrete overlay on the top of the deck and shear keys on the corners of the girder.

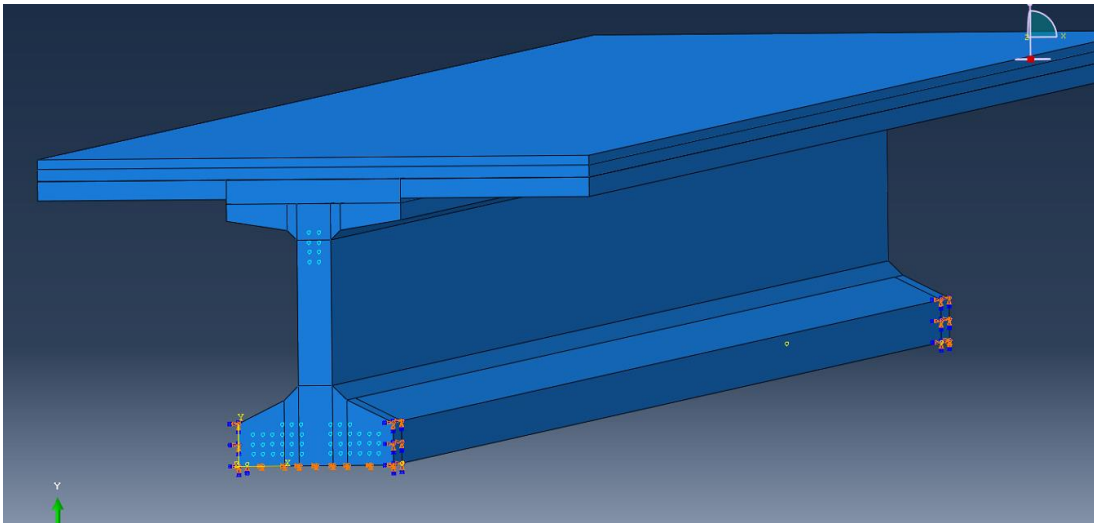


Figure 7- 29: Dense concrete overlay with shear keys (2'' on the top) modeled in ABAQUS

Table 7-12 provides a comparison of the natural frequency for an interior girder of the calibrated and the retrofitted models.

Table 7- 12: Comparison of the natural frequency for an interior girder of the calibrated and the retrofitted model

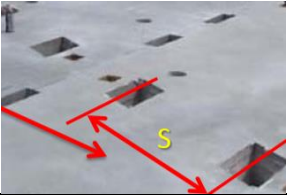
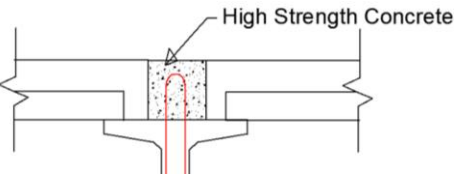
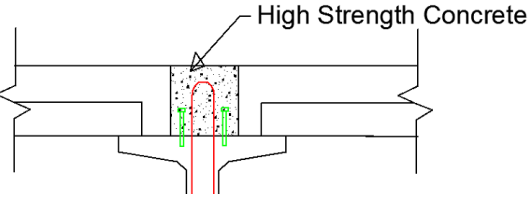

<b>Model</b>	<b>Natural Frequency (Hz.)</b>	<b>Remark</b>
Calibrated Model	2.41	Natural Frequency increased by 9%
2'' Dense Concrete Overlay	2.63	
4'' Dense Concrete Overlay	2.85	Natural Frequency increased by 18%
2'' Overlay+ Shear Keys	3.36	Natural Frequency increased by 39%
4'' Overlay+ Shear Keys	3.59	Natural Frequency increased by 49%



It can be observed that 2'' overlay with shear key increased the natural frequency by 39%. This retrofitting can easily be completed with a relatively lower cost and in shorter time period than the other methods.

## 7.2 Summary of the Retrofitting Methods

A summary of the proposed retrofitting methods is provided in Table 7-13.

Table 7- 13: Summary of the proposed retrofitting methods

Retrofitting methods	Previous application	Traffic closure	Cheap/Costly
<p>Recasting on the girder lines and shear pockets on the panel line</p> 	<p>Previously used on a new concrete bridge, not as a retrofitting method.</p>	<p>Required</p>	<p>Expensive</p>
<p>Recasting on the girder lines and panel lines</p> 	<p>A similar technique was used on a steel bridge in Norway</p>	<p>Required</p>	<p>Expensive</p>
<p>Recasting with additional shear connectors</p> 	<p>A similar technique was used on a steel bridge in Norway</p>	<p>Required</p>	<p>Very expensive</p>
<p>Undercut Anchors</p> 	<p>Never been used/Similar techniques been used in laboratory testing previously</p>	<p>Not required</p>	<p>Moderate</p>

<p style="text-align: center;">Shear Keys</p> 	<p>Previously used on a concrete pedestrian bridge</p>	<p>Not required</p>	<p>Cheap</p>
<p style="text-align: center;">Dense Concrete Overlay</p> 	<p>Regularly used on bridge decks as overlay</p>	<p>Required</p>	<p>Moderate</p>

**7.5 Cost Analysis**

(\*All these costs are estimated based on Average Low Bid Unit Prices of **January 2021** from Texas Department of Transportation following the Standard Specifications for Construction and Maintenance of Highways, Streets, and Bridges, TxDOT. The detailed cost estimation is provided in Appendix D).

**7.5.1 Removing 2” overlay and replacing it with Dense Concrete Overlay**

The cost of this retrofitting depends on the span length and deck width which is shown in Table 7-14.

Table 7- 14: Cost analysis of removing a 2” overlay and replacing it with dense concrete overlay

Span Length →			
Deck Width ↓	50 ft.	100 ft.	150 ft.
50 ft.	70,770 \$	1,41,540 \$	2,12,310 \$
98 ft.	1,38,709 \$	2,77,418 \$	4,16,127 \$
150 ft.	2,12,310 \$	4,24,619 \$	6,36,929 \$

### 7.5.2 Constructing Shear Keys at the end of the Girders (Item 420- Class C Concrete Bent, HPC)

(\*\*Traffic closure is not required)

The cost depends on the number of girders and the girder spacing which is shown in Table 7-15.

Table 7- 15: Cost analysis of constructing shear keys at the end of the girders

No of Girders →			
Girder Spacing ↓	5	11	15
5 ft.	1,117 \$	2,457 \$	3,350 \$
9.5 ft.	2,122 \$	4,668 \$	6,365 \$
15 ft.	3,350 \$	7,371 \$	10,051 \$

### 7.5.3 Removing 12'' wide concrete from the girder line/panel line and replacing it with high strength/regular strength concrete

The cost of this retrofitting depends on the number of girders and the span length which is shown in Table 7-16.

Table 7- 16: Cost analysis of removing 12'' wide concrete from the girder/panel line and replacing it with high strength/regular strength concrete

No of Girders →			
Span Length ↓	5	11	15
50 ft.	13,068 \$	28,750 \$	39,205 \$
100 ft.	26,137 \$	57,500 \$	78,409 \$
150 ft.	39,205 \$	86,250 \$	1,17,614 \$

**7.5.4 Removing 12'' wide concrete from the girder line and replacing it with high strength/regular strength concrete (Adding additional shear rebar)**

Additional 2% cost is assumed for adding additional shear rebar which is shown in Table 7-17.

Table 7- 17: Cost analysis of removing 12'' wide concrete from the girder line and replacing it with high strength/regular strength concrete (Adding additional shear rebar)

No of Girders →			
Span Length ↓	5	11	15
50 ft.	13,330 \$	29,325 \$	39,989 \$
100 ft.	26,659 \$	58,650 \$	79,977 \$
150 ft.	39,989 \$	87,975 \$	119,966 \$

**7.5.5 Removing 24'' wide concrete from the girder line/panel line and replacing it with high strength/regular strength concrete**

The cost of this retrofitting depends on the number of girders and the span length which is shown in Table 7-18.

Table 7- 18: Cost analysis of removing 24'' wide concrete from the girder line and replace it with high strength/regular strength concrete

No of Girders →			
Span Length ↓	5	11	15
50 ft.	26,136 \$	57,500 \$	78,409 \$
100 ft.	52,273 \$	1,15,000 \$	1,56,818 \$
150 ft.	78,409 \$	1,72,500 \$	2,35,227 \$

**7.5.6 Removing 24'' wide concrete from the girder line and replacing it with high strength/regular strength concrete (Adding additional shear rebar)**

Additional 2% cost is assumed for adding additional shear rebar which is shown in Table 7-19.

Table 7- 19: Cost analysis of removing 24'' wide concrete from the girder line and replacing it with high strength/regular strength concrete (Adding additional shear rebar)

No of Girders →			
Span Length ↓	5	11	15
50 ft.	26,659 \$	58,650 \$	79,977 \$
100 ft.	53,318 \$	117,300 \$	159,955 \$
150 ft.	79,977 \$	1,75,954 \$	23,99,32 \$

**7.5.7 Undercut Anchor**

(This was calculated from the Hilti Website)

The final cost of using undercut anchors is shown in Table 7-20.

Table 7- 20: Cost analysis of using undercut anchors

No of Anchors (on both side of the girders)	1 Girder (with GPR)	5 Girders \$ (with GPR)	9 Girders \$ (with GPR)
20	8,505 \$	42,525 \$	76,545 \$
40	16,290 \$	81,450 \$	1,46,610 \$
60	24,075 \$	1,20,375 \$	2,16,675 \$
80	31,860 \$	1,59,300 \$	2,86,740 \$

**\*\* A \$2000 boom lift rent will be added with each final cost.**

## Chapter 8

# CONCLUSION AND RECOMMENDATIONS

### 8.1 Summary

The SH-75 SB Bridge over Wilson Creek in McKinney, Texas was observed to have excessive vibration, cracking and potholes on the concrete deck. A concerned authority from TxDOT requested assistance from the NDE and Load Test team at the University of Texas at Arlington to evaluate the bridge. Since the bridge was built in 2011, it was highly unusual for such a new highway bridge to have such structural issue. Therefore, to evaluate the bridge with vibration issue, a complete testing scheme of NDE evaluation, diagnostic load testing, ambient vibration testing, dynamic vibration testing, Finite Element Modeling, model calibration and retrofitting were prepared and executed successfully.

GPR and IE were used to evaluate the deck condition of the SB Bridge. Span 3 was selected for optimization and most of cracks were found on this span. A cover contour was plotted from GPR, while delamination map was created using IE results. A diagnostic load test was conducted to find out the location of the neutral axis in order to calculate the composite action between the girders and the deck-panel system. A novel method was used to combine the NDE and load test results for the load rating purpose of the girder and the deck. Lastly, a follow-up load test was conducted after a year to observe the rate of deterioration of the bridge.

Ambient vibration testing was conducted under regular traffic on the SB bridge to obtain the maximum accelerations of the girders and the deck in the lateral and vertical directions. In order to compare the results with other control bridges, the SH-75 NB bridge and the West Virginia Parkway bridge were also tested under ambient vibration testing condition. To evaluate the stiffness of the SB bridge, dynamic vibration testing was also conducted to acquire the natural frequency of the bridge.

Static and a dynamic Finite Element Models of the bridge were created in ABAQUS CAE as a representation of the SB bridge. Both models were calibrated using the experimental load tests, NDE and dynamic vibration data to generate an actual field condition of the bridge. Then various unique retrofitting and stiffening methods were modeled and their effectiveness was evaluated.



A rough cost analysis was conducted for the retrofitting and some general recommendations were made. Recommendations future research were also made regarding the vibration study of highway bridges to improve the existing codes and specifications.

## **8.1 Findings and Conclusions**

The NDE evaluation, live load tests, ambient and dynamic vibration tests and Finite Element Modeling yielded enough data to characterize the behavior of the SH-75 SB bridge. The findings and conclusions based on the experiment and Finite Element Modeling are presented in this chapter.

### **8.1.1 NDE and Load Tests**

NDE and Load test were performed on the SH-75 SB over Wilson Creek bridge to evaluate the current condition. The conclusions from the tests are as follows:

- It was found that the bridge exhibited significant vibrations as observed from the strain and rotational readings from the load test. New cracks and a pothole were also observed on the deck.
- The Ground Penetrating Radar B scans showed satisfactory results for top rebar cover of the deck indicating little or no corrosion.
- It was evident from the Impact Echo data that the bridge deck contains delamination. This finding was supported by the load test as the neutral axis of the composite section was found to be in the web. However, according to AASHTO guidelines the neutral axis is supposed to be in the deck.
- The load test also indicates that there is nonlinear behavior in the bridge resulting in residual strain. Non-consistent responses and residual strain show that the structural integrity of the bridge is compromised. Based on the location of the neutral axis, only 9.5% composite action was calculated for the girders. However, the shifting of the neutral axis was insignificant compared to the previous load test.
- The strain gages under the deck showed very little response and very high noise. The noise and the response were almost inseparable due to the vibration of the deck.

- Based on the rating, both the deck and girders were capable of carrying the HS-20 load. However, since the components are not acting monolithically, the serviceability and the durability of the deck are a matter of concern for the bridge.

### **8.1.2 Ambient and Dynamic Vibration Tests**

The following conclusions can be deduced from the dynamic vibration test:

- The maximum accelerations of the girders in the transverse direction under regular rush hour traffic were significantly higher for the SB bridge than the NB and Virginia PKWY bridges. The transverse cracking and the potholes on the SB deck appeared as a result of the higher transverse vibration of the girders.
- Dynamic strains reduced with speeds for path P2 and showed erratic patterns for path P3 during the dynamic load test of Wilson Creek SB bridge. This phenomenon took place due to non-linear, complex load paths introduced as a result of partial composite action between the girders and the deck/panel system.
- The fundamental natural frequency of the SB bridge was significantly lower than the acceptable frequency mentioned in literature. Additionally, reduced stiffness due to partial composite action was the reason behind lower fundamental frequency.
- Calculating the frequencies and mode shapes experimentally is very challenging and sensitive. Even small disturbance on the top of the bridge might affect the data drastically. Therefore, only a single vehicle was allowed on the top during the dynamic load test which yielded more precise data. In addition, all the data were averaged while obtaining the frequencies and mode shapes. This approach yielded reliable data which were used for the calibration of the Finite Element Model.

### **8.1.3 Finite Element Modeling and Retrofitting**

The following conclusions can be deduced from the Finite Element Modeling and Retrofitting:

- The FEM models were calibrated by varying the composite action between the girders and the deck-panel and by adjusting the stiffness of the deck. The strain and rotation values

from the load tests and the natural frequencies from the dynamic vibration tests matched with the calibrated models with little deviation.

- The accuracy of the FEM models was verified by stability check using the residual energy method.
- Recasting on the girder lines and panel lines directly improved the composite action ranging from 70%-91% based on the concrete strength and the recasting length. This method also greatly increased the natural frequency when combined with the shear keys.
- Undercut anchors directly increased the composite action by 70%- 82% based on the numbers of anchors. The anchors also increased the natural frequencies by increasing the stiffness.
- Shear keys, by themselves or combined with other methods, significantly improved the natural frequency of the system. This method is very cheap, does not require any traffic closure and is a highly effective method to reduce lateral vibration.
- Dense concrete overlay reduced the top delamination of the deck and significantly increased the natural frequency when combined with the shear keys.

## **8.2 General Recommendation and Future Research**

### **Assumptions and Limitations:**

The following assumptions were made when proposing the general recommendations:

- All the recommendations were made based on the modeling data of the SB Bridge.
- These recommendations are rough estimation using engineering judgements. Future research is needed to verify and improve the accuracy of the recommendations.

### **1) Recasting on the Girder Line (12''/24'') and Shear Pocket on the Panel Line**

The proposed retrofitting method improves the composite action between the girders and the deck/panel system. The proposed method additionally reduces the delamination of the deck concrete on the girder line.

This method is not effective for bridges where decks and girders are monolithically casted such as box girder bridges. For regular strength casting, 24'' and 12'' recasting improved the composite

action to 70% and 51% respectively from 32%. Based on linear interpolation, the following general recommendations shown in Table 8-1 were made.

Table 8- 1: General recommendation for the proposed retrofitting

Girder Type	Increase of Composite Action (%)
Tx28- Tx54	70
Tx62 & Tx70	80

## 2) Recasting on the Girder Line (12’’/24’’) and the Panel Line

The proposed retrofitting method improves the composite action between the girders and the deck/panel system. The method reduces the delamination of the deck concrete on the girder line and the panel line.

This method is not effective for bridges where decks and girders are monolithically casted such as box girder bridges. For regular strength casting, 24’’ and 12’’ recasting improved the composite action to 79% and 61% respectively from 32%. Based on linear interpolation, the following general recommendations shown in Table 8-2 were made:

Table 8- 2: General recommendation for the proposed retrofitting

Girder Type	Increase of Composite Action (%)
Tx28- Tx54	79
Tx62 & Tx70	88

## 3) Recasting on the Girder Line (12’’/24’’) and the Panel Line with Additional Shear Rebars

The proposed retrofitting method improves the composite action between the girders and the deck/panel system. It also reduces the delamination of the deck concrete on the girder line and the panel line.

This method will not be effective for bridges where decks and girders are monolithically casted such as box girder bridges. For regular strength casting, 24’’ and 12’’ recasting improved the composite action to 83% and 64% respectively from 32%. Based on linear interpolation, the following general recommendations shown in Table 8-3 were made:

Table 8- 3: General recommendation for the proposed retrofitting

Girder Type	Increase of Composite Action (%)
Tx28- Tx54	83
Tx62 & Tx70	93

#### 4) Removing 2” Deck and Replacing with Dense Concrete Overlay

The proposed retrofitting method improves the stiffness of the girders and the deck/panel system. This method also reduces the delamination of the deck concrete on the top of the deck.

This method increases the natural frequency of the deck-girder system from 2.41 Hz. to 2.63 Hz. for an average existing delamination of 30% on the top of the deck. Based on linear interpolation, the following general recommendations shown in Table 8-4 were made:

Table 8- 4: General recommendation for the proposed retrofitting

Average Delamination on the Deck (%)	Increase of Natural Frequency (%)
30	10
50	17
80	27
15	5

#### 5) Constructing Shear Keys at the end of the Girders

The proposed retrofitting method improves the stiffness of the girders and the deck/panel system by providing lateral supports to the system. This is the cheapest retrofitting method to reduce the vibration of highway bridges.

Longer span bridges have low natural frequency and high vibration. Thus, this method will be more effective for shorter span bridges than longer ones. Based on linear interpolation, the following general recommendations shown in Table 8-5 were made:

Table 8- 5: General recommendation for the proposed retrofitting

Span Length	Increase of Natural Frequency (%)
100	22.5
150	15
50	45

**6) Installing Undercut Anchors under the Girders**

The proposed retrofitting method improves the composite action between the girders and the deck/panel system.

Based on linear interpolation, the following general recommendations shown in Table 8-6 were made:

Table 8- 6: General recommendation for the proposed retrofitting

Span Length ↓		Number of Anchors on each side of the Girders			
		20	40	60	80
100	% Increase of Composite Action →	37	43	46	50
150		25	29	31	34
50		74	86	92	100

## Appendix

### Appendix A

#### Theoretical NA Location (Non-Composite)

For an Interior girder (A-F)

No. of strand = 36

$$f_u = 270 \text{ ksi}$$

$$e_{mid} = 18.37''$$

$$f'_c = 6.2 \text{ ksi}$$

The spacing of girders = 9'

Type Tx-54 girder,  $y_t = 30.49''$

$$y_b = 23.51''$$

$$A = 817 \text{ in}^2$$

$$I = 299740 \text{ in}^4$$

$$A_{ps} = 50 * 0.153 = 7.65 \text{ in}^2$$

$$\beta_1 = 0.74$$

$$d_p = y_t + e_{mid} = 30.49 + 18.37 = 48.86''$$

$$C = \frac{A_{sp} f_{pu}}{0.85 f'_c \beta_1 b + k A_{ps} \frac{f_{pu}}{d_p}}$$
$$= \frac{7.65 * 270}{0.85 * 6.2 * 0.74 * 36 + 0.28 * 7.65 * \frac{270}{48.86}}$$
$$= 13.57'' \text{ [from top]}$$

$$\therefore \text{Location of NA from bottom} = 54'' - 13.57'' = 40.43''$$

Theoretical NA Location (Fully Composite)

$$C_{com} = \frac{7.65 * 270}{0.85 * 4 * 0.85 * (9.0 * 12) + 0.28 * 7.65 * \frac{270}{58.36}}$$

$$= 6.08'' \text{ [from top]}$$

$$d_p = y_t + e + 8.25''(t)$$

$$= 48.86 + 9.5$$

$$= 58.36''$$

$$\therefore \text{Location of NA from bottom}$$

$$= 54'' + 9.5'' - 6.08''$$

$$= 57''$$



## Appendix B

### Deck Rating

#### Positive moment capacity:

*Precab*<sup>+</sup> panels width = 7.5'

Length of panel = 8.33'

Panel thickness = 4''

The number of strands:

$$n = \frac{8.33 * 12 - 4''}{6} + 1$$
$$= 17$$

$$\therefore m_n = A_{ps} f_{ps} \left( d_p - \frac{a}{2} \right)$$

$$A_{ps} = 17 * 0.153 = 2.601 \text{ in}^2$$

$$d_p = 8.5 - \frac{4}{2} = 6.5''$$

$$\beta_1 = 0.8$$

$$c = \frac{A_{ps} f_{pu}}{0.85 * f'_c \beta_1 b + k A_{ps} \frac{f_{pu}}{d_p}}$$

$$= \frac{2.601 * 270}{0.85 * 4 * 0.8 * (8.33 * 12) + 0.28 * 2.601 * \frac{270}{6.5}}$$
$$= 2.32''$$

$$a = \beta_1 c = 2.32 * 0.8 = 1.86''$$

$$\therefore f_{ps} = f_{pu} \left( 1 - k \frac{c}{d_p} \right)$$

$$= 270 \left( 1 - 0.28 * \frac{2.32}{6.5} \right)$$

$$= 243.02 \text{ ksi}$$

$$\phi m_n = 1 * 2.601 * 243.02 * \left( 6.5 - \frac{1.86}{2} \right)$$

$$= 3521 \text{ k-in/panel}$$

$$= 293.4 \text{ k-ft/panel}$$

For 1 ft strip →

$$\phi m_n = \frac{293.4 \text{ k-ft}}{8.33 \text{ ft}}$$

$$= 35.22 \text{ k-ft/ft}$$

Applying 30% delamination

$$\phi m_n = 35.22 * 0.7$$

$$\phi m_n = 25 \text{ k-ft/ft}$$

Negative moment capacity:

From GPR, top cover in negative zone = 2.5''

$$d = 9.5 - 2.5 - \frac{5}{8 * 2}$$

$$= 6.6875''$$

#5 @ 6'' O.C.

$$a = \frac{A_s f_y}{0.85 f_c' b}$$

$$= \frac{2 * 0.31 * 60}{0.85 * 4.5 * 12}$$

$$= 0.81''$$

$$\therefore m_n = A_s f_y \left( d - \frac{a}{2} \right)$$

$$= 2 * 0.31 * 60 * \left( 6.6875 - \frac{0.81}{2} \right)$$

$$= 233.8 \text{ k-in/ft}$$

$$= 19.48 \text{ k-ft/ft}$$

Apply 30% delamination →

$$\therefore \phi m_n = 0.7 * 19.48 = 13.64 \text{ k-ft/ft}$$

$$\rho = \frac{A_s}{b_d}$$

$$= 0.012$$

$$\rho_{max} = 0.02$$

$$\rho < \rho_{max}, \text{ tension controlled}$$

Deck Rating:

$$DL = 0.1 * \left( \frac{8.5}{12} * 1' * 0.15 \right) * 9.5^2$$

$$= 0.96 \text{ k-ft}$$

$$LL = 0.8 * \left( \frac{9.5 + 2}{32} \right) * P$$

$$= 4.6 \text{ k-ft}$$

LL equation is for continuous slab, P=16 kip for HS-20.

$$LL + IM = 1.3 * 4.6 \text{ k-ft/ft}$$

$$= 5.98 \text{ k-ft}$$

R.F. For HS-20 (Inventory level):

$$RF = \frac{C - A1XDL}{A2X(LL + IM)}$$

$$= \frac{13.64 - 1.3 * 0.96}{2.17 * 5.98}$$

$$= 0.96 = 1.00$$

Bridge Member rating = 36\*1

= 36 tons

=72,000 lb.

R.F. For HS-20 (Operating level):

$$RF = \frac{C - A1XDL}{A2X(LL + IM)}$$

$$= \frac{13.64 - 1.3 * 0.96}{1.3 * 5.98}$$

$$= 1.6$$

Bridge Member rating =  $36 * 1.6$

= 57.39 tons

= 114,770 lb.

## Appendix C

### Girder Load Rating

#### Dead Load Analysis:

$$SW \text{ of girder} = \frac{817}{144} * 0.15 = 0.851 \text{ k/ft}$$

$$\begin{aligned} \text{Weight of slab + haunch} &= \left[ \frac{9.5}{12} * 9 \right] * 0.15 \\ &= 1.07 \text{ k/ft} \end{aligned}$$

$$\therefore DC_1 = 1.92 \text{ k/ft}$$

$$m_{DC_1} = \frac{1.92 * 100^2}{8} = 2400 \text{ k-ft}$$

$$\text{barrier} = 3.22 * 0.15 * 2 = 0.97 \text{ k/ft}$$

$$\therefore \text{barrier load per beam} = \frac{0.97}{11} = 0.09 \text{ k/ft}$$

$$m_{DC_2} = \frac{0.09 * 100^2}{8} = 112.5 \text{ k-ft}$$

#### Live Load Analysis:

Two or more lanes loaded →

$$\begin{aligned} g_{m_1} &= \frac{S}{5.5} \\ &= 1.72 \end{aligned}$$

Maximum LL effect for HS -20:

HS-20 moment = 762 k-ft. (From AASHTO Manual for Bridge Evaluation)

$$\begin{aligned} I &= \frac{50}{L+125} \leq 0.3 \\ &= \frac{50}{100 + 125} \\ &= 0.22 \end{aligned}$$

$$\begin{aligned} \therefore m_{LL+I} &= 762 * 1.22 * 1.72 \\ &= 1599 \text{ k-ft} \end{aligned}$$

Flexural resistance at mid span: [full composite action assumed]

$$\begin{aligned}d_p &= y_t + haunch + t_s + C_m \\ &= 58.36''\end{aligned}$$

$$\begin{aligned}C &= \frac{A_{ps}f_{pu}}{0.85f'_c\beta_1b + kA_{ps}\frac{f_{pu}}{d_p}} \\ &= 6.08''\end{aligned}$$

$$a = \beta_1C = 0.85 * 6.08 = 5.17'' < t_s$$

Rectangular section behavior

$$\begin{aligned}f_{ps} &= 270 \left( 1 - 0.28 * \frac{6.08}{58.36} \right) \\ &= 262.12 \text{ ksi}\end{aligned}$$

$$\begin{aligned}\therefore m_n &= A_{ps}f_{ps} \left( d_p - \frac{a}{2} \right) \\ &= 7.65 * 262.12 * \left( 58.36 - \frac{5.17}{2} \right) \\ &= 9320 \text{ k-ft}\end{aligned}$$

Rating Assuming Full Composite Action

R.F. For HS-20 (Inventory level):

$$\begin{aligned}RF &= \frac{C - A1XDL}{A2X(LL + IM)} \\ &= \frac{9320 - 1.3 * 2512.5}{2.17 * 1599} \\ &= 1.74\end{aligned}$$

$$\text{Bridge Member rating} = 36 * 1.74$$

$$= 62.64 \text{ tons}$$

$$= 125,280 \text{ lb.}$$

R.F. For HS-20 (Operating level):

$$RF = \frac{C - A1XDL}{A2X(LL + IM)}$$

$$= \frac{9320 - 1.3 * 2512.5}{1.3 * 1599}$$

$$= 2.91$$

$$\text{Bridge Member rating} = 36 * 2.91 \text{ ton}$$

$$= 104.76 \text{ tons}$$

$$= 209,520 \text{ lb.}$$

Flexural resistance at mid span: [Partial-composite action]

$$C = 54'' + 9.5'' - 42''$$

$$= 21.5'', \text{ from top}$$

$$a = \beta_1 C = 0.85 * 21.5$$

$$= 18.275''$$

$$f_{ps} = 270 \left( 1 - 0.28 * \frac{21.5}{58.36} \right)$$

$$= 242.15 \text{ ksi}$$

$$m_n = A_{ps} f_{ps} \left( d_p - \frac{a}{2} \right) + \alpha_1 f'_c (b - b_w) h_f \left( \frac{a}{2} - \frac{h_f}{2} \right)$$

$$= 7.65 * 242.15 * \left( 58.36 - \frac{18.275}{2} \right) + 0.85 * 4(9.5 * 12 - 36) * 8.5 \left( \frac{18.275}{2} - \frac{8.5}{2} \right)$$

$$= 8517 \text{ k-ft}$$

$$\text{Loss of moment capacity} = \frac{9320 - 8517}{9320} * 100 \cong 8.6\%$$

Rating Using Partial-Composite Action:

R.F. For HS-20 (Inventory level):

$$RF = \frac{C - A1XDL}{A2X(LL + IM)}$$

$$= \frac{8517 - 1.3 * 2512.5}{2.17 * 1599}$$

$$= 1.51$$

$$\text{Bridge Member rating} = 36 * 1.51$$

$$= 54.47 \text{ tons}$$

=108,955 lb.

R.F. For HS-20 (Operating level):

$$RF = \frac{C - A1XDL}{A2X(LL + IM)}$$
$$= \frac{8517 - 1.3 * 2512.5}{1.3 * 1599}$$
$$= 2.53$$

Bridge Member rating = 36\*2.53

= 90.93 tons

=181,870 lb.



## Appendix D

### Cost Analysis for Bridge Retrofitting

#### Removing 2” overlay and replacing it with Dense Concrete Overlay:

(\*All these costs are estimated based on Average Low Bid Unit Prices of **January 2021** from Texas Department of Transportation following the Standard Specifications for Construction and Maintenance of Highways, Streets, and Bridges, TxDOT).

##### **a) Removing Concrete: (Item 483)**

“This Item will be measured by the square yard of concrete bridge deck surfaced.”

“The work performed, and equipment furnished in accordance with the Item and measured as provided under “Measurement” will be paid for at the unit price bid for “Milling Concrete Slab” to the depth required, “Hydro Demolition” to the depth required, “Shot Blasting,” “Diamond Grinding Slab,” and “Saw Grooving.” This price is full compensation for removing all material to the depths shown; preparing the surface; texturing the surface; saw grooving the surface; loading, hauling, unloading, and disposing of the cuttings; and equipment, labor, tools, and incidentals.”

**Cost:** Statewide Maximum: 60 \$/SY.

For SH-75 SB Bridge over McKinney, TX (Span 3 only):

Total amount of concrete to be removed = (100\*98) SF

$$= 9800 \text{ SF}$$

$$= 1089 \text{ SY}$$

**Cost** = (1089\*60) = **65,340 \$**

##### **b) Bridge Deck Overlays: (Item 439)**

“**Concrete overlay**, latex-modified concrete overlay, and multi-layer polymer overlay will be measured by the **square yard of surface** overlaid using the dimensions shown on the plans. Overlay is a plans quantity measurement item.”

“Payment for “**Concrete Overlay**” or “Latex-Modified Concrete Overlay” is **full compensation for cleaning surface, furnishing and placing grout; cleaning and restoration of reinforcing steel; furnishing and placing reinforcing steel; and furnishing, placing, finishing and curing the concrete overlay.**”

**Cost:** Statewide Maximum: 102 \$/SY.

For SH-75 SB Bridge over McKinney, TX (Span 3 only):

Total amount of concrete to be placed = (100\*98) SF

= 9800 SF

= 1089 SY

**Cost = (1089\*102) = 111,078 \$**

**c) Traffic Closure: (Item 7148 6003)**

(Assuming 2 lane closure of a 4-lane road, Medium production rate)

Cost= 1000 \$/lane/hour

Removing concrete pavement= 2000 SY/day

Concrete overlay= 300 SY/day

Number of days for removing concrete= 1089/2000= 0.55 day= 13 hours

Number of days for overlay casting= 1089/300= 3.63 days= 88 hours

Total number of hours= 101 hours

Total cost for lane closure= 101\*1000 = 1,01,000 \$

**Total cost= 65,340+ 1,11,078+ 101,000= 2,77,418 \$**

**The cost depends on the span length and deck width.**

<b>Span Length</b> →			
<b>Deck Width</b> ↓	50 ft.	<b>100 ft.</b>	150 ft.
50 ft.	70,770 \$	1,41,540 \$	2,12,310 \$
<b>98 ft.</b>	1,38,709 \$	<b>2,77,418 \$</b>	4,16,127 \$
150 ft.	2,12,310 \$	4,24,619 \$	6,36,929 \$

**Constructing Shear Keys at the end of the Girders (Item 420- Class C Concrete Bent, HPC):**

(\*All these costs are estimated based on Average Low Bid Unit Prices of **January 2021** from Texas Department of Transportation following the Standard Specifications for Construction and Maintenance of Highways, Streets, and Bridges, TxDOT).

(\*\*Traffic closure is not required)

“This Item will be measured by the cubic yard, square yard, foot, square foot, or by each structure.”

“The work performed and materials furnished in accordance with this Item and measured as provided under “Measurement” will be paid for at the unit price bid for the class of concrete and element identified and by the special designation when appropriate. This price is full compensation for furnishing, hauling, and mixing concrete materials; furnishing, bending, fabricating, splicing, welding and placing the required reinforcement; clips, blocks, metal spacers, ties, wire, or other materials used for fastening reinforcement in place; furnishing, placing, and stressing post-tensioning system; placing, finishing, and curing concrete; mass placement controls; applying ordinary surface finish; furnishing and placing drains, metal flashing strips, and expansion-joint material; excavation, subgrade preparation; and forms and falsework, equipment, labor, tools, and incidentals

**Cost:** Statewide Maximum: 1010.27 \$/CY.

For SH-75 SB Bridge over McKinney, TX (Span 3 only):

Amount of concrete per shear key =  $(15 \times 82 \times 8.75 / 1728)$  CF

= 6.23 CF

(Length of each key= 15’’

Width of each key= 82’’

Height of each key= 8.75’’)

Total number of shear key for span 3= 10\*2= 20 (11 girders, 10 shear keys, 2 bents)

Total amount of concrete= 6.23\*20 CF

=124.6 CF

= 4.62 CY

**Total Cost = (4.62\*1010.27) = 4,668 \$**

**The cost depends on the number of girders and the girder spacing.**

<b>No of Girders</b> →			
<b>Girder Spacing</b> ↓	5	<b>11</b>	15
5 ft.	1,117 \$	2,457 \$	3,350 \$
<b>9.5 ft.</b>	2,122 \$	<b>4,668 \$</b>	6,365 \$
15 ft.	3,350 \$	7,371 \$	10,051 \$

**Removing 12’’ wide concrete from the girder line/panel line and replace it with high strength/regular strength concrete:**

(\*All these costs are estimated based on Average Low Bid Unit Prices of **January 2021** from Texas Department of Transportation following the Standard Specifications for Construction and Maintenance of Highways, Streets, and Bridges, TxDOT).

**a) Concrete Structure Repair (Deck Repair, Full Depth): (Item 429)**

“This Item will be measured by the square foot, in place, as measured on the specified horizontal, vertical, or overhead surfaces of the completed repair as shown below or by the cubic yard for full element or member replacement. When a repair involves multiple surfaces, such as a corner,

measurement will be made of all surfaces repaired. Bridge deck repairs will be measured by the square foot in place of the completed repair.”

“The work performed and materials furnished in accordance with this Item and measured as provided under “Measurement” will be paid for at the unit price bid for “Concrete Structure Repair” of the kind specified. This price is full compensation for furnishing, placing, and curing all repair materials; removing concrete; saw cutting; cleaning reinforcing steel; supplying and installing replacement or supplemental reinforcing steel, drive pins, studs, or expansion bolts; and equipment, labor, and incidentals.”

**Cost:** Statewide Maximum: 305 \$/SY.

For SH-75 SB Bridge over McKinney, TX (Span 3 only):

For one girder, amount of concrete to be repaired=  $(100 \times 12/12) = 100 \text{ SF} = 11.12 \text{ SY}$

**Cost** =  $(11.12 \times 305) = \mathbf{3,392 \$}$

For all girders (9, excluding two exteriors), amount of concrete to be repaired=  $(100 \times 9) = 900 \text{ SF} = 100 \text{ SY}$

**Cost** =  $(100 \times 305) = \mathbf{30,500 \$}$

For alternate girders (5, excluding two exteriors), amount of concrete to be repaired=  $(100 \times 5) = 500 \text{ SF} = 55.56 \text{ SY}$

**Cost** =  $(55.56 \times 305) = \mathbf{16,946 \$}$

**b) Traffic Closure: (Item 7148 6003)**

(Assuming 2 lane closure of a 4-lane road, Medium production rate)

Cost= 1000 \$/lane/hour

Removing concrete = 280 CY/day

Bridge Deck= 900 SF/day

Removed Concrete for 9 girders=  $900 \text{ SF} = (900 \times 9.5/12) = 712.5 \text{ CF} = 26.39 \text{ CY}$

Number of days for removing concrete for 9 girders=  $(26.39/280) = 3 \text{ hours}$

Number of days for deck casting for 9 girders= 900/900= 24 hours

Total number of hours= 27 hours

Total cost for lane closure= 27\*1000 = **27,000 \$**

**Total Cost= 30,500+ 27,000= 57,500 \$**

**The cost depends on the number of girders and the span length.**

No of Girders →			
Span Length ↓	5	<b>11</b>	15
50 ft.	13,068 \$	28,750 \$	39,205 \$
<b>100 ft.</b>	26,137 \$	<b>57,500 \$</b>	78,409 \$
150 ft.	39,205 \$	86,250 \$	1,17,614 \$

**Removing 12'' wide concrete from the girder line and replace it with high strength/regular strength concrete (Adding additional shear rebar):**

Additional 2% cost is assumed for adding additional shear rebar:

No of Girders →			
Span Length ↓	5	<b>11</b>	15
50 ft.	13,330 \$	29,325 \$	39,989 \$
<b>100 ft.</b>	26,659 \$	<b>58,650 \$</b>	79,977 \$
150 ft.	39,989 \$	87,975 \$	119,966 \$

**Removing 24'' wide concrete from the girder line/panel line and replace it with high strength/regular strength concrete:**

(\*All these costs are estimated based on Average Low Bid Unit Prices of **January 2021** from Texas Department of Transportation following the Standard Specifications for Construction and Maintenance of Highways, Streets, and Bridges, TxDOT).

**The cost depends on the number of girders and the span length.**

No of Girders →			
Span Length ↓	5	11	15
50 ft.	26,136 \$	57,500 \$	78,409 \$
100 ft.	52,273 \$	1,15,000 \$	1,56,818 \$
150 ft.	78,409 \$	1,72,500 \$	2,35,227 \$

**Removing 24” wide concrete from the girder line and replace it with high strength/regular strength concrete (Adding additional shear rebar):**

Additional 2% cost is assumed for adding additional shear rebar:

**The cost depends on the number of girders and the span length.**

No of Girders →			
Span Length ↓	5	11	15
50 ft.	26,659 \$	58,650 \$	79,977 \$
100 ft.	53,318 \$	117,300 \$	159,955 \$
150 ft.	79,977 \$	1,75,954 \$	23,99,32 \$

**Undercut Anchor:**

(This was calculated from the Hilti Website)

**For every 40 anchors (20 anchors on both side of a girder):**

Undercut anchor HAD-P M20 x 250/50- 2 pc (40)- Price 5920 \$

Setting tool HAD M20 w/TE-Y- 1 pc- Price 204 \$

Stop drill bit TE-Y-HAD-B 37 x 250- 1 pc- Price 1602 \$

Blow-out-pump- 1 Pc- Price 59 \$

**Total cost = 5920+ 204+ 1602+ 59 = 7,785 \$**

**For every 80 anchors (40 anchors on both side of a girder):**

**Total cost =  $7,785 \times 2 = 15,570$  \$**

**For every 120 anchors (60 anchors on both side of a girder):**

**Total cost =  $7,785 \times 3 = 23,355$  \$**

**For every 160 anchors (80 anchors on both side of a girder):**

**Total cost =  $7,785 \times 4 = 31,140$  \$**

Additional cost:

GPR scanning cost=  $(80+160)/\text{hour} = 240$  \$/hour [One technician 80 \$/hour and one Engineer 160 \$/hour]

Total/Girder=  $240 \times 3 = 720$  \$

Boom lift rent = 2000 \$

No of Anchors (on both side of the girders)	1 Girder (with GPR)	5 Girders \$ (with GPR)	9 Girders \$ (with GPR)
20	8,505 \$	42,525 \$	76,545 \$
40	16,290 \$	81,450 \$	1,46,610 \$
60	24,075 \$	1,20,375 \$	2,16,675 \$
80	31,860 \$	1,59,300 \$	2,86,740 \$

**\*\* A 2000 \$ boom lift rent will be added with each final cost.**



## References

1. AASHTO (2017). *Load resistance and factor design: Bridge design specifications*, 8th ed., American Association of State Highway and Transportation Officials, Washington, D.C.
2. AASHTO (2018). *The Manual For Bridge Evaluation*, 3<sup>rd</sup> Edition, American Association of State Highway and Transportation Officials, Washington, D.C.
3. ABAQUS (2018). *ABAQUS standard user's manual*. Version 6.14, vol. I–III. Pawtucket (America): Hibbitt, Karlsson & Sorensen, Inc.
4. Albraheemi, M. (2018), *Evaluation of Non-Composite Steel Girder Bridges Using Field Load Testing and a Calibrated Finite Element Model*, Electronic Theses and Dissertations, The University of Maine.
5. Austroads (1996). *Australian bridge design code*, Austroads, Haymarket, NSW, Australia.
6. Amman, W. (1995). *Vibration induced by traffic and construction activity - bridge*, *Vibration Problems in Structures: Practical Guidelines*, Birkhauser, Boston, 125-127.
7. American Association of State Highway and Transportation Officials. (2018). *Manual for Bridge Evaluation, 3<sup>rd</sup> Edition*” C3, Washington, DC.
8. Alampalli (2001). *Correlation Between Bridge Vibration and Bridge Deck Cracking: A Qualitative Study*. Special report 136, Transportation Research and Development Bureau, New York State Department of Transportation, George E. Pataki, Governor/ Joseph H. Boardman, Commissioner.
9. American Association of State Highway and Transportation Officials. (2016). *Manual for Bridge Evaluation, 2nd Edition*, with 2011, 2013, 2014, 2015, and 2016 Interim Revisions.” C3, Washington, DC.

10. Benzeggagh, M. L., and M. Kenane (1996), *Measurement of Mixed-Mode Delamination Fracture Toughness of Unidirectional Glass/Epoxy Composites with Mixed-Mode Bending Apparatus*, Composites Science and Technology, vol. 56, pp. 439–449, 1996.
11. Barr, P. J., Woodward, C. B., Najera, B., & Amin, M. N. (2006). *Long-term structural health monitoring of the San Ysidro Bridge*. Journal of performance of constructed facilities, 20(1), 14-20.
12. Bujnakova, P., Jost, J., Farbak, M. (2018). *Load testing of Highway Bridges*. MATEC Web of Conferences 196, 02020, XXVII R-S-P Seminar 2018, Theoretical Foundation of Civil Engineering. DOI: 10.1051/mateconf/201819602020.
13. Bakht, B., & Jaeger, L. G. (1990). *Bridge testing—A surprise every time*. Journal of Structural Engineering, 116(5), 1370-1383.
14. Barker, M. G. and Staebler, J. (2011). *Serviceability Limits and Economical Steel Bridge Design*. US Department of Transportation, Federal Highway Administration, Publication No. FHWA-HIF-11-044.
15. Billing, J. R. and Green, R. (1984). *Design provisions for dynamic loading of highway bridges*, Transportation Research Record 950.
16. Barr, P. J., Woodward, C. B., Najera, B., & Amin, M. N. (2006). *Long-term structural health monitoring of the San Ysidro Bridge*. Journal of performance of constructed facilities, 20(1), 14-20.
17. CSiBridge (2015). *Introduction to CSiBridge*. Computer & Structures, Inc.
18. CEB-FIP Model Code (1990). *Design Code*. Comité euro-international du béton, Fédération Internationale de la Précontrainte T. Telford, 1993 - Technology & Engineering

19. Cicekli, U., Voyiadjis, G. Z., and Abu Al-Rub, R. K. (2007). *A plasticity and anisotropic damage model for plain concrete*. Int. J. Plast., 23(10–11), 1874–1900.
20. Chung, W., & Sotelino, E. D. (2006). *Three-dimensional finite element modeling of composite girder bridges*. Engineering Structures, 28(1), 63-71.
21. CSA (1990). *CSA. S6- 88 and commentary, Design of Highway Bridges, Canadian Standards Association*, Rexdale, Ontario, Canada.
22. Chung, W., & Sotelino, E. D. (2006). *Three-dimensional finite element modeling of composite girder bridges*. Engineering Structures, 28(1), 63-71.
23. C.R. Farrar, C. R. and James III, G.H. (1997). *System identification from ambient vibration measurements on a bridge*, J. of Sound and Vibration, 205(1), 1–18.
24. Citak, S.O., Ohori, M. and Nakamura, T. (2012). *Microtremor measurements and earthquake response analysis on Urado Bridge*, The 15th World Conferences of Earthquake Engineering LISBOA, Kochi, Japan.
25. Collin, P., Häggström, J. & Hällmark, R. (2015). *International Workshop on Strengthening of Steel/Composite bridges*, Lulea: Lulea University of Technology.
26. Craig, R. E., Kennedy Reid, I. L. & Milne, D. M. (2001). *Steel Bridge Strengthening: a study of assessment and strengthening experience and identification of solutions*. London: Thomas Telford Ltd.
27. Collin, P., Häggström, J. & Hällmark, R. (2015). *International Workshop on Strengthening of Steel/Composite bridges*, Lulea: Lulea University of Technology.
28. Damodarasamy, S.R. and Kavitha, S. (2009). *Basic of Structural Dynamics and Seismic Design*, PHI Learning, New Delhi.

29. El Shahawy, M., and Garcia, A. M. (1989). *Structural research and testing in Florida*. Structural Res. Rep. No. SRR-01-89, Fla. Dept. of Transp., Tallahassee, Fla
30. Fountain, R. S. and Thunman, C. E. (1987). *Deflection criteria for steel highway bridges*, Proceedings of the AISC National Engineering Conference in New Orleans.
31. Farrar, C.R., Duffey, T.A., Cornwell, P.J. and Doebling, S.W. (1984). *Excitation methods for bridge structures*, 1063–1068.
32. Fu, G., Sardis, P., and Tang, I. (1992). *Proof testing of highway bridges*. Res. Rep. 153, Engineering. Res. and Development Bureau, N.Y. State Dept. of Transp., Albany, N.Y.
33. Grassl, P., and Jirásek, M. (2006). *Damage-plastic model for concrete failure*. Int. J. Solid. Struct., 43(22–23), 7166–7196.
34. Gaunt, J. T. and Sutton, C. D. (1981). *Highway bridge vibration studies, Joint Highway Research Project (Report No. JHRP–81-11)*, Purdue University & Indiana State Highway Commission.
35. Goldman, D. E. (1948). *A review of subjective responses to vibratory motion of the human body in the frequency range 1 to 70 cycles per second*, Naval Medical Research Institute National, Naval Medical Center. Bethesda, Maryland.
36. Grimmelman, K.A. (2006). *Experimental characterization of towers in cable-supported bridges by ambient vibration testing*, PhD Thesis, Drexel University.
37. Gucunski, N., Romero, F. A., Shokouhi, P., Makresias, J. (2005). *Complementary Impact Echo and Ground Penetrating Radar Evaluation of Bridge Decks on I-84 Interchange in Connecticut*. GSP 133 Earthquake Engineering and Soil Dynamics, ASCE.

38. Gucunski, N., Slabaugh, G. G., Wang, Z., Fang, T. and Maher, A. (2008). *Impact echo data from bridge deck testing: Visualization and interpretation*. Transportation Research Record(2050), pp. 111-121. doi: 10.3141/2050-11
39. Gucunski, N., Wang, Z., Fang, T. and Maher, A. (2009). *Rapid Bridge Deck Condition Assessment Using Three-Dimensional Visualization of Impact Echo Data*. NDTCT'09, Non-Destructive Testing in Civil Engineering Nantes, France, June 30<sup>th</sup>- July 3<sup>rd</sup>, 2009.
40. Hag-Elsafi, O., Kunin, J. (2006). *Load Testing for Bridge Rating: Route 22 Over Swamp River*. New York State Department of Transportation, 50 Wolf Road, Albany, NY 12232.
41. Hasan, M. I., Yazdani, N. (2015). *Experimental Study for Quantitative Estimation of rebar Corrosion in Concrete Using Ground Penetrating Radar*. Hindawi Publishing Corporation, Journal of Engineering, Volume 2016, Article ID 8536850.
42. Hasan, M. I., Yazdani, N. (2014). *Ground Penetrating Radar Utilization In Exploring Inadequate Concrete Covers In A New Bridge Deck*. Case Studies in Construction Materials, Elsevier. DOI: <http://dx.doi.org/doi:10.1016/j.cscm.2014.04.003>, Reference: CSCM 8
43. Harik, I.E., Allen, D.L., Street, R.L., Guo, M., Harison, J. and Gawry, M.J. (1997) *Free and ambient vibration of Brent-Spence bridge*, J. of Structural Engineering, 123, 1262–1268.
44. ISO 2631 (1997). *Mechanical vibration and shock - Evaluation of human exposure to whole-body vibration*. Part 1 General requirements, International Standard ISO-2631/1, Geneva, Switzerland.
45. Irwin A. (1978). *Human response to dynamic motion of structures*. Structural Engineers, Vol. 56A, No. 9, pp. 237-44.

46. Kee, S. H., Oh, T., Popvics, J. S., Arndt, R. W., Zhu, J. (2012). *Nondestructive Bridge Deck Testing with Air-Coupled Impact-Echo and Infrared Thermography*. Journal of Bridge Engineering, 17 (6): 928-939, ASCE, DOI: 10.1061/(ASCE) BE.1943-5592.000350
47. Krstevska, L.S., Kustura, M. and Tashkov, L.A. (2008) *Experimental in-situ testing of reconstructed old bridge in Mostar*, The 14th World Conference on Earthquake Engineering, Beijing, China, 1-8.
48. Kwon, G., Engelhardt, M. D. & Klingner, R. E. (2009). *Implementation Project: Strengthening of a Bridge near Hondo, Texas using Post-Installed Shear Connectors*, Austin, Texas: The University of Texas at Austin.
49. Kwon, G. et al. (2007). *Strengthening Existing Non-Composite Steel Bridge Girders Using Post-Installed Shear Connectors*. Austin: The University of Texas at Austin.
50. Lubliner, J., Oliver, J., Oller, S., & Onate, E. (1989). *A plastic-damage model for concrete*. International Journal of solids and structures, 25(3), 299-326
51. Lichtenstein, A. G. (1995). *Bridge rating through nondestructive load testing*. National Cooperative Highway Research Program Project, 12-28.
52. Lin, C.W. and Yang, Y.B. (2005). *Use of a passing vehicle to scan the fundamental bridge frequencies: An experimental verification*, Engineering Structures, 27(13), 1865–1878.
53. Le, H. X. and Hwang, E.S. (2017). *Investigation of Deflection and Vibration Criteria for Road Bridges*, KSCE Journal of Civil Engineering, Korean Society of Civil Engineers, DOI 10.1007/s12205-016-0532-3, Vol. 21, No.3.
54. Lucas, J., Cousins, T., E., Brown, M., C., Sharp, S., R., Lane, D., S. (2004). *Structural Load Testing and Flexural Analysis of the Route 701 Bridge in Louisa county, Virginia*. Virginia Transportation Research Council, Charlottesville, Virginia.

55. Mabsout, M. E., Tarhini, K. M., Frederick, G. R., & Tayar, C. (1997). *Finite-element analysis of steel girder highway bridges*. Journal of Bridge Engineering, 2(3), 83-87.
56. Matta, F., Bastianini, F., Galati, N., Casedei, P., Nanni, A. (2005). *In-site Load Testing of Bridge A6358 (Part 1) and of Bridge A6101 and Bridge A6102 (Part 2)*. MODOT Research Development and Technology, 1617 Missouri Blvd, Jefferson City, MO 65109.
57. Markey, I. (1991). *Load testing of Swiss bridges*. Steel Construction Today, 5(1), 15-20.
58. Moses, E, Lebet, J. P., and Bez, R. (1994). *Applications of field testing to bridge evaluation*. Journal of Structural Engineering, ASCE, 120(6), 1745-1762
59. Mallock, H. R. A. (1902). *Vibrations produced by the working of traffic on the central London railway*, Board of Trade Report, Command Papers, n. 951.
60. Mabsout, M. E., Tarhini, K. M., Frederick, G. R., & Tayar, C. (1997). *Finite-element analysis of steel girder highway bridges*. Journal of Bridge Engineering, 2(3), 83-87.
61. MLTM (2010). *Korean highway bridge design code*, Korea Ministry of Land, Transportation and Maritime Affairs, Seoul, Korea.
62. Malla, R.B, Jacobs, D., Dhakal, S., Baniya, S. (2017). *Dynamic Impact Factors on Existing Long Span Truss Railway Bridges, Final report for rail safety IDEA project 25*, Transportation Research Board.
63. Mohseni, I., Ashin, A., Choi, W., Kang, J. (2018). *Development of Dynamic Impact Factor Expressions for Skewed Composite Concrete-Steel Slab-On-Girder Bridges*, Hindawi, Advances in Material Sciences and Engineering, Volume 2018, Article ID 4313671, 9 Pages.

64. Nagayama, T., Reksowardojo, A., P., Su, D., Mizutani, T., Zhang, C. (2015). *Bridge Natural Frequency Estimation by Extracting the Common Vibration Component from the Response of Two Vehicles*, 6<sup>th</sup> International Conference on Advances in Experimental Structural Engineering, University of Illinois, Urbana-Champaign, United States.
65. Neitzel, F., Resnik, B., Weisbrich, S., Friedrich, A. (2011). *Vibration Monitoring of Bridges*, *Reports on Geodesy*, Volume 90, Issue 1, Page 331-340.
66. Nguen, T., X., Tran, D., V. (2015) *Determination of Dynamic Impact Factor for Continuous bridge and Cable-stayed bridge due to vehicle braking force with experimental investigation*, 16th Asia Pacific Vibration Conference, Hanoi, Vietnam.
67. Olsson, D., 2017, *Achieving Composite Action in Existing Bridges With post installed-shear connectors*, Civil Engineering Masters level, Luleå University of Technology Department of Civil, Environmental and Natural Resources Engineering.
68. Oehler, L. T. (1970). *Bridge vibration – summary of questionnaire to state highway departments*, Highway Research Circular, Highway Research Board (No. 107).
69. Peiris, A. & Harik, I. (2011). *Innovative Retrofit for Upgrading Reinforce Concrete Deck on Non-Composite Steel Girder Bridges*. Singapore, CI-Premier PTE LTD.
70. RADAN (2017). *RADAN 7 Manual*. Geophysical Survey System. Inc, 40 Simon Street, Nashua, NH, USA.
71. Raju, R. K., Hasan, I., Yazdani, N. (2018). *Quantitative Relationship Involving Reinforcing Bar Corrosion and Ground-Penetrating Radar Amplitude*. ACI Materials Journal 115 (3), DOI: 10.14359/51702187.
72. Roeder, C. W., Barth, K. B., and Bergman, A. (2002). *Improved live load deflection criteria for steel bridges*, Final Report NCHRP 20-07/133, University of Washington, Seattle, WA.



73. Ren, W., Peng, X. and Lin, Y. (2005). *Experimental and analytical studies on dynamic characteristics of a large span cable-stayed bridge*, *Engineering Structures*, 27(4), 535–548.
74. Ren, W., Sneed, L., H., Yang, Y., He, R. (2015). *Numerical Simulation of Prestressed Precast Concrete Bridge Deck Panels Using Damage Plasticity Model*. *International Journal of Concrete Structures and Materials*, Vol.9, No.1, pp. 45-54, DOI 10.1007/240069-014-0091-2.
75. SAP2000 (2016). *CSI Analysis Reference Manual*. Computer & Structures, Inc.
76. Schulz, J. L. (1993). *In search of better load ratings*. *Civil Engineering*, 63(9), 62.
77. Siringoringo, D., Fujiano, Y. (2012). *Estimating Bridge Fundamental Frequency from Vibration Response of Instrumented Passing Vehicle: analytical and Experimental Study*, *Advances in Structural Engineering*, DOI 10.1260/1369-4332-15.3.417.
78. Schulz, J. L. (1993). *In search of better load ratings*. *Civil Engineering*, 63(9), 62.
79. Sinoars (2016). [Online] Available at: <http://www.sinoars.com/wp-content/uploads/2015/11/shear-stud-weld-to-beam-process.jpg>.
80. Szerszen, M., M., Linzell, D., G., Azam, S., E., Al-Hajami, A., Steelman, J., Wood, R., L. (2019). *Protocol to Evaluate and Load Rate Existing Bridges Using Field Testing*, NTRC Project, SC-11. NEBRASKA Department of Transportation.
81. University of Ljubljana, 2016. [Online] Available at: <http://www.fgg.uni-lj.si/~pmoze/esdep/master/wg10/10100.htm>.
82. TxDOT Bridge Division (2009). *The Perfect Storm: Lateral Vibration of a TxDOT Pedestrian Bridge*, Dean Van Landuyt.

83. Veljkovic, M., Markovic, Z., Spremic, M. & Pavlovic, M. (2013). *Headed shear studs versus highstrength bolts in prefabricated composite decks*. Palm Cove, Australia, s.n.
84. Wright, D. T. and Green, R. (1964). *Highway bridge vibration. Part II: Report No. 5 Ontario test program*, Ontario Department of Highways and Queen's University, Kingston, Ontario.
85. Wright, R. N. and Walker, W. H. (1971). *Criteria for the deflection of steel bridges, Bulletin for the American Iron and Steel Institute*, No. 19.
86. Yost, J. R., Schulz, J. L., & Commander, B. C. (2005). *Using NDT data for finite element model calibration and load rating of bridges*. In Structures Congress 2005: Metropolis and Beyond (pp. 1-9).
87. Yost, J. R., Schulz, J. L., & Commander, B. C. (2005). *Using NDT data for finite element model calibration and load rating of bridges*. In Structures Congress 2005: Metropolis and Beyond (pp. 1-9).
88. Zenunovic, D., Topalovic, M., Folic, R. (2015). *Identification of Modal Parameters of Bridges Using Ambient Vibration Measurements*, Hindawi Publishing Corporation, Shock and Vibration, Volume 2015, Article ID 957841, 21 Pages.
89. Zaki, A., Johari, M. A. M., Hussin, W. M. A. W., Jusman, Y. (2018). *Experimental Assessment of Rebar Corrosion in Concrete Using Ground Penetrating Radar (GPR)*. Hindawi, International Journal of Corrosion, Volume 2018, Article ID 5389829.